Doctoral theses at NTNU, 2021:187

Kristian Fredrik Klepp Thorbjørnsen

Iridium-based electrocatalysts for PEM water electrolysis prepared via galvanic displacement

Doctoral thesis

NTNU
Norwegian University of Science and Technology
Thesis for the Degree of
Philosophiae Doctor
Faculty of Natural Sciences
Department of Materials Science and Engineering

NTNU
Norwegian University of
Science and Technology

Kristian Fredrik Klepp Thorbjørnsen

Iridium-based electrocatalysts for PEM water electrolysis prepared via galvanic displacement

Thesis for the Degree of Philosophiae Doctor

Trondheim, May 2021

Norwegian University of Science and Technology
Faculty of Natural Sciences
Department of Materials Science and Engineering

NTNU
Norwegian University of
Science and Technology

NTNU
Norwegian University of Science and Technology

Thesis for the Degree of Philosophiae Doctor

Faculty of Natural Sciences
Department of Materials Science and Engineering

ISBN 978-82-326-6931-8 (printed ver.)
ISBN 978-82-326-5812-1 (electronic ver.)
ISSN 1503-8181 (printed ver.)
ISSN 2703-8084 (online ver.)

Doctoral theses at NTNU, 2021:187

Printed by NTNU Grafisk senter

Acknowledgements

Funding through contract no. 254976 "Metal(-oxide) catalyst-monolayer as cost-effective electrocatalysts for PEM water electrolysis" from the Research Council of Norway is greatly appreciated.

The Research Council of Norway is acknowledged for the support to the Norwegian Micro- and Nano-Fabrication Facility, NorFab, project number 295864.

During my almost five years as a PhD student, I have recieved great help and assistance from the people around me.

First my supervisor, professor Svein Sunde. Your insight in theoretical electrochemistry and materials science has helped me understand the fundamentals of my research. I really enjoyed our common preference for coding everything from plots to presentations.

My co-supervisor, Dr. Magnus Thomassen, has provided valuable input to my work during the weekly project meetings.

SINTEF Industry, Sustainable Energy has been part of the project. I want to give credit to Dr. Julian Tolchard, who has been my main source of knowledge for everyting related to electron microscopy, X-ray diffraction and other things not-electrochemistry. Dr. Tor Olav Sunde, Dr. Anita Hamar Reksten and others have provided valuable input and insigt during the project meetings. Dr. Thulile Khoza has been a great discussion partner regarding experimental electrochemistry.

To Dr. Maidhily Manikandan and Dr. Gurvinder Singh; thank your for assisting me through the first chapter of this thesis.

Engineers Magnus B. Følstad (former), Agnes Digranes (current) and Anita Storsve has all been of great help in everything related to laboratory operations and in helping me get various experimental setups running.

The professors in the electrochemistry group deserves a thank you for being unknowing participants in my game of "find a free professor", which was initiated

if Svein was nowhere to be found and I needed someone to talk to about some electrochemistry problem.

During my years as a PhD student, I have consumed an obscene amount of coffee, so the coffee maker in K1 deserves a thank you. I hope to never see a news article about the health risks of caffeine.

Last, but not least, I would like to thank my fiancee, Karina Asheim, for putting up with my workaholic tendencies while also working on her own PhD. As my time as a PhD student is now over, you will never have to listen to any monologues about theoretical electrochemistry ever again... or at least you don't have to pretend that you are listening. A special thank you goes to our daughter, Katrine Klepp Asheim, for mostly sleeping through the night.

Abstract

In the transition away from non-renewable energy sources, the use of fluctuating power sources such as wind and solar are increasing. This creates a need for temporary storage of excess energy when production exceeds demand. Excess energy can be used to electrochemically convert water into hydrogen and oxygen, which has several uses and can easily be converted back to electricity in a fuel cell.

The current state of the art PEM water electrolyzers contain various expensive components, one of which is the Ir catalyst at the anode. Reducing the initial investment cost of water electrolyzers will help reducing the overall cost of an energy grid based on renewable sources. There are currently no viable replacements for the Ir catalyst at the anode, so cost reduction must necessarily come from reducing the usage without sacrificing performance.

Core/shell catalysts where Ir is applied as a thin film on a suitable substrate is a promising way to significantly reduce the Ir usage without sacrificing performance. Galvanic displacement has emerged as a suitable method to prepare such catalysts.

In this thesis, we explore how galvanic displacement can be used to prepare core/Ir-shell catalysts for the oxygen evolution reaction at PEM water electrolyzer anodes. We show how Ni-core/Ir-shell electrocatalysts easily can be prepared in an aqueous procedure and how the initial particle size of the Ni core is a critical parameter in the synthesis. Further, we show how Cu can be used as a template- and reducing agent to prepare Cu-core/Ir-shell electrocatalysts, where the procedure is more robust than when using Ni.

Electrocatalysts are preferably distributed on a support as nanoparticles to maximize the electrochemical surface area (ECSA) per geometric surface area. We show that insufficient electronic conductivity in the support will render the catalyst inactive.

Through galvanic displacement of Cu monolayers on Au and Pd electrodes, and Au and Pd nanoparticles with Ir, we show how thin films of Ir can be prepared on

suitable substrates. The resulting catalysts are highly active towards the oxygen evolution reaction and demonstrate how not only the activity, but also the *stability* of the catalysts are of critical importance. Moreover, we show how hydrogen absorption into Pd can be utilized to cover Pd with metallic Ir.

We also show how microkinetic simulations are a powerful tool which allows us to model both kinetics *and* mass transport in galvanic displacement reaction systems.

In the end, a procedure for preparation of oxide supported core/Ir-shell electrocatalysts are suggested.

Preface

This thesis is a summary of research carried out at the department of Materials Science and Engineering at the Norwegian University of Science and Technology between August 2016 and March 2021.

The thesis is divided into four main parts. Part I contains two chapters; Introduction and Experimental methods.

Chapter 1: Introduction, is a summary of the most important literature which forms the basis for the research in parts II and III. Chapter 2 contains a short introduction to the most important experimental methods used in this thesis.

Parts II and III are separated into eight chapters in total, and contains the scientific work presented in this thesis.

Chapters 6, 9 and 10 are written up as complete manuscripts or first drafts, and contains therefore introductions summarizing the most important literature related to the work presented in the chapter.

Chapter 3: Galvanic displacement of carbon supported Ni by Ir; contains a summary of work carried out spring/summer 2017. Carbon supported Ni nanoparticles were prepared by postdoctoral researcher Dr. Maidhily Manikandan. Imaging of the samples in a S(T)EM was done by postdoctoral researchers Dr. Maidhily Manikandan and Dr. Gurvinder Singh. All other work was performed by myself.

Chapter 4: Galvanic displacement of Cu and Ni on titanium oxides by Ir; contains a summary of work carried out from spring 2017 until autumn 2018. Doped and exsolved titanium oxides were prepared by researcher Dr. Julian Richard Tolchard from SINTEF Industry, Sustainable Energy. Imaging of samples in the S(T)EM was done by, or with the assistance of, Dr. Julian Richard Tolchard. All other work was performed by myself.

Chapter 5: Galvanic displacement of Cu by Ir; contains a summary of work performed from autumn 2017 to spring 2018, where all the work was performed by myself.

Chapter 6: Ir deposition by galvanic displacement of Cu in a one-pot configuration: This chapter contains a summary of work performed from 11th of October 2018 until spring 2019. It is written up as a complete manuscript intended for submission to Journal of the Electrochemical Society, but with one important detail missing. It became clear that DFT calculations were necesarry in order to answer an important question related to different aqueous complexes involed in the experiments. This was outside the scope if this thesis, and so the calculations are currently being performed by professor Svein Sunde. The results from those calculations will be included in the final submission, but is expected to only cause minor changes to the discussion. AFM was performed under supervision by master student Jens Sørensen. All electrochemical experiments was performed by myself.

Chapter 7: Investigation of the Ir-Cu SLRR system: This chapter is a natural continuation of chapter 6 and was performed autumn 2019, and three days in June 2020. It contains a somewhat crude optimization of a procedure for preparation of Au/Ir core/shell electrocatalysts presented in chapter 6. The intention was to demonstrate a scalable procedure to prepare the aforementioned catalysts. This work was unfortunuately cut short due to the Covid-19 lockdown, but conclusions can nevertheless be drawn from the available data. All the work in this chapter was performed by myself.

Chapter 8: Ir deposition onto Pd by SLRR of Cu: During the work on preparing Au/Ir core/shell electrocatalysts, an opportunity to travel to the Diamond Light Source appeared. Due to overlapping X-ray adsorption energies of Ir and Au, the Au core had to be replaced by Pd. This required some of the experiments from chapter 7 to be repeated. The work in this chapter was performed from January to March 2020, until the Covid-19 lockdown cut the work short and postponed the intended trip to Diamond. The most important results are nevertheless presented. One palladium catalyst sample was provided by researcher Dr. Thulile Khoza from SINTEF Industry, Sustainable Energy. The sample itself was prepared by Dr. Jørgen Svendby on a different project years prior. All other work was performed by myself. Preparation of Pd/Ir core/shell catalysts is being continued by engineer Agnes Digranes in order to have samples ready for when a new opportunity to travel to Diamond opens up.

Chapter 9: Ir deposition onto Pd by galvanic displacement of PdH_x: This chapter is an offspring of chapter 8 and was performed in parallel, from January to March 2020. During exploratory work on galvanic displacement of underpotentially deposited copper on palladium by iridium, we realized that copper could be replaced by palladium hydride in the procedure. The intention was for the work to culminate in a demonstration of a simple, scalable procedure for preparation of Pd/Ir core/shell catalysts. This work was unfortunuately also cut short due to the Covid-19

lockdown. One palladium catalyst sample was provided by researcher Dr. Thulile Khoza from SINTEF Industry, Sustainable Energy Technology. The sample itself was prepared by Dr. Jørgen Svendby on a different project years prior. All other work was performed by myself.

Chapter 10: Simulation of SLRR reactions: This chapter contains work that was performed during the Covid-19 lockdown from March to May 2020, and a few days in March 2021. With the labs closed until further notice, it was decided to numerically simulate the experiments from chapter 7. It was believed this would provide much needed insight into the electrode processes that is much discussed in the rest of this thesis.

Part IV: Supplementary information; contains supplementary information which may be of interrest to the reader.

Kristian Fredrik Klepp Thorbjørnsen

Trondheim, 26. March 2021

Contents

I Introduction, literature and experimental methods 1

1 Introduction 3
1.1 The Hydrogen Economy . . . 3
1.2 Water electrolysis . . . 4
1.2.1 Thermodynamics . . . 4
1.2.2 Alkaline water electrolysis . . . 5
1.2.3 Solid oide water electrolysis . . . 6
1.2.4 PEM water electrolysis . . . 6
1.3 Electrode kinetics . . . 8
1.4 Electrochemistry of some noble metals . . . 9
1.4.1 Gold . . . 10
1.4.2 Palladium . . . 11
1.4.3 Iridium . . . 13
1.5 Underpotential deposition . . . 15
1.6 Galvanic Displacement . . . 16
1.6.1 Thermodynamics . . . 17
1.6.2 Kinetics . . . 18
1.6.3 Surface Limited Redox Replacement . . . 18
1.6.4 Monitoring of galvanic displacement and SLRR reactions . . . 20
1.6.5 Modelling of SLRR reactions . . . 20
1.6.6 Galvanic displacement of palladium hydride . . . 21
1.7 Chemistry of Ir-aquo-chloro systems . . . 22
1.8 Electrodeposition of iridium . . . 23
1.9 The oxygen evolution reaction . . . 25
1.10 Catalysts for the oxygen evolution reaction . . . 27

2 Experimental methods 29
2.1 Cyclic voltammetry . . . 29
2.2 Determination of electrochemical surface area . . . 31
2.3 Fitting of polarization curves . . . 32

II Galvanic displacement of Cu, Ni and Cu and Ni on titanium oxides by Ir **35**

3 Galvanic displacement of carbon supported Ni by Ir **37**
3.1 Experimental . . . 37
3.1.1 Materials and equipment . . . 37
3.1.2 Preparation of Ir@Ni/C catalysts . . . 38
3.2 Electrochemical characterization . . . 38
3.3 Results . . . 40
3.4 Discussion . . . 48
3.5 Conclusions . . . 51

4 Galvanic displacement of Cu and Ni on titanium oxides by Ir **53**
4.1 Experimental . . . 53
4.1.1 Materials and equipment . . . 53
4.1.2 Preparation of (Ir−Cu)@TiO_2 and (Ir−Cu)@Nb_xTiO_2 . . . 54
4.1.3 Preparation of (Ir−Ni)@$Nb_xTi_4O_7$ . . . 54
4.1.4 Physical characterization . . . 54
4.1.5 Electrochemical characterization . . . 55
4.2 Results . . . 55
4.2.1 Water- to isopropanol ratio . . . 55
4.2.2 TiO_2 based samples . . . 57
4.2.3 Ti_4O_7 based samples . . . 61
4.3 Discussion . . . 65
4.4 Conclusions . . . 66

5 Galvanic displacement of Cu by Ir **67**
5.1 Experimental . . . 67
5.1.1 Electrochemical preparation of Cu/Au(poly) deposits . . . 67
5.1.2 Electrochemical preparation of particulate Cu/GC deposits . . . 67
5.1.3 Preparation of (Ir-Cu/Au) and (Ir-Cu/GC) films . . . 68
5.1.4 Physical characterization . . . 68
5.1.5 Electrochemical characterization . . . 68
5.2 Results . . . 69
5.2.1 Preparation of (Ir−Cu)@Au . . . 69
5.2.2 Preparation of (Ir−Cu)@GC . . . 70
5.2.3 Electrochemical properties . . . 73
5.3 Discussion . . . 75
5.3.1 Morphology and growth . . . 75
5.3.2 Electrochemical properties . . . 77
5.4 Conclusions . . . 77

Summary of the work presented thus far **81**

III Manuscripts 83

6 Ir deposition by galvanic displacement of Cu in a one-pot configuration 85
6.1 Introduction . . . 86
6.2 Experimental . . . 90
6.3 Results . . . 92
6.4 Discussion . . . 109
6.5 Conclusions . . . 113

7 Investigation of the Ir-Cu SLRR system 115
7.1 Experimental . . . 115
7.2 Results . . . 118
7.2.1 Underpotential deposition of copper . . . 118
7.2.2 Effect of Ir precursor and UPD formation potential . . . 120
7.2.3 Effect of electrode rotation and mass transport . . . 127
7.2.4 Au nanoparticles . . . 135
7.3 Discussion . . . 145
7.4 Conclusions . . . 148

8 Ir deposition onto Pd by SLRR of Cu 149
8.1 Experimental . . . 149
8.2 Results . . . 151
8.2.1 Polycrystalline palladium . . . 151
8.2.2 10 wt% Pd/C . . . 155
8.3 Discussion . . . 159
8.4 Conclusions . . . 161

9 Ir deposition onto Pd by galvanic displacement of PdH_x 163
9.1 Introduction . . . 163
9.2 Experimental . . . 165
9.3 Results . . . 168
9.4 Discussion . . . 176
9.5 Conclusions . . . 177

10 Simulation of SLRR reactions 179
10.1 Description of Cu underpotential deposition . . . 179
10.2 Reduction of Ir precursors . . . 180
10.3 General model for galvanic displacement of Cu_{UPD} by Ir . . . 182

10.4 Dimensionless variables . . . 185
10.5 Solution procedure . . . 188
10.6 Results . . . 193
10.7 Discussion . . . 202
10.8 Conclusions . . . 203

Summary and outlook **205**

Bibliography **207**

IV Supplementary information 237

A Galvanic displacement of carbon supported Ni by Ir **239**

B Galvanic displacement of Cu by Ir **243**

C Galvanic displacement of Cu and Ni on titanium oxides by Ir **247**

D Ir deposition by galvanic displacement of Cu in a one-pot configuration **251**
D.1 Limiting current of $Ir_6^{2-} + e^- \rightleftharpoons IrCl_6^{3-}$ . . . 252
D.2 Adjustment for background currents . . . 253

E Investigation of the Ir-Cu SLRR system **257**
E.1 Cu UPD . . . 257
E.2 Experiment 1 . . . 259
E.3 Experiment 2 . . . 261
E.4 Experiment 3 . . . 265
E.5 Experiment 4 . . . 269
E.6 Experiment 5 . . . 273
E.7 Experiment 6 . . . 277
E.8 Experiment 7 . . . 281
E.9 Experiment 8 . . . 285
E.10 Experiment 9 . . . 289
E.11 Experiment 10 . . . 293
E.12 Experiment 11 . . . 297
E.13 Experiment 12 . . . 301
E.14 Experiment 13 . . . 305
E.15 Experiment 14 . . . 309
E.16 Open circuit potential of the Au electrode under addition of Ir precursor solution . . . 313
E.17 Synthesis of Au_{np} . . . 313

F Ir deposition onto Pd by galvanic displacement of PdH_x **317**

G Simulation of SLRR reactions **323**
G.1 Discrete solution of the transport equation 323
G.1.1 Discretization 323
G.1.2 The linear equation set 325
G.2 Pseudocode 327

Part I

Introduction, literature and experimental methods

Chapter 1

Introduction

1.1 The Hydrogen Economy

As power generation from renewable sources such as wind and solar is increasing, so is the need for intermittent storage when supply exceeds demand [1]. This can be achieved in numerous ways such as flywheels, compressed air, supercapacitors, batteries, hydrogen or pumped-hydroelectric storage [2]. Due to the fluctuant nature of such sources, the energy storage system must be able to respond rapidly to those fluctuations. Hydrogen production by water electrolysis is a promising technology for grid stabilization where excess power is electrochemically converted to oxygen- and hydrogen, which can be stored for long periods of time [1]. Another alternative is large-scale battery units which are charged and discharged as the supply and demand for power fluctuates.

In order to replace internal combustion engines, both fuel cells and batteries wil be important technologies with different advantages and disadvantages. While batteries face challenges related to availability and production of important elements (*e.g.* Li, P and Co) and recycling [3], fuel cells require high quality hydrogen as fuel, and scarce and costly noble metal catalysts.

About 500 billion cubic meters of hydrogen was produced annually in 2019, of which 96 % was from non-renewable fossil fuels [4]. Hydrogen production from fossil fuels is mainly achieved by steam reforming of methane [4, 5], which yields hydrogen of low purity with contaminants such as carbon monoxide. This process is dependent on fossil fuels and contributes to the emission of greenhouse gasses. Electrochemical conversion of water to oxygen and hydrogen, water electrolysis (WE) produces hydrogen of high quality, but at about 5 times the cost of fossil fuel dependent methods [4]. This will be elaborated more in detail in the following sections.

1.2 Water electrolysis

Water can be converted to oxygen and hydrogen using electricity. The overall reaction is given in reaction (1.1).

$$\mathrm{H_2O(l)} \rightleftharpoons \mathrm{H_2(g)} + \frac{1}{2}\mathrm{O_2(g)} \tag{1.1}$$

In an acidic media, the anodic- and cathodic half cell reactions can be described as reactions (1.2) and (1.3), respectively expressed as reduction reactions.

$$2\mathrm{H^+(aq)} + \frac{1}{2}\mathrm{O_2(g)} + 2\mathrm{e^-} \rightleftharpoons \mathrm{H_2O(l)} \tag{1.2}$$

$$2\mathrm{H^+(aq)} + 2\mathrm{e^-} \rightleftharpoons \mathrm{H_2(g)} \tag{1.3}$$

There are three main technologies available, alkaline water electrolysis (AWE), solid oxide water electrolysis (SOWE) and polymer electrolyte membrane electrolysis (PEMWE).

1.2.1 Thermodynamics

Some thermodynamic quantities of reaction (1.1) are given in table 1.1 [6]. The reaction is endothermic, meaning that the reaction absorbs heat from the surroundings.

Table 1.1: Standard values of gibbs energy, enthalpy and entropy of the conversion of liquid water and water vapor to oxygen and hydrogen [6].

	$\mathrm{H_2O(l)}$	$\mathrm{H_2O(g)}$
$\Delta_r G^\circ$	$237\,\mathrm{kJ\,mol^{-1}}$	$229\,\mathrm{kJ\,mol^{-1}}$
$\Delta_r H^\circ$	$286\,\mathrm{kJ\,mol^{-1}}$	$242\,\mathrm{kJ\,mol^{-1}}$
$\Delta_r S^\circ$	$163.5\,\mathrm{J\,K^{-1}\,mol^{-1}}$	$44.5\,\mathrm{J\,K^{-1}\,mol^{-1}}$

The standard potential, E°, of reaction (1.1) at standard conditions (25 °C and 1 atm pressure) is given by equation (1.4). This is the thermodynamically minimum voltage required to electrochemically convert water to oxygen and hydrogen.

$$E^\circ = \frac{\Delta_r G^\circ}{n_e \times F} = \frac{\Delta_r H^\circ - T \times \Delta_r S^\circ}{n_e \times F} = \frac{237 \times 10^3\,\mathrm{J\,mol^{-1}}}{2 \times 96\,485\,\mathrm{C\,mol^{-1}}} = 1.228\,\mathrm{V} \tag{1.4}$$

The reaction consumes electrical energy, W_{el}, equal to $\Delta_r G^\circ$ at E°. The heat consumed,Q, is given by the entropy term, $Q = T\Delta_r S^\circ$. The thermoneutral voltage, E_{tn}, is defined as when the system does not exhange heat with the surroundings, *i.e.* $Q = 0$. At standard conditions, E_{tn} is given by equation (1.5) where $Q = T \times \Delta_r S^\circ = 0$.

$$E_{\text{tn}} = \frac{\Delta_r H^\circ}{n_e \times F} = \frac{286 \times 10^3\,\text{J mol}^{-1}}{2 \times 96\,485\,\text{C mol}^{-1}} = 1.482\,\text{V} \tag{1.5}$$

Figure 1.1 plots the enthalpy ($\Delta_r H$), entropy ($\Delta_r S$), gibbs free energy ($\Delta_r G$), thermoneutral voltage and standard potential as a function of temperature.

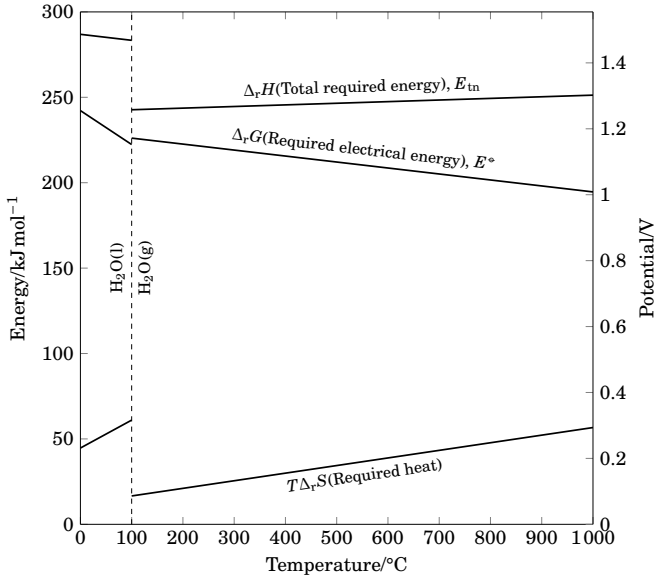

Figure 1.1: Entropy, enthalpy, gibbs energy and the corresponding potentials of the water electrolysis reaction as a function of temperature.

1.2.2 Alkaline water electrolysis

Alkaline water electrolysis (AWE) was first discovered by Troostwijk and Diemann in 1789 [5]. Although alkaline water electrolysis is the dominant industrial electrolysis method, most hydrogen produced is through steam reforming of hydrocarbons [5].

An AWE cell is comprised of two electrodes immersed in a liquid alkaline electrolyte, 20 %-30 % KOH, separated by diaphragm. This technology has three major drawbacks, all related to the liquid electrolyte and diaphragm. The diaphragm suffers from some crossover of product gasses, leading to lower efficiency and safety risks. AWE units are also not able to operate at high current densities due to high ohmic losses over the liquid electrolyte and diaphragm. The design is also quite bulky. The diaphragm is not selectively permeable to hydroxyl ions. Increasing the operating pressure at the cathode increases the crossover rate of hydrogen gas over to the anode compartment which is dangerous due to the low explosion limit of $H_2(g)/O_2(g)$ mixtures. Both the anodic and cathodic reacitons are typically catalyzed by transition metals such as Ni, Fe and Co [5].

1.2.3 Solid oide water electrolysis

A solid oxide electrolyzer (SOWE) was first reported by Dönitz and Erdle in the 1980s [5]. The structure is conceptially the same as other electrolyzer cells. Two porous ceramic electrodes separated by a dense O^{2-} or H^+ conducting ceramic membrane, where the H^+ conducting oxides are still in the early development stage [7, 8]. Both planar and tubular designs are possible. Solid oxide water electrolyzers operate at a much higher temperatrue than AWE and PEMWE, typically 600 °C to 850 °C. This is necessary to achieve good ionic conductivity. Because of the high temperature, SOWE operate at lower cell potentials, higher current densities and with high efficiency than AWE and PEMWE [7]. SOWE are also not dependent on precius metals such at Pt and Ir.

1.2.4 PEM water electrolysis

Replacing the diaphragm in alkaline water electrolyzers with a proton conducting membrane allows many of the drawbacks of the alkaline technology to be overcome. First developed by General Electric in the 1960s [9], PEMWEs utilize a polymer electrolyte membrane (PEM) to achieve a compact design with low gas crossover, high current densities and the ability to operate at high pressure [5]. The PEM is much thinner than the diaphragm in AWE, usually 20 µm-300 µm thick, and the proton transport across the membrane can respond much more rapidly to fluctuations in the power grid than the heavier hydroxyl ions in the liquid electrolyte of AWE units. The main drawbacks of PEMWEs is the highly corrosive enviroment requiring the use of expensive materials, increasing the initial cost of investment and reducing the lifetime of the components. Both the cathode and the anode reactions are catalyzed by expensive platinum group metals (PGM), Pt at the cathode and Ir at the anode. At the anode, the high potentials and low pH renders IrO_2 as the only catalyst with a sufficent activity and stability. With iridium being much less abuntant than *e.g.*

gold and platinum, this drives up the cost of PEMWE units. Even though IrO_2 is the current catalyst of choice on the anode, no known material has sufficient activity and stability for use on PEMWE anodes [1].

A schematic of a PEMWE unit is given in Figure 1.2 [5].

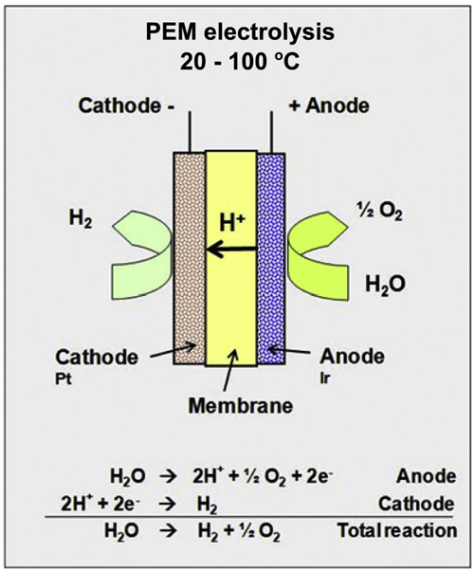

Figure 1.2: Schematic of a EM water electrolyzer. Reprinted from [5] with permission.

To reduce the cost of PEMWE units, the current strategies are to do so through design and the construction of larger stacks. As the cost of a stack is decreasing, the noble metal catalysts share of the total cost will increase. Thus, decreasing the noble metal loading becomes a vital part in reducing the total cost of a stack. However, a membrane electrode assembly (MEA) with a low catalyst loading suffers from more rapid degradation than that of a MEA with a higher catalyst loading [1].

Ever since 1973, the catalyst of choice has been IrO_2, due superior stability [10] compared to the more electrochemically active RuO_2 [9,11]. Ir is one of the least abundant stable elements in the earth's crust and the high loading of around $3\,mg\,cm^{-2}$ on the anode (compared to 0.5-1 $mg\,cm^{-2}$ Pt/C on the cathode) opens up for substantial cost reductions though reductions in the Ir loading. Moreover, availability of Ir is a significant bottleneck if one is to reach hydrogen production by PEMWE on a terrawatt scale in the future [12]. Due to the high Ir loading, lack of support and low surface area, the Ir utilization on the anode is quite low [5]. However, IrO_2

dissolves at higher anodic overpotentials [1, 13] meaning that there is a tradeoff between catalyst loading and MEA stability [1].

1.3 Electrode kinetics

The rate of a redox reaction consisting of a single elementary step with transfer of one electron, reaction (1.6),

$$\mathrm{O(aq)} + \mathrm{e^-} \underset{\mathrm{k}_a}{\overset{\mathrm{k}_c}{\rightleftharpoons}} \mathrm{R(aq)} \tag{1.6}$$

is given by equation (1.7) [14–16]

$$-v = \frac{j}{F} = a_{\mathrm{R}}^{\sigma} k_a^{\circ} \exp\left[\left(1-\beta\right)\frac{F}{RT}E\right] - a_{\mathrm{O}}^{\sigma} k_c^{\circ} \exp\left[-\beta\frac{F}{RT}E\right] \tag{1.7}$$

where k_c° and k_a° are the standard cathodic and anodic rate constants, and a_{O}^{σ} and a_{R}^{σ} are the activities of O(aq) and R(aq) *at the electrode surface*, respectively. β is the symmetry factor. F, R and T are Faradays constant, the universal gas constant and temperature, respectively. E is the electrode potential. From here on out, we will assume the activity to be equal to the concentration, $a_i \approx c_i$. Equation (1.7) is commonly expressed as equation (1.8), known as the Butler-Volmer equation [14–16].

$$j = j_0 \left\{ \left(\frac{c_{\mathrm{R}}^{\sigma}}{c_{\mathrm{R}}^{\infty}}\right) \exp\left[\left(1-\beta\right)\frac{F}{RT}(E-E^{\circ})\right] - \left(\frac{c_{\mathrm{O}}^{\sigma}}{c_{\mathrm{O}}^{\infty}}\right) \exp\left[-\beta\frac{F}{RT}(E-E^{\circ})\right] \right\} \tag{1.8}$$

where c_{O}^{∞} and c_{R}^{∞} are the bulk concentrations of O(aq) and R(aq), respectively. E° is the standard reduction potential of reaction (1.6). Equation (1.8) is found by some algebra after replacing E in equation (1.7) with $E = E^{\mathrm{eq}} + \eta$, where η is the overpotential defined as the difference between the electrode potential, E, and the equilibrium potential, E^{eq}, in equation (1.9).

$$\eta = E - E^{\mathrm{eq}} \tag{1.9}$$

E^{eq} is given by the Nernst equation, equation (1.10),

$$E^{\mathrm{eq}} = E^{\circ} - \frac{RT}{F}\ln\left(\frac{c_{\mathrm{R}}^{\infty}}{c_{\mathrm{O}}^{\infty}}\right) \tag{1.10}$$

which can be derived by setting equation (1.7) equal to zero and solving for the potential. The exchange current density, j_0, is given by equation (1.11).

$$j_0 = F\left(k_a^{\ominus}\right)^{\beta}\left(k_c^{\ominus}\right)^{(1-\beta)}\left(c_{\mathrm{R}}^{\infty}\right)^{\beta}\left(c_{\mathrm{O}}^{\infty}\right)^{(1-\beta)} \tag{1.11}$$

At high anodic overpotentials, where $\exp\left[-\beta\frac{F}{RT}(E-E^{\ominus})\right] \approx 0$, one can approximate equation (1.8) as equation (1.12)

$$(E-E^{\ominus}) = a + b\log(j) \tag{1.12}$$

where $a = -\ln\left(j_0\frac{c_{\mathrm{R}}^{\sigma}}{c_{\mathrm{R}}^{\infty}}\right)\frac{RT}{(1-\beta)F}$ and $b = \ln(10)\frac{RT}{(1-\beta)F}$. A similar derivation can be made for high cathodic overpotentials. $b = \frac{\partial E}{\partial \log(j)}$ is usually known as the Tafel slope.

At low overpotentials, a linearized form of equation (1.8) is obtained as equation (1.13) [14]

$$j = j_0\frac{F}{RT}\eta \tag{1.13}$$

It should be noted that the above relations are only valid for a single elementary step. Most reactions consist of multiple elementary steps such as electron transfer, adsorption, dissociation, etc. To obtain an expression of the rate of such a reaction, one must analyze the kinetics under the assumption of a rate determining step (rds)[1]. This usually leads to multiple rate expressions, which may be compared to experimental data. Good examples of this are given in [15] and [17]. High- and low overpotential approximations similar to equations (1.12) and (1.13) can be done on the more complex rate expressions, but will be valid in different potential regions. This gives different expressions for the Tafel slope than given above [17]. It is important to remember that for any sequence of elementary steps, the rate determining reaction may change with potential, so application of a rate expression over a wide potential range must be done with care.

1.4 Electrochemistry of some noble metals

Noble metals such as Pt, Pd, Au, Ag, Ru and Ir have a wide usage, including electrochemical applications due for their corrosion resistance and catalytic properties. The following sections will give a quick glance at the electrochemical properties of some noble metals relevant for this thesis.

[1] A series of reactions may also be treated as an initial value problem where the assumption of a rate determining step is not necessarry.

1.4.1 Gold

Gold is a noble metal forming a trivalent oxide, accoring to reaction (1.14) [18], where $E^{\ominus}_{Au_2O_3/Au} = (1.362 \pm 0.002)\,V$ and $E^{\ominus}_{Au^{3+}/Au} = 1.52\,V$ [19]

$$\frac{1}{2}Au_2O_3(s) + 3H_3O^+(aq) + 3e^- \rightleftharpoons Au(s) + 6H_2O(l) \tag{1.14}$$

More accurately, the oxidation product of Au is hydrated $Au(OH)_3$ or $Au_2O_3 \cdot 3H_2O$ at 1.457 V [18] and anhydrous Au_2O_3 at 1.511 V [18]. A typical voltammogram of polycrystalline gold in sulfuric acid is shown in figure 1.3 [18]. The voltammogram show no notable features between 0 V and 1.36 V in the anodic sweep. Monolayer formation of Au_2O_3 commences as 1.36 V and is identified by the rising anodic current. The position of the corresponding cathodic peak depends on the upper potential limit used in the voltammogram [20].

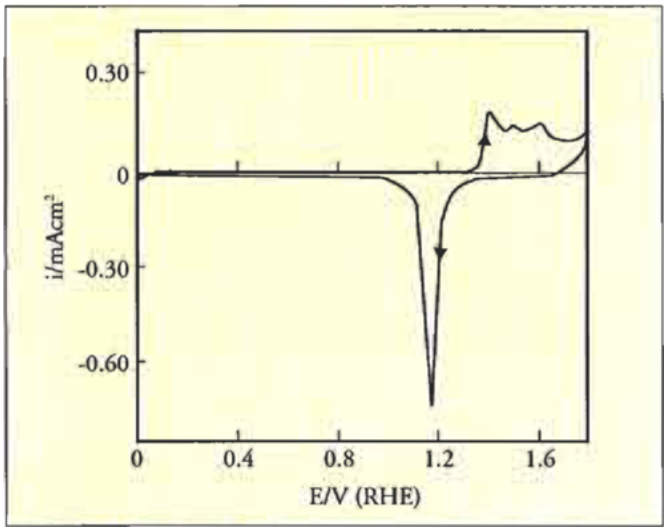

Figure 1.3: Typical voltammogram of a polycrystalline gold disc electrode in $1\,mol\,dm^{-3}$ H_2SO_4 at 25 °C recorded at $50\,mV\,s^{-1}$. Reprinted from [18] with permission.

The region between 0 V and 1.36 V in the anodic sweep in the voltaommogram in figure 1.3 may appear featureless, however; sulfate and bisulfate adsorbs onto gold, appearing as peaks in the double layer region [21–25]

1.4.2 Palladium

Oxide formation and dissolution

Palladium may take oxidation states ranging from +1 to +6, where only +2 and +4 is stable in aqueous solutions [19]. Formation of Pd(II) hydroxides and oxides proceeds according to reactions (1.15) and (1.16) [19], where Pd(IV) also forms oxides and hydroxides which may be reduced to Pd(s), PdO(s), $Pd(OH)_2$(s) or Pd^{2+}(aq) [19].

$$Pd(OH)_2(s) + 2H^+(aq) + 2e^- \rightleftharpoons Pd(s) + 2H_2O(l) E^\circ = 0.897\,V \quad (1.15)$$

$$PdO(s) + 2H^+(aq) + 2e^- \rightleftharpoons Pd(s) + H_2O(l) \quad E^\circ = 0.79\,V, 0.917\,V \quad (1.16)$$

A typical voltammogram of polycrystalline palladium in acid is given in figure 1.4 [26].

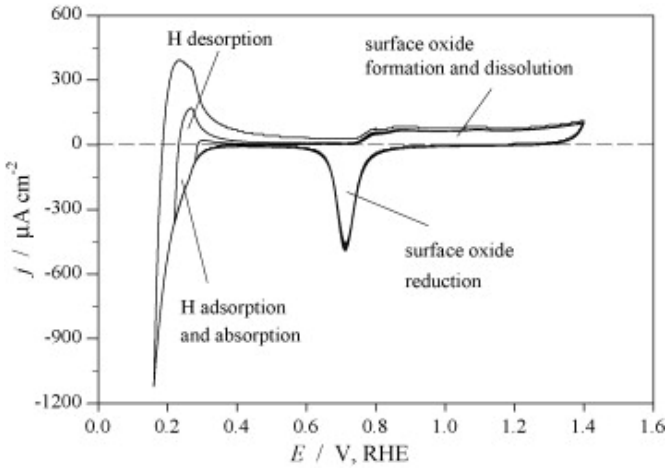

Figure 1.4: Typical voltammograms of a polycrystalline palladium disc electrode in 0.5 mol dm^{-3} H_2SO_4 at 298 K recorded at 50 mV s^{-1}. Reprinted from [26] with permission.

Palladium simultaneously starts to form oxides and dissolve around 0.75 V in the anodic scan, and is reduced in the cathodic scan where the cathodic peak potential depends on the upper potential limit used in the voltammogram [27,28]. At potentials less positive than 0.4 V, hydrogen is adsorbed as H_{UPD} and absorbed as the α and β hydride phases form.

Hydride formation

Palladium is perhaps most known for it's ability to absorb hydrogen as palladium hydride (PdH_x) [29–31].

Palladium hydride can be formed both physically [32–35] and electrochemically [33, 34, 36–39] at room temperature. As hydrogen enters the Pd lattice, two phases form; the dilute PdH_α phase and the PdH_β phase. Both phases co-exist, but the hydrogen content is significantly different. In the α phase, the H/Pd ratio is ≈ 0.015, whereas in the β phase it is ≈ 0.7 [31]. The α phase, which is actually a solid solution, forms at low H_2(g) partial pressure before a phase transition to the hydride β phase takes place over a wide miscibility gap. The minimum and maximum values of α and β in PdH_α and PdH_β is particle size dependent [34, 37], where the width of the miscibility gap is reduced for smaller particles. Electrochemically, the α phase is formed at $E < 300\,\text{mV}$. The PdH_β forms at potential less positive than PdH_α, right before the onset of hydrogen evolution, around 40 mV [36–39]. Figure 1.5 shows the atomic ratio of adsorbed+absorbed hydrogen to palladium in acid as a function of electrode potential for different palladium film thicknesses.

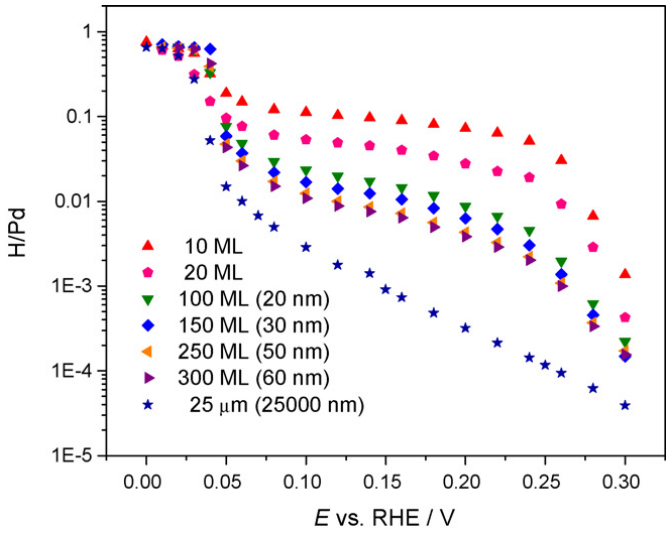

Figure 1.5: Total hydrogen adsorption/absorption isotherms for different palladium film thicknesses as a function of potential in $0.5\,\text{mol}\,\text{dm}^{-3}$ H_2SO_4. Reprinted from [38] with permission.

A simple scheme describing formation of palladium hydride is given in reactions (1.17) and (1.18) [39], although the actual mechanisms involved in the formation of the α-

and $\beta-$ phases are more complex [40].

$$H^+(aq) + Pd_{surface} + e^- \rightleftharpoons PdH_{ads} \tag{1.17}$$

$$PdH_{ads} + Pd_{subsurface} \rightleftharpoons Pd_{surface} + PdH_{abs} \tag{1.18}$$

1.4.3 Iridium

Metallic Ir is a very hard noble metal with a high melting point and excellent corrosion resistance [41]. It is used as an alloying element with other noble metals, in surgical instruments, electronics and in high temperature thermocouples [42]. When oxidized to iridium oxides, IrO_x, a range of other uses appear. Possible and current uses of IrO_x films includes; in supercapacitors [43–45], as an electrochromic material [46–48], in pH-electrodes [49–52], biomedical devices [53] and most important for this thesis; as a catalyst for the oxygen evolution reaction [5, 17, 54–61]

Chemical and thermal formation of IrO_x

Thin films and powders of iridium oxides may be prepared by numerous methods such as sputtering [44, 62], electrochemical deposition [46, 53, 63, 64], the Adams Fusion method [65–67], hydrolysis [17] or polymeric precursor synthesis [68]. Polymeric precursor synthesis has been shown to produce Ir/IrO_2 core/shell catalsysts if heat treated under insufficient oxygen supply [68].

Electrochemical formation of IrO_x - AIROF

When subjected to potential cycling in acid or base, metallic Ir is oxidized to IrO_x. This form of IrO_x is also known as Anodically Formed Iridium Oxide Films, AIROF. Unlike RuO_2 on Ru which can be grown potentiostatically [69], IrO_x must be grown layer-by-layer by potential cycling or potential switching [48, 70, 71]. Initially, a compact oxide layer is grown on the bare Ir metal. The outer monolayer of the compact oxide layer is further oxidized and hydrated at potentials above 1.2 V. This hydrated layer blocks further oxidation of the compact oxide layer. Upon reduction, the inner oxide layer is reduced to Ir metal while the outer hydrated layer is reduced to hydrous Ir_2O_3. With continued potential cycling or switching, this process is repeated at the metal - hydrous oxide interface, causing the hydrous oxide layer to grow. About half of the metallic surface atoms can be converted to hydrous oxide in one growth cycle [72]. The lower and upper potential limits which must be exceeded for the hydrous layer to grow is 0.3 V and 1.15 V. AIROF will typically have a cracked-mud like structure [69, 73, 74].

The transition between Ir(III) and Ir(IV), with a formal potential of $E^{\ominus}_{\mathrm{Ir(IV)/Ir(III)}} = 0.97\,\mathrm{V}$ [75], is usually associated with incorporation of ions from the electrolyte, as according to reaction (1.19) [76, 77] (also printed as reaction (2.3)).

$$\mathrm{IrO_2 \cdot nH_2O + (1+\delta)H^+ + \delta A^- + e^- \rightleftharpoons IrO_{1-\delta}(OH)_{1+\delta}A_\delta \cdot mH_2O + (n-m)H_2O} \quad (1.19)$$

This transition is also associated with coloring and bleaching of the film [47, 48] and a switch from an insulating (Ir(III)) to a conductive state (Ir(IV)) [78]. While the Ir(III) state is transparent, the color of the film changes to blue-black upon oxidation to Ir(IV). If the film reaches a sufficient thickness, it stays blue-black at all potentials [70]. A typical voltammogram of AIROF grown on metallic Ir in a solution containing H_2SO_4 is given in figure 1.6 [69]. The main pair of anodic and cathodic peaks around 1 V shows the transition between Ir(III) and Ir(IV). The anodic and cathodic peaks below 0.5 V show underpotential deposition of hydrogen at the underlaying Ir metal [48]. The protons inserted into the film upon reduction from Ir(IV) to Ir(III) are mobile within the film [48], and thus IrO_x is in a sense transparent to protons.

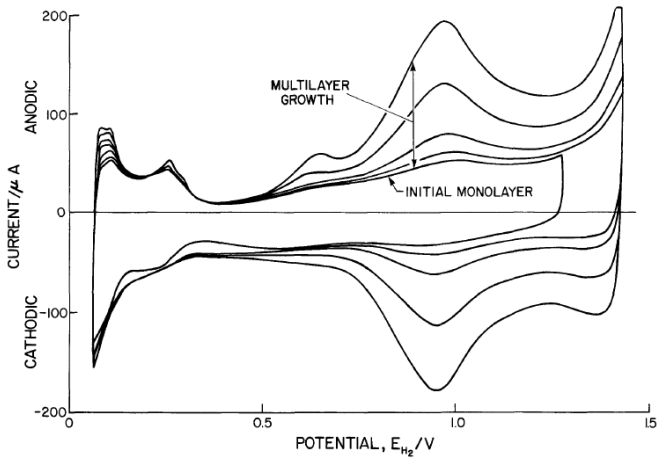

Figure 1.6: Typical voltammograms of a polycrystalline iridium electrode in $1\,\mathrm{mol\,dm^{-3}}$ H_2SO_4 at 295 K. Growth of AIROF is shown as the transition from monolayer to multilayer growth of hydrous IrO_x. Reprinted from [69] with permission.

The reversibility of reaction (1.19) depends on the film thickness and the potential sweep rate [79]. The main peak potentials in voltammograms similar to figure 1.6

are independent on the potential sweep rate up to some limit, which decreases with increasing film thickness.

1.5 Underpotential deposition

Underpotential deposition (UPD) of metal monolayers is the deposition of a monolayer of a metal M onto a different metal N at potentials well positive of the reversible potential for deposition of M onto itself, through reaction (1.20). This is depicted graphically in figure 1.7.

$$\mathrm{M}^{m+}(\mathrm{sol}) + m\,\mathrm{e}^- \rightleftharpoons \mathrm{M}_{\mathrm{UPD}} \tag{1.20}$$

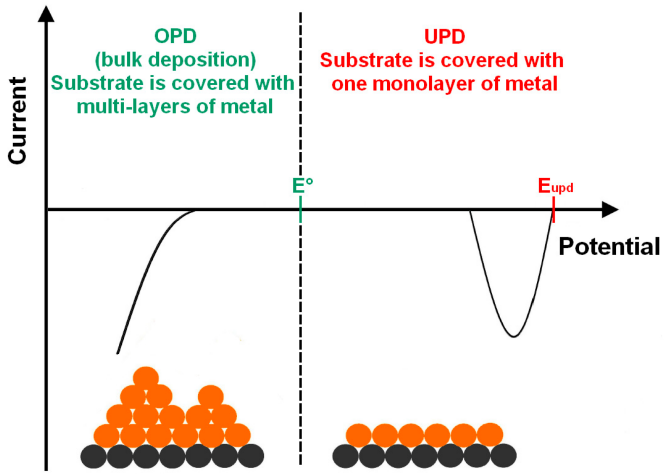

Figure 1.7: Schematic representation of a the current-potential profile of underpotential (UPD) and overpotential (OPD) deposition of a metal (orange) onto a substrate (black) at potentials well positive of the reversible potential for OPD. Figure reprinted from [80] with permission.

The Nernst reversible potential for deposition of M onto itself, $E^{\mathrm{rev}}_{\mathrm{M}^{m+}/\mathrm{M}}$, is given by equation (1.21)

$$E^{\mathrm{rev}}_{\mathrm{M}^{m+}/\mathrm{M}} = E^{\ominus}_{\mathrm{M}^{m+}/\mathrm{M}} - \frac{RT}{mF}\ln\left(\frac{a_{\mathrm{M}}}{a_{\mathrm{M}^{m+}}}\right) \tag{1.21}$$

The difference between the onset of UPD, E_{UPD}, and $E^{\mathrm{rev}}_{\mathrm{M}^{m+}/\mathrm{M}}$, ΔE_{UPD}, is related to the difference in work function between the substrate N and the depositing metal M through equation (1.22) [80, 81]

$$\Delta E_{\mathrm{UPD}} = \left(E_{\mathrm{UPD}} - E^{\mathrm{rev}}_{\mathrm{M}^{m+}/\mathrm{M}}\right) \approx \frac{1}{2}\Delta\Phi \tag{1.22}$$

where $\Delta\Phi = (\Phi_{\mathrm{N}} - \Phi_{\mathrm{M}})$.

The equilibrium potential of reaction (1.20) depends on the coverage of M on the substrate, θ, and can be described through several types of adsorption isotherms such as Langmuir, Temkin-Frumkin or more complex models taking into account multiple surface states and partial charge transfer [82].

$$E^{\mathrm{rev}}_{\mathrm{UPD}} = E^{\theta\to 0} - \frac{RT}{mF}\ln\left(\frac{\theta}{1-\theta}\right) \qquad \text{Langmuir} \tag{1.23}$$

$$E^{\mathrm{rev}}_{\mathrm{UPD}} = E^{\theta\to 0.5} - \frac{RT}{mF}\left[\ln\left(\frac{\theta}{1-\theta}\right) + f\theta + g\theta^{3/2}\right] \qquad \text{Temkin Frumkin} \tag{1.24}$$

In equation (1.24), f and g is the Temkin and Frumkin parameters representing adatom-substrate interactions and adatom-adatom interactions [82].

Underpotential depositon of Cu onto Au is a well known system, where anions present in the electrolyte greatly influence both the onset potential of underpotential depositon and the structure of the forming adlayer [80]. Figure 1.8 shows voltammograms of underpotential deposition of copper onto gold in H_2SO_4 [83]. The left voltammogram is onto a polycrystalline Au disc electrode and the right is onto a 4 wt% Au/C catalyst. EXAFS revealed that at the onset of Cu overpotential deposition onto Au nanoparticles, the Cu structure was that of clusters at the Au surface. This was in contrast to the monolayer predicted from single crystal studies [83].

1.6 Galvanic Displacement

Galvanic displacement, also known as galvanic exchange, is the coupled oxidation of a metal M and and the reduction of a more noble metal cation N^{n+} [84, 85]. The reaction can be expressed as reaction (1.25) where the reaction stoichiometry is determined by oxidation state of M and N, m and n, respectively.

$$n\,\mathrm{M(s)} + m\,\mathrm{N}^{n+}\mathrm{(aq)} \rightleftharpoons n\,\mathrm{M}^{m+}\mathrm{(aq)} + m\,\mathrm{N(s)} \tag{1.25}$$

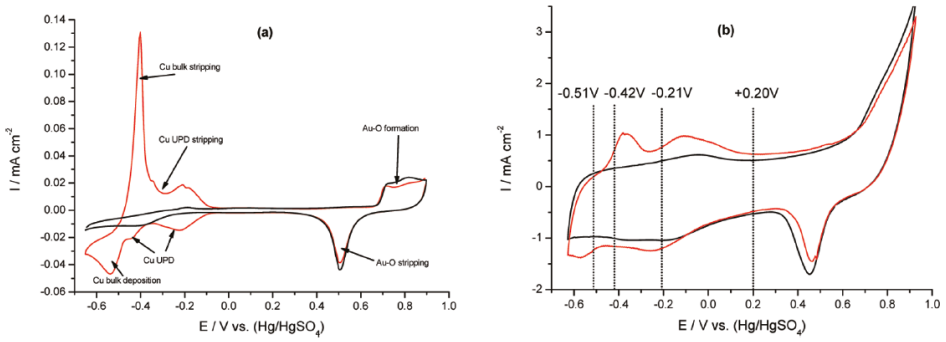

Figure 1.8: Cyclic voltammograms showing underpotential depositon (red curve) of Cu onto a polycrystalline Au disc electrode (a) and a 4 wt% Au/C calayst electrode (b) in 0.5 mol dm^{-3} H_2SO_4 and 2 mmol dm^{-3} $CuSO_4$. Reprinrinted from [83][`https://pubs.acs.org/doi/10.1021/ja206763e`] with permission. Further permissions related to the material excerpted should be directed to the ACS.

Reaction (1.25) can be written as the two half-cell reactions, reactions (1.26) and (1.27).

$$M^{m+}(aq) + m\,e^- \rightleftharpoons M(s) \tag{1.26}$$

$$N^{n+}(aq) + n\,e^- \rightleftharpoons N(s) \tag{1.27}$$

Alternatively, $MO_{m/2}$ may grow under conditions where this is the stable product from oxidation of M [84, 86], written here in reaction (1.28).

$$n\,M(s) + N^{n+}(aq) + \frac{nm}{2}\,H_2O(l) \rightleftharpoons n\,MO_{m/2}(s) + m\,N(s) + n\,m\,H^+(aq) \tag{1.28}$$

Electrocatalysts have previously been prepared by galvanic displacement of for example Ni with Ir [86–92], Co with Ir [92], Ti with Ir [86] or Cu with Pd, Pt and Au [93]. The resulting morphology will range from dendrites to dense thin films, core/shell or hollow structures, depending on experimental conditions [84, 85, 93].

1.6.1 Thermodynamics

$\Delta_r G^\circ$ of the galvanic displacement reaction, reaction (1.25), is expressed as equations (1.29) to (1.32)

$$\Delta_r G^\circ = n\Delta_f G^\circ_{\mathrm{M}^{m+}} + m\Delta_f G^\circ_{\mathrm{N(s)}} - n\Delta_f G^\circ_{\mathrm{M(s)}} - m\Delta_f G^\circ_{\mathrm{N}^{n+}} \tag{1.29}$$

$$\Delta_r G^\circ = n\left(\Delta_f G^\circ_{\mathrm{M}^{m+}} - \Delta_f G^\circ_{\mathrm{M(s)}}\right) - m\left(\Delta_f G^\circ_{\mathrm{N}^{n+}} - \Delta_f G^\circ_{\mathrm{N(s)}}\right) \tag{1.30}$$

$$\Delta_r G^\circ = n\left(-mFE^\circ_M\right) - m\left(-nFE^\circ_N\right) \tag{1.31}$$

$$\Delta_r G^\circ = mnF\left(E^\circ_N - E^\circ_M\right) \tag{1.32}$$

It is easy to see from equation (1.32) that the main driving force for galvanic displacement is the difference in standard reduction potential between N and M [84].

1.6.2 Kinetics

Galvanic displacement is analogous to a corrosion reaction. From charge conservation, the total current related to oxidation of a metal M, reaction (1.26), must equal the total current related to reduction of the cation N^{n+}, reaction (1.27). This is expressed in equation (1.33), where each J is the total current for each reaction, and E is the electrode potential.

$$J_{\mathrm{N}}(E) + J_{\mathrm{M}}(E) = 0 \tag{1.33}$$

If assuming both reactions (1.26) and (1.27) to follow Butler-Volmer kinetics, equation (1.8), one may derive an expression for the rate of the galvanic displacement reaction [84]. However, as noted earlier in section 1.3, such an expression will not account for reaction mechanisms or transient mass transport. More complex expressions for $J_{\mathrm{N}}(E)$ and $J_{\mathrm{M}}(E)$ may be derived in a similar manner to the rate expression for oxygen evolution on IrO_x in acidic conditions, equation (1.54) in section 1.9 [17, 55]. The assumption of a rate determining step must be applied with care, as the rate of an electron transfer reaction is potential dependent. If one of the reactions are known to be mass transport limited, a much simpler expression may be obtained [84].

1.6.3 Surface Limited Redox Replacement

Surface limited redox replacement (SLRR) is when the leaving metal M is restricted to a single monolayer prepared by underpotential deposition (UPD, reaction (1.34)) onto a substrate. The leaving metal M is typically Pb [94–108] or Cu [94, 99, 100, 104, 105, 108–139]. Other metals such as Te, Co and Ag has also been utilized [140–142].

$$\mathrm{M}^{m+}(\mathrm{aq}) + m\,\mathrm{e}^- \rightleftharpoons \mathrm{M}_{\mathrm{UPD}} \tag{1.34}$$

The SLRR reaction is generally described by reaction (1.35) involving the metal cation N^{n+} with a charge $n+$ and the aforementioned less noble metal M.

$$m\,N^{n+}(aq) + n\,M_{UPD} \rightleftharpoons m\,N(s) + n\,M^{m+}(aq) \tag{1.35}$$

This method originating from Adzic's pioneer work [109] and has since spawned numerous publications [83, 94–102, 104–106, 108, 110, 111, 113–132, 134–136, 138–141, 143–146].

This method is usually employed to prepare one or multiple layers of a metal on a substrate by shuffling the working electrode between electrochemical cells containing different solutions. A UPD layer is formed in one cell, and the working electrode is moved to another cell containing noble metal cations where the galvanic displacement reaction proceeds [111]. The working electrode is usually rinsed in DI water and/or H_2SO_4, $HClO_4$ or HNO_3 when moved between the cells, and the whole setup is ideally placed in a glove box or a similar construction to avoid unwanted side reactions related to oxygen [111, 147, 148]. Layered structures may be prepared as well, with the use of additional beakers containing different metal cations. The method is shown schematically in figure 1.9.

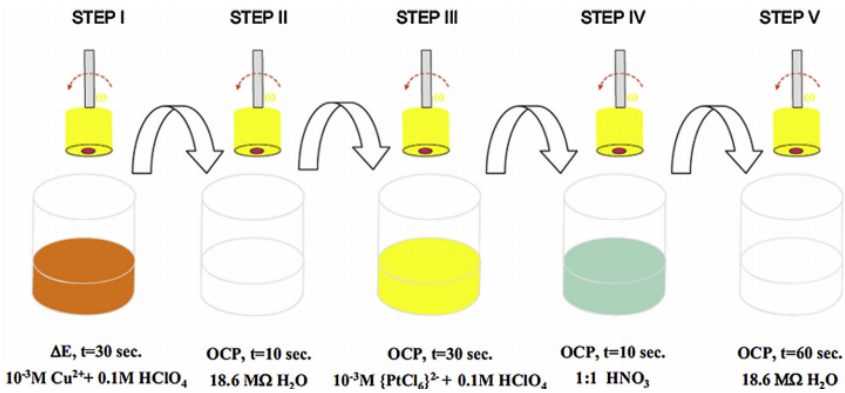

Figure 1.9: Schematic representation of the conventional SLRR proceedure. The working electrode is characterized in cell A, before a UPD layer is formed on the working electrode in cell B. The SLRR reaction proceeds in cell C, before the working electrode is once again characterized in cell A. Reprinted from [111] with permission.

SLRR has also been applied to flow cells [132, 139] and *one-pot* methods [103, 106, 107, 134, 137, 144]. A flow cell can be set up in a very complex manner. The predictable hydrodynamics, switchable electrolytes and possibility for *in-situ* monitoring by

scanning probe microscopy and other methods allows for very sophisticated experiments [149]. A completely automated SLRR setup in a flow cell with a controlled atmosphere and *in-situ* monitoring renders flow cells very suitable for characterization of thin films of multiple layers, or multiple layers of multiple metals.

The *one-pot* or *single-cell* approach exploits the difference in the rate of the half cell reactions reactions (1.27) and (1.34). This is a significant simplification over the traditional shuffling approach and the aforementioned flow cell approach. The working electrode is immersed in a solution containing both the UPD forming M^{m+}(aq) and more noble metal cations N^{n+}. A fast- forming UPD layer of M is formed during a short potential hold where the rate of noble metal deposition is very low and the amount of N deposited by direct electrolysis is negligible [98, 106, 149]. The main drawbacks of this method is direct electrolysis of noble metals and incorporation of sacrificial metal impurities in the noble metal film [98, 149].

While the *one-pot* method is a significant simplification over the traditional and flow cell approaches, it suffers from contamination of the leaving metal in the noble metal film. This can be alleviated by removing the leaving metal alltogether. Hydrogen may be underpotentially deposited onto some metal surfaces such as Pt, Au or Pd and subsequently replaced by another noble metal in a *one-pot* setup [102, 144].

Gram-scale methods for preparation of core/shell electrocatalysts, typically Pd/Pt_{ML}, usually involves forming a Cu-UPD layer in a custom cell followed by addition of a platinum precursor solution [115–117, 119, 121, 130]. The reaction vessel used for *gram-scale* preparation of core/shell electrocatalysts is typically a titanium cylinder [116] or a glass cell equiped with a large carbon sheet electrode [130]. Different additives has been added to the displacement solution to improve the morphology of the noble metal deposit [119, 130, 131, 150] which in reality is often particulate in nature [119, 122, 130].

1.6.4 Monitoring of galvanic displacement and SLRR reactions

The most widely used method to monitor galvanic displacement and SLRR reactions *in-situ* is the open circuit potential of the working electrode [96, 97, 99–103, 106, 124]. Other methods such as surface reflectivity [106], EQCM [101] and EXAFS/XANES [122] has also been employed.

1.6.5 Modelling of SLRR reactions

Reports on modelling of SLRR reactions has been done by expressing the fraction coverage of M on the substrate, θ_M as an initial value problem, equation (1.36)

[99, 106, 124], where k_N is a rate constant and N is the reaction order with respect to θ_M.

$$\frac{\partial\theta}{\partial t} = -k_N\theta^N \tag{1.36}$$

The following relationships, equations (1.37) to (1.39), was obtained to express the value of θ_M as a function of time where θ_0 represents θ at $t = 0$.

$$\theta(t) = \theta_0 - k_0 t \qquad N = 0 \tag{1.37}$$

$$\theta(t) = \theta_0 \times \exp(-k_1 t) \qquad N = 1 \tag{1.38}$$

$$\theta(t) = \theta_0 \times \sqrt[1-N]{(N-1)k_N t} \qquad N > 1 \tag{1.39}$$

More general expressions correcting for multiple reactions, *i.e.* multiple species reacting with M was found as

$$\frac{\partial\theta}{\partial t} = \sum_{i=0}^{N} -k_i\theta^i \tag{1.40}$$

The potential of the working electrode was modelled by inserting the expression for $\theta(t)$ into a Temkin-Frumkin type isotherm (see equation (1.24) in section 1.5), here printed in equation (1.41).

$$E = E_{\mathrm{UPD}}^{\theta\to 0} - \frac{RT}{mF}\left[\ln\left(\frac{\theta(t)}{1-\theta(t)}\right) + f\theta(t) + g\theta(t)^{\frac{3}{2}}\right] \tag{1.41}$$

The modelled potential transients were compared and fitted to experimentally obtained open circuit potential transients. The obtained expressions for $\theta(t)$ appeared to be consistent with *in-situ* surface reflectivity measurements [106].

1.6.6 Galvanic displacement of palladium hydride

Zolfaghari and Conway [151] first reported electroless deposition of Pt onto Pd where a PdH_x Pd | H | H^+(aq) internal reference electrode reacted with $[PtCl_6]^{2-}$ and $[PtCl_4]^{2-}$ as according to reactions (1.42) and (1.43), where H is in the PdH_x phase.

$$4\,\mathrm{H}|(\mathrm{PdH}_x) + [\mathrm{PtCl_6}]^{2-}(\mathrm{aq}) \rightleftharpoons \mathrm{Pt(s)}|(\mathrm{PdH}_x) + 6\,\mathrm{Cl}^-(\mathrm{aq}) + 4\,\mathrm{H}^+(\mathrm{aq}) \quad (1.42)$$

$$2\,\mathrm{H}|(\mathrm{PdH}_x) + [\mathrm{PtCl_4}]^{2-}(\mathrm{aq}) \rightleftharpoons \mathrm{Pt(s)}|(\mathrm{PdH}_x) + 4\,\mathrm{Cl}^-(\mathrm{aq}) + 2\,\mathrm{H}^+(\mathrm{aq}) \quad (1.43)$$

Low concentrations of $[\mathrm{PtCl_6}]^{2-}$(aq) led to the formation of Pt(s) dendrites due to diffusion-controlled reduction of $[\mathrm{PtCl_6}]^{2-}$(aq).

This concept was later refined by Cappillino *et al*. [152] who recognized the simplicity of electroless atomic layer deposition (E-ALD) by galvanic displacement of palladium hydride. PdH_α were prepared chemically by exposing Pd(s) powder suspended in $0.1\,\mathrm{mol\,dm^{-3}}$ $\mathrm{H_2SO_4}$ to 1 % $\mathrm{H_2}$(g) in $\mathrm{N_2}$(g). Subsequent addition of $\mathrm{RhCl_3}$(aq) or $(\mathrm{NH_4})_2(\mathrm{PtCl_4})$ resulted in a high fractional coverage of Rh or Pt on the Pd surface. This phenomenon, where hydrogen absorbed into the bulk of Pd participates in the displacement reaction, has been noted by others as well when multiple monlayers of Pd was grown onto different substrates by SLRR of $\mathrm{H_{UPD}}$ [144]

1.7 Chemistry of Ir-aquo-chloro systems

Ir(III) and Ir(IV) may form many six-coordinated octahedral aquo-chloro complexes in aqueous solutions [153–157] on the form given in reactions (1.44) and (1.45), where hydroxy ligands (OH^-) has been omitted for readability.

$$\mathrm{IrCl_6^{3-}(aq) + H_2O(l) \rightleftharpoons Ir(OH_2)_xCl_{6-x}^{-3+x}(aq) + xCl^-(aq)} \quad (1.44)$$

$$\mathrm{IrCl_6^{2-}(aq) + H_2O(l) \rightleftharpoons Ir(OH_2)_xCl_{6-x}^{-2+x}(aq) + xCl^-(aq)} \quad (1.45)$$

Rapid exchange of ^{192}Ir between $\mathrm{IrCl_6^{3-}}$(aq) and $\mathrm{IrCl_6^{2-}}$(aq) has been observed using tracer solutions of ^{192}Ir, even though both complexes are substitution inert with blocked coordination spheres, and it is likely that exchange of ^{192}Ir between $\mathrm{IrCl_6^{3-}}$(aq) and $\mathrm{IrCl_6^{2-}}$(aq) occurs by an electron transfer mechanism [158]. The rate of aquation decreases with an increasing number of aquo ligands [153–156], where the reaction follows the S_N1 mechanism and the slow step is the removal of the Cl^- ligand [156]. $\mathrm{IrO_2}$(s) tends to precipitate from solutions containing the $\mathrm{Ir(OH_2)_3Cl_3}$ complex at elevated temperatures [156]

The Ultraviolet–Visible (UV-Vis) spectroscopy adsorption spectra of different Ir(III)-chloro complexes are quite similar. Solutions of Ir(III)-chloro complexes show two separate adsorption peaks between 300 nm and 500 nm, where the exact position of the peaks vary with the composition of the complex. For solutions of Ir(IV), the shape

of the adsorption spectrum depends on the composition of the complex. Solutions of $IrCl_6^{2-}$(aq) exhibit a distinct peak at 488 nm, as well as a pair of peaks at 415 nm and 432 nm [90, 153]. Figure 1.10 shows UV-Vis adsorption spectra of $Ir(OH_2)_xCl_{6-x}^{-3+x}$(aq) (a) and $Ir(OH_2)_xCl_{6-x}^{-2+x}$(aq) (b) where (A,B,C,D) and (a,b,c,d) correspond to $x = 0$, 1, 2 and 3, respectively [154]. The molar adsorption coefficient of Ir(IV) is at least one order of magnitude larger than that of Ir(III) [90, 153, 154]

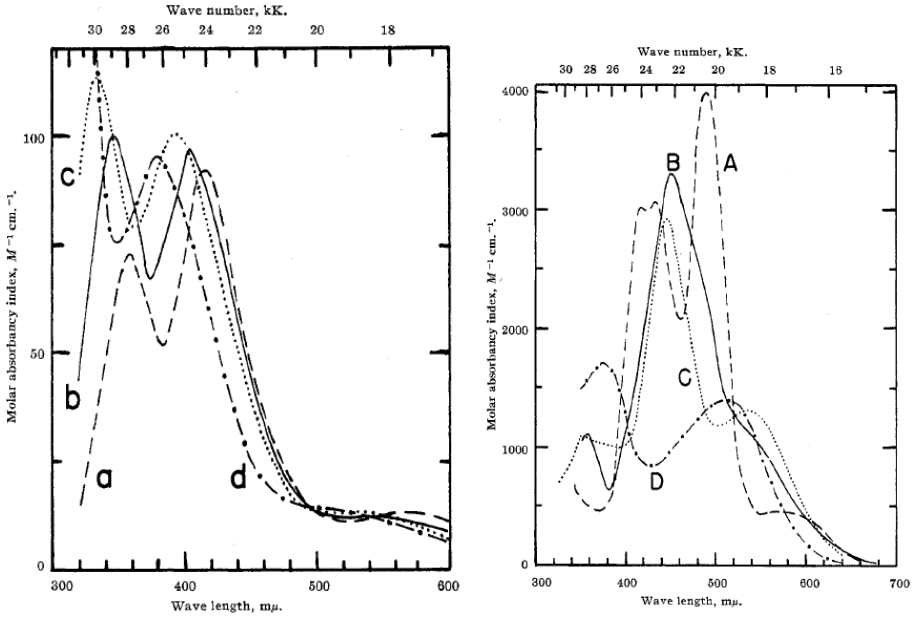

Figure 1.10: UV-Vis adsorption spectra of solutions containing $Ir(OH_2)_xCl_{6-x}^{-3+x}$(aq) (a) and $Ir(OH_2)_xCl_{6-x}^{-2+x}$(aq) (b) where (a,b,c,d) and (A,B,C,D) correspond to $x = 0$, 1, 2 and 3, respectively. Reprinted from [154] with permission.

1.8 Electrodeposition of iridium

The first systematic work found on electrodeposition of Ir is from 1962 [41], although mentions have been made earlier [159, 160]. Through galvanostatic electrodeposition of solutions containing H_2IrCl_6, Na_2IrCl_6, $BrIrCl_6$, $IrCl_3$, $IrCl_4$, $IrBr_3$ and $IrBr_4$, metallic Ir deposits were obtained from solutions containing hexachloro- and hexabromo iridates (IrX_6^{2-}(aq)). The lower the concentration of H_2IrCl_6, the higher the temperature was needed to obtained an Ir deposit. The current efficiency de-

creased with increasing current density and increased with increased temperature, although the authors do not mention whether other reactions, *i.e.* hydrogen evolution, occurred or electrode potential [41]. The H_2IrCl_6 solutions used also contained rather high amounts of Pt, Pd and Rh, which later has been shown to assist in electroplating of Ir due to deposition of Pt and subsequent underpotential deposition of hydrogen [161]. Other electroplating studies using aqueous solutions of different Ir compounds and substrates have later been released [162–175], where Ir(IV) compounds appear to be favourable over Ir(III).

Sawy and Birss [176–178] investigated electroplating of Ir from aqueous solutions containing K_2IrCl_6 using EQCM gold crystals and cyclic voltammetry. They argued a three step process, reactions (1.46) to (1.48), where $IrCl_6^{2-}(aq)$ is first reduced to $IrCl_6^{3-}(aq)$ in a single electron transfer, where the first step, reaction (1.46), is well known reaction [19]. They showed a decreased faradic efficiency with increased degree of electrolyte agitation. This was attributed to a slow adsorption step of $IrCl_6^{3-}(aq)$, where the flux of $IrCl_6^{3-}(aq)$ away from the electrode surface increased with higher rates of electrolyte agitation. At room temperature, the current attributed to reduction of adsorbed Ir(III), reaction (1.48), overlapped with that of hydrogen underpotential deposition on allready deposited Ir, and was constant with time [176] at constant potential. It was suggested that underpotentially deposited hydrogen acted as a reduction agent for the adsorbed $IrCl_6^{3-}(ads)$. The current efficiency reached a maximum around 50 % H_{UPD} coverage on Ir, and decreased at higher and lower values [176–179]. This was in contrast to Pt deposition from solutions containing $PtCl_6^{2-}(aq)$, which was reduced directly to Pt^0 onto the electrode [177].

$$IrCl_6^{2-}(aq) + e^- \underset{k_{-1}}{\overset{k_1}{\rightleftharpoons}} IrCl_6^{3-}(aq) \tag{1.46}$$

$$IrCl_6^{3-}(aq) + S \underset{k_{-2}}{\overset{k_2}{\rightleftharpoons}} IrCl_6^{3-}(ads) \tag{1.47}$$

$$IrCl_6^{3-}(ads) + 3\,e^- \underset{k_{-3}}{\overset{k_3}{\rightleftharpoons}} Ir(s) + 6\,Cl^-(aq) \tag{1.48}$$

Ahn, Moffat and coworkers [180] investigated electrodeposition of Ir onto Au, Pt and Ni substrates from aqueous sulfate based solutions containing K_3IrCl_6. The electrodeposition process was shown to be quenched at the onset of $H_2(g)$ evolution, with a maximum deposition rate around 50 % H_{UPD} coverage. Reduction of $IrCl_6^{3-}(aq)$ was also shown to be thermally activated between 20 °C and 70 °C [180]. By UV-Vis spectroscopy and voltammetry, the authors showed that the $IrCl_6^{3-}(aq)$ and $Ir(OH_2)Cl_5^{2-}(aq)$ complexes were present in the K_3IrCl_6 solutions at elevated temperatures. Changing from a sulfate based electrolyte to one containing NaCl(aq)

effectively quenched to Ir electrodeposition reaction. This was attributed to stabilization of the iridium-chloro complexes and blocking of the elecrode surface by the additional Cl^-(aq), and is consistent with another study on galvanic displacement of Ni using solutions containing H_2IrCl_6(aq) and H_2IrCl_6(aq) + HCl(aq) [90]. Similar studies on electrodeposition of Ir from solutions containing K_3IrCl_6(aq) was recently published [64, 181].

Involvement of an adosorption step and reduction involving H_{UPD} has also been also suggested by others [182]. The overpotential for depositon onto a clean glassy carbon surface was significantly larger than for one already decorated with Ir nuclei where H_{UPD} may form [182], and the optimal potential for deposition onto Pt was where H_{UPD} coverage on Pt was around 50 %. Similarly, co-deposition of Pt allowed deposition of Ir from solutions containing $IrCl_3$(aq) and $PtCl_6^{2-}$(aq) onto glassy carbon at potentials where Ir could not be deposited from solutions containing only $IrCl_3$(aq) [161].

Reduction of Ir(IV) solutions appear to involve formation- and adsorption of Ir(III) as intermediate steps [176, 177, 180, 182, 183]. Further reduction of Ir(III), reaction (1.48), has been reported to likely consist of a slow step where adsorbed Ir(III) is reduced to Ir(I) followed by fast reduction to Ir(0) [183], reactions (1.49) and (1.50). It has also been suggested that Ir(IV) is reduced to Ir(0) *via* Ir(I) in parallel with reduction of Ir(IV) to Ir(III), where Ir(I) is very easily oxidized to Ir(III) [184].

$$IrCl_6^{3-}(ads) + 2e^- \underset{k_{-3,1}}{\overset{k_{3,1}}{\rightleftharpoons}} IrCl_4^{3-}(ads) + 2Cl^-(aq) \tag{1.49}$$

$$IrCl_4^{3-}(ads) + e^- \underset{k_{-3,2}}{\overset{k_{3,2}}{\rightleftharpoons}} Ir(s) + 4Cl^-(aq) \tag{1.50}$$

1.9 The oxygen evolution reaction

Oxygen evolution takes place at the anode in acidic conditions, according to reaction (1.2). The reaction mechanism follows a a series of possible elementary steps [17, 55] as utlined in figure 1.11.

A series of different rate expressions may be derived for the different mechanisms [17, 55], where the electrochemical oxide path (blue diagonal in the figure) in acidic conditions may be written as reactions (1.51) to (1.53) [17, 55, 185]

$$H_2O(l) \rightleftharpoons OH_{ad} + H^+(aq) + e^- \tag{1.51}$$

$$OH_{ad} \rightleftharpoons O_{ad} + H^+(aq) + e^- \tag{1.52}$$

$$O_{ad} \rightleftharpoons \frac{1}{2} O_2(g) \tag{1.53}$$

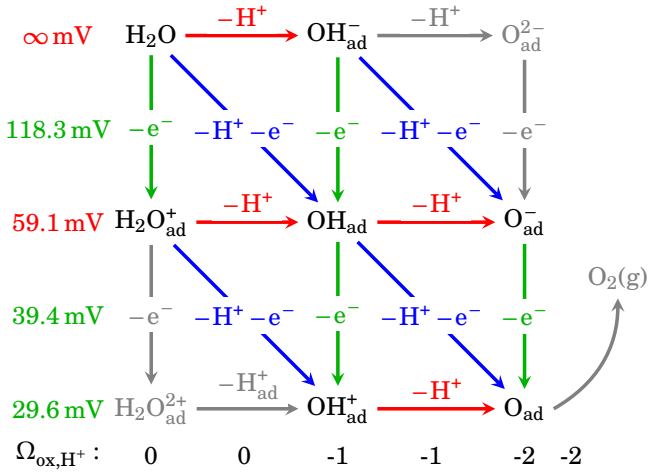

Figure 1.11: Possible reaction pathways of elementary steps during oxygen evolution in acidic enviroments. Figure inspired by [17, 55].

It has been shown that with reaction (1.52) as the rate determining step, the rate of oxygen evolution at IrO_x is well described by equation (1.54) [17, 55]

$$j = \frac{4F\Gamma_i k_2^\circ \exp\left[\frac{(1-\alpha_2)F}{RT}(E-E^\circ)\right]}{1+Ka_{H^+}\exp\left[-\frac{F}{RT}(E-E^\circ)\right]} \tag{1.54}$$

With $\alpha_2 = 0.5$, equation (1.54) predicts a tafel slope of $40\,\mathrm{mV\,dec^{-1}}$ at low potentials, and $120\,\mathrm{mV\,dec^{-1}}$ at higher potentials [17, 55]. Equation (1.54) may be expressed in a simplified form as equation (1.55),

$$j = \frac{p_1 \exp\left[(1-\alpha_2)\frac{F}{RT}E\right]}{1+p_2\exp\left[-\frac{F}{RT}E\right]} \tag{1.55}$$

where

$$p_1 = 4F\Gamma_i k_2^\circ \exp\left[-(1-\alpha_2)\frac{F}{RT}E^\circ\right] \tag{1.56}$$

$$p_2 = Ka_{H^+}\exp\left[\frac{F}{RT}E^\circ\right] \tag{1.57}$$

The Tafel slope of equations (1.54) and (1.55) at different potentials is easily visualized by plotting the slope $\partial E/\partial \log_{10}(j)$ as a function of E.

Figure 1.12 plots equation (1.55) (a) and the and the corresponding Tafel Slope (b). Values of p_1, p_2 and α_2 were obtained from [17, 55], where rate expressions for different reaction mechanisms were compared to experimental data at different pH.

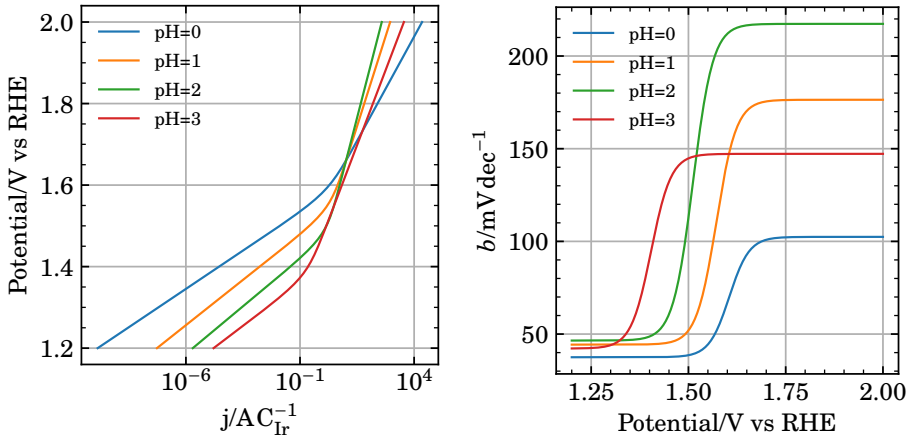

(a) (b)

Figure 1.12: (a) Plots of equations (1.54) and (1.55) and (b) the corresponding Tafel slope of the oxygen evolution reaction on IrO_2 at different pH. The constants used for plotting the rate expression, equation (1.55), were approximated from [55] with permission.

1.10 Catalysts for the oxygen evolution reaction

In order to improve the durability of OER catalysts, lower the cost or reduce the anode overpotential, many different approaches has been attempted. IrO_2 and RuO_2 has been diluted by physical mixtures or by preparation of mixed oxides with materials such as such as NiO_2 [186, 187], SnO_2 [188–190], TiO_2 [191], Nb_2O_5 [192], Sb_2O_5 [190], MnO_2 [55] or Ta_2O_5 [193, 194]. Alloys has been made with more abuntant materials, followed by post-synthesis-treatment such as de-alloying or surface enrichment [187, 195, 196], or the use of core-shell structures [195–197].

Various IrO_x based catalysts have also been supported on oxides and other materials in order to increase utilization of Ir at the anode [58, 64, 196, 198–205], where

antimony-doped tin oxide (ATO) has been identified as the most promising material for use as catalyst support on PEMWE anodes [201, 202].

The oxygen evolution reaction involves many intermediates, where the binding energy of the intermediates are linearly dependent through the so-called scaling relations [12,185]. This imposes a fundamental limit on the catalytic efficiency, which has caused the catalysts for OER to improve only incrementaly for decades [12]. Figure 1.13 shows the theoretical activity for four charge transfer steps of oxygen evolutution on an oxide surface as a funtion of binding energy. The activity of each step depends on the binding energy of the intermediates involved. This forms a volcano in the lower right part, where RuO_2 is near the top.

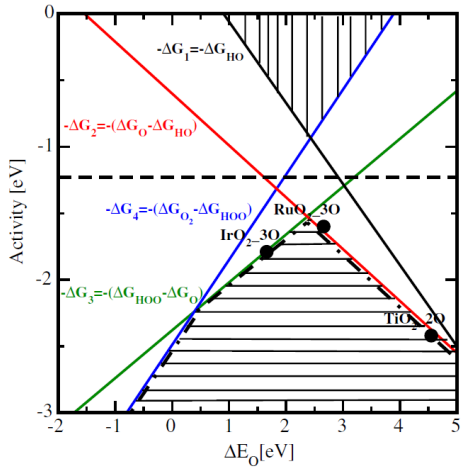

Figure 1.13: Figure showing the relation between the theoretical activity for four charge transfer steps of oxygen evolution on an oxide surface as a function of binding energy. Figure reprinted from [185] with permission.

Although highly active catalysts exist, there is often an inverse relationship between activity and stability [206, 207]. High stability of the anode catalyst is of utmost importance for a water electrolysis cell, which must operate in corrosive conditions for a long time. A recent large scale DFT study [13] identified 68 oxides (out of 47814 studied) which may be acid-stable. In general, Sb/Ti/Sn/Ge/Mo/W based systems was found to be acid-stable.

Chapter 2

Experimental methods

2.1 Cyclic voltammetry

Cyclic voltammetry (CV) is a very usefull surface sensitive technique. In a cyclic voltammetry experiment, a triangular waveform is imposed on the working electrode potential, as depicted schematically in figure 2.1.

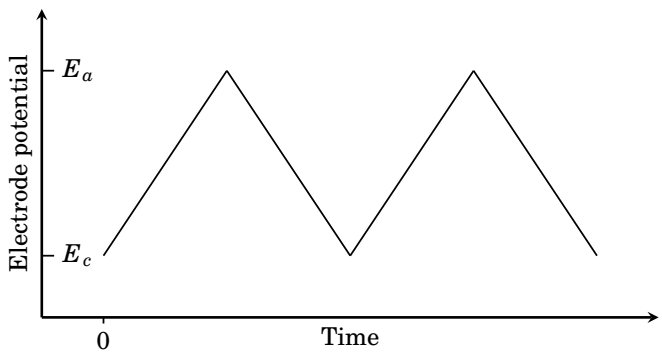

Figure 2.1: Schematic representation of the triangular potential-time waveform imposed in the working electrode in a cyclic voltammetry experiment. Figure inspired by [208].

The electrode potential is cycled linearly between two vertex potentials, E_c and E_a, while the total current at the electrode is recorded. This is repeated continiously for as many cycles as desired. Only scanning from one potential to another is known as linear sweep voltammetry (LSV). The current response is the sum of all faradic (electron transfer) and non-faradic (*i.e.* charging of the double layer)

currents at the electrode, where the reactions contributing to the total current may involve the electrode itself and species in solution. The positive going direction, when the potential is increasing with time, is often refered to as the *anodic sweep*. Consequently, the negative going direction is often refered to as the *cathodic sweep*. A typical voltammogram of a polycrystalline Pt electrode is given in figure 2.2, where the current is presented as a function of the electrode potential.

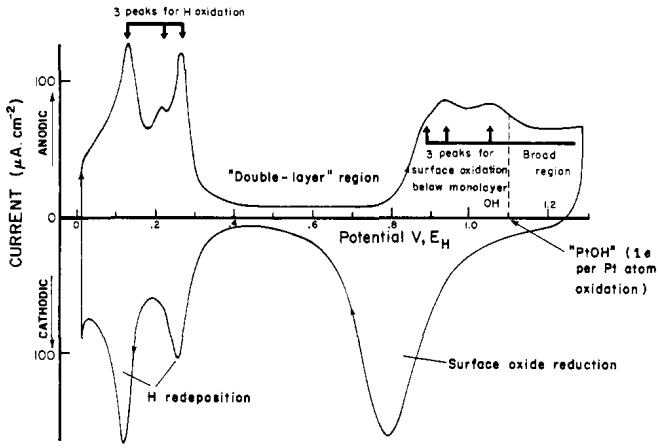

Figure 2.2: Cyclic voltammogram of a polycrystalline Pt electrode in a solution containing $1\,\mathrm{mol\,dm^{-3}}$ H_2SO_4 at 25 °C. The voltammogram was recorded at a potential sweep rate of $50\,\mathrm{mV\,s^{-1}}$. Reprinted from [209] with permission.

In figure 2.2, formation of PtOH and PtO in the positive going sweep is seen as an increasing current at potentials positive of 0.8 V. The opposite reaction, reduction of PtOH and PtO to metallic Pt, is represented by a cathodic peak around 0.8 V in the negative going sweep. The anodic and cathodic peaks seen at potentials negative of 0.4 V is from underpotential deposition of hydrogen, H_{UPD}, at Pt metal. Between 0.4 V and 0.8 V, the current in the positive going sweep is constant. This plateu is usually refered to as the *double layer region*, where the current, j_{dl}, is equal to equation (2.1) [208]

$$j_{dl} = C_{dl}\frac{\partial E}{\partial t} \tag{2.1}$$

where C_{dl} is the capacitance of the double layer and $\partial E/\partial t$ is usually taken as the electrode potential sweep rate, ν. The charge of the currents within an interval ΔE can be obtained by integrating the area under the curve by equation (2.2),

$$Q_{\Delta E} = \int_{\Delta E} j(E)\,\mathrm{d}t \tag{2.2}$$

which is commonly used to quantify the amount of material involved in a reaction, or to determine the surface area of electrodes from the anodic stripping charge of adsorbed or underpotentially deposited species such as CO_{ads}, H_{UPD} or Cu_{UPD} [80, 208, 210, 211].

Steady state polarization curves may be approximated by employing a sufficiently low potential sweep rate. This is commonly used when evaluating the activity of a catalyst, where only the steady state (*i.e.* time-independent) current response is of interrest.

2.2 Determination of electrochemical surface area

The oxide region, 0.4 V-1.4 V, in voltammograms of IrO_2 and RuO_2 is normally associated with a proton insertion reaction such as reaction (2.3) in which A^- is an anion present in the electrolyte.

$$IrO_2 \cdot nH_2O + (1+\delta)H^+ + \delta A^- + e^- \rightleftharpoons IrO_{1-\delta}(OH)_{1+\delta}A_\delta \cdot mH_2O + (n-m)H_2O \tag{2.3}$$

The voltammetric charge associated with reaction (2.3), q or Q, is potential sweep rate dependent [188, 212] and is thought of has having two contributors; the easily accessible outer regions, q_s or Q_s, and less acessible inner regions (pores, cracks, etc), q_i or Q_i. As the potential sweep rate is increased, more and more of the inner regions are excluded. At infinite sweep rate, only the easily accessible regions are included. Determination of the most easily accessible outer regions are typically done by extrapolating equation (2.4) to $v \to \infty$

$$q = q_s + b\frac{1}{\sqrt{v}} \tag{2.4}$$

where q is experimentally obtained values, v is the electrode potential sweep rate and b is an arbitrary constant.

As the potential sweep rate goes towards zero, all of the inner regions are included. The sum of q_i and q_s, q_t, are estimated by extrapolation of equation (2.5) to zero sweep rate,

$$\frac{1}{q} = \frac{1}{q_t} + a\sqrt{\nu} \tag{2.5}$$

where a is an arbitrary constant. The above relations, equations (2.4) and (2.5), are phenomenological. They assume the inclusion of deep regions to be diffusion dependent, and thus q is inversely proportional to $\sqrt{\nu}$. Equations (2.4) and (2.5) were obtained by assuming semi infinite linear diffusion of protons to the inner regions [212].

q_i is simply estimated from equation (2.6).

$$q_i = q_t - q_s \tag{2.6}$$

This method is often used to normalize the current on electrodes of IrO_x in order to compare different electrodes [17, 55].

2.3 Fitting of polarization curves

The simplified rate expression for the oxygen evolution reaction, equation (1.55) (reprinted below in equation (2.7)), can be fitted to polarization curves obtained in the region 1.3 V through 1.65 V. The values of $\log_{10}(p_1)$, $\log_{10}(p_2)$ of equations (1.56) and (1.57) (reprinted below as equations (2.8) and (2.9)) and α_2 are then optimized using the Trust Region Reflective algorithm [213] as implemented in the curve fitting procedure included in the optimization module of Scipy [214]. The optimizer is supplied an analytical jacobian, constructed from the partial derivatives of equation (2.7) with respect to $\log_{10}(p_1)$, $\log_{10}(p_2)$ and α_2 given in equations (2.10) to (2.12). Python code is available upon request.

$$j = \frac{p_1 \exp\left[(1-\alpha_2)\frac{F}{RT}E\right]}{1 + p_2 \exp\left[-\frac{F}{RT}E\right]} \tag{2.7}$$

where

$$p_1 = 4F\Gamma_i k_2^{\ominus} \exp\left[-(1-\alpha_2)\frac{F}{RT}E^{\ominus}\right] \tag{2.8}$$

$$p_2 = K a_{H^+} \exp\left[\frac{F}{RT}E^{\ominus}\right] \tag{2.9}$$

and

$$\frac{\partial j}{\partial \log_{10}(p_1)}|_E = p_1 \frac{\exp[(1-\alpha_2)fE]\ln(10)}{1+p_2\exp[-fE]} \tag{2.10}$$

$$\frac{\partial j}{\partial \log_{10}(p_1)}|_E = -p_1 p_2 \frac{\exp[-\alpha_2 fE]\ln(10)}{(1+p_2\exp[fE])^2} \tag{2.11}$$

$$\frac{\partial j}{\partial \alpha_2}|_E = -p_1 fE \frac{\exp[(1-\alpha_2)fE]}{1+p_2\exp[-fE]} \tag{2.12}$$

where $f = \frac{F}{RT}$.

Part II

Galvanic displacement of Cu, Ni and Cu and Ni on titanium oxides by Ir

Chapter 3

Galvanic displacement of carbon supported Ni by Ir

3.1 Experimental

3.1.1 Materials and equipment

All electrochemical experiments were performed in a glass cell. A glassy carbon rotating disc electrode (GC RDE) (5 mm internal diameter, PTFE shroud; Pine) served as working electrode. The electrode was polished to a mirror finish with successively 0.3 µm and 0.05 µm alumina suspensions (Allied) on a microcloth (Buehler) and rinsed using DI water (Millipore, 18.2 MΩ@25 °C) prior to each experiment. The working electrode was mounted on a Pine Standard RDE Shaft (12 mm OD PTFE shroud, stainless steel rod) attached to a Pine MSR rotator. The potentiostat used was a Gamry reference 600. The ohmic drop was determined by the built in utility, of which 85% was compensated through positive feedback compensation. The counter- and reference electrodes were Pt-foil and a reversible hydrogen electrode (RHE), respectively. All potentials reported are versus RHE. The current sampling in the potentiostat was set to *surface*, where the measured current is the average of the entire voltage step.

The electrolyte was 0.5 mol L^{-1} H_2SO_4 (96.3%, VWR). The electrolyte was purged using Ar(g) for at least 30 min prior to each experiment and kept under an Ar(g) atmosphere for the duration of the experiments.

Ni nanoparticles supported on carbon Vulcan XC/72 (Ni/C) were provided by Maidhily Manikandan [215]. The synthesis involved reduction of $Ni(acac)_2$ by oleyliamine and is described elsewhere [215]. The formal Ni/C weight ratio was 33 wt% or 20 wt% Ni

to carbon, and the mean Ni particle size was either 100 nm or 25 nm, respectively. The two batches of Ni/C are labelled Ni/C_{100} and Ni/C_{25}, respectively.

Ir precursor was a H_2IrCl_6 solution(Heraus, 20.56 wt% Ir), diluted in DI water to desired concentration.

Ultraviolet–Visible (UV-Vis) spectrophotometry adsorption spectra of H_2IrCl_6 solutions before and after the galvanic displacement experiments was obtained *ex-situ* using a Fischer Scientific Evolution 220 UV-Visible Spectrophotometer with plastic cuvettes (Eppendorf UVette, 220 nm - 1600 nm).

X-ray diffractograms of the resulting Ir@Ni/C catalysts were obtained with a Bruker D8 Advance Da-Vinci with a LynxEye Xe detector, using CuK_α radiation. The XRD samples were prepared by applying a droplet of the Ir@Ni/C catalyst suspended in isopropanol to a Si single crystal sample holder.

A HITATCHI S-5500 Scanning (Transmission) Electron Microscope, S(T)EM, equipped with a Bruker XFlash EDX detector was used to image the samples on a TEM grid. The S(T)EM imaging was performed by Gurvinder Singh (Ir@Ni/C) and Maidhily Manikandan (Ni/C).

3.1.2 Preparation of Ir@Ni/C catalysts

In a typical synthesis, Ni/C was added to N_2(g) saturated solution of H_2IrCl_6. The temperature of the H_2IrCl_6 solution was kept constant in a thermostat controlled water bath. The details of each experiment are given in table 3.1. The reaction mixture was stirred by N_2(g)-bubbling, and the product was rinsed using DI water by decanting and centrifugation five times. The experimental setup is imaged in figure 3.1. The final, washed IrNi/C product was suspended in isopropanol and dried in a heating cabinet at 60 °C overnight. Samples 3-5 were small samples intended for S(T)EM and UV-Vis analysis only.

3.2 Electrochemical characterization

Inks of the (Ir-Ni)/C catalysts were prepared by mixing catalyst with 250 $\mu L mg^{-1}$ DI water, 125 $\mu L mg^{-1}$ isopropanol and 10 $\mu L mg^{-1}$ 5wt% Nafion solution followed by sonication for 20 min. Electrodes were prepared by pipetting 2 aliquots of 10 µL onto a glassy carbon roatating disc electrode mounted on an inverted rotator [216–218]. The rotation rate of the electrode was slowly increased to 700 rpm [217], and each droplet was dried fully before the next one was applied. The total catalyst loading on the electrode was 265 $\mu g cm^{-2}$.

The Ir@Ni/C catalyst was first transformed IrO_x (anodically formed iridium oxide

Table 3.1: Overview of IrNi/C catalysts prepared by galvanic displacement of Ni/C by a H_2IrCl_6 solution. The columns, from left to right, contains batch no., Ni/C sample, concentration of the H_2IrCl_6 solution, duration and temperature of the experiment, and sample name.

#	Ni/C	$\frac{n_{Ir}}{n_{Ni}}$	C_{Ir}/mmol dm^{-3}	t/h	T/°C	Name
1	$Ni_{100}C$	5:1	1.6	1	60	$IrNi_{100}C$:60
2	$Ni_{100}C$	5:1	1.6	1	85	$IrNi_{100}C$:85
3	$Ni_{25}C$	1:1	0.6	72	25	$IrNi_{25}C$:1
4	$Ni_{25}C$	1:1	0.6	4	60	$IrNi_{25}C$:2
5	$Ni_{25}C$	1:1	0.6	4	85	$IrNi_{25}C$:3
6	$Ni_{25}C$	5:1	1.6	4	60	$IrNi_{25}C$:4

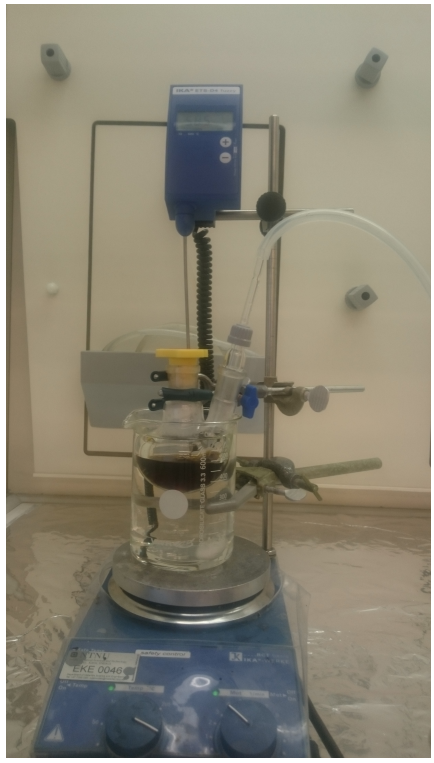

Figure 3.1: The experimental setup used for galvanic displacement of carbon supported Ni by Ir.

film, AIROF) by potential cycling between 0.05 V and 1.45 V at 50 $mV s^{-1}$ until the voltammogram did not change significantly from one cycle to the next. The amount of IrO_x in some sense close the the surface was evaluated from voltammograms performed at sweep rates 10 $mV s^{-1}$ through 500 $mV s^{-1}$, as per the method outlined earlier in section 2.2. The electrode impedance was also measured at a fixed frequency of 1 Hz over the same potential range. Activity towards the OER reaction and stability was evaluated by a slow potential cycle from 1.45 V to 1.65 V at 5 $mV min^{-1}$. Voltammograms between 0.05 V and 1.45 V was obtained at 50 $mV s^{-1}$ prior and after the slow potential cycle.

3.3 Results

Figures 3.2 and 3.3 show UV-Vis adsorption spectra of the H_2IrCl_6 solutions before and after the galvanic displacement experiments described above in table 3.1. The solutions at 1.6 $mmol dm^{-3}$ were diluted with 1 part solution and 9 parts DI water to circumvent problems with signal saturation in the spectrophotometer. The spectra obtained before the addition of Ni/C all show the typical peaks characteristic for solutions of $IrCl_6^{2-}$(aq) [90, 153], with clear peaks at 415 nm,432 nm and 488 nm. This is similar to spectra the of $IrCl_6^{2-}$(aq) shown in figure 1.10 (b). After the galvanic displacement with H_2IrCl(aq) where $IrCl_6^{2-}$(aq) was in in excess in equation (3.1), experiment 1 and 2 6, the magnitude of the $IrCl_6^{2-}$(aq) peaks in figure 3.2 (a,b) and figure 3.3 ($IrNi_{25}C$:4) were reduced, but the overall shape and features was the same. In experiments 3-5 where $IrCl_6^{2-}$(aq) was the limiting reactant in equation (3.1), figure 3.3 ($IrNi_{25}C$:1, $IrNi_{25}C$:2, $IrNi_{25}C$:3), the adsorption spectrum appear as that of a $IrCl_6^{3-}$(aq) solution [90, 153], and all $IrCl_6^{2-}$(aq) appear to have been depleted.

$$IrCl_6^{2-}(aq) + 2\,Ni(s) \rightleftharpoons Ir + 2\,Ni^{2+}(aq) + 6\,Cl^{-}(aq) \tag{3.1}$$

Figure 3.4 shows X-ray diffractograms of $Ni_{100}C$, $IrNi_{100}C$:60 and $IrNi_{100}C$:85. Peaks consistent with metallic Ni are present in the diffractogram of Ni_{100}/C. After deposition of Ir, the spectra of $IrNi_{100}C$:60 and $IrNi_{100}C$:85 show a shift in the Ni peaks to lower values of 2θ. The peaks are also broadened. For $IrNi_{100}C$:85, the peaks are almost gone.

Figure 3.5 shows a S(T)EM image of $IrNi_{100}$/C:60 and an EDS linescan across a particle. The particle appears brigther at the periphery. This is usually associated with an Ir shell on a dense or hollow Ni core [196, 219]. The intensity of the Ir and Ni signals weakens towards the center of the particle, and is likely an effect of the shape of the particle or a hollow core. Images of Ni_{100}/C are given in figure A.1.

Figure 3.6 show S(T)EM a image of $IrNi_{100}$/C:85 and an EDS linescan across the

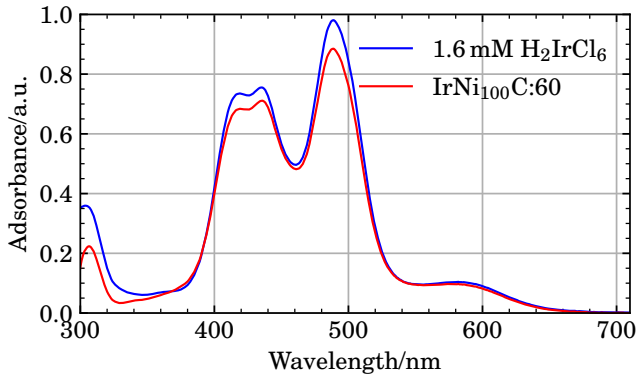

(a)

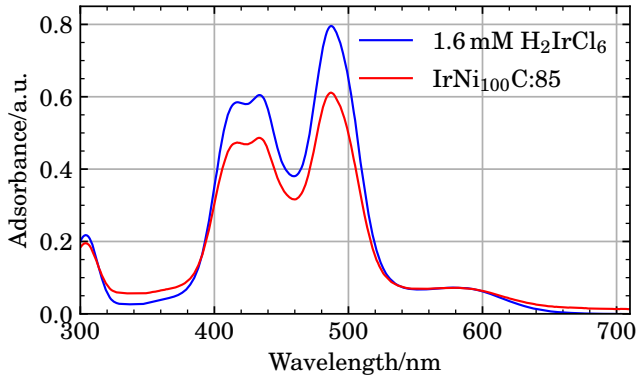

(b)

Figure 3.2: UV-Vis adsorption spectra of 1.6 mmol dm^{-3} H_2IrCl_6 before and after galvanic displacement with 33 wt% Ni_{100}/C at 60 °C (a) or 85 °C (b) for 1 h. Solutions were diluted with 1 part solution and 9 parts DI water for UV-Vis analysis.

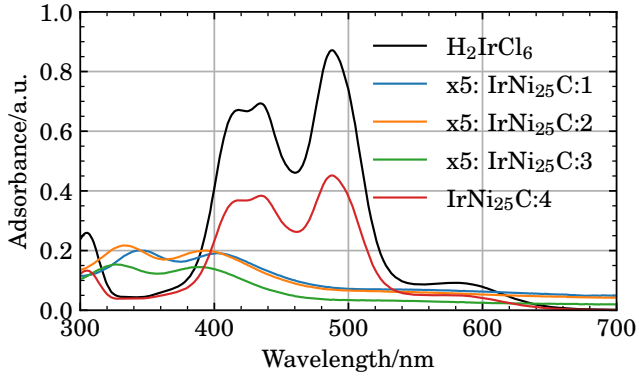

Figure 3.3: UV-Vis adsorption spectra of 0.16 mmol dm^{-3} H_2IrCl_6 before (black) and after (blue, orange, red, green) galvanic displacement with 20 wt% Ni_{25}/C at 25 °C for 72 h ($IrNi_{25}C$:1), 60 °C for 4 h ($IrNi_{25}C$:2), 95 °C for 4 h ($IrNi_{25}C$:3). $IrNi_{25}C$:4 was prepared with 1.6 mmol dm^{-3} H_2IrCl_6 at 60 °C for 4 h, and the product supernatant was diluted with 1 part solution and 9 parts DI water for UV-Vis spectroscopy.

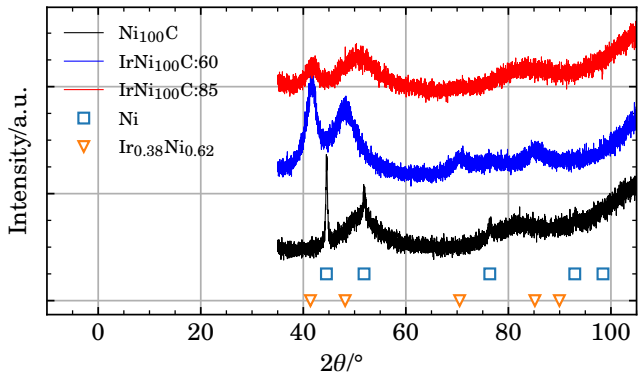

Figure 3.4: X-ray diffractogram of of $Ni_{100}C$, $IrNi_{100}C$:60 and $IrNi_{100}C$:85

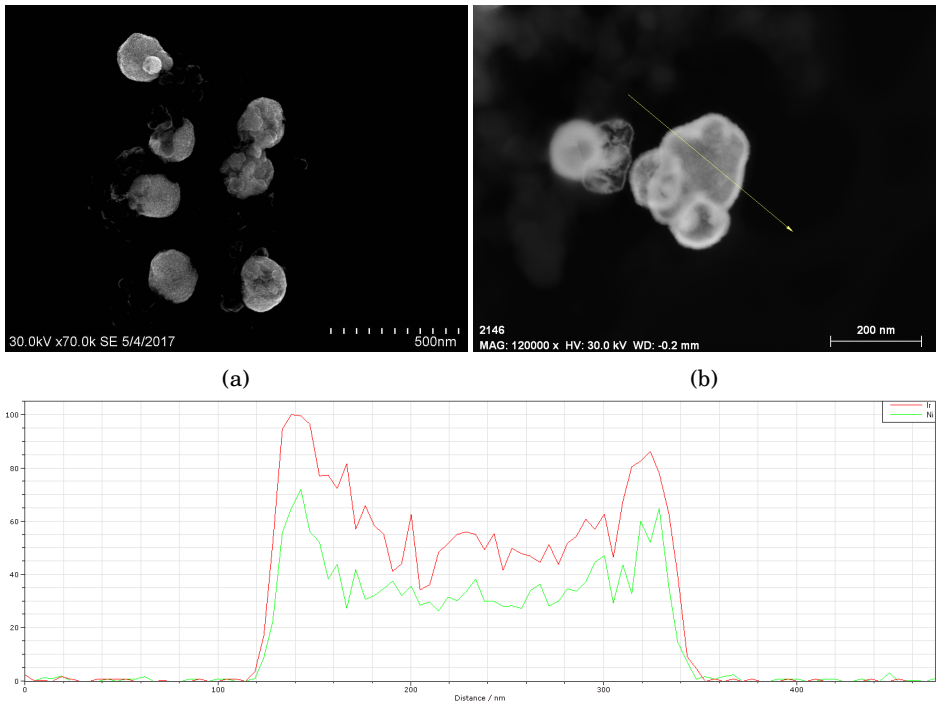

Figure 3.5: S(T)EM image and EDS linescan across a particle of of $IrNi_{100}$/C:60. S(T)EM was operated by Dr. Gurvinder Singh

particle. The particle appears brigther at the periphery. This is usually associated with an Ir shell on a dense or hollow Ni core [196, 219]. The intensity of the Ir and Ni signals weakens towards the center of the particle, and is likely an effect of the shape of the particle or a hollow core. There appear to be one or more holes in the particle, consistent with pinhole dissolution of the core.

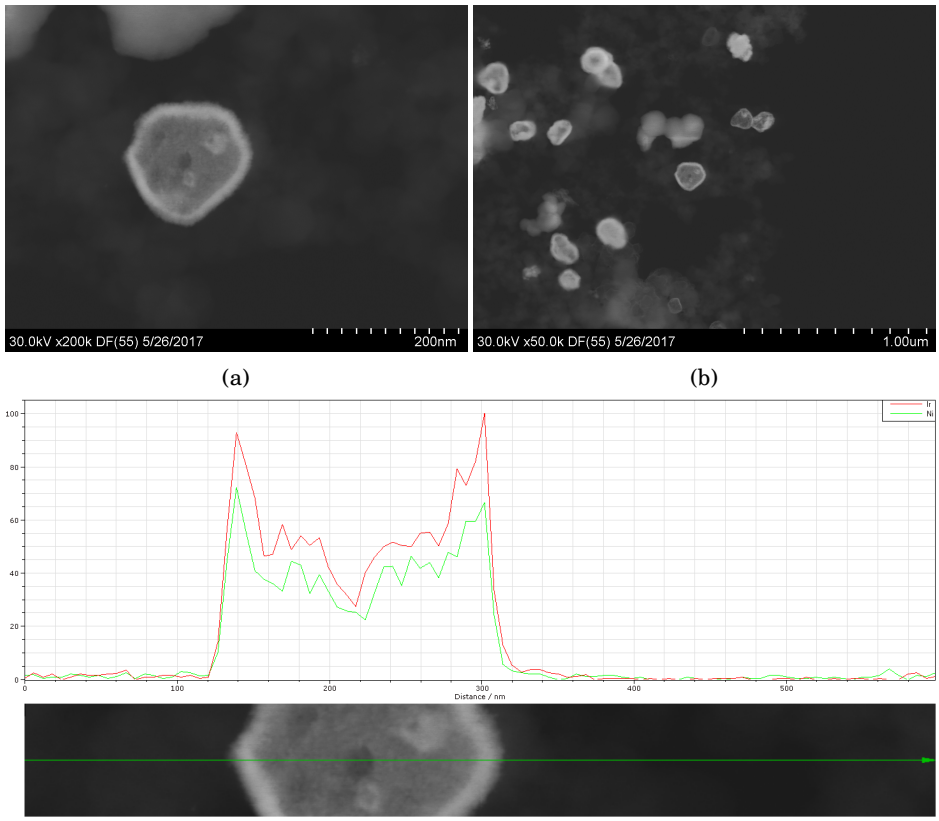

Figure 3.6: S(T)EM image and EDS linescan across a particle of $IrNi_{100}$/C:85. S(T)EM was operated by Dr. Gurvinder Singh

Samples 3-6, $IrNi_{25}$C:1-$IrNi_{25}$C:4, were reported to contain either only Ni/C (samples 3-5) or only C (sample 6) (Dr. Gurvinder Singh, private communication, S(T)EM analysis).

Figure 3.7 shows the first voltammogram of freshly prepared electrodes of $IrNi_{100}$C:60

and $IrNi_{100}C$:85 Voltammograms were obtained in 0.5 mol dm^{-3} H_2SO_4 at 50 mV s^{-1}. $IrNi_{100}C$:60 displayed a cathodic hydrogen underpototential wave and a corresponding anodic stripping peak between 0.05 V and 0.4 V, which diminished with potential cycling. $IrNi_{100}C$:85 displayed a hydrogen underpotential stripping peak of the same magnitude, but also showed a symmetrical pair of broad peaks centered around 1 V, as well as an anodic prepeak at 0.6 V.

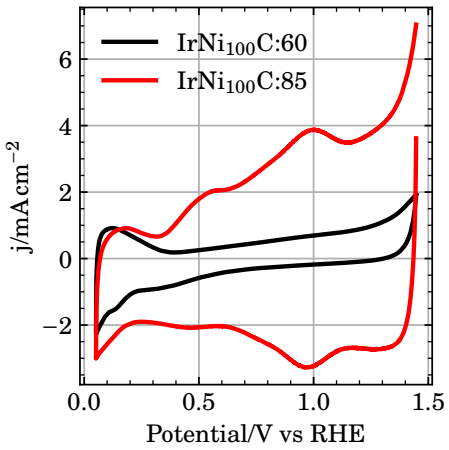

Figure 3.7: Voltammograms of freshly prepared electrodes of $IrNi_{100}C$:60 (black) and $IrNi_{100}C$:85 (red), obtained in 0.5 mol dm^{-3} H_2SO_4 at 50 mV s^{-1}.

Figure 3.8 shows a Mott Schottky plot together with a voltammogram of $IrNi_{100}C$:60 (a) and $IrNi_{100}C$:85 (b) after transformation to IrO_x by potential cycling, as described earlier. Both voltammograms display a symmetrical pair of peaks centered slightly cathodically of 1 V, as well as an anodic prepeak around 0.6 V, both of which is characteristic for AIROF. [48, 220] [48, 70, 72, 73, 76, 77, 221–228]. The Mott Schottky plots of both $IrNi_{100}C$:60 and $IrNi_{100}C$:85 display a flat band potential, *i.e.* the potential where the inverse of the squared capacitance goes towards zero, coinciding with the onset potential of the anodic prepeak around 0.6 V. This is also consistent with IrO_x prepared by other methods [78]. The geometric current density in the voltammogram of of $IrNi_{100}C$:85 is roughly 3 times that of $IrNi_{100}C$:60. The initial metallic state of $IrNi_{100}$:60 before potential cycling and transformation to IrO_x with potential cycling is consistent with previous reports on galvanic displacement of Ni with Ir [89, 91, 229].

The total amount of IrO_x participating in the proton insertion reaction, reaction (2.3), was estimated as (3.8 ± 0.7) mC and (10.5 ± 0.9) mC for $IrNi_{100}C$:60 and $IrNi_{100}C$:85,

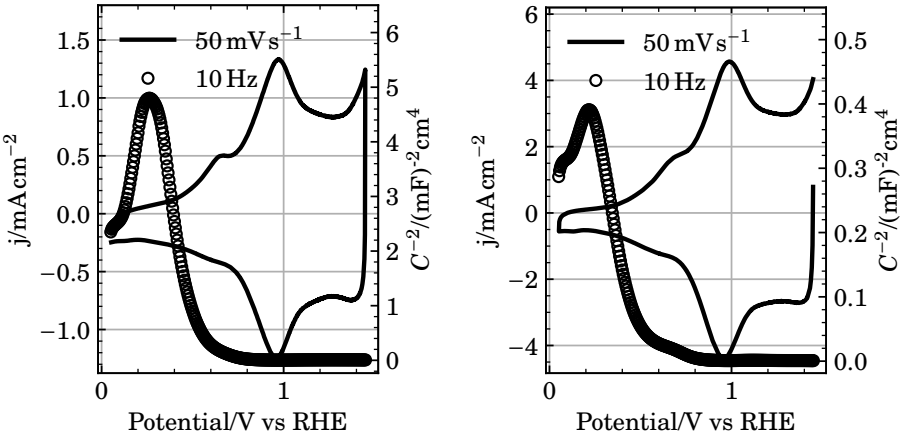

(a) $IrNi_{100}C$:60 (b) $IrNi_{100}C$:85

Figure 3.8: Voltammograms and Mott Schottky plots of $IrNi_{100}C$:60 (a) and ($IrNi_{100}C$:85 b), obtained in 0.5 mol dm^{-3} H_2SO_4 at 50 mV s^{-1} after the voltammograms did not change significantly with further cycling.

respectively using 3 electrodes of each catalyst and the method outliner earlier in section 2.2 [212]. The voltammograms and linearization to equations (2.4) to (2.6) is given in figures A.2 to A.4.

Figure 3.9 shows a pair of polarization curves of $IrNi_{100}C$:60 a and $IrNi_{100}C$:85 b, after transformation to IrO_x by potential cycling, obtained by a slow potential sweep cycle from 1.45 V to 1.65 V at 5 mV min^{-1} in 0.5 mol dm^{-3} H_2SO_4 while rotating the electrode at 1600 rpm. At currents above 40 mA cm^{-2}, the rate of O_2(g) oxygen formation exceeded the rate of oxygen removal and the electrode was quickly covered in a large bubble, as can be seen in figure 3.10 and the polarization curve in figure 3.9 (b). The geometric current density of $IrNi_{100}C$:85 is roughly twice that of $IrNi_{100}C$:60, whereas the charge-normalized and mass-normalized current densities of $IrNi_{100}C$:60 are roughly the same. On the reverse (cathodic) sweep, both samples show a lower current density compared to the forward sweep. This is attributed to blockage of the active sites due to buildup of oxygen gas, and degradation of the electrode. The mass specific activities are lower than what has been reported for other IrNi@IrO_x core/shell electrocatalysts previously [219]. The charge specific acitvities are higher than what has been reported previously for different compositions of $Ir_xRu_{1-x}O_2$ [17, 55].

Figure 3.11 displays voltammograms of $IrNi_{100}C$:60 and $IrNi_{100}C$:85 similar to

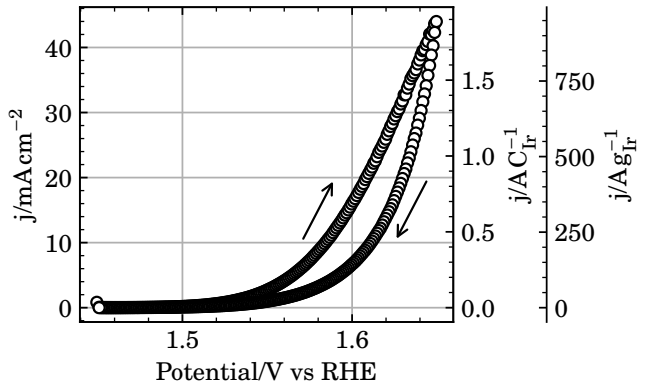

(a)

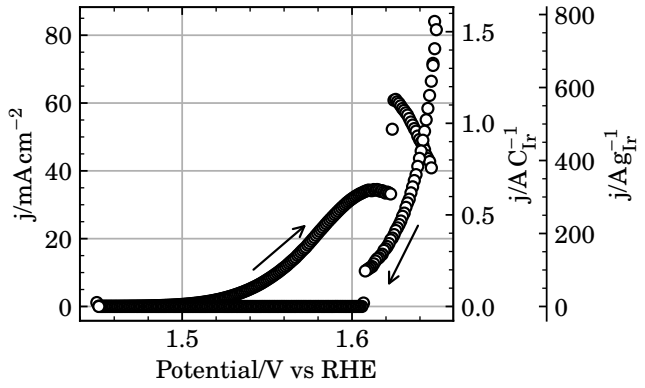

(b)

Figure 3.9: Polarization curves of $IrNi_{100}C$:60 a and $IrNi_{100}C$:85 b, after transformation to IrO_x by potential cycling, obtained by a slow potential sweep cycle from 1.45 V to 1.65 V at 5 mV min^{-1} in 0.5 mol dm^{-3} H_2SO_4 while rotating the electrode at 1600 rpm.

Figure 3.10: Bubble formation during oxygen evolution at $IrNi_{100}C$:85. A large bubble is seen covering most of the electrode surface, blocking most of the surface.

those in figure 3.8, obtained before and after the polarization curves in figure 3.9. The overall shape of the voltammograms are preserved, but the magnitude of the Ir(III)/Ir(IV) peaks at 1 V is reduced.

Figure 3.12 shows a voltammogram of $IrNi_{25}$/C:C1 obtained after extensive potential cycling between 0.05 V and 1.4 V in 0.5 mol dm^{-3} H_2SO_4 at 500 mV s^{-1}. A pair of ill-defined peaks may be present around 1 V.

3.4 Discussion

Preparation of Ni/Ir@C core/shell electrocatalysts by galvanic displacement in aqueous solutions appear to primarily yield core/shell particles. The S(T)EM images and EDS linescan in figures 3.5 and 3.6 indicate that both $IrNi_{100}C$:60 and $IrNi_{100}C$:85 contain core/shell particles, possibly with hollow cores. This is evident from the dark-field transmission images being brigter at the particle periphery, where the electrons travel through more material. The signal for both Ir and Ni in the linescans across the particles shows a higher intensity at the periphery, which is also indicative of more material in this area. As Ir grows on the particle surface, the Ni core is dissolved through pinhole dissolution with electrons traveling through the particle.

Some of the Ir in $IrNi_{100}C$:85 is likely the result of hydrolysis and condensation of

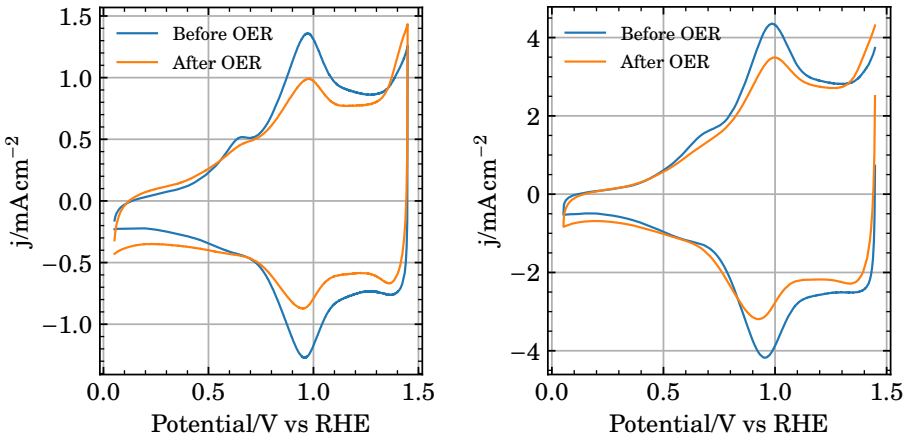

Figure 3.11: Voltammograms of $IrNi_{100}C$:60 and $IrNi_{100}C$:85 before and after oxygen evolution. Voltammograms were obtained in 0.5 mol dm^{-3} H_2SO_4 at 50 mV s^{-1}

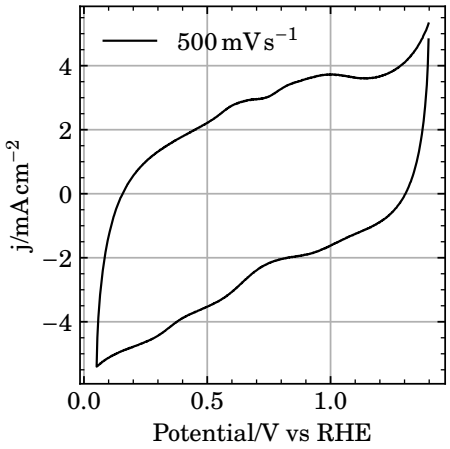

Figure 3.12: Voltammogram of $IrNi_{25}$/C:C1 in 0.5 mol dm^{-3} H_2SO_4 after extensive cycling at 500 mV s^{-1}

the H_2IrCl_6 solution at 85 °C [90, 230]. The pair of peaks centered around 1 V and the H_{UPD} peak in the voltammogram of freshly prepared electrode films in figure 3.7 indicates that $IrNi_{100}C$:85 was comprised of both IrO_x and metallic Ir before any potential cycling, *i.e.* formation of AIROF, had taken place. The voltammogram of $IrNi_{100}C$:60 did not show a peak around 1 V and was comprised of only metallic iridium. Additionally, the electrodes of $IrNi_{100}C$:85 appear to contain more Ir in total compared to $IrNi_{100}C$:60, as is seen in the higher geometric current density in figures 3.8 and 3.9 and the total charge of IrO_x determined earlier. The additional IrO_x is likely from the increased temperature causing hydrolysis and condensation.

Although the UV-Vis adsorption spectra in figure 3.2 indicate that the H_2IrCl_6 solutions consists of primarily $IrCl_6^{2-}$(aq); not $Ir(OH_2)Cl_5^-$(aq) or higher aquation products [153], the spectra were obtained *ex-situ* and does not represent the state of the H_2IrCl_6 solution during displacement. pH changes locally at the surface of each Ni particle from reaction (3.2) may contribute to precipitation of IrO_x or $Ir(OH)_x$ [90, 231–234].

$$Ni(s) + 2H^+(aq) \rightleftharpoons Ni^{2+}(aq) + H_2(g) \tag{3.2}$$

The low concentration of H_2IrCl_6 and consequently high pH in experiment 3-5 prevented Ir(IV) to be reduced to a lower oxidation state than Ir(III). The UV-Vis spectra in figure 3.3 (Ni_{25}/C:1, Ni_{25}/C:2, Ni_{25}/C:3) indicate that all the $IrCl_6^{2-}$(aq) was reduced to $IrCl_6^{3-}$(aq) when Ni as Ni_{25}/C was in excess and the concentration of H_2IrCl_6 was low. The consumption of $IrCl_6^{2-}$(aq) implies that the Ni surface was active and not covered in a passivating oxide film. A reported absence of Ir in the samples after displacement (S(T)EM analysis, private communication, Dr. Gurvinder Singh) implies that reduction of Ir(IV) did not proceed further than Ir(III). The apparent inertness of the formed Ir(III) species in experiment 3-5 is likely due to the specific composition of the reaction solution. Depending on the excact solution composition, the complexes of Ir(IV) and Ir(III) is more correctly expressed as $Ir(OH)_x(OH_2)_yCl_{6-x-y}^{-(2+y)}$ and $Ir(OH)_x(OH_2)_yCl_{6-x-y}^{-(3+y)}$. In other words, the exact H_2IrCl_6 concentration used likely lead to unfavorable values of x and y, where Ir(IV) was not reduced beyond Ir(III).

The results indicate that when the Ni nanoparticles are sufficiently small, they are consumed by proton etching and reduction of Ir(IV) to Ir(III) before any significant amount of Ir(0) is formed. The UV-Vis spectra of $IrNi_{25}C$:4 in figure 3.3 is similar to that of $IrNi_{100}C$:60 and $IrNi_{100}C$:85 in figures 3.2a and 3.2b, except the consumption of Ir(IV) appear to be somewhat higher. A reported absence of both Ni and Ir from the S(T)EM analysis (Dr. Gurvinder Singh, private communication) does not represent the average of the entire sample, only a few isolated particles. The pair of ill-defined

peaks around 1 V in the voltammogram of $IrNi_{25}C$:4 in figure 3.12 may indicate the presence of *some* Ir, although in smaller amounts. Likely, the smaller size of Ni in Ni_{25}/C compared to Ni_{100}/C results in most of the Ni being consumed by proton etching and the first reduction of Ir(IV) to Ir(III) before further reduction to Ir(0) had time to proceed to any significant extent.

While the results above indicate the feasibility of galvanic displacement of Ni nanoparticles to produce Ni/Ir core/shell catalysts, simplification is desired. The Ni nanoparticles used in this work were prepared by reduction of oleylamine in a schlenk line. Conducting the galvanic displacement reaction in an aqueous solution is an unnecessary extra step, complicating the preparation of Ni/Ir core/shell catalysts. A more logical approach is addition of an Ir precursor like iridium(III) acetylacetonate to the reaction vessel after the formation of Ni cores [235].

We will only make a small comment on the polarization curves in figure 3.9 and not discuss the results further. The activity appears promising, but the use of a carbon support and clear signs of degradation (hysterisis in the polarization curves in figure 3.9 and reduced magnitude in the main Ir(IV)/Ir(III) peak in the voltammgrams in figure 3.11) means that we will leave the results as such; *promising*, and rather refer the reader to the work by Strasser and coworkers [187, 195, 196, 203, 219, 236] and Sotiropoulos and coworkers [89, 229] for more details on oxygen evolution at Ir-Ni based electrocatalysts.

3.5 Conclusions

Preparation of Ni/Ir core/shell electrocatalysts for the oxygen evolution reaction by galvanic displacement in aqueous solutions is feasible. The procedure appear to be sensitive to both the H_2IrCl_6 concentration, temperature, pH and Ni particle size. Avoiding precipitation of IrO_x due to hydrolysis and condensation requires optimization of pH, temperature and concentration of H_2IrCl_6. To avoid premature dissolution of the Ni core, the particle size need to be optimized as well. A general recommendation can be drawn from the results of the experiments in table 3.1. Since the catalyst (Ir) is only applied as a thin film on a (Ni) core, it is not necesarry to aim for very small nanoparticles. A more robust procedure can be achieved when the initial nickel cores are somewhat large. To avoid unwanted hydrolysis and condensation of the Ir precursor solution, it is recommended to keep the solution temperature within 50 °C-70 °C.

In order to simplify the procedure, it is suggested to to conduct the galvanic displacement procedure in directly after formation of the Ni cores.

Chapter 4

Galvanic displacement of Cu and Ni on titanium oxides by Ir

4.1 Experimental

4.1.1 Materials and equipment

All electrochemical experiments were performed in a glass cell. A glassy carbon rotating disc electrode (GC RDE) (5 mm internal diameter, PTFE shroud; Pine) served as working electrode. The electrode was polished to a mirror finish with successively 0.3 µm and 0.05 µm alumina suspensions (Allied) on a microcloth(Buehler) and rinsed using DI water (Millipore, 18.2 MΩ@25 °C) prior to each experiment. The working electrode was mounted on a Pine Standard RDE Shaft (12 mm OD PTFE shroud, stainless steel rod) attached to a Pine MSR rotator. The potentiostat used was a Gamry reference 600. The ohmic drop was determined by the built in utility, of which 85% was compensated through positive feedback compensation. The counter- and reference electrodes were Pt-foil and a reversible hydrogen electrode (RHE), respectively. All potentials reported are versus RHE. The current sampling in the potentiostat was set to *surface*, where the measured current is the average of the entire voltage step.

The electrolyte was 0.5 mol L^{-1} H_2SO_4 (96.3%, VWR). The electrolyte was purged using N_2(g) for at least 30 min prior to each experiment and kept under a N_2(g) atmosphere for the duration of the experiments.

Ir precursor was a H_2IrCl_6 solution(Heraus, 20.56 %).

Cu@TiO_2, Cu@Nb_xTiO_2, Ti_4O_7, Ni@Ti_4O_7 and Ni@$Nb_xTi_4O_7$ was supplied by researcher Julian Richard Tolchard from SINTEF Industry, Sustainable Energy Tech-

nology. Prearation of TiO_2 based samples involved spray pyrolysis of precursors followed by heat treatment in hydrogen, leading to reduction and exsolution of the Cu dopant as Cu metal. The nominal Cu content was 4wt% in Cu@TiO2 and 5wt% in Cu@Nb_xTiO_2. Prearation of Ti_4O_7 based samples involved spray pyrolysis of precursors followed by mixing with Ti-metal and heat treatment in hydrogen, leading to reduction of TiO_2 to Ti_4O_7 and exsolution of the Ni dopant as Ni metal. The Ni content was 4wt%. Cu@Nb_xTiO_2 was wet-mortared in ethanol until dry upon reception.

4.1.2 Preparation of (Ir−Cu)@TiO_2 and (Ir−Cu)@Nb_xTiO_2

(Ir−Cu)@TiO_2 and (Ir−Cu)@Nb_xTiO_2 was prepared by adding Cu@TiO_2 or Cu@Nb_xTiO_2 to a 1 mmol dm^{-3} or 3.4 mmol dm^{-3} solution of H_2IrC_6 in a three neck flask equipped with a water cooled condenser. The solution was kept at 70 °C in a thermostat-controlled water bath and stirred by a magnet bar. N_2(g) was continuously flushed through the solution to keep the concentration of dissolved O_2(g) to a minimum. The molar ratio of Ir:Cu was 1:1. The reaction mixture was left for 4 h. The finished product was rinsed with DI water by centrifugation and decanting 5 times, and 1 final time with isopropanol. A small aliquot of the reaction solution was extracted before addition of the oxide and after the mixture had been centrifuged the first time, for analysis by UV-Vis spectroscopy.

4.1.3 Preparation of (Ir−Ni)@$Nb_xTi_4O_7$

385 mg Ni@$Nb_xTi_4O_7$ was added to 100 mL N_2(g) saturated 1 mmol dm^{-3} solution of H_2IrCl_6 kept at 60 °C. The reaction mixture was stirred by N_2(g)-bubling for 60 min and the product was rinsed using DI water, centrifugation and decanting 5 times. A small aliquot of the reaction solution was extracted before addition of the oxide and after the mixture had been centrifuged the first time for analysis by UV-Vis spectroscopy. The formal Ir:Ni molar ratio was 0.38, *i.e.*, Ni was in a slight with respect to the galvanic displacement reaction, equation (3.1).

4.1.4 Physical characterization

A HITATCHI S-5500 Scanning (Transmission) Electron Microscope (S(T)EM) was used to image the samples on a TEM grid (Lacey Carbon covered Cu, 200 mesh, Emsdiasum). Changes in the H_2IrCl_6 solution after galvanic displacement experiments were evaluated by UV-Vis adsorption spectroscopy using a Fischer Scientific Evolution 220 UV-Visible Spectrophotometer with plastic cuvettes (Eppendorf UVette, 220 nm - 1600 nm).

4.1.5 Electrochemical characterization

Due to problems with preparing inks of $Cu@TiO_2$ and $(Ir-Cu)@TiO_2$, $Cu@Nb_xTiO_2$ was wet-mortared in ethanol before galvanic displacement and ink preparation. Inks of different samples were prepared by mixing a known amount of oxide or catalyst with DI water and isopropanol in different ratios. A small amount of 5wt% Nafion solution was sometimes added to the ink. One ink was prepared using carbon-black and $(Ir-Cu)@TiO_2$ at 50 wt% carbon black. with 500 µL DI water, 250 µL isopropanol and 20 µL 5wt% Nafion solution. The as-prepared inks were sonicated for 15 min prior to electrode preparation.

Electrodes were prepared by pipetting 2 10 µL aliquots of the sonicated ink onto a glassy carbon rotating disc electrode mounted on an inverted (upside down) rotator [216–218]. The droplets were dried at room temperature while slowly increasing the rotation rate of the electrode to 700 rpm. For inks prepared without addition of Nafion, 2 10 µL aliquots of 0.5 wt% Nafion in isopropanol was added on the top of the dried film.

An attempt at finding the optimal water:isopropanol volume:volume ratio was done by drying 10 µL droplets of water and isopropanol mixtures on a GC RDE as described above. Optimal here refers to the ability to dry multiple droplets of 10 µl successively on an inverted GC electrode rotating at 700 rpm in an acceptable time.

The as-prepared catalyst films were then cycled between 0.05 V and 1.45 V at $50\,mV\,s^{-1}$ in $0.5\,mol\,dm^{-3}$ H_2SO_4 at room temperature. Activity towards the OER reaction and was evaluated by a slow potential scan from 1.45 V to 1.65 V at $5\,mV\,min^{-1}$.

An overview of the inks prepared is given in table 4.1

4.2 Results

4.2.1 Water- to isopropanol ratio

Table 4.2 gives an overview of the different water- to isopropanol ratios used to asses the optimal ratio of water- to isopropanol. 7 droplets was used for each composition. Too much water took too long to dry at room temperature to be practically applicable, and too much isopropanol proved impossible to deposit a droplet restricted to the glassy carbon surface on the electrode. This is important when preparing thin films of known loading on an electrode using multiple droplets. A 2:1 ratio appeared as as a good compromise.

Table 4.1: Overview of the different inks prepared for electrochemical characterization of TiO_2 and Ti_4O_7 based samples.

TiO_2 based				
#	Sample	$\frac{m_{cat}}{V_{liq}}$/mg mL^{-1}	$V_{H_2O} : V_{iso-P}$	Naf wt% /solids
1	Cu@TiO_2	13	2:1	10
2	Cu@TiO_2	1	2:1	10
3	Cu@TiO_2	13	2:1	0
4	Cu@Nb_xTiO_2	13	2:1	10
5	Cu@Nb_xTiO_2	1	2:1	10
6	Cu@Nb_xTiO_2	13	2:1	0
7	Cu@Nb_xTiO_2	-	2:1	0
8	(Ir−Cu)@TiO_2	5	2:1	25
9	(Ir−Cu)@TiO_2	5	0:1	25
10	(Ir−Cu)@TiO_2	7.5	0:1	37.5
11	(Ir−Cu)@TiO_2 + C	3.4	1:2	38
12	(Ir−Cu)@TiO_2	-	2:1	0
13	(Ir−Cu)@Nb_xTiO_2	10	2:1	12.7
14	(Ir−Cu)@Nb_xTiO_2	1	2:1	12.7
15	(Ir−Cu)@Nb_xTiO_2	10	1:0	0
16	(Ir−Cu)@Nb_xTiO_2	10	0:1	0
17	(Ir−Cu)@Nb_xTiO_2	10	2:1	0
18	(Ir−Cu)@Nb_xTiO_2	-	2:1	0

Ti_4O_7 based				
#	Sample	$\frac{m_{cat}}{V_{liq}}$/mg mL^{-1}	$V_{H_2O} : V_{iso-P}$	Naf wt% /solids
1	(Ir−Ni)@$Nb_xTi_4O_7$	12.5	2:1	0
2	Ni@$Nb_xTi_4O_7$	11.2	2:1	0
3	Ni@Ti_4O_7	15	2:1	0
4	$Nb_xTi_4O_7$	12.5	2:1	0

Table 4.2: Overview of how long a 10 µL droplet of DI water and isopropanol on a glassy carbon electrode took to dry, and how easy it was to make the droplet stay at the glassy carbon surface.

H_2O:iP	Drying time	Droplet stability	Good droplets
5:1	Long	Good	6/7
3:1	Long	Acceptable	5/7
2:1	Acceptable	Acceptable	5/7
1:1	Acceptable	Insufficient	3/7
1:2	Fast	Insufficient	2/7

4.2.2 TiO_2 based samples

The inks prepared from the TiO_2 based samples sedimented too quickly to produce a reproducible catalyst loading and and an electrode giving reproducible electrochemical measurements. Inks 7, 12 and 18 were prepared by mixing a larger amount of catalyst with DI water and isopropanol as in table 4.1 followed by sonication. Most of the material sedimented quickly after. The resulting suspension were used to prepare electrodes as described earlier. Wet-mortaring of Cu@Nb_xTiO_2 did not appear to make a difference with respect to sedimentation rate of the the inks, compared to Cu@TiO_2.

Figure 4.1 shows S(T)EM images of Cu@Nb_xTiO_2. The Nb_xTiO_2 support appear to be covered in spherical particles 100 nm to 200 nm in diameter. These particles were not present before heat treatment in hydrogen, figure C.1 and can thus be assumed to be exsolved Cu. The spherical shape of the Cu particles means that Cu does not wet the oxide support. Figure 4.1 is also expected to be representative for Cu@TiO_2 (private communication, Dr. Julian Tolchard).

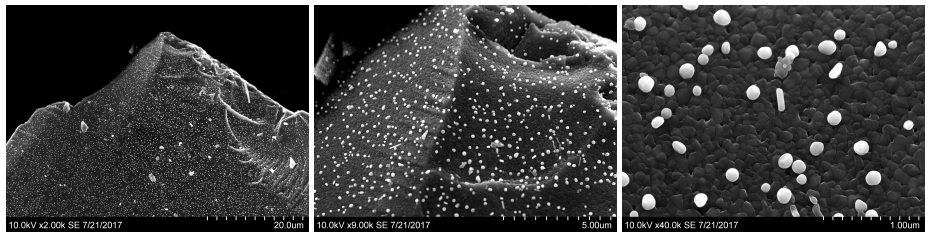

(a) (b) (c)

Figure 4.1: S(T)EM Images of Cu@Nb_xTiO_2. Images provided by Dr. Julian Tolchard

Figure 4.2 shows UV-Vis adsorption spectra of a 3.4 mmol dm^{-3} solution of H_2IrCl_6

before and after galvanic displacement with $Cu@Nb_xTiO_2$. The solutions were diluted using 200 µL solution and 1800 µL DI water to avoid signal startvation in the photospectrometer. The concentration analyzed is then approximately 0.34 mmol dm^{-3}. Both spectra are characteristic of $IrCl_6^{2-}$(aq), with peaks at 415 nm, 432 nm and 488 nm [90, 153]. The height of the main peaks were reduced to $\frac{1}{2} - \frac{1}{3}$ after the displacement.

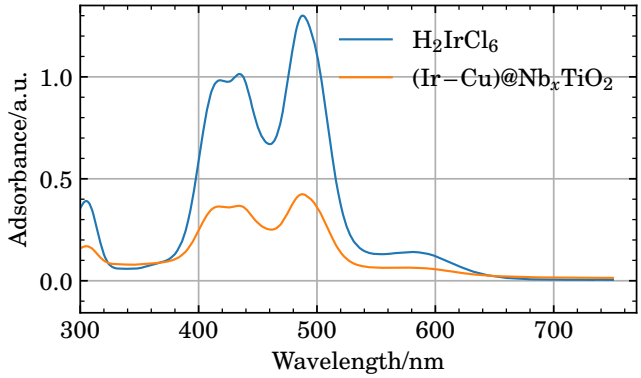

Figure 4.2: UV-Vis adsorption spectra of 1.6 mmol dm^{-3} H_2IrCl_6 before and after galvanic displacement with $Cu@Nb_xTiO_2$ at 70 °C for 4 h. The solutions were diluted with 200 µL solution and 1800 µL DI water to avoid signal saturation/startvation in the photospectrometer.

Figure 4.3 shows S(T)EM images of $(Ir-Cu)@TiO_2$ obtained in SE (a,b), BF transmission (c) and DF transmission (d) mode. The dark and bright dots in figure 4.3 (c,d) suggests that the surface of the TiO_2 support was covered in finely distributed particles, ≈ 2 nm, of a heavier element. The surface texture of the ≈ 100 nm particles particles in figure 4.3 (g) appear to be different after the displacement reaction when compared to figure 4.1.

Figure 4.4 shows S(T)EM images of $(Ir-Cu)@Nb_xTiO_2$ The main features appear to be the same as for $(Ir-Cu)@TiO_2$, figure 4.3. Figure 4.4 (d) appear to contained the same small bright particles as in figure 4.3 (c,d), and the surface texture of the large ≈ 100 nm particles appear to be different from figure 4.1.

Figure 4.5 (a,b,c) shows voltammograms of $Cu@Nb_xTiO_2$ (a), $(Ir-Cu)@TiO_2$ (b) and $(Ir-Cu)@Nb_xTiO_2$ (c). In figure 4.5 (a,b), an anodic wave can be observed starting around 0.3 V-0.4 V in the first (blue) anodic sweep. A second wave grows at potentials more anodically than 0.8 V. On the reverse sweep, there is a small cathodic wave at potentials below 0.3 V. The first anodic wave diminishes greatly with cycling. A

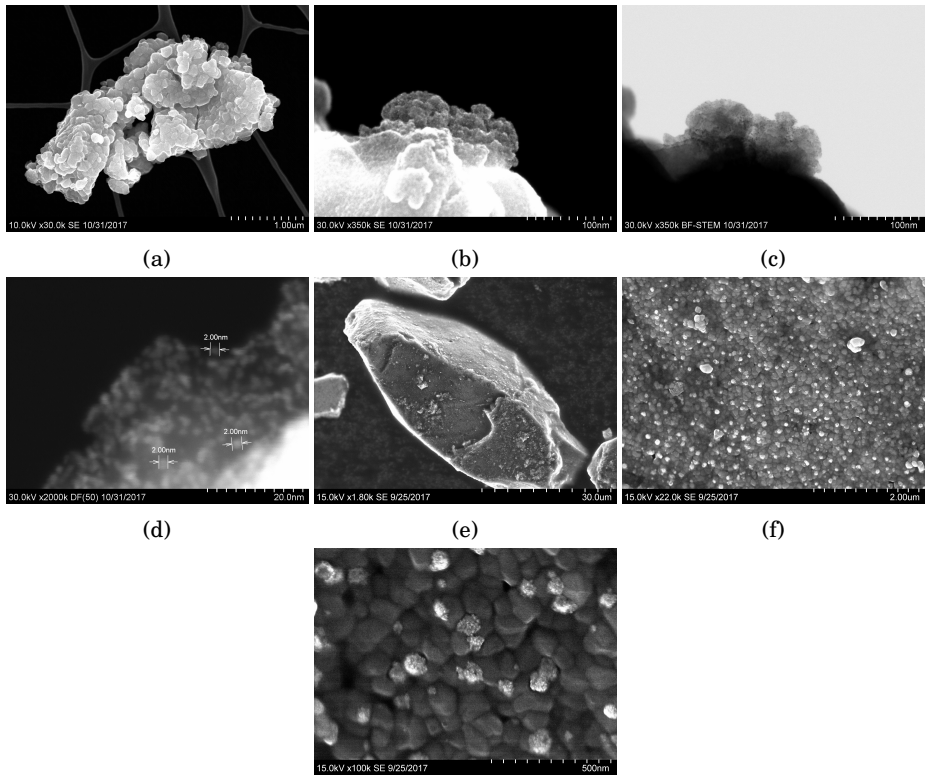

Figure 4.3: S(T)EM Images of $(Ir-Cu)@TiO_2$ obtained in secondary electron (a,b,e,f,g), brightfield transmission (c) and darkfield transmission (d) mode. (e,f,g) provided by Dr. Julian Tolchard.

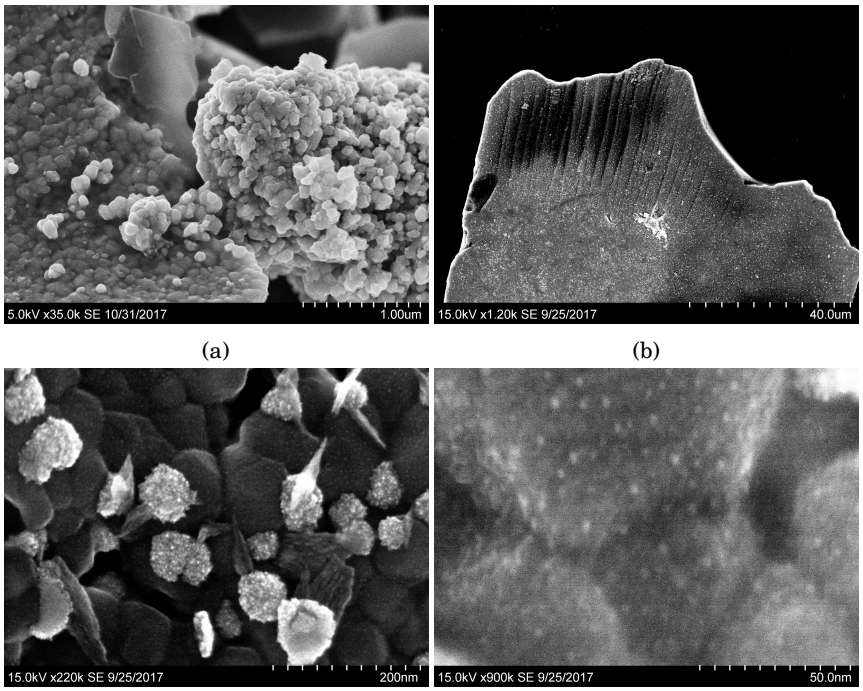

Figure 4.4: S(T)EM Images of (Ir−Cu)@Nb_xTiO_2.

plateau appears between 0.8 V and 1.2 V in the CV for the 50th cycle, which indicate capacitive charging in this potential region. A broad pair of peaks also appear around 0.6 V, which is commonly associated with the glassy carbon electrode [237].

The voltammogam in figure 4.5 (c) shows a broad pair of peaks centered around 0.9 V that are reduced in magnitute upon cycling.

Polarization curves of $Cu@Nb_xTiO_2$, $(Ir-Cu)@TiO_2$ and $(Ir-Cu)@Nb_xTiO_2$ are shown in figure 4.5 (d). $(Ir-Cu)@Nb_xTiO_2$ display a significantly higher geometric current density in the oxygen evolution region than $Cu@Nb_xTiO_2$ and $(Ir-Cu)@TiO_2$. The current actually decreases for $(Ir-Cu)@Nb_xTiO_2$ and $(Ir-Cu)@TiO_2$ at potentials above 1.63 V and 1.6 V.

Figure 4.6 shows voltammograms at $50\,mV\,s^{-1}$ of an electrode of $(Ir-Cu)@Nb_xTiO_2$ obtained before and after the polarization curve in figure 4.5 (d). The broad peaks around 1 V was gone after the polarization curve, and the voltammogram resembled that of $Cu@TiO_2$ and $(Ir-Cu)@TiO_2$ in figure 4.5 (a,b).

4.2.3 Ti_4O_7 based samples

Figure 4.7 shows UV-Vis adsorption spectra of a $1\,mmol\,dm^{-3}$ solution of H_2IrCl_6 before and after galvanic displacement with $Ni@Nb_xTi_4O_7$. The adsorption spectra of H_2IrCl_6 has been described earlier for figure 4.2, where the main peaks at 415 nm, 432 nm and 488 nm are characteristic for solutions of $IrCl_6^{2-}$(aq) [90, 153]. The adsorption spectra obtained after the galvanic displacement experiment is similar to that of Ir(III) solutions of $IrCl_3$ and K_3IrCl_6 [90, 153]. $IrCl_6^{3-}$(aq) has peaks at 360 nm 415 nm [90, 153]. The spectra for $(Ir-Ni)@Nb_xTi_4O_7$ has peaks at 336 nm and 402 nm. This is likely $Ir(OH_2)Cl_5^{2-}$(aq) or $Ir(OH_2)_2Cl_4^{-}$(aq), as the 2 peaks of $Ir(OH_2)_xCl_{6-x}^{(3-x)-}$(aq) shifts to lower wavelengths with increasing aquation [153].

Figure 4.8 shows cyclic voltammograms of Ti_4O_7 (a), $Ni@Ti_4O_7$ (b), $Ni@Nb_xTi_4O_7$ (c) and $(Ir-Ni)@Nb_xTi_4O_7$ (d). The voltammograms were obtained by cycling a freshly prepared electrode in $0.5\,mol\,dm^{-3}$ H_2SO_4 at $50\,mV\,s^{-1}$. The voltammograms show the same main features. The first anodic sweep is comprised of a rising anodic wave, with a peak around 1 V. The reverse sweep does not contain a corresponding cathodic wave, and the voltammogram quickly becomes featureless. This is the same as was observed for $(Ir-Cu)@TiO_2$ and $Cu@Nb_xTiO_2$ in figure 4.5 (b,a). We were unable to obtain good data of $Ni@Ti_4O_7$, so the voltammogram in figure 4.8 (b) is not discussed further, other than pointing out that the CVs in figure 4.8 (b) are similar to those in figure 4.8 (a,c,d)

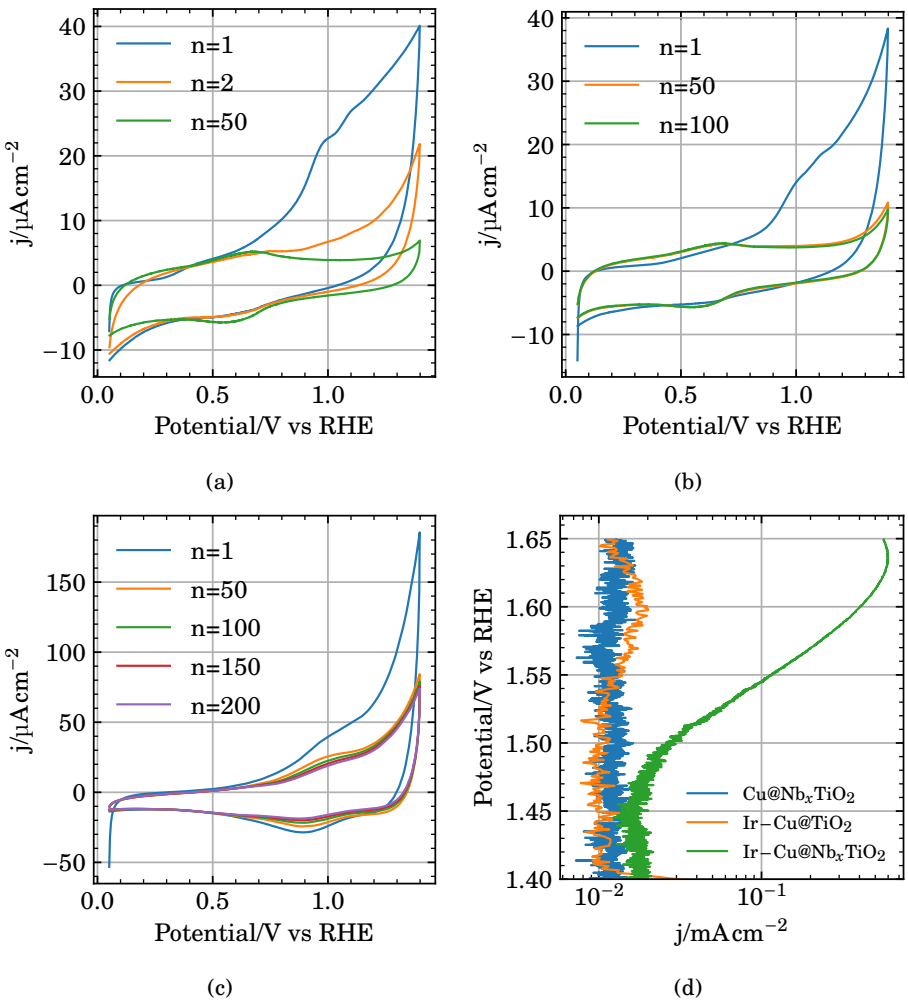

Figure 4.5: Cyclic voltammograms (a,b,c) and polarization curves (d) of Cu@Nb$_x$TiO$_2$ (a,d), (Ir−Cu)@TiO$_2$ (b,d) and (Ir−Cu)@Nb$_x$TiO$_2$ (c,d). Voltammograms were obtained at in 0.5 mol dm^{-3} H_2SO_4 with a sweeprate of 50 mV s^{-1}. Polarization curves were obtained after the voltammograms, in the same electrolyte, at 3 mV min^{-1} with an electrode rotation rate of 1600 rpm.

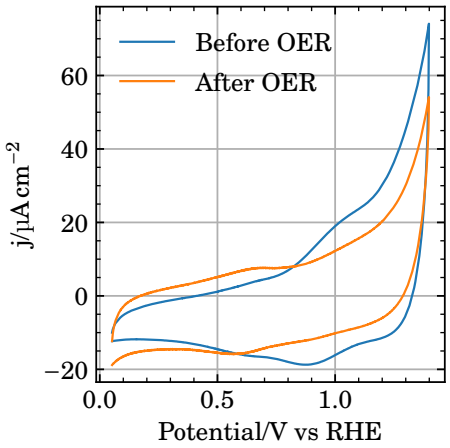

Figure 4.6: Cyclic voltammograms of (Ir−Cu)@Nb_xTiO_2 obtained before and after a 3 mV min^{-1} potential sweep from 1.4 V to 1.65 V. Voltammograms were obtained with a sweeprate of 50 mV s^{-1}. Electrolyte was 0.5 mol dm^{-3} H_2SO_4.

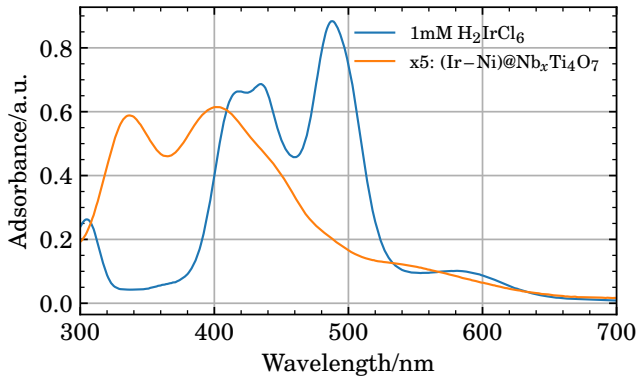

Figure 4.7: UV-Vis adsorption spectra of 1 mmol dm^{-3} H_2IrCl_6 before and after galvanic displacement with Ni@$Nb_xTi_4O_7$ at 60 °C for 1 h.

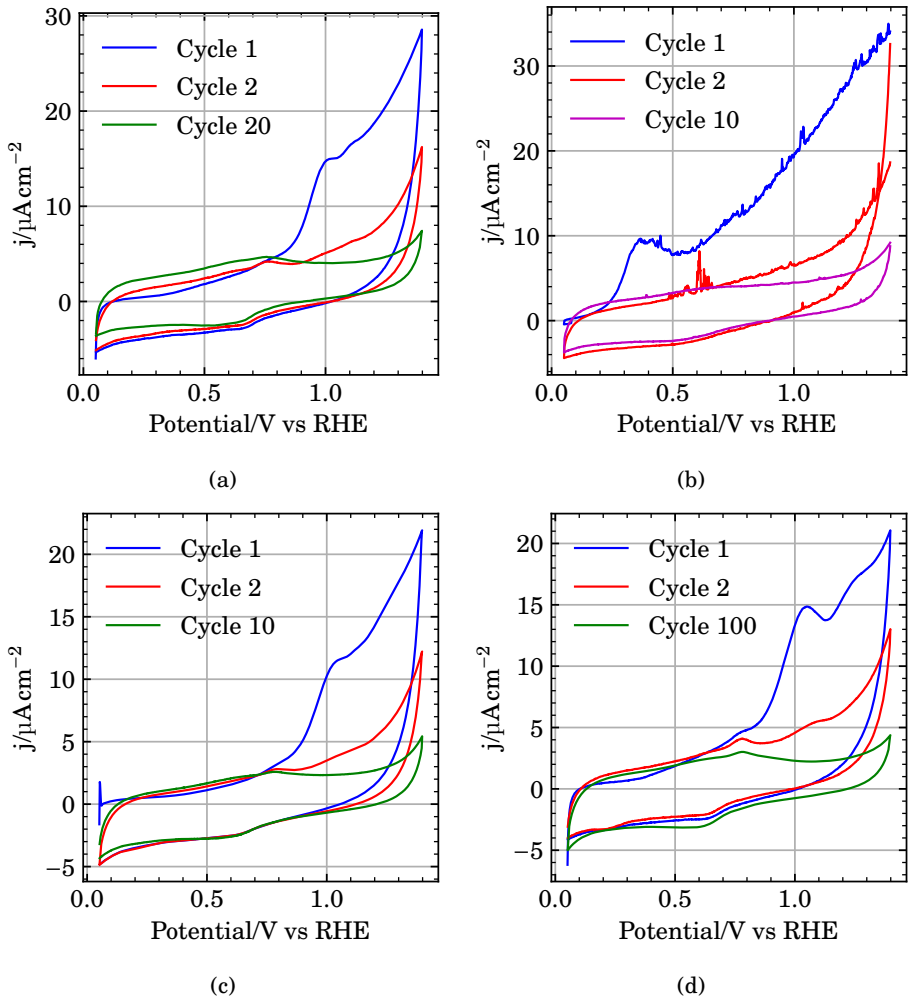

Figure 4.8: Cyclic voltammograms of Ti_4O_7 (a), Ni@Ti_4O_7 (b), Ni@$Nb_xTi_4O_7$ (c) and (Ir−Ni)@$Nb_xTi_4O_7$ (d). Voltammograms were obtained in 0.5 mol dm^{-3} H_2SO_4 with a sweeprate of 50 mV s^{-1}.

4.3 Discussion

Only (Ir−Cu)@Nb_xTiO_2 appears to contain electrochemically active Ir. The pair of peaks around 1 V in the voltammogram of (Ir−Cu)@Nb_xTiO_2 in figure 4.5c, which is not present in the voltammogram of Cu@Nb_xTiO_2, figure 4.5a is typical for IrO_x in H_2SO_4 [48, 48, 70, 72, 73, 76, 77, 220–228]. The voltammogram of (Ir−Cu)@Nb_xTiO_2, figure 4.5c, is also very similar to that of IrO_2/$Nb_{0.05}Ti_{0.95}O_2$ in H_2SO_4 [198]. Additionally, (Ir−Cu)@Nb_xTiO_2 show a catalytic activity towards oxygen evolution in figure 4.5d, where Cu@Nb_xTiO_2 and (Ir−Cu)@TiO_2 is basically inactive.

Ir may be present in (Ir−Cu)@TiO_2 also, but the conductivity of the undoped oxide is unsufficient to detect any Ir electrochemically. The presence of small ≈ 2 nm particles of heavier elements on the surface of (Ir−Cu)@TiO_2 and (Ir−Cu)@Nb_xTiO_2 in figures 4.3 and 4.4, and the change in surface texture of the large ≈ 100 nm Cu particles when comparing Cu@Nb_xTiO_2 in figure 4.1 to (Ir−Cu)@TiO_2 in figure 4.3 and (Ir−Cu)@Nb_xTiO_2 in figure 4.4 is indicative that the surface of (Ir−Cu)@TiO_2 and (Ir−Cu)@Nb_xTiO_2 being modified the same way. The main difference between the two samples is the conductivity of the support, and is likely why any Ir on (Ir−Cu)@TiO_2 is electrochemically inactive.

The electrochemically active Ir in (Ir−Cu)@Nb_xTiO_2 is not from galvanic displacememt of H_2IrCl_6 with Cu. The first potential sweep in figure 4.5 (c) does not show any sign of underpotential deposition of hydrogen between 0.05 V and 0.4 V. H_{UPD} on metallic Ir is expected in this potential region [113, 210]. Peaks of H_{UPD} was present in the Ir/Ni catalysts prepared in chapter 3, figure 3.7.

The larger, ≈ 100 nm, particles on (Ir−Cu)@TiO_2 and (Ir−Cu)@Nb_xTiO_2 in figures 4.3 and 4.4 are consistent with the bright spherical Cu particles on Cu@Nb_xTiO_2 in figure 4.1 being modified by galvanic displacement with Ir. The smaller ≈ 2 nm particles on (Ir−Cu)@TiO_2 and (Ir−Cu)@Nb_xTiO_2 in figures 4.3 and 4.4 are not. They can be rationalized by one of:

(i) The oxide is sufficiently conductive so that Cu oxidation and Ir reduction need not proceed at the same location [84].

(ii) The oxide support itself is oxidized, reducing Ir onto the surface.

(iii) Iridium hydrolyzed and condensed onto the surface of the titanium oxide support.

The first point is not consistent with the absence of electrochemically active Ir on (Ir−Cu)@TiO_2 in the voltammogram in figure 4.5 (b). The first two points are not consistent with the lack of any H_{UPD} peaks in the voltammogram of (Ir−Cu)@Nb_xTiO_2 in figure 4.5 (c), as mentioned above. Only the last two points are consistent with

the presence of peaks around 1 V in the first potential sweep of (Ir−Cu)@Nb_xTiO_2 in figure 4.5 (c) and the absence of any H_{UPD} peaks, which implies that iridium was present as Ir(IV)/Ir(III), similar to what was argued for Ir/Ni in chapter 3. In other words; we can conclude that we have not modified the titanium oxides with Ir by galvanic displacement of Cu, but rather by hydrolysis and condensation.

The titanium oxide based supports all appear to be irreversibly oxidized at potentials exceeding 0.8 V. Ebonex, a mixture of mainly Ti_4O_7 and Ti_5O_7, does not exhibit peaks between 0 and 2 V vs RHE in 1 mol dm^{-3} H_2SO_4 at room temperature [238, 239]. The oxidation waves in the first cycles in figures 4.5 and 4.8 are present in both both TiO_2 and Ti_4O_7, with and without Nb doping. It is then likely related to oxidation of the oxide surface, which was exposed to a reducing hydrogen atmosphere after spray pyrolisis in order to exsolve the Cu and Ni dopants. Formation of insulating TiO_2 is consistent with the voltammograms exhibiting no distinguishable features, even with the apparent presence of Ir at the (Ir−Cu)@TiO_2 surface. The voltammograms of Cu@Nb_xTiO_2 and (Ir−Cu)@TiO_2, figures 4.5a and 4.5b, are virtually identical. This means that the apparent Ir nanoparticles at the surface of (Ir−Cu)@TiO_2 are not detected electrochemically. The pair of broad peaks in the voltammogram of (Ir−Cu)@Nb_xTiO_2, figure 4.5c is likely due to the increased conductivity from the Nb doping allowing some iridium to be detected electrochemically. After the polarization curve in figure 4.5d, the voltammogram of (Ir−Cu)@Nb_xTiO_2 also took on the same shape as the voltammograms of the remaining samples. The Ir present was either lost, or the surface became completely insulating. At high potentials, > 1.6 V, IrO_x is known to corrode [1, 13, 240]. Catalysts with small nanoparticles of IrO_x, as the finely distributed nanoparticles seen in figures 4.3 and 4.4 can not be expected to be very stable over time at high potentials.

4.4 Conclusions

We have shown that insufficient conductivity of the catalyst support will render the catalyst inactive. We have also shown that even though it is possible to create IrO_x nanoparticles finely distributed on a TiO_2 based support, the small size severely reduces the stability of the catalyst. Preparation of TiO_2/IrO_x-based core/shell electrocatalysts for oxygen evolution by galvanic displacement did not succeed. The H_2IrCl_6 precursor solution appear to have hydrolyzed and condensed onto the surface of the TiO_2-based supports as $Ir(OH)_3$, IrO_x or similar. Ti_4O_7-based supports appear to not be stable in 0.5 mol dm^{-3} H_2SO_4 at potentials relevant for oxygen evolution.

Chapter 5

Galvanic displacement of Cu by Ir

5.1 Experimental

5.1.1 Electrochemical preparation of Cu/Au(poly) deposits

A gold rotating disc electrode (Au RDE) (5 mm internal diameter, PEEK shroud; Pine) was polished to a mirror finish using successively 0.3 µm and 0.05 µm alumina suspensions on a microcloth and rinsed using deionized water(DI water) (Millipore) prior to Cu deposition. Cu films were prepared from 0.1 mol dm^{-3} $CuSO_4$(>99.0%, Sigma Aldrich) + 0.1 mol dm^{-3} H_2SO_4(96.3%, VWR) de-aerated solutions. The electroplating process was performed under potentiostatic control at 0.05 V vs RHE until a total charge of 500 mC had passed. The resulting Cu/Au film was rinsed by immersion into DI-water.

5.1.2 Electrochemical preparation of particulate Cu/GC deposits

A glassy carbon rotating disc electrode (GC RDE) (5 mm internal diameter, PEEK shroud; Pine) was polished to a mirror finish using successively 0.3 µm and 0.05 µm alumina suspensions on a microcloth and rinsed using DI water prior to Cu deposition. Cu deposits were prepared from 0.1 mol dm^{-3} $CuSO_4$(>99.0%, Sigma Aldrich) + 0.1 mol dm^{-3} H_2SO_4(96.3%, VWR) de-aerated solutions. The electroplating process was performed using repeating chronoamperometry with a total of 200 potential pulses. Cathodic- and anodic potentials were 0.05 V and 0.33 V with hold times of 0.1 s and 2 s, respectively. The resulting Cu/GC film was rinsed by immersion into

DI water.

5.1.3 Preparation of (Ir-Cu/Au) and (Ir-Cu/GC) films

The as-prepared Cu films were immersed for 30 min in 50 mL de-aerated 1 mmol dm^{-3} H_2IrCl_6 (Heraeus) solutions kept at (70 ± 1) °C under a N_2(g) atmosphere. The electrodes was either kept stagnant or rotated at 1600 rpm using a Pine MSR rotator with a 15mm RRDE shaft. The resulting (Ir-Cu)-films were rinsed in de-aerated 1 mol dm^{-3} HCl and DI water to remove any contaminants from the H_2IrCl_6 solution. The films are denoted (Ir-Cu/Au)s, $(Ir\text{-}Cu/Au)_r$ and (Ir-Cu/GC) respectively, where s and r is short for stagnant and rotation. (Ir-Cu/GC) was prepared with rotation only.

5.1.4 Physical characterization

The Cu and (Ir-Cu) films were imaged using a Hitatchi S-3400N scanning electron microscope equipped with an Oxford instruments Aztec Energy-dispersive X-ray spectroscopy (EDS) system.

5.1.5 Electrochemical characterization

Electrochemical characterization of the (Ir-Cu) deposits was carried out using a Gamry reference 600 potentiostat, controlled by the Gamry Framework software, a Pt-foil counter electrode and a reversible hydrogen (RHE) reference electrode in de-aerated 0.5 mol dm^{-3} H_2SO_4(96.3%, VWR) solution. The following electrochemical procedure was utilized: The ohmic drop in the electrolyte was determined by electrochemical impedance spectroscopy (EIS) at open circuit potential using a different GC electrode without any (Ir-Cu) deposit and 85% was compensated using the built in positive feedback utility. The (Ir-Cu) films were transformed to IrO_x by cyclic voltammetry (CV). CV was performed by sweeping the potential of the electrode between 0.05 V and 1.3 V (Au RDE) or 1.4 V (GC RDE) vs RHE for 200 cycles at 50 mV s^{-1}. The total, inner and total charge of the resulting IrO_x film was found from CVs performed at sweep rates ranging from 2mV s^{-1} to 500mV s^{-1} using the method outlined in section 2.2 [212]. The impedance of the transformed IrO_x films was measured at a fixed frequency of 1 Hz through the same potential range as the voltammograms, in potential steps of 10 mV.

The activity for the oxygen evolution reaction was evaluated by linear sweep voltammetry from 1.3 V to 1.65 V, using a potential sweep rate of 3 mV min^{-1}. The rate expression for the oxygen evolution reaction, equation (1.54), was fitted to the polarization curves as outlined previously in section 2.3

5.2 Results

5.2.1 Preparation of (Ir – Cu)@Au

Figure 5.1 depicts a typical Cu-film on Au(poly) prepared potentiostatically. The film was flat and continuous, but with a rough surface.

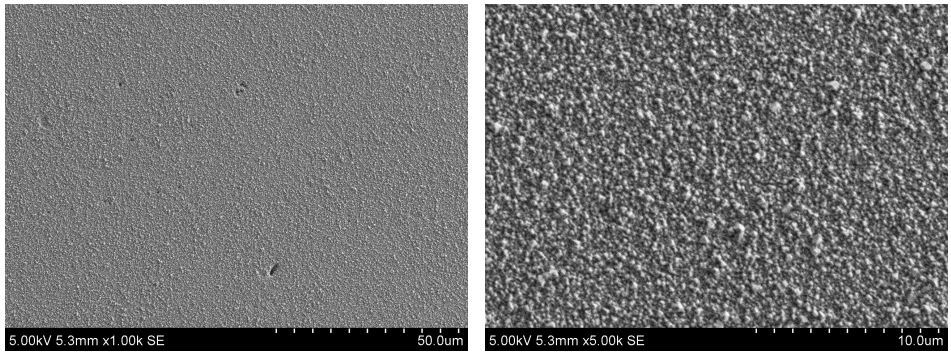

(a) (b)

Figure 5.1: A typical Cu@Au film prepared by potentiostatic deposition at 0.05 V in 0.1 mol dm^{-3} $CuSO_4$ + 0.1 mol dm^{-3} H_2SO_4 de-aerated solutions. The total charge passed during preparation of the film was 500 mC.

Figure 5.2 shows the electrode surface after performing the galvanic displacement procedure in stagnant conditions, (Ir-Cu/Au)$_s$. The surface of (Ir-Cu/Au)$_s$ was homogeneously covered by Ir nanoparticles $\leq 1\,\mu$m in diameter.

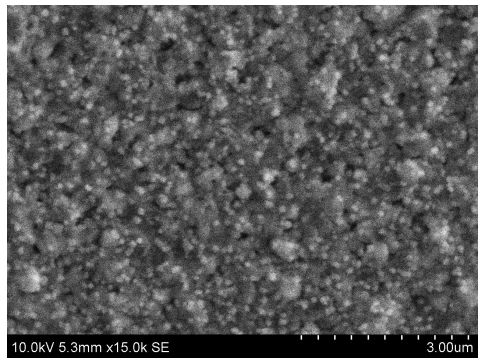

Figure 5.2: Ir nanoparticles covering the (Ir-Cu)$_s$-film.

Figure 5.3 shows the periphery of the (Ir-Cu/Au)$_s$ electrode. The edge of the Au disc. It was comprised a porous Ir-layer followed by the aforementioned Ir-particles (figure 5.2). Figure 5.3b is an EDS linescan across the edge of the film and in towards the centre of (Ir-Cu/Au)$_s$. Starting at the edge, the Ir-L$_\alpha$ signal drops towards the center. The Cu-K$_\alpha$ signal is inversely proportional to the Ir-L$_\alpha$ signal. This is consistent with an exchange reaction which rate is limited by the transport of Ir(IV) towards the surface, where the flux is higher at the disc edge.

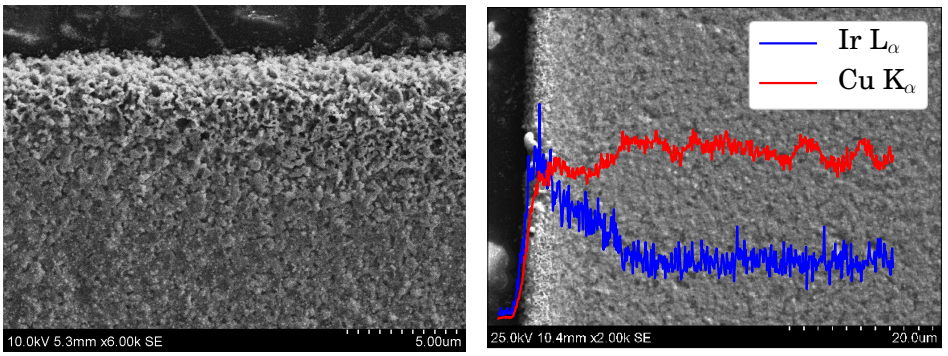

(a) (b)

Figure 5.3: SEM image(left) and EDS linescan(right) of the periphery of the (Ir-Cu)/Au$_s$ film.

Upon introducing forced convection to the system, the primary size and morphology of the Ir-deposits changed.

Figure 5.4 is a SEM image of the electrode surface after displacement under forced convection, labeled (Ir-Cu/Au)$_r$. In figure 5.4b, the clear edge-effect where a defined region has more Ir is not present. Figure 5.4a is the centre of the electrode. The morphology is clearly different than that of (Ir-Cu/Au)$_s$.

5.2.2 Preparation of (Ir–Cu)@GC

A typical particulate Cu/GC film is depicted in figure 5.5. It was comprised of densely packed Cu particles around 1 µm which covered the entire surface.

Figure 5.6 depicts the electrode surface after replacement of the particulate Cu/GC film under forced convection, labeled (Ir-Cu/GC). The particulate morphology is retained. The outer layer of the particles appear brighter, indicative of a hollow core and an Ir shell. There appears to be no Ir growth onto the glassy carbon substrate, which is consistent with the high overpotentials needed to deposit Ir on to GC [161, 182]. The particle in figure 5.7 apear to have a solid core.

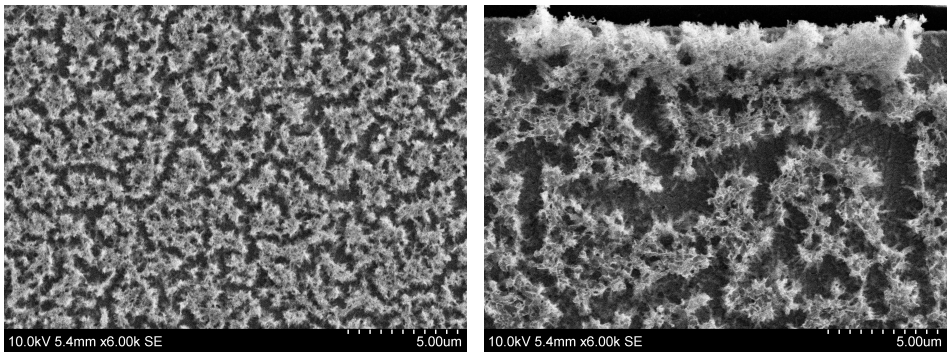

(a) (b)

Figure 5.4: SEM image of $(Ir\text{-}Cu/Au)_r$. Centre of the electrode(left) and the edge(right).

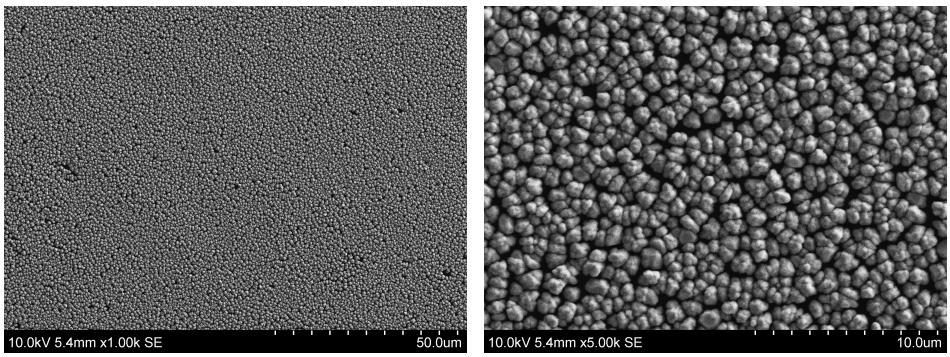

(a) (b)

Figure 5.5: SEM image of a particulate Cu/GC film prepared by pulse deposition

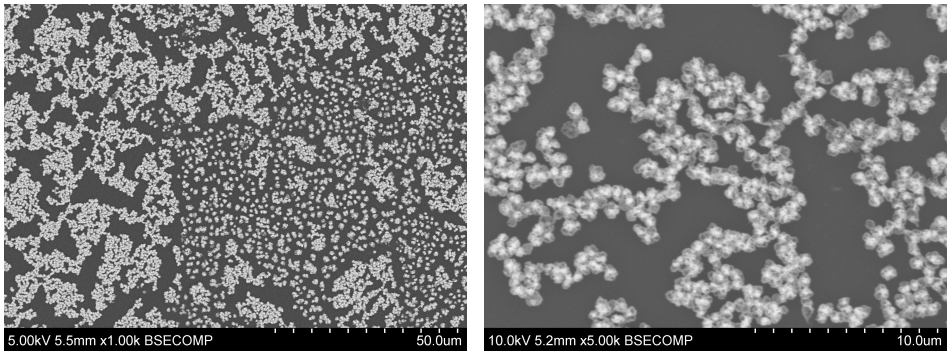

(a) (b)

Figure 5.6: The (Ir-Cu/GC) film prepared by galvanic displacement under forced convection.

The EDS linescan data in figure 5.7 shows the presence of Ir as well as Cu in the particles of (Ir-Cu/GC).

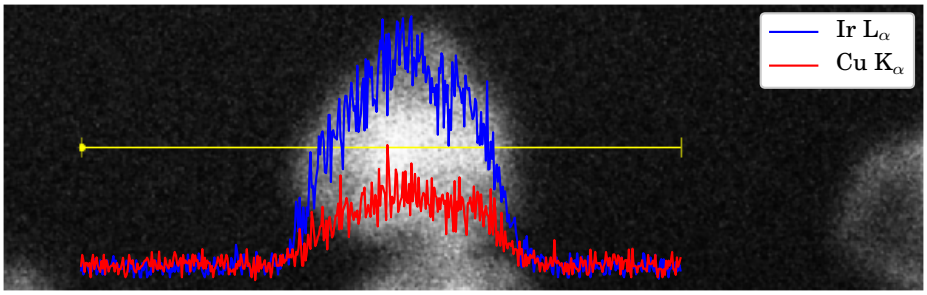

Figure 5.7: Linescan EDS of (Ir-Cu/GC)

5.2.3 Electrochemical properties

Figure 5.8 presents cyclic voltammograms(CV, black) and Mott Schottky plot(MS, red) of $(Ir\text{-}Cu/Au)_r$ (a), $(Ir\text{-}Cu/Au)_s$ (b) and (Ir-Cu/GC) (c) after transformation to IrO_x by potential cycling, recorded at $50\,mV\,s^{-1}$ (CV) and 1 Hz (MS), in $0.5\,mol\,dm^{-3}$ H_2SO_4. All the voltammograms displayed a pair of peaks around 1 V, typical for IrO_x formed by potential cycling [48, 220] [48, 70, 72, 73, 76, 77, 221–228]. The apparent flat-band potential, the potential where $1/C^2$ goes towards zero, coincides with the onset of the Ir(III) $\longrightarrow$ Ir(IV) peak. This is consistent with that of anodically formed IrO_x [78]. The current in the voltammogram of (Ir-Cu/Au)s appear to be one order of magnitude lower than that of $(Ir\text{-}Cu/Au)_r$ and (Ir-Cu/GC). The main peaks in voltammogram of $(Ir\text{-}Cu/Au)_s$ are not symmetrical. The anodic peak is $\approx 18\,\mu A\,cm^{-2}$, whereas the cathodic peak is $\approx 10\,\mu A\,cm^{-2}$

The amount of IrO_x participating in the proton insertion reaction, reaction (2.3), determined using the method outlined in section 2.2 is given in table 5.1. The voltammograms and extrapolations of anodic charge to zero and infinite sweeprates are given in figures B.4 to B.6. The total amount of IrO_x in $(Ir\text{-}Cu/Au)_r$ and (Ir-Cu/GC), q_t appear to be approximately 10 times that of $(Ir\text{-}Cu/Au)_s$. The fraction of IrO_x at the surface, $q_s q_t^{-1}$ is higher for the hollow/core-shell structure of (Ir-Cu/GC) than that of the porous particulate structure of $(Ir\text{-}Cu/Au)_r$ and $(Ir\text{-}Cu/Au)_s$. This is consistent with the large amount of residual Cu in $(Ir\text{-}Cu/Au)_s$, which was oxidized in the first few potential cycles in figure B.3, meaning that the galvanic displacement reaction had not gone to completition.

Table 5.1: Total, outer and inner charge obtained after extrapolating the anodic charge of the voltammograms in figure B.4 to infinite and zero potential sweep rate.

Sample	q_t/μC	q_s/μC	q_i/μC	$q_s q_t^{-1}$/a.u.
$(Ir\text{-}Cu/Au)_r$	1389	998	391	0.72
$(Ir\text{-}Cu/Au)_s$	146	104	42	0.71
(Ir-Cu/GC)	1519	1288	232	0.85

The polarization curves of the (Ir-Cu) films are shown in figure 5.9 where the rate expression, equation (1.54), has been fitted to each polarization curve. Parameters refined to the charge normalized current density are given in table 5.2. The fit appears good at potentials above 1.56 V. (Ir-Cu/GC) shows a higher charge normalized activity towards oxygen evolution than $(Ir\text{-}Cu/Au)_r$ and $(Ir\text{-}Cu/Au)_s$, where $(Ir\text{-}Cu/Au)_r$ is slighly higher than $(Ir\text{-}Cu/Au)_s$, but the charge-normalized activities are all within the same order of magnitude.

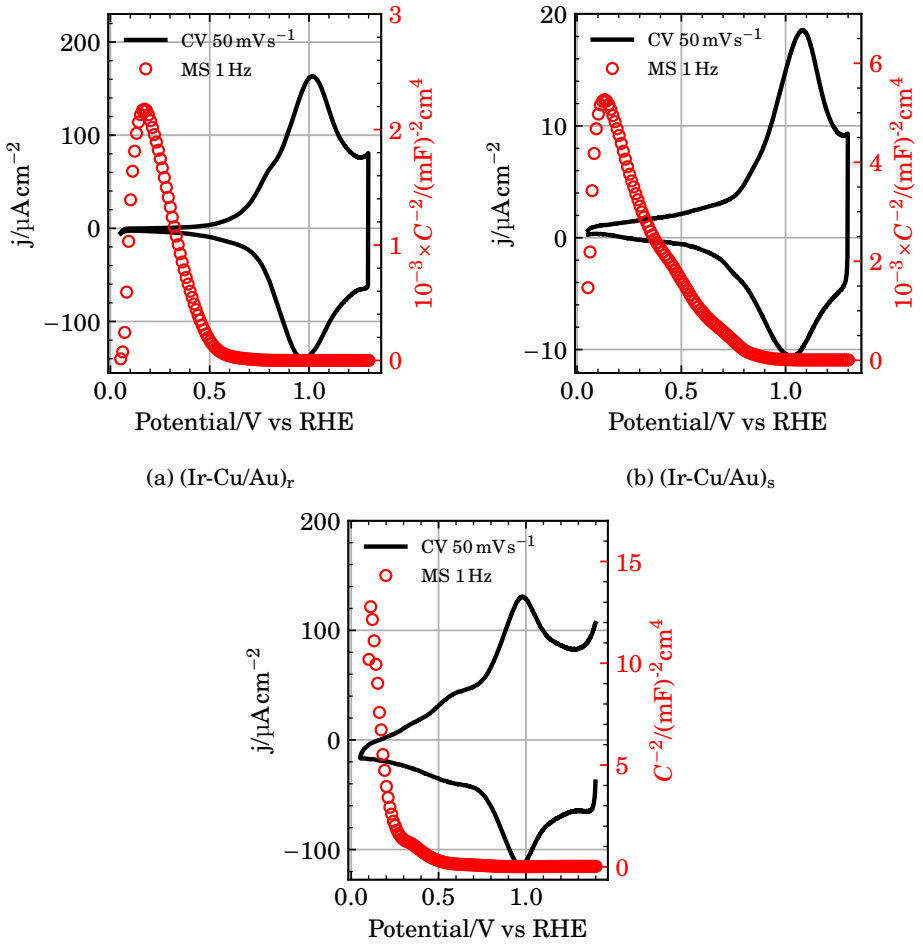

Figure 5.8: Cyclic voltammograms (black) and Mott Schottky plots (red) of (Ir-Cu/Au)$_r$ (a), (Ir-Cu/Au)$_s$ (b) and (Ir-Cu)/GC (c). Voltammograms were obtained after transforming the Ir deposit to IrO_x by potential cycling in 0.5 mol dm^{-3} H_2SO_4 at 50 mV s^{-1}. Mott Schottky impedance data were obtained using single frequency impedance at 1 Hz.

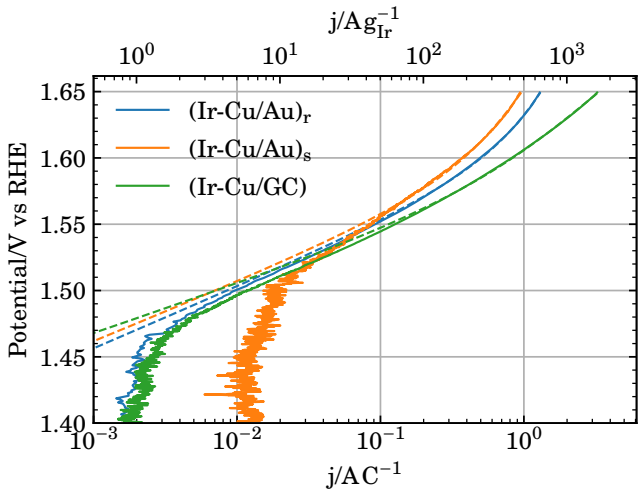

Figure 5.9: Polarization curves for (Ir-Cu/Au)$_s$, (Ir-Cu/Au)$_r$ and (Ir-Cu/GC) after transformation to IrO_x by potential cycling in 0.5 mol dm^{-3} H_2SO_4. Polarization curve was obtained in 0.5 mol dm^{-3} H_2SO_4 using a sweep rate of 3 mV/min.

Table 5.2: Obtained values after fitting $\log_{10} p_1$, $\log_{10} p_2$ and α_2 in equations (1.55) and (2.7) to the polarization curves in figure 5.9.

Sample	$\log_{10} p_1$	$\log_{10} p_2$	α_2
(Ir-Cu/Au)$_r$	-7.48 ± 0.16	26.88 ± 0.01	0.73 ± 0.01
(Ir-Cu/Au)$_s$	-9.34 ± 0.10	26.65 ± 0.01	0.66 ± 0.00
(Ir-Cu/GC)	-16.68 ± 0.03	26.44 ± 0.00	0.38 ± 0.00

5.3 Discussion

5.3.1 Morphology and growth

The rate of the galvanic displacement reaction between $IrCl_6^{2-}$(aq) and Cu(s) is affected by the mass transport to and from the reaction surface, as is clear from the increased Ir growth at the stagnant disc edge in figure 5.3b compared to the more uniform Ir film across the rotated electrode in figure 5.4. We assume that reduction of H_2IrCl_6 follows the reaction scheme given in section 1.8, reactions (1.46) to (1.48), where Ir(IV) is first reduced to Ir(III) as an intermediate step [90,176,177,183]. When the electrode was kept stagnant, more of the intermediately formed Ir(III) species was reduced to Ir(0). At 1600 rpm, the rate of Ir(III) formation was sufficiently high

so that Ir(III) was present all though the porous (Ir-Cu) electrode and was reduced directly onto the Au substrate. In figure 5.4b, it may appear as the Ir deposit has grown directly on the Au substrate. This is only possible if Ir(III) was present at the surface, which means the rate of formation exceeded the rate of removal.

The lack of Ir-growth extending onto the GC substrate is consistent with the results reported by Le Vot et al.(2012, 2013) [161, 182], where large overpotentials, well negative of the onset of hydrogen evolution on Ir, are required to reduce Ir onto carbon. The mixed potential arising from Cu-oxidation and Ir-reduction is not sufficient to reduce Ir onto glassy carbon, as it should be higher than ≈0.3 V for Cu to be oxidized.

The particulate Ir deposit in figure 5.5 appears to have a hollow core/shell structure. This is similar to the hollow core structure of (Ir-Ni)/C reported earlier in chapter 3.

Some Cu was present in all the samples, figures 5.3b, 5.7 and B.2. The displacement reaction did not run to completition during preparation of $(\text{Ir-Cu/Au})_\text{s}$, as is clear from the large amounts of Cu detected by EDS in figure 5.3b and the large amounts of Cu being oxidized in the first potential sweep in figure B.3b. For $(\text{Ir-Cu/Au})_\text{r}$ and (Ir-Cu/GC), the Cu detected by EDS implies either one of;

(i) The galvanic displacement reaction did not reach completition.

(ii) The remaining Cu was protected by a dense Ir overlayer

(iii) The mixed potential arising from oxidation of Cu and reduction of H_2IrCl_6 was close to the equilibrium potential for Cu oxidation, leading to alloying [93].

There was no clear signs of large amounts of Cu being oxidized in the first potential sweeps of $(\text{Ir-Cu/Au})_\text{r}$ and (Ir-Cu/GC) in figures B.3a and B.3c, but some was still detected by EDS as stated above. The apparent large overpotentials required to reduce solutions of Ir(III) and Ir(IV) to the metallic state [161, 176, 177, 180, 182] is consistent with reduction of Ir(III) to metallic iridium being the slow step when the electrode was rotated at 1600 rpm. This would make it possible to form a protective Ir film on top of Cu. If the rate of the galvanic displacement reaction is determined by slow reduction of Ir(III), the mixed potential may have been sufficiently low for an $Ir_{1-x}Cu_x$ alloy to form since the cathodic direction of the Cu^{2+}/Cu redox couple would not be negligible. We can not conclude on the last two points, and will leave this discussion open.

Attempts at replacing a smooth Cu film on glassy carbon were made, but the film would always deform/peel off the electrode before a displacement experiment, or crack and fall apart during/after (figure B.1). Hence, we made the switch to the Au RDE in the above paragraphs.

5.3.2 Electrochemical properties

The total amount of Cu initially present on (Ir-Cu/Au)$_s$ and (Ir-Cu/Au)$_r$ equaled to 500 mC. If Ir(IV) had only been reduced to Ir(III) and not futher to metallic Ir, this would correspond to a reduction in the $IrCl_6^{2-}$ concentration by 10.4 %. We attempted to measure the UV-Vis adsorption of the H_2IrCl_6-solutions before the immersion of the Cu electrodes and after the completion of the experiment, but water evaporation during the course of the experiment had a larger effect on the $IrCl_6^{2-}$-concentration than the changes due to the galvanic displacement reaction, as is evident by the characteristic peak of $IrCl_6^{2-}$-peak at 488 nm in figure B.7. Even so, the yield appear to be quite poor, with the amount of IrO_x in table 5.1 being two orders of magnitude less than the initial amount of Cu.

(Ir-Cu/Au)$_s$ and (Ir-Cu/Au)$_r$ are thick and porous, whereas the cage/eggshell structure of (Ir-Cu/GC) behaves more like a thin film, since both the inner and outer part of the shell is accessible for the electrolyte. The porous structure of (Ir-Cu/Au)$_s$ and (Ir-Cu/Au)$_r$ is easily seen in figures 5.3 and 5.4. Pickup and Birss [79] showed how the voltammogram of AIROF changes from reversible to irreversible depending on the film thickness and potential sweep rate due to diffusion limitations on the proton injection reaction reaction (2.3) as the potential sweeprate is increased. A 100 nm film was reversible up to 740 mV s^{-1}. Thicker films showed irreversible voltammogram behaviour at lower sweep rates. Plotting some of the voltammograms used to find q_t, q_s and q_i, figure B.4, normalized by the maximum anodic current in each voltammogram, $j/max(j)$ demonstrates this effect. The main anodic peak in the voltammograms of (Ir-Cu/Au)$_s$ and (Ir-Cu/Au)$_r$, (a, b) shifts to higher potentials as the potential sweep rate is increased while the voltammograms of (Ir-Cu/GC) (c) remains fairly constant as the potential sweep rate is increased. This is consistent with the higher surface fraction of IrO_x in (Ir-Cu/GC) compared to (Ir-Cu/Au)$_s$ and (Ir-Cu/Au)$_r$.

This can be seen when plotting the anodic peak potential versus the potential sweep rate in figure 5.11. Due to the potential limits used, the peak potential appear to be independent of high sweep rates. This is because the peak was never reached at high sweep rates. *I.e.*, the peak lies beyond the anodic turnaround potential.

5.4 Conclusions

Cu can be used as a reduction agent to reduce H_2IrCl_6 solutions to Ir metal on a substrate by galvanic exchange. The yield of the reaction appear to be quite poor, and the rate is afffected by the mass transport of the reaction solution. The resulting Ir deposit appear to be porous, and a true core/shell structure may be hard to achieve. Use of Ir(III) precursors may prove beneficial in order to improve the

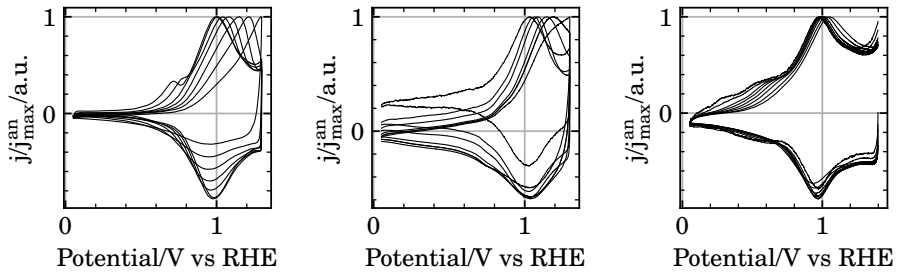

(a) $(Ir\text{-}Cu/Au)_r$ (b) $(Ir\text{-}Cu/Au)_s$ (c) (Ir-Cu/GC)

Figure 5.10: Selected voltammograms from figure B.4 plotted as j/j^{an}_{max}. The voltammograms was obtained at potential sweep rates ranging from $2\,mV\,s^{-1}$ to $500\,V\,s^{-1}$ in $0.5\,mol\,dm^{-3}$ H_2SO_4.

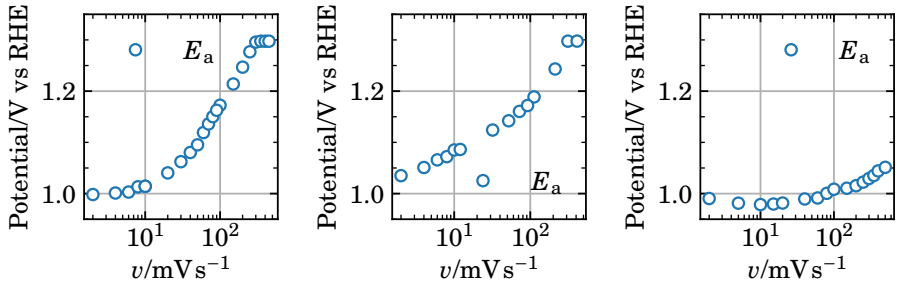

(a) $(Ir\text{-}Cu/Au)_r$ (b) $(Ir\text{-}Cu/Au)_s$ (c) (Ir-Cu/GC)

Figure 5.11: Potential of the main anodic peak in the voltammograms in figure 5.10 and figure B.4.

yield of the galvanic displacement reaction. This is both since one less electron is required, and since it may reduce the loss from formed Ir(III) diffusing away from the reaction surface. In order to gain a more fundamental understanding of the galvanic displacement reaction between Cu and Ir(III)/Ir(IV), a study on displacement of underpotential deposited monolayers of copper, Cu_{UPD} should be conducted. It is then possible to examine in depth how different parameters, *e.g.* mass transport, temperature, choice of Ir precursor, affects the reaction yield and morphology of the resulting Ir deposit.

Summary of the work presented thus far

In this first part, we have shown how different Ir structures (hollow core-shell, porous films) can be prepared by galvanic displacement of Ni and Cu nano/micro-particles and tick Cu deposits on different substrates. The results indicate a not-straighforward reaction scheme where a fundamental understanding is needed if one is to prepare Ir/core catalysts with a dense Ir shell.

The original intended purpose of this work was to exsolve a dopant metal, *e.g.* Ni, Cu, etc, from an oxide such as Nb_xTiO_2 or Sb_xSnO_2 to create an oxide/M core/shell structure. Galvanic displacement would then be used to form an Ir shell on the oxide core. As is shown in chapter 4, the use of titanium oxides as supports had problems related to the durability of the catalyst, the galvanic displacement reaction and the conductivity of the support itself. In chapters 3 to 5, the results indicated that as the temperature of the galvanic displacement reaction was increased, the iridium precursor solution hydrolyzed and condensed onto the surfaces of solids in the reaction micture as Ir(III) or Ir(IV) compounds.

This all led to the suggestion to perform a series of studies on the galvanic displacement of underpotentially deposited copper on gold, Cu_{UPD}/Au using different precursors of Ir(III) and Ir(IV) to gain a more fundamental understanding of the different reactions involved.

Part III

Manuscripts

Chapter 6

Ir deposition by galvanic displacement of Cu in a one-pot configuration

Abstract

We have investigated Ir plating onto a polycrystalline gold electrode by successive galvanic displacmenet of Cu monolayers. By using low concentrations of H_2IrCl_6 and $IrCl_3$ in H_2SO_4, Cu submonolayers could be formed on a Au(poly) rotating disc electrode by underpotential deposition without any significant direct Ir electrolysis. The formed Cu submonolayer could then react with the Ir precursor before a new Cu submonolayer was formed. By evaluating the amount of Cu deposited in each submonolayer and the resulting Ir deposit, our results indicate that H_2IrCl_6 is reduced onto the Au electrode as metallic Ir *via* the formation of Ir(III). Due to transport of Ir(III) away from the reaction surface, a low yield is achieved. No Ir deposited was achieved from $IrCl_3$ solutions, possibly due to adsorption of irreducible species onto the Au surface.

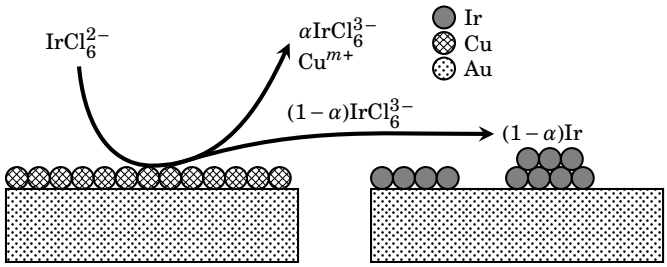

6.1 Introduction

To facilitate the renewable-energy future, efficient and robust hydrogen production is necessary. The compact PEM water electrolysis (PEMWE) and fuel cell technologies may play a vital role in the future infrastrucutre. The hydrogen evolution, hydrogen oxidation and oxygen reduction reactions are all effectively catalyzed by platinum. Platinum is less active for the oxygen-evolution reation (OER), however. Iridium oxide is a highly active catalyst for the OER and which is also reasonably stable at the high potentials and corrosive environment in PEMWE anodes (OER) [5, 241]. Iridium is costly and scarce, and better utilization of it is an obvious point of improvement of PEMWE technology. This can be achieved in various ways, such as dilution by mixing with other cheaper materials such as SnO_2 [188] or Ta_2O_5 [193], alloying with more abundant metals followed by post-synthesis-treatment such as de-alloying or surface enrichment [187, 195], or the use of core-shell structures [242].

Galvanic displacement is the coupled oxidation of a metal M and the reduction of a more noble metal cation N^{n+}(sol) driven by the difference in the electrode potential of the two components, $E^{\circ}_{N} - E^{\circ}_{M} > 0\,V$. The reaction may be written as reaction (6.1).

$$M(s) + \frac{m}{n}N^{n+}(sol) \longrightarrow M^{m+}(sol) + \frac{m}{n}N(s), \tag{6.1}$$

If the sacrificial metal, i.e. the metal M that is being displaced, is present as a thin layer on a substrate and the latter is thermodynamically stable with respect to galvanic displacement by the precursor N in reaction (6.1), the layer of N will be correspondingly thin. Galvanic displacement therefore appears as a particularly simple method for applying thin layers of noble metals to the surface of nanoparticle substrates [84, 149], thus offering a straightforward synthesis route to core-shell structures.

First introduced by Brankovic *et al.* (2001), the surface limited redox replacement (SLRR) method restricts the thickness of the layer of the leaving metal M to a single monolayer by underpotential deposition (UPD) [109]. This allows for the controlled growth of mono- and multilayers of N on a substrate, as well as multilayered structures of N_1,N_2,..N_n using flow-cells or approaches based on multiple electrolytes [114, 149]. A self-terminated monolayer of metals such as Cu or Pb can easily be applied to a suitable substrate (Au, Pd, Pt, Ir, Ru) and subsequently displaced by a more noble metal of choice [149]. Electroless [104] and *gram*-scale methods have been reported for this approach [116, 117, 119, 130].

Some reports on Ir deposition through galvanic displacement of Ni by Ir have

appeared, such as on Ni foil [88,90] and electrodeposited Ni [87,89,91] with Ir. Alia *et al.* (2018) exposed Ni and Co nanowires to $IrCl_4$ at 90 °C and removed any excess Ni or Co by acid wash [92]. PdIr-shell/Ni-core has also been prepared by simultaneous displacement of the outer layers of Ni nanoparticles with Ir and Pd [135]. Duca *et al.* (2013) reported displacement of Ni with Ir from 1×10^{-3} mol dm^{-3} H_2IrCl_6 solutions with a pH of 1, but did not disclose the acid used for acidification [88]. It was most likely HCl as, this was used to assess the level of Ni leeching due to the low pH. They reported a slow displacement reaction, with immersion times up to 18 h at room temperature. Papaderakis et. al.(2016) reported displacement of Ni at 65 °C where only 15 min was necessary to obtain significant Ir deposits [89]. Mellsop et. al.(2015) reported a lower yield when Ni was plated with Ir when HCl was added to a H_2IrCl_6 solution relative to HCl-free H_2IrCl_6. They also reported that the yield was lower from $IrCl_3$+HCl solutions compared to H_2IrCl_6 solutions, but did not assess HCl-free $IrCl_3$ solutions [90].

Whichever the procedure and substrate employed, the resulting iridium film needs to be oxidized to IrO_2 or possibly a substoichiometric variety [236] before employment as an OER catalyst. This is easily achieved by cycling the potential of the electrode supporting the iridium through appropriate potential limits.

Recent results indicate that the SLRR is not necessarily complete in the sense that a fully reduced metal layer evolves. Yuan *et al.* (2018) [136] demonstrated that after Pt deposition on Au(111) through SLRR of Cu-UPD, 60% of the Pt at the electrode consisted of adsorbed square-planar $PtCl_4^{2-}$(ads)-species, Pt(0) clusters of one monolayer thickness making up the balance. The presence of Pt(II) species at the surface could be detected i a cyclic voltammogram during the first negative potential sweep in cathodic direction from the open circuit potential due to reduction to Pt(0). Such a relation; $\theta_{Pt} = \theta^0_{Pt} + \alpha\theta_{Cu}$ where $\theta^0_{Pt} \neq 0$, has also been reported at an earlier occasion [111].

Štrbac *et al.* (2018) reported spontaneous deposition of Ir nanoislands onto Au from $IrCl_3$+H_2SO_4 solutions without any applied potential or displacement reactions [243], where an almost full coverage was achieved in a matter of minutes. The deposit was comprised of adsorbed non-reducible hydrated $IrCl_3$ and some $Ir(OH)_3$. From these results and those of Yuan *et al.* (2018) [136], it appears that one may expect a mixture of partially and fully reduced metal at the surface following an SLRR procedure.

Any prediction of the outcome of an SLRR involving iridium and an associated rational design of synthesis of iridium oxide through this approach require mechanistic knowledge of the processes involved. For the reduction step some information can be gathered from the literature on electrodeposition of iridium oxide. Sawy and Birss (2009) [176] argue that the reaction path during direct Ir electrolysis from

Ir(IV)-solutions can be described with at least tree distinct steps. *(i)* The one-electron reduction of Ir(IV) to Ir(III) followed by *(ii):* The adsorption of Ir(III) onto the substrate and *(iii):* The reduction of adsorbed Ir(III) to Ir(0). These steps are given in reactions (6.2) to (6.4),

$$\mathrm{IrCl_6^{2-}(aq) + e^- \underset{k_{-1}}{\overset{k_1}{\rightleftharpoons}} IrCl_6^{3-}(aq)} \tag{6.2}$$

$$\mathrm{IrCl_6^{3-}(aq) + S \underset{k_{-2}}{\overset{k_2}{\rightleftharpoons}} IrCl_6^{3-} - S} \tag{6.3}$$

$$\mathrm{IrCl_6^{3-} - S + 3\,e^- \underset{k_{-3}}{\overset{k_3}{\rightleftharpoons}} Ir - S + 6\,Cl^-(aq)} \tag{6.4}$$

Later work by Le-Vot et al.(2012) [161, 182], Sawy and Birrs(2013) [177, 178] and Ahn et al.(2015) [180] support this mechanism, although the last three-electron step should in reality be more complex. Both Le-Vot and Ahn demonstrate a high overpotential for Ir-reduction onto glassy carbon electrodes, possibly related to Ir(III) species not adsorbing onto glassy carbon. Sawy and Birss(2009) [176] also showed that an (arbitrarily) increased rate of stirring in the electrolyte increased the mass gain during H_2IrCl_6 deposition onto a Au-coated quartz crystal, but reduced the current efficiency. This was attributed to an increased amount of the Ir(III) formed diffusing away from the electrode surface due to slow adsorption. Ahn et al. also show that electroplating of K_3IrCl_6 on Au is significantly slower in NaCl than in Na_2SO_4, consistent with the report in Ni displacement by Ir by Mellsop *et al.* (2015) mentioned earlier.

It is unclear whether nickel underpotential deposition takes place at gold substrates or not, and reports are conflicting [244–246]. Bubendorff *et. al* [247] reported Ni UPD on Au(111) in sulfamate baths from adsorbed Ni-sulfamate complexes. Vaskevich *et al.* [245] demonstrated Ni UPD at {111}-textured gold electrodes in dimethyl sulfoxide (DMSO). The deposition mechanism involved the reduction of DMSO and coadsorption of Ni and sulfur species. The stripping reaction did not remove the sulfur species, and the authors suggested the formation of a NiAu surface alloy [245].

Cu-UPD on gold surfaces is widely studied and has been extensively used for studies on Pt- and Pd plating by SLRR [149]. Using Cu as the sacrificial metal (M in reaction (6.1)) instead of Ni would give a wider pH range in which M is not spontaneously oxidized or covered by an oxide layer. This is important, since SLRR for iridium at Ni tends to result in some changes in the electrode morphology not associated with the deposition of iridium *per se* [89]. An SLRR synthesis based on displacement of Cu for iridium would thus be highly desirable.

SLRR has previously been used to replace Cu monolayers on Pd by Ir, but then only as a part of the core in core-shell particles with Pt shells, targeting the ORR [113]. This synthesis was based on $IrCl_3$ as the iridium precursor. Due to the difference in the valence states between Ir^{3+} and Cu^{2+}, Knupp et al.(2010) reported that a single replacement event yielded a 2/3 monolayer of Ir [113]. To our knowledge, this is the only work reported on galvanic displacement of Cu ML prepared by UPD with Ir in aqueous solution. Galvanic displacement reactions between Cu and Ir in various organic solvents have been reported, though [248–254].

As is evident by the reaction stoichiometry in reactions (6.5) and (6.6), whether iridium forms from Ir(IV)

$$IrCl_6^{2-}(aq) + 2\,Cu(s) \rightleftharpoons Ir(s) + 2\,Cu^{2+}(aq) + 6\,Cl^-(aq) \tag{6.5}$$

or from Ir(III),

$$Ir^{3+}(aq) + \frac{3}{2}\,Cu(s) \rightleftharpoons Ir(s) + \frac{3}{2}\,Cu^{2+}(aq) \tag{6.6}$$

a one-to-one exchange with Cu atoms is not compatible with the charge requirements of the Cu half reaction,

$$Cu^{2+}(aq) + 2\,e^- \rightleftharpoons Cu(s) \tag{6.7}$$

Furthermore, even small traces of chloride at the electrode surface has been reported to affect the Cu oxidation reaction, reaction (6.7), and stabilize Cu as Cu(I), further increasing the Cu consumption [99, 111, 136]. Stabilization of Cu(I) species is the reason for the well-known activation of the electrodeposition of copper in the presence of chlorides [255].

From this one might expect that starting from solutions of $IrCl_6^{2-}(aq)$ a fraction of the Ir(III) formed in reaction (6.2) may be transported away from the electrode and thus not proceed to reactions (6.3) and (6.4). Choosing an Ir^{3+} compound as the Ir precursor may then improve the yield due to both the change in reaction stoichiometry and the elimination of loss due to mass transport. Accordingly, the yield of Ir plating by galvanic displacement of Cu would be expected to be low when the Ir(IV) precursors are used, especially in highly stirred systems. With the use of Ir(III) precursors, a significantly higher yield should be obtained. This may not be the case, as adsorption of irreducible $IrCl_3 \cdot xH_2O$ and $Ir(OH)_3$ species [243] may inhibit a large fraction of the substrate, significantly reducing the the yield that may be obtained.

Below we report a *one-pot* method for Ir plating *via* successive galvanic displacement of electrochemically prepared Cu-submonolayers formed by underpotential deposition on polycrystalline Au. Using a polycrystalline Au rotating disc electrode, we successively form Cu monolayers by underpotential deposition which are subsequently displaced by Ir from H_2IrCl_6 and $IrCl_3$ solutions in the same electrolyte. We

argue that the galvanic displacement reaction between Cu and Ir(IV) species occurs *via* the formation of intermediate Ir(III), leading to reaction yield determined by the mass transport in the system. Through evaluating the amounts of underpotentially deposited copper and the corresponding iridium film obtained, we argue that a lot a of the formed Ir(III) diffuses away from the electroded surface, leading to a low yield. Furthermore, we suggest that not only the oxidation state but also the choice of Ir-precursor for any given oxidation state, such as ligands of the metal cation, is of significant importance to the end results.

6.2 Experimental

All experiments were performed in a glass cell equipped with a water jacket. A polycrystalline gold rotating disc electrode (Au RDE) (5 mm internal diameter, PEEK shroud; Pine) or a flat polycrystalline Ir electrode embedded in epoxy served as working electrodes. The electrodes were polished to a mirror finish with successively 0.3 µm and 0.05 µm alumina suspensions (Allied) on a microcloth(Buehler) and rinsed using DI water (Millipore, 18.2 MΩ@25 °C) prior to each experiment. The gold electrode was mounted on a Pine Classic RDE/RRDE Shaft (15 mm OD PEEK shroud, stainless steel rod) attached to a Pine MSR rotator. The potentiostat used was a Gamry reference 600. The ohmic drop was determined by the built in utility, of which 85% was compensated through positive feedback compensation. The counter- and reference electrodes were Pt-foil and a reversible hydrogen electrode (RHE), respectively. All potentials reported are versus RHE. SLRR was performed using solutions of 0.5 mol L^{-1} H_2SO_4 (96.3%, VWR) + 1 mmol L^{-1} $CuSO_4$ (Sigma, 99.995 %) with 10 µmol dm^{-3} H_2IrCl_6 (Heraeus) or $IrCl_3 \cdot xH_2O$ (Merck). The electrolytes were purged using Ar(g) for at least 30 min prior to each experiment and kept under an Ar(g) atmosphere for the duration of the experiments. The electrolyte temperature was kept at (70 ± 1) °C by circulating water from a water bath through the water jacket.

Voltammograms of the copper under potential deposition reaction (Cu-UPD) on a polished Au(poly) RDE in 0.5 mol dm^{-3} H_2SO_4 + 1 mmol L^{-1} $CuSO_4$ were obtained at 70 °C at a sweep rate of 50 mV s^{-1}. The anodic potential limit was always 0.8 V whereas the cathodic limit was varied from 0.7 V to 0.25 V in steps of −10 mV.

Cu-UPD on Ir(poly) and IrO_x was also investigated by cyclic voltammetry of a flat polycrystalline Ir electrode embedded in epoxy. The electrode was polished following the same procedure as for the gold electrode above. The polished iridium was converted to iridium oxide following a similar procedure as above, i.e. by potential cycling from 0.05 V through 1.35 V in 0.5 mol dm^{-3} H_2SO_4 at 150 mV s^{-1} at room temperature (RT, 24 °C).

The following potential pulse routine was used to perform SLRR in a single cell: The potential was held at 0.7 V for 5 s in order to strip off any residual Cu still left at the surface from the previous experiment. Cu-UPD layers were formed by applying 0.34 V for 2 s to the working electrode. After each deposition the open circuit potential (OCP) was recorded for 60 s (in solutions containing H_2IrCl_6 or $IrCl_3$) or 1800 s (in solutions containing $IrCl_3$ only), thus monitoring the electrode potential during the SLRR reaction. This procedure was repeated 10 times. Current- and charge was recorded during each potential pulse. The electrode was then rinsed gently by immersion in DI water thrice, changing the water each time. The following combinations of electrolytes were used: 10 µmol dm^{-3} H_2IrCl_6 and 0.5 mol dm^{-3} H_2SO_4, 10 µmol dm^{-3} $IrCl_3$ and 0.5 mol dm^{-3} H_2SO_4, 1 mmol dm^{-3} $CuSO_4$ and 0.5 mol dm^{-3} H_2SO_4, 10 µmol dm^{-3} H_2IrCl_6, 1 mmol dm^{-3} $CuSO_4$, and 0.5 mol dm^{-3} H_2SO_4, 10 µmol dm^{-3} $IrCl_3$, 1 mmol dm^{-3} $CuSO_4$ and 0.5 mol dm^{-3} H_2SO_4. To ensure that mass transport was well defined, the electrode was rotated at 1600 rpm during the SLRR experiments experiments.

The iridium deposits emerging from the SLRR procedure were oxidized to iridium oxide by potential cycling from 0.05 V through 1.35 V in 0.5 mol dm^{-3} H_2SO_4 at 50 mV s^{-1} at room temperature (RT, 24 °C) until stable voltammograms characteristic of those of IrO_2 [77, 256] were obtained The first sweep was performed from the open circuit potential in cathodic direction. The activity of the formed IrO_x film towards oxygen evolution was evaluated using linear sweep voltammetry. The potential of the electrode was swept from 1.35 V to 1.65 V at 3 mV min^{-1}. The electrode was rotated at 1600 rpm. The total amount of Ir in the formed IrO_x film was found from CVs performed at sweep rates 10 mV s^{-1}, 25, 50, 100, 150, 200, 250, 300, 350 and 500 mV s^{-1}, using a method outlined by Ardizonne *et al.* (1989) [212]. Mott-Schottky impedance data of the IrO_x films was obtained at 100 Hz at potentials from 0.1 V to 1.35 V using 10 mV steps and analyzed assuming an R-C series circuit.

Voltammograms of solutions of 10 µmol dm^{-3} H_2IrCl_6 + 0.5 mol dm^{-3} H_2SO_4 and 10 µmol dm^{-3} $IrCl_3$ + 0.5 mol dm^{-3} H_2SO_4 was obtained at (70 ± 1) °C using a Au RDE working electrode rotated at 1600 rpm. The potential of the working electrode was swept between 0.05 V and 1.2 V (H_2IrCl_6) or 0.75 V ($IrCl_3$) at 5 mV s^{-1} for 5 cycles.

The electrode was then rinsed with DI water and transferred to a fresh electrolyte of 0.5 mol dm^{-3} H_2SO_4. The electrode was then treated the same way as for the Ir deposits made my SLRR, as described earlier.

Atomic force microscopy (AFM) micrographs was obtained of the Au(poly) surface before and after SLRR by H_2IrCl_6. The instrument was an Agilent 5500 AFM equiped with a AC mode III module. The tip was an Nanoworld PNP-TR-50 used in

non-contact mode.

UV-Vis adsorption spectroscopy was performed on a 1 mmol dm^{-3} solution of H_2IrCl_6 before and after reduction by a piece of Cu wire(>99.9%). The instrument was a Thermo Fisher Evolution 220 UV-Visible Spectrophotometer. The light source was scanned from 700 nm to 290 nm in steps of 1 nm, averaging the signal for 2 s for each step. The reduction of the H_2IrCl_6 solution by the Cu metal was carried out at 70 °C in a three-neck flask in an oil bath overnight. The solution was kept under a N_2(g) atmosphere and the flask was equipped with a water cooled condenser to minimize evaporation.

The charge data recorded during the SLRR routine was sometimes adjusted for small background currents as per the method outlined in appendix D.2 unless otherwise noted.

6.3 Results

Figure 6.1a presents a series of cyclic voltammograms of the Au(poly) RDE in a solution containing 1 mmol dm^{-3} $CuSO_4$(aq) and 0.5 mol dm^{-3} H_2SO_4(aq) at 70 °C (Voltammograms obtained at room temperature given in figure D.2). The sweep rate was 50 mV s^{-1}. The initial potential was 0.8 V for each cycle, whereas the reversal potential was made more negative by −10 mV per cycle. The current became significantly more negative as the potential was swept to more negative potentials than approximately 0.6 V, which is above the reversible electrode potential for the Cu^{2+}/Cu redox couple (reaction (6.7), $E^{\mathrm{rev}}\left(Cu^{2+}/Cu\right) \approx 0.24\,\mathrm{V@70\,°C}$). At 0.4 V the current increases slightly and then decreases sharply at 0.34 V. At 0.28 V, there is a small bump in the cathodic direction of the voltammogram. We associate the cathodic currents below 0.6 V and above 0.28 V in the negative-going potential sweep with under-potential deposision (UPD) of Cu and those below 0.28 V with over-potential deposision (OPD) of Cu [257]. Integration of the anodic current for the voltammogram with reversal potential of 0.34 V gives the charge 368 µC cm^{-2}, which we associate with the amount of Cu deposited. We chose 0.34 V as the potential to underpotentially deposited copper in further experiments in order to minimize any direct electrolysis of the Ir precursors [176, 177].

Figure 6.1b presents a cyclic voltammogram of the Ir(poly) plate electrode in 0.5 mol L^{-1} in aqueous solutions of H_2SO_4 without and with the addition of 1 mmol L^{-1} $CuSO_4$. Results are shown both for the bare iridium electrode and the iridium electrode after the formation of a layer of iridium oxide (IrO_x) at its surface.

A Cu-nucleation loop is clearly seen on the metallic Ir surface(red), while at the IrO_x surface(blue) only a small cathodic current is present at $E < E^{\mathrm{rev}}(Cu^{2+}/Cu) = 0.25\,\mathrm{V}$.

IrO_x appears to have a larger overpotential than Ir for Cu-nucleation.

Unlike the Au(poly) RDE in figure 6.1a, there is no clear indications of Cu-UPD on Ir(poly) or IrO_x at $E > E^{\text{rev}}(Cu^{2+}/Cu)$.

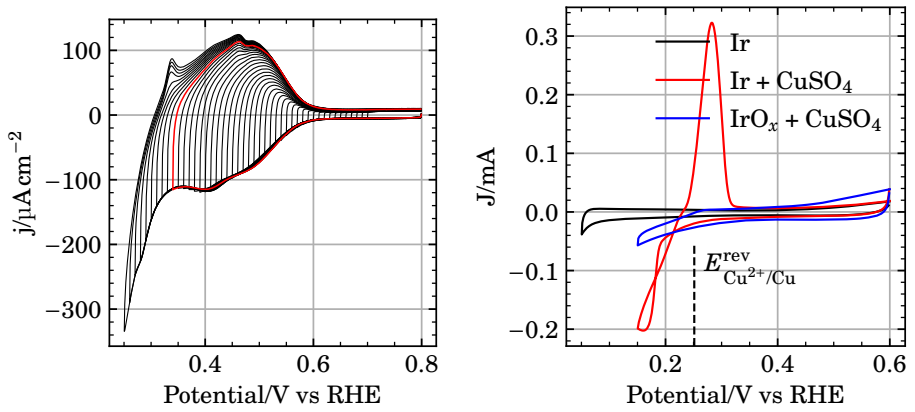

Figure 6.1: (a) Cyclic voltammograms of the Au(poly) RDE in a solution containing 1×10^{-3} mol dm^{-3} $CuSO_4$ and 0.5 mol dm^{-3} H_2SO_4 at 70 °C. The sweep rate was 50 mV s^{-1}. The electrode potential was swept from 0.8 V in each cycle, whereas the reversal potential was made more negative for each cycle. The red curve shows the voltammogram for which the revesal potential was $E^0_{Cu^{2+}/Cu} = 0.34$ V. (b) Cyclic voltammogram of Ir and IrO_x in 0.5 mol L^{-1} H_2SO_4+1 mmol L^{-1} $CuSO_4$ obtained at 5 mV s^{-1}.

Figure 6.2a shows cyclic voltammograms of the Au(poly) RDE in aqueous solutions of 0.5 mol dm^{-3} H_2SO_4 with either 10 µmol dm^{-3} H_2IrCl_6 or $IrCl_3$ added. The voltammograms were obtained at 70 °C sweeping at 5 mV s^{-1} with an electrode rotation rate of 1600 rpm. Cycle 1 (solid) and 5 (dashed) are shown. Neither in the H_2IrCl_6- nor in the $IrCl_3$-solution do the voltammograms display any peaks or waves readily associated with reduction of the iridium precursor in the potential window 0.6 V through 0.34 V, i.e. the same potential range used for underpotential deposition of Cu at gold . In the H_2IrCl_6-containing solutions a significant cathodic current at potentials lower than 0.2 V vs. RHE indicates electrochemical reduction of the iridium precursor. Upon reversal of the first sweep, no H-UPD peak is present, but during further potential-cycling of this electrode H-UPD peaks as well as a reduction wave between 0.7 V and 0.4 V did gradually appear in the voltammograms. On the

other hand, the voltammograms for the solution containing $IrCl_3$ do not to indicate any direct electrolysis of Ir in any of the potential range investigated.

Figure 6.2b presents the current at selected potentials during cathodic sweeps at $5\,mV\,s^{-1}$ versus the square root of the angular velocity of the Au RDE in aqueous solutions of $0.5\,mol\,dm^{-3}$ H_2SO_4 and $10\,\mu mol\,dm^{-3}$ H_2IrCl_6 (green curve) or $IrCl_3$ (blue curve). The rotation rates were 100 rpm, 400 rpm, 900 rpm, 1600 rpm, and 2500 rpm and the temperature was 70 °C. The voltammograms from which the data were collected are are given in figure D.4 of the supporting information. At all three potentials, the current in the H_2IrCl_6 solution is linearly dependent with the square root of the electrode rotation rate, whereas in the $IrCl_3$ solution the current is independent of the electrode rotation rate. This is consistent with reaction (6.2) proceeding at limiting current in the H_2IrCl_6 solution, with no mass-transport limited reactions occurring in the $IrCl_3$ solution.

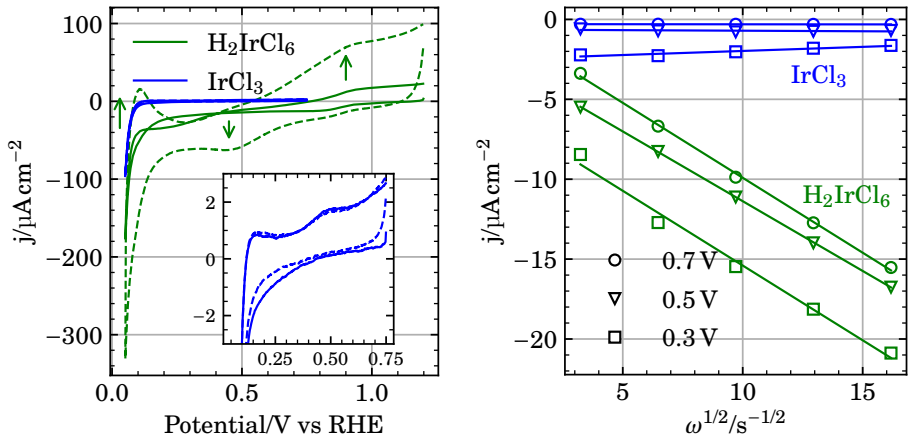

Figure 6.2: (a): First (solid) and fifth (dashed) cycles during cyclic voltammetry of a Au(poly) RDE in aqueous solutions of $0.5\,mol\,dm^{-3}$ H_2SO_4 containing also either $10\,\mu mol\,dm^{-3}$ H_2IrCl_6 or $10\,\mu mol\,dm^{-3}$ $IrCl_3$. The voltammograms were recorded at 70 °C. The sweep rate was $5\,mV\,s^{-1}$ and the rotation rate was 1600 rpm. (b): Current at selected potentials versus electrode rotation rate at 100 rpm, 400 rpm, 900 rpm, 1600 rpm, and 2500 rpm.

Figure 6.3 shows cyclic voltammograms of Au(poly) RDE electrodes after having been subjected to five potential cycles between 0.05 V and 1.2 V (H_2IrCl_6 or 0.75 V ($IrCl_3$) in $0.5\,mol\,dm^{-3}$ H_2SO_4 and $10\,\mu mol\,dm^{-3}$ of either H_2IrCl_6 or $IrCl_3$ at $5\,mV\,s^{-1}$ at

70 °C with an electrode rotation rate of 1600 rpm as in figure 6.2. The first (figure 6.3a) cycle and one obtained after extensive cycling (figure 6.3b) both show clearly that significantly more Ir was reduced onto the Au(poly) substrate from the H_2IrCl_6 solution compared to the $IrCl_3$ solution. The insets show that some Ir was obtained from the $IrCl_3$ solution. The H-UPD peaks in figure 6.3a show that Ir was reduced onto the gold electrode as metallic Ir by the potential cycling in figure 6.2a. The voltammograms in figure 6.3 is similar to those of porous Ir films plated onto Au substrates at constant potentials before and after transformation to IrO_x [176].

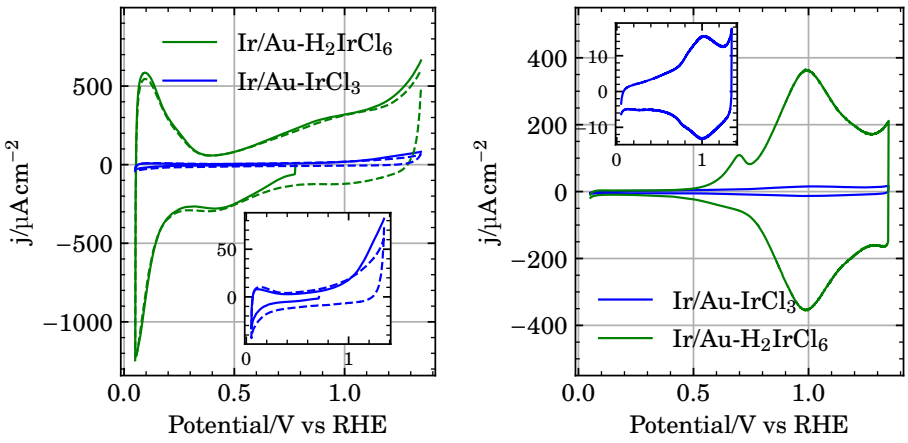

(a) (b)

Figure 6.3: Cyclic voltammograms of the modified Au RDE's in 0.5 mol dm^{-3} H_2SO_4 at 50 mV s^{-1} at room temperature. The electrodes were modified by cyclic voltammetry between 0.05 V and 0.75 V ($IrCl_3$) or 1.2 V (H_2IrCl_6) for five cycles in 0.5 mol dm^{-3} H_2SO_4 + 10 μmol dm^{-3} H_2IrCl_6 or $IrCl_3$ at 70 °C with an electrode rotation rate of 1600 rpm. The electrodes were rinsed using DI water before immersion into the fresh H_2SO_4 electrolyte. (a) shows the first (solid) and second (dashed) sweeps.(b) shows the voltammograms obtained after extensive cycling. Inset shows the Ir/Au-$IrCl_3$ voltammograms.

The results above far demonstrate that at potentials of which $CuSO_4$ is reduced onto the electrode as underpotentially deposited Cu, Ir does not appear to be reduced onto the gold surface from neither the H_2IrCl_6- nor the $IrCl_3$ solutions. There are no apparent currents in figure 6.2a which can attributed to direct reduction of the Ir precursor solutions at potentials above 0.2 V. The voltammograms in figure 6.3 shows that both the H_2IrCl_6 and $IrCl_3$ solutions did yield metallic Ir at the gold surface, which could subsequently be transformed to IrO_2, however the H_2IrCl_6

solution resulted in significantly larger amounts.

Figures 6.4a to 6.4c presents the OCP transients obtained after 10 successive 2 s UPD potential holds at 0.34 V with an intermittent time at open circuit for 60 s between each potential hold in an electrolyte containing either $CuSO_4$, H_2IrCl_6, and both, respectively. The electrode prepared as in figure 6.4c is from hereon labeled $(Ir/Au)^{IV}$. Figure 6.4c could not be reproduced as a linear combination of figures 6.4a and 6.4b.

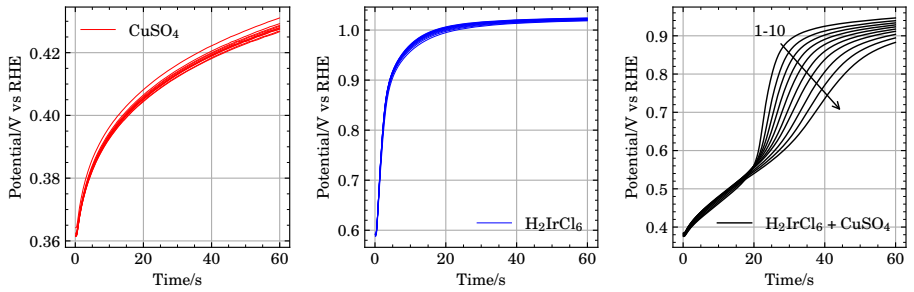

(a) (b) (c)

Figure 6.4: Ten OCP transients recorded over 60 seconds after applying 0.34 V for 2 s to a Au(poly) RDE in 0.5 mol L^{-1} H_2SO_4 and 1 mmol L^{-1} $CuSO_4$ (a), 10 µmol L^{-1} H_2IrCl_6(b) or 10 µmol L^{-1} H_2IrCl_6 and 1 mmol L^{-1} $CuSO_4$(c).

Figure 6.5 shows the charge passed during each 2 s Cu-UPD potential hold at 0.34 V in the presence of $CuSO_4$, H_2IrCl_6 or both, respectively. The OCP of the electrode was recorded for 60 s between each potential hold.

Figures 6.6a to 6.6c presents 10 open circuit potential transients of a Au(poly) RDE measured for 60 seconds after 2 s UPD potential holds at 0.34 V in an electrolyte containing either $CuSO_4$, $IrCl_3$, and both, respectively. The electrode prepared as in figure 6.6c is from hereon labeled $(Ir/Au)^{III}$.

Figure 6.7 shows the charge passed during each potential pulse prior to each 60 s OCP transient in figures 6.6a to 6.6c in the presence of $CuSO_4$, $IrCl_3$ or both, respectively.

After introducing $IrCl_3$ to the electrolyte, the charge passed *before* the first displacement event was somewhat lower than in the $IrCl_3$-free electrolyte. The charge decreased more or less in proportion to the number of preceding displacements.

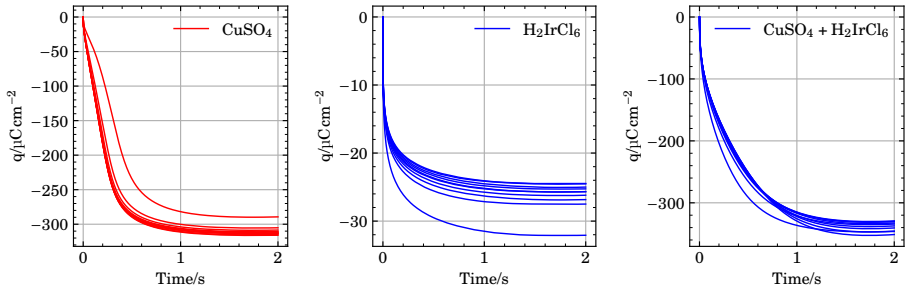

(a) (b) (c)

Figure 6.5: Total charge passed over time at a Au(poly) RDE during 2 s potential holds at 0.34 V in aqueous solutions of 0.5 mol L^{-1} H_2SO_4 and 1 mmol L^{-1} $CuSO_4$ (a), 10 µmol L^{-1} H_2IrCl_6 (b) or 10 µmol L^{-1} H_2IrCl_6 and 1 mmol L^{-1} $CuSO_4$ (c). The open circuit potential of the electrode was measured for 60 s after each potential hold.

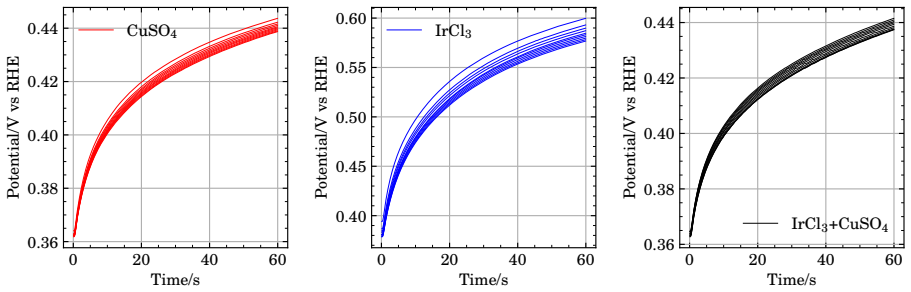

(a) (b) (c)

Figure 6.6: Ten OCP transients recorded over 60 seconds after applying 0.34 V for 2 s to a Au(poly) RDE in 0.5 mol L^{-1} H_2SO_4 and 1 mmol L^{-1} $CuSO_4$ (a), 10 µmol L^{-1} $IrCl_3$(b) or 10 µmol L^{-1} $IrCl_3$ and 1 mmol L^{-1} $CuSO_4$(c).

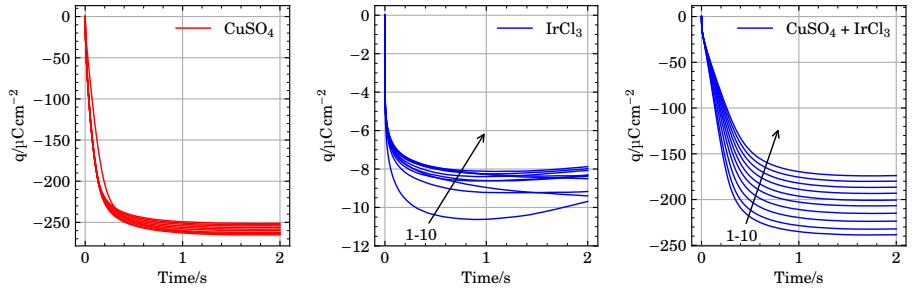

(a) (b) (c)

Figure 6.7: Total charge passed over time at a Au(poly) RDE during 2 s potential holds at 0.34 V in aqueous solutions of 0.5 mol L^{-1} H_2SO_4 and 1 mmol L^{-1} $CuSO_4$ (a), 10 μmol L^{-1} $IrCl_3$ (b) or 10 μmol L^{-1} $IrCl_3$ and 1 mmol L^{-1} $CuSO_4$ (c). The open circuit potential of the electrode was measured for 60 s after each potential hold.

Figure 6.8 shows all the 60 s potential transients recorded during the SLRR routine. The different combinations of $CuSO_4$, H_2IrCl_6 and $IrCl_3$ in the electrolyte are given in the graph.

There is a significant difference between the different potential transients. In the the copper sulfate solution, i.e with no iridium precursor present, the potential increased by no more than 100 mV over the course of 60 s, going from 0.36 V to 0.44 V. The transients recorded with $IrCl_3$ and $CuSO_4$ was similar to those with $CuSO_4$ only. Transients recorded in solutions containing only $IrCl_3$ were similar to the the transients in solutions of $CuSO_4$ or $CuSO_4$ and $IrCl_3$, increasing by 200 mV to stabilize at around 0.58 V. In solutions with H_2IrCl_6 as the only solute, the potential rapidly increased by 400 mV over the initial 10 s before it stabilized at ≈ 1.02 V. The potential transients recorded in the presence of both H_2IrC_6 and $CuSO_4$ differs significantly. The potential increased slowly from ≈0.4 V to 0.6 V during the first ≈20 seconds, before it increased more rapidly and stabilized at 0.88 V-0.95 V for a total change of ≈ 500 mV.

Figure 6.9 compares the fist two voltammograms of $(Ir/Au)^{IV}$ and $(Ir/Au)^{III}$, prepared the same way as those in figures 6.4c and 6.6c. Figures 6.9a and 6.9b corresponds to $(Ir/Au)^{IV}$ and $(Ir/Au)^{III}$, respectively.

The electrode prepared by SLRR from H_2IrCl_6 resulted in a deposit for which the voltammograms are consistent with metallic Ir, as indicated by the anodic H-UPD peak in figure 6.9a. The peak current for the anodic H-UPD peak at approximately 0.1 V is slightly smaller in the second sweep than in the first. In the first sweeps

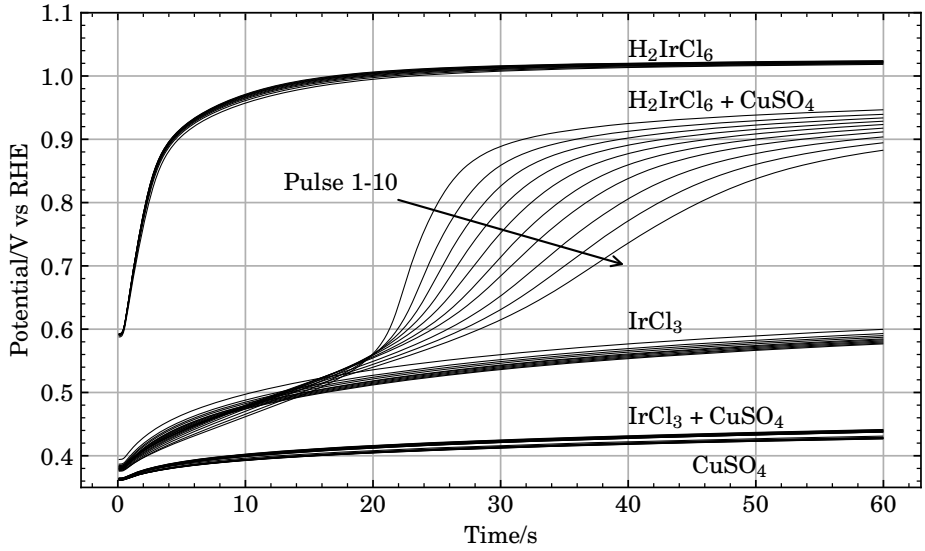

Figure 6.8: 10 OCP transients recorded over 60 s after applying 0.34 V for 2 s to a Au(poly) RDE in 0.5 mol dm^{-3} H_2SO_4 and 1 mmol dm^{-3} $CuSO_4$, 10 µmol dm^{-3} H_2IrCl_6, 10 µmol dm^{-3} $IrCl_3$, 1 mmol dm^{-3} $CuSO_4$ + 10 µmol dm^{-3} H_2IrCl_6 or 1 mmol dm^{-3} $CuSO_4$ + 10 µmol dm^{-3} $IrCl_3$. The different electrolytes are marked in the graph.

an oxidation wave begins at approximately 0.8 V. For the electrode prepared from the $IrCl_3$-containing electrolyte (figure 6.9b) only an insignificant anodic current flows in the potential region corresponding to H-UPD (0.05 V through approximately 0.35 V). An onset of an anodic peak at approximately 0.8 V is apparent also for this electrode, but more sharply defined in this case. The total magnitude of the currents for the electrode prepared from $IrCl_3$ in figure 6.9b is smaller than those for the electrode prepared from H_2IrCl_6 in figure 6.9a. The anodic oxidation waves in the first sweeps are all accompanied by broad reduction peaks in the negative-going part of the voltammogram.

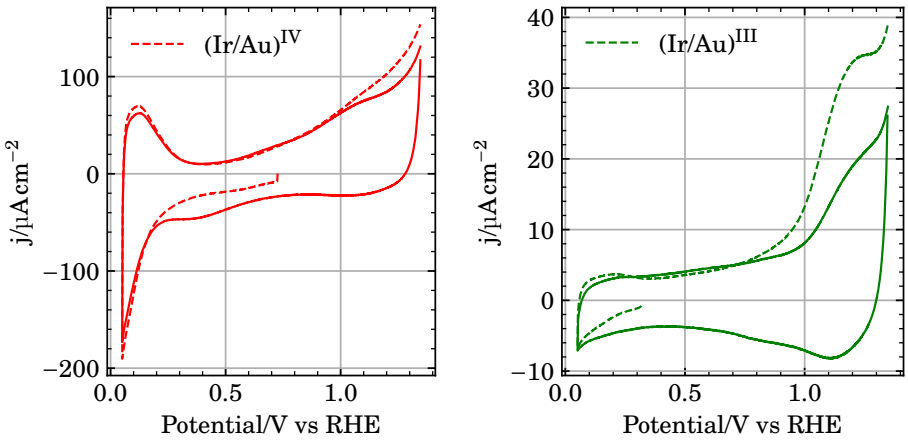

Figure 6.9: Comparison of the first two voltammetry cycles of the Au(poly) RDE after performing the SLRR routine using H_2IrCl_6 and $IrCl_3$. The voltammogram was obtained at 50 mV s^{-1} in 0.5 mol L^{-1} H_2SO_4.

The two electrodes describe above were subjected to repeated potential cycling until there were no significant changes from one voltammogram to the next. Figure 6.10 compares the final cyclic voltammograms in such a procedure for $(Ir/Au)^{IV}$ and $(Ir/Au)^{III}$, prepared as in figures 6.4c and 6.6c. Figures 6.10a and 6.10b corresponds to $(Ir/Au)^{IV}$ and $(Ir/Au)^{III}$, respectively. We have included a cyclic voltammogram of a polycrystalline iridium electrode after potential cycling between 0.05 V and 1.35 V at 150 mV s^{-1} for 500 cycles in an aqueous solution containing 0.5 mol dm^{-3} H_2SO_4, figure 6.10c for reference.

The appearance of a voltammogram similar to those in figure 6.10c is normally associated with the formation of an iridium oxide film (anodically formed iridium

oxide film, AIROF) [48, 220], and the various peaks in the voltammogram with transitions between oxidation states in the film accompanied by incorporation of solutions species in the film [48, 70, 72, 73, 76, 77, 221–228].

$$IrO_2 \cdot nH_2O + (1+\delta)H^+ + \delta A^- + e^- \rightleftharpoons IrO_{1-\delta}(OH)_{1+\delta}A_\delta \cdot mH_2O + (n-m)H_2O \quad (6.8)$$

in which A is an anion present in the electrolyte. Comparison of figure 6.10a with figure 6.10c indicates that we may associate the SLRR in H_2IrCl_6-containing electrolytes and the subsequent potential cycling also with the formation of an iridium oxide film. For example, both the anodic peaks at 0.65 V and 1 V for the AIROF are also present in the SLRR-manufactured film, figure 6.10a, albeit with a different ratio between the peak currents. Also, both voltammograms display one single reduction wave at approximately 1 V in the negative-going sweep. The appearance of the voltammogram for the electrode exposed to the same SLRR in $IrCl_3$-containing solutions (and subsequent cycling), on the other hand, is much less convincing in terms of the formation of an iridium oxide-like film. Only one approximately symmetric pair of peaks is present, and at a potential in between the anodic peaks for AIROF.

Finally, the difference in the amount of Ir deposited is also very different and demonstrated by comparing figures 6.10a and 6.10b. It thus appears that only a negligible amount of Ir, if any, was deposited onto the Au(poly) RDE by the SLRR routine from the $IrCl_3$-containing electrolyte, whereas the electrode exposed to the SLLR in a solution containing H_2IrCl_6 shows clear signs of formation of iridium oxide.

To elucidate whether a longer reaction time was needed for $IrCl_3$ to displace Cu, an additional experiment was performed using a transient time of 1800 s, from hereon referred to as $(Ir/Au)^{III}_{1800}$. In all other respects the manufacturing procedure was identical to that for $(Ir/Au)^{III}$, figures 6.6c, 6.7, 6.9b and 6.10b. Figure 6.11 shows the potential transients recorded over 1800 s after a 2 s Cu-UPD potential hold at 0.34 V in the presence of $CuSO_4$(aq) and $CuSO_4$(aq) and $IrCl_3$(aq). SLRR transients 1,2, 5 and are 10 shown.

The first displacement potential transient was very similar to that of the Cu-UPD layer alone.

Figure 6.12 shows the cumulative charge passed during each 2 s UPD potential hold at 0.34 V prior to each 1800 s transient in figure 6.11 in the absence (**a**, 1 pulse) and presence (**b**, 10 pulses) of $IrCl_3$. These data were not adjusted for background currents.

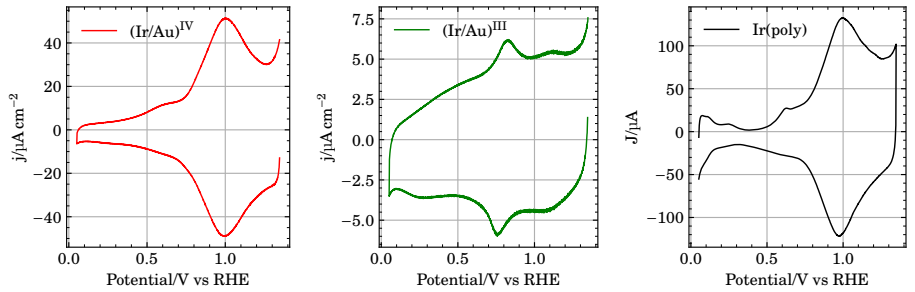

(a) (b) (c)

Figure 6.10: Voltammograms of $(Ir/Au)^{IV}$ (b) and $(Ir/Au)^{III}$ (b) after potential cycling between 0.05 V and 1.35 V at 50 mV s^{-1} at room temperature in 0.5 mol dm^{-3} H_2SO_4. The voltammograms presented (a, b) were obtained in identical conditions. A voltammogram for an AIROF electrode in a solution of 0.5 mol dm^{-3} H_2SO_4 recorded at a sweep rate of 5 mV s^{-1} is included in (c) for comparison.

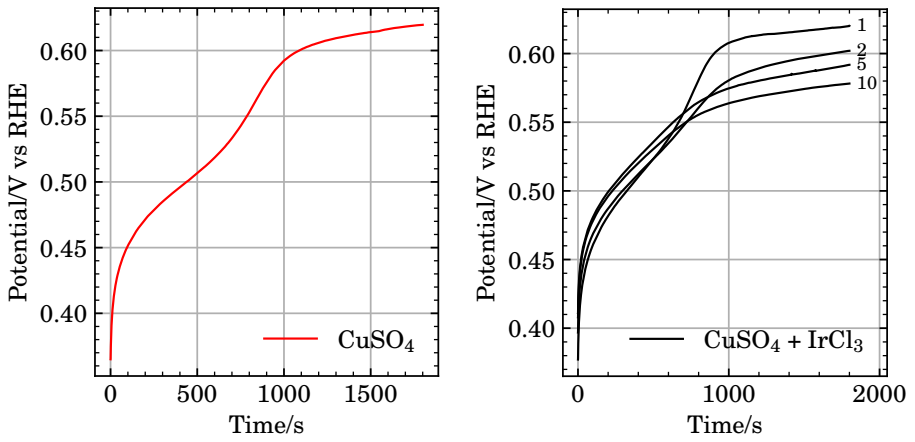

(a) (b)

Figure 6.11: 10 OCP transients recorded over 1800 seconds after applying 0.34 V for 2 s to a Au(poly) RDE in 0.5 mol dm^{-3} H_2SO_4 and 1 mmol dm^{-3} $CuSO_4$ (a) or 1 mmol dm^{-3} $CuSO_4$ and 10 µmol dm^{-3} $IrCl_3$ (b, transients 1, 2, 5 and 10 shown).

The charge passed at the potential at which we deposited Cu by UPD (0.34 V) decreased in electrolytes containing $IrCl_3$ with respect to the $CuSO_4$ electrolyte without any $IrCl_3$. For each time the electrode was left at the open-circuit potential following a Cu-UPD, the charge passed during the subsequent Cu-UPD decreased, for the first few times quite substantially figure 6.12.

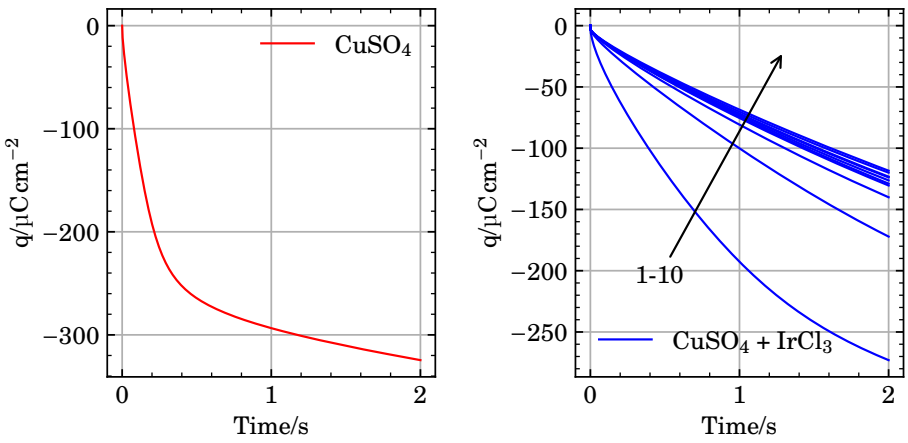

Figure 6.12: Charge passed over time at a Au(poly) RDE during a 2 s potential hold at 0.34 V in solutions containing 0.5 mol dm^{-3} H_2SO_4 and 1 mmol dm^{-3} $CuSO_4$ or 0.5 mol dm^{-3} H_2SO_4, 1 mmol dm^{-3} $CuSO_4$ and 10 μmol dm^{-3} $IrCl_3$. Temperature was 70 °C and the electrode was rotated at 1600 rpm. The OCP of the electrode was measured for 1800 seconds after each potential hold.

Figure 6.13 shows the first cyclic voltammogram and a voltammogram recorded after stable voltammograms had been obtained by repeated cycling for $(Ir/Au)^{III}_{1800}$.

Very similar to $(Ir/Au)^{III}$, figures 6.9b and 6.10b, no apparent Ir deposit was produced from $IrCl_3$ by extending the reaction time from 60 s to 1800 s.

Figure 6.14 shows a voltammogram for $(Ir/Au)^{IV}$ prepared by the SLRR routine in a solution containing H_2IrCl_6 and $CuSO_4$ and one electrode subjected to the same sequence of potential pulses in a solution which contained H_2IrCl_6 but no $CuSO_4$. The voltammograms were recorded after a stable response had been obtained. Figure 6.14 also includes the inverse of the square of the electrode capacitance obtained at 100 Hz, recorded at potentials from 0.1 V to 1.35 V with 10 mV steps.

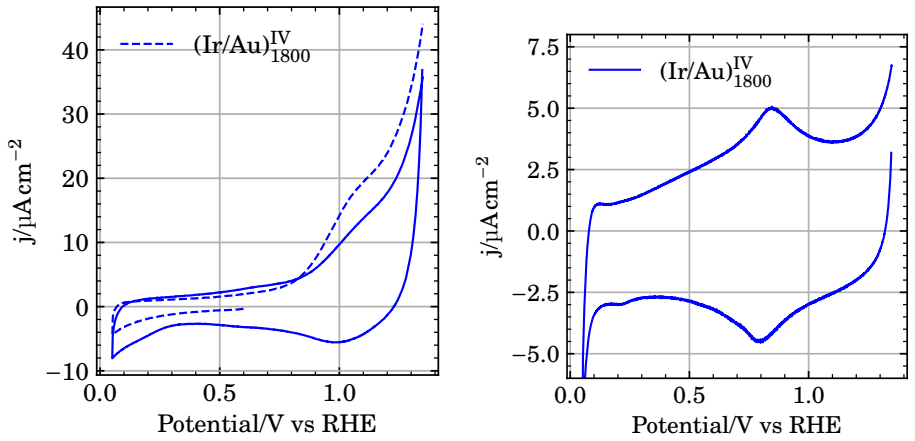

Figure 6.13: Voltammograms of $(Ir/Au)^{III}_{1800}$ in 0.5 mol dm^{-3} H_2SO_4 at 50 mV s^{-1} at room temperature. The first two sweeps (a) and one botained after the voltammogram did not change upon further cycling (b are shown. The potential limits were 0.05 V and 1.35 V.

The figure clearly shows the modification of the Au-surface by the galvanic displacement reaction, reaction (6.5) from the solution containing both H_2IrCl_6 and $CuSO_4$. The electrode subjected to the potential pulses in the electrolyte containing H_2IrCl_6, and a lack of direct electrolysis of the iridium precursor by the repeated application of the potential used for Cu-UPD (0.34 V) in the solution containing the H_2IrCl_6 precursor only and no $CuSO_4$.

The capacitance data is consistent with IrO_x prepared by other methods [78], where the inverse squared capacitance goes to zero around the onset of the anodic peak representing the oxidation of the film according to the the process in reaction (6.8).

Figure 6.15a shows a polarization curve of $(Ir/Au)^{IV}$ prepared by a procedure corresponding to that in figures 6.4c and 6.10a. The corresponding slope along the curve, obtained by differentiating the potential with respect to the base-10 logarithm of the current, $\frac{\partial E}{\partial(\log j)}$, is shown in figure 6.15b. Figure 6.15c are voltammograms corresponding to the one in figure 6.10a recorded before and after the polarization curve. The slope is not constant in any current region and increases rapidly above 1.6 V. The Tafel slope is close to 50 mV, which is a value typical for oxygen evolution at iridium oxide [17, 258, 259]

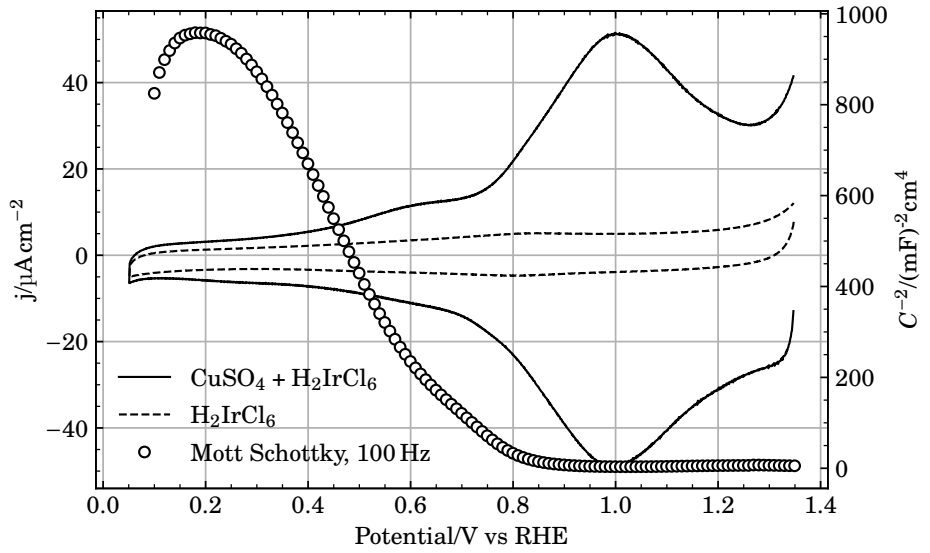

Figure 6.14: Cyclic voltammogram of Au(poly) electrodes that were modified by the application of ten repeated potential pulses to 0.34 V from the open-circuit potential. The duration of the 0.34 V pulses were 2 s and the duration of the interleaving periods at OCP were 60 s. The solutions contained either H_2SO_4 (0.5 mol dm^{-3}), Cu_2SO_4 (1 mmol dm^{-3}) and H_2IrCl_6 (10 μmol dm^{-3}) (solid line) or H_2SO_4 (0.5 mol dm^{-3}) and H_2IrCl_6(10 μmol dm^{-3}) only (dashed line). The voltammograms were recorded in 0.5 mol dm^{-3} H_2SO_4 at a sweep rate of 50 mV s^{-1} and at (23 ± 1) °C. The figure also includes the electrode capacitance recorded at 100 Hz as a function of electrode potential for the electrode prepared in the solution containing both $CuSO_4$ and H_2IrCl_6 (○).

The current density with respect to Ir mass at 1.51 V was $5.5\,\mathrm{A\,g^{-1}}$. This significantly lower than the $100\,\mathrm{A\,g^{-1}}$ recently reported by Lettenmeier *et al.* [57] in similar conditions ($0.5\,\mathrm{mol\,dm^{-3}}$ H_2SO_4, 25 °C, rotating disc electrode) and about half of the Ir-black used for reference in the same work. The geometrical current density at 1.51 V was $4.76\,\mu\mathrm{A\,cm^{-2}}$. This, rather low value. is by itself indicative a very low coverage of Ir on the gold surface when compared to the geometrical current density in the aforementioned work ($\approx 6.5\,\mathrm{mA\,cm^{-2}}$) [12].

The higher slope above 1.6 V in figure 6.15(a) may be associated with degradation or the oxygen evolution itself. Such high slopes would result at high potential for example if the OER follows the oxide path mechanism [17]. However, at the very highest potential an ever so slightly backwards bending of the curve is visible indicating the the amount of iridium oxide at the electrode is diminishing. Voltammograms before and after the LSV in figure 6.15(c) show that the charge has decreased substantially during the OER. Potential-cycling did not restore the voltametric response of the electrode. This indicates that the electrode has actually degraded during the LSV.

Figure 6.16 shows $1\,\mu\mathrm{m} \times 1\,\mu\mathrm{m}$ AFM images of a Au(poly) RDE before (a) and after (b) the application of 10 2 s potential holds at 0.34 V with 60 s intermittent time at open circuit between each pulse, in an aqueous electrolyte of $0.5\,\mathrm{mol\,dm^{-3}}$ H_2SO_4, $1\,\mathrm{mmol\,dm^{-3}}$ $CuSO_4$ and $10\,\mu\mathrm{mol\,dm^{-3}}$ H_2IrCl_6 at 70 °C and an electrode rotation rate of 1600 rpm. Figure 6.16b correspond to $(\mathrm{Ir/Au})^{\mathrm{IV}}$ before potential cycling and transformation to IrO_x. The root mean square (rms) surface roughness, given by the rms of the deviation from average height, $z_{\mathrm{rms}} = \sqrt{\frac{1}{n}\sum_{i=1}^{n}(z-\overline{z})^2}$, was 4.81 nm and 7.70 nm for figures 6.16a and 6.16b, respectively.

The surface appears to be more particulate after the galvanic displacement routine, as is also indicated by the increased surface roughness.

The total amount of Ir obtained by the SLRR routine was evaluated by assuming that the voltammograms for the electrode after conversion of the iridium deposits to iridium oxide correspond to the intercalation process in reaction (6.8) [77]. δ is unknown for our samples, but in cases in which it has been evaluated it tends to be small, in the order of 0.1 through 0.35. In this work we therefore consider δ negligible. Here, $\delta << 1$. Also, we assumed that the intercalation process is diffusive. Following the approach of Ardizzone *et al.* [212] we thus evaluated the surface charge q_S^* by extrapolation of plots of the voltammetric charge q^* vs. the inverse of the square root of the sweep rate v to $1/\sqrt{v} = 0$, i.e. from

$$q^*(v) = q_S^* + A' \frac{1}{\sqrt{v}} \tag{6.9}$$

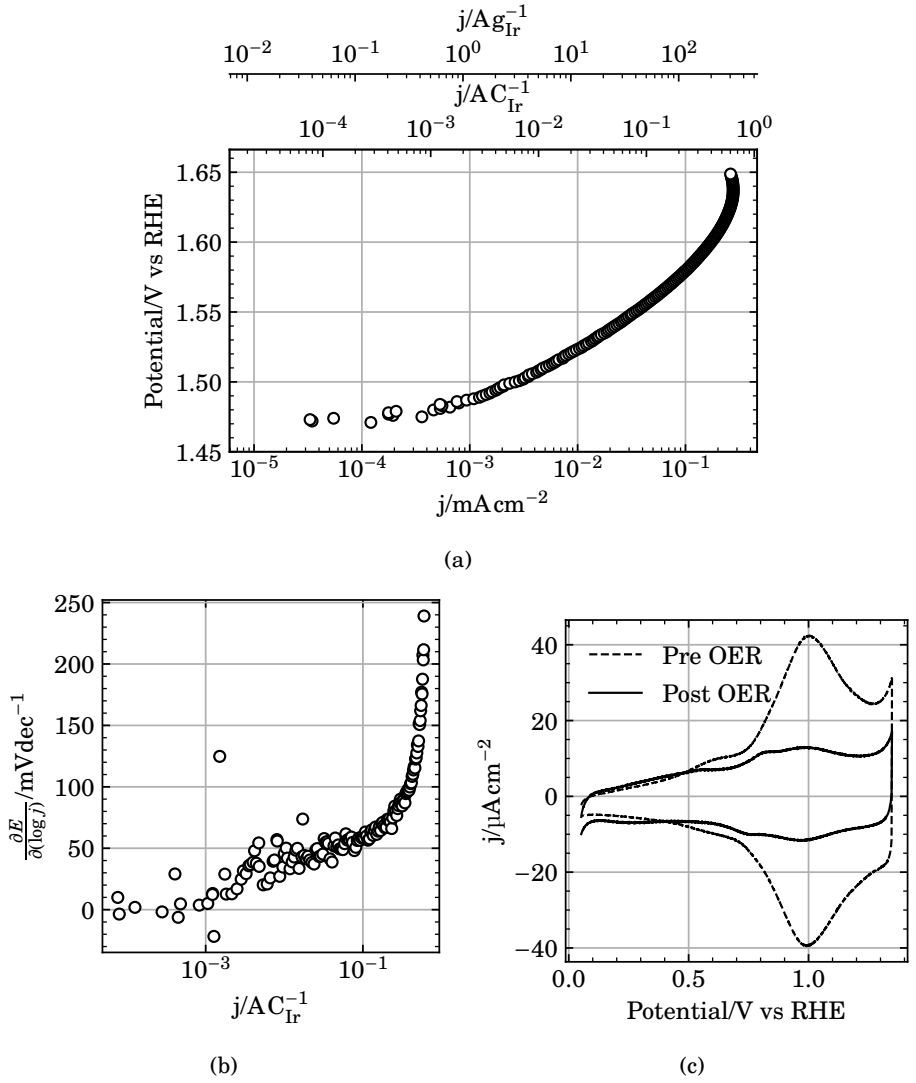

Figure 6.15: (a): Polarization curve of an IrO_x film made by potential cycling of an Ir deposit obtained by SLRR of H_2IrCl_6 and $CuSO_4$. The sweep was performed at $3\,mV\,min^{-1}$ while rotating the electrode at 1600 rpm. The potential was increased in steps of 1 mV The measurements were performed in an aqueous electrolyte containing $0.5\,mol\,dm^{-3}$ H_2SO_4. (b): Derivative of the potential with respect to the base ten logarithm of the current in (a). (c): Cyclic voltammograms of $(Ir/Au)^{IV}$ in $0.5\,mol\,dm^{-3}$ H_2SO_4 before and after OER. The sweep rate was $50\,mV\,s^{-1}$.

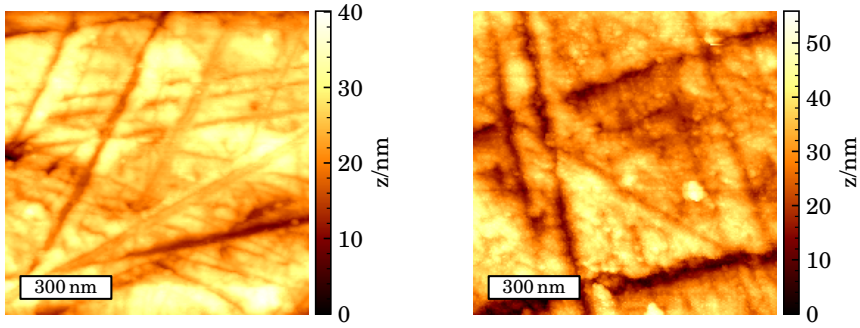

(a) Au(poly) RDE (b) Ir/Au(poly) RDE

Figure 6.16: AFM micropraphs of the Au(poly) surface before(left) and after(right) deposition of Ir by galvanic displacement of Cu using H_2IrCl_6.

The charge q^* was evaluated by integration of the anodic part of the voltammograms in figure D.1 from 0.3 V through 1.3 V. The total charge, q_T^* was evaluated from

$$\frac{1}{q^*(v)} = \frac{1}{q_T^*} + A\sqrt{v} \tag{6.10}$$

By this procedure we found the total and outer (surface) charges to be $(410 \pm 2)\,\mu C\,cm^{-2}$ and $(394 \pm 1)\,\mu C\,cm^{-2}$, respectively, for an IrO_x-covered electrode as obtained by conversion of a $(Ir/Au)^{IV}$ electrode by potential cycling. This gives a fraction of $q_S^*/q_T^* = 0.962$, which indicates that majority of the iridium atoms in the oxide participates in the intercalation process and therefore are in some sense close to the surface of the oxide.

The total yield of the galvanic displacement reaction appears to be low, 33 %-45 %,

The total amount of Cu plated on to the Au RDE is given by

$$n_{Cu} = n_{cy}\left(\frac{Q_{UPD}}{m_{Cu}F}\right) \tag{6.11}$$

where n_{Cu} is the total number of moles of Cu, n_{cy} is the number of potential cycles, Q_{UPD} is the charge passed during copper underpotential deposition at 0.34 V, m_{Cu} is the number of electrons transferred in the copper oxidation reaction (c. f. reaction (6.7)) and F is Faraday's constant. Consequently, the maximum amount of

Ir that may be obtained by galvanic displacement of Cu is given

$$n_{\mathrm{Ir}}^{\max} = \frac{m_{\mathrm{Cu}}}{z\mathrm{Ir}} n_{\mathrm{Cu}} = \frac{m_{\mathrm{Cu}}}{z_{\mathrm{Ir}}} n_{\mathrm{cy}} \left(\frac{Q_{\mathrm{UPD}}}{m_{\mathrm{Cu}} F} \right) = \frac{n_{\mathrm{cy}}}{z_{\mathrm{Ir}}} \left(\frac{Q_{\mathrm{UPD}}}{F} \right) \tag{6.12}$$

where z_{Ir} is the oxidation state of the Ir precursor, either 3 or 4. The amount of Ir on the electrode is expressed as equation (6.13), where Q_{IrO_x} is the charge obtained by linear regression of equation (6.10) and n_{Ir} is the amount of Ir in moles.

$$n_{\mathrm{Ir}} = \frac{Q_{\mathrm{IrO}_x}}{F} \tag{6.13}$$

Hence, the yield of the displacement reaction, ξ, may be expressed as equation (6.14).

$$\xi = \frac{n_{\mathrm{Ir}}}{n_{\mathrm{Ir}}^{\max}} = \frac{z_{\mathrm{Ir}}}{10} \frac{Q_{\mathrm{IrO}_x}}{Q_{\mathrm{UPD}}} \tag{6.14}$$

The resulting yield is calculated to be $\xi = 45\,\%$ and $\xi = 33\,\%$ using $Q_{\mathrm{UPD}} = 368\,\mu\mathrm{C\,cm^{-2}}$ and $Q_{\mathrm{IrO}_x} = 410\,\mu\mathrm{C\,cm^{-2}}$ for $z_{\mathrm{Ir}} = 4$ and $z_{\mathrm{Ir}} = 3$, respectively.

Figure 6.17 shows UV-Vis adsorption spectra of $1\,\mathrm{mmol\,dm^{-3}}$ H_2IrCl_6 before and after reduction by a piece of Cu wire at 70 °C overnight, After completely covering the Cu surface with an Ir layer, the galvanic displacement reaction stopped. The complete removal of the characteristic peak at 488 nm and the appearance of adsorption spectra characteristic of Ir(III) solutions [90, 153] shows that reaction (6.2) proceeded until there was no $IrCl_6^{2-}$ was left.

6.4 Discussion

The most important finding in this work is that the results demonstrate that a one-pot Ir plating procedure involving repeated galvanic displacement of Cu-UPD layers on Au by H_2IrCl_6 is feasible. This means that OER catalyst preparation *via* galvanic displacement using gram scale *one-pot* methods may be achievable.

This is shown clearly by the voltammogram in figure 6.14 where H_2IrCl_6 could *not* be reduced onto the Au electrode in any significant amounts without applying a Cu-UPD layer as an intermediate step.

The absence of any iridium layer forming from $IrCl_3$-containing solutions is likely to be related to Ir(III) species adsorbing on the Au [243] and thereby preventing the copper access. This prevents the Cu-UPD by the Ir(III) species blocking the Au surface, and therefore no galvanic displacement reactions are possible. Therefore, if

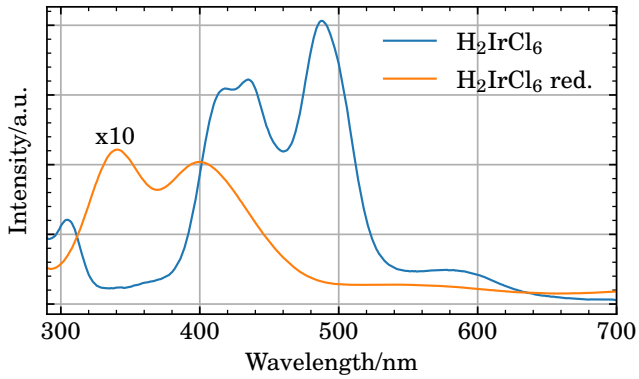

Figure 6.17: UV-Vis adsorption spectra of a 1 mmol dm^{-3} H_2IrCl_6 solution before and after reduction by Cu.

SLRR is to be performed from $IrCl_3$ precursors the Cu-UPD will have to be performed in a separate step.

In Knupp et. al (2010) [113], a Cu-UPD layer were formed on Pd *before* addition of $IrCl_3$. The reported 2/3 coverage of Ir on Pd was consistent with the reaction stoichiometry in reaction (6.6). This is different from our procedure, where $IrCl_3$ was already present *before* the attempted formation of Cu-UPD layers. This is supported by the fact that the charge passed during the UPD pulse in figures 6.7 and 6.12 was significantly lowered after the addition of $IrCl_3$, even before any displacement event had occurred. The oxidation waves and lack of IrO_x on electrodes $(Ir/Au)^{III}$ and $(Ir/Au)^{III}_{1800}$ (figures 6.9b, 6.10b, 6.13a and 6.13b) correspond well with adsorbed Ir(III) species being oxidized to Ir(IV), which is slowly lost to the bulk of the electrolyte over time.

The iridium that forms on the surface by SLRR of solutions of H_2IrCl_6 is metallic. This follows from the voltammograms in figure 6.9.

Starting from the open circuit potentials, the first cathodic sweeps in figure 6.9 does not show any cathodic peaks other than H-UPD in figure 6.9a, corresponding to $(Ir/Au)^{IV}$. This implies that no adsorbed Ir(IV) or Ir(III) species was reduced to Ir(0) during the first cathodic sweep [136]. The oxidation waves seen in the first sweep in the voltammograms in Figures 6.9 and 6.13a all indicates that Ir species were present at the surface of the Au electrode after the SLRR routine. Only $(Ir/Au)^{IV}$, figure 6.9a, showed a H-UPD peak indicative of metallic Ir at the surface. Hence, we attribute the oxidation wave in figure 6.9a to the formation of IrO_x.

The *one-pot* procedure does not appear to involve any direct reduction of iridium species, but is a true galvanic displacement reaction involving reactions of the type in reactions (6.2) to (6.4) and (6.7).

A direct evidence for this is that no Ir was deposited during the pulse procedure in the absence of Cu^{2+}. The cyclic voltammogram in figure 6.14 clearly show the absence of IrO_x at the Au electrode surface after the pulse procedure in the absence of $CuSO_4$. In addition, the voltammogram of the H_2IrCl_6 electrolyte in figure 6.2 does not appear to contain any significant currents that can be attributed to other reactions than reaction (6.2) at potentials above 0.34 V.

This is consistent with earlier reports on electrodeposition of Ir [176, 180, 182, 260], meaning that the applied potential of 0.34 V is insufficient to reduce any significant amount of Ir onto the substrate.

The growth of Ir is therefore controlled by the amount of Cu deposited onto the Au substrate, whereas the morphology of the Ir deposit is not necessarily controlled by the Cu layer morphology.

This follows from the reaction stoichiometry of the exchange reaction in reactions (6.2) to (6.4), since this reaction dictates that at least two Cu atoms must be removed to supply the required charge to reduce one Ir(IV) to Ir(0).

Reduction of Ir(IV) during SLRR proceeds *via* the formation of Ir(III). Reaction (6.2) is well known [176, 180], and electron transfer steps involving more than one electron is unlikely. Reaction (6.4) likely proceeds *via* multiple elementary steps. The intermittently formed Ir(III) may diffuse away from the electrode surface and thus lower the yield. This is consistent the reaction scheme in reactions (6.2) to (6.4) [176] and our low obtained yield.

The significant- and counter intuitive difference in the yield of the SLRR routine using Ir(IV) and Ir(III) could be indicative of a reaction mechanism as suggested in reaction (6.15), where β represents the probability of $IrCl_6^{2-}(aq)$ overcoming an activation energy barrier for direct reduction to Ir(s).

On the contrary, this is not consistent with the lack of direct Ir(IV) electrolysis, nor the displacement of Cu on Pd using $IrCl_3$ by Knupp *et al.* (2010) [113]. Mayne *et al.*(1984) [184] proposed the reduction *via* Ir(I), and that formation of Ir(III) was a competing bi-reaction, but this is also not consistent with the above arguments.

$$IrCl_6^{2-}(aq) + \frac{3+\beta}{n} Cu_{UPD} \rightleftharpoons \beta Ir(s) + (1\text{-}\beta) IrCl_6^{3-}(aq) + \frac{3+\beta}{n} Cu^{n+} \qquad (6.15)$$

The Ir(III) formed during reduction of the H_2IrCl_6 solution, reaction (6.2), is likely differently coordinated than the species present in the $IrCl_3$ solution. The latter has a formal coordination of $IrCl_3(OH_2)_3$ and does not contain sufficient chloride to exist as more than 50 % $IrCl_6^{3-}$(aq), which would require the other 50 % to exist as $Ir(OH)_x(OH_2)_{6-x}^{(3-x)+}$(aq). Aquation of K_3IrCl_6 in H_2SO_4 at *pH=3* by Van Ooy and Houtman [156] showed that a K_3IrCl_6 solution contains mostly $IrCl_3(OH_2)_3$(aq) with some $IrCl_4(OH_2)_2^-$(aq) and $IrCl_2(OH)_4^+$(aq) after 30 h at 75 °C. $IrCl_6^{3-}$(aq) and $IrCl_5(OH_2)^{2-}$(aq) was quickly depleted from their solution. It is therefore likely that our $IrCl_3$ solution consists of mainly $IrCl_3(OH_2)_3$(aq) with smaller amounts of higher aquation products. Due to the slower aquation of $IrCl_6^{2-}$(aq) compared to $IrCl_6^{3-}$(aq) [153, 154, 157], not progressing past $IrCl_4(H_2O)_2$(aq) in 2*N* H_2SO_4 [157], it is likely that reduction of Ir(IV) species in our electrolyte proceeds *via* $IrCl_6^{3-}$(aq), $IrCl_5(OH_2)^{2-}$(aq) and/or $IrCl_4(OH_2)_2^-$(aq), which is not present in the $IrCl_3$ electrolyte. Aquation of the formed Ir(III) species is sufficiently slow for them to be further reduced. This is also supported by the work done by Mellsop *et al.* [90] where the peak position and height in the UV-Vis spectra of $IrCl_3$ + HCl and H_2IrCl_6 + HCl after galvanic displacement with Ni platelets are different. This is indicative of differently coordinated Ir(III) aquo-chloro complexes [153, 154]. Ligand exchange and redox-reactions in the Ir(IV)/Ir(III) aquo-chloro system is shown schematically in figure 6.18. Hydrolysis has been omitted. All $(OH_2)_x$ is short for $(OH)_h(OH_2)_{x-h}$, *i.e.* $IrCl_5(OH_2)_2^{1-}$ is short for $Ir(OH)_hCl_5(OH_2)_{2-h}^{(1-h)-}$.

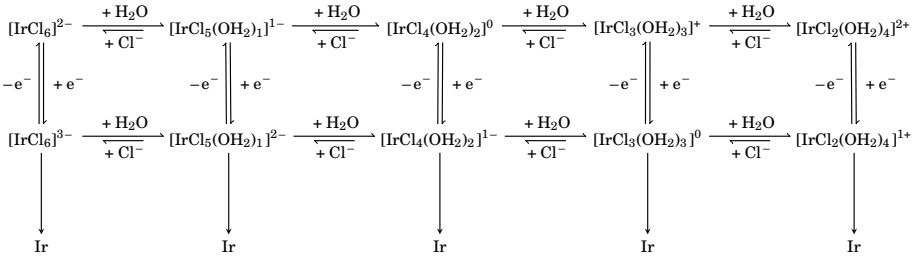

Figure 6.18: Reaction possible reaction paths during reduction chloride iridium complexes. Compiled from information from [153–157].

The particulate nature of the Ir deposit seen in the AFM micrograph in figure 6.16 suggests that Ir grows preferentially onto already formed Ir sites. Over 10 consecutive SLRR cycles in 0.5 mol dm^{-3} H_2SO_4, 1 mmol dm^{-3} $CuSO_4$ and 10 µmol dm^{-3} H_2IrCl_6 at 70 °C, the charge passed during 2 s at 0.34 V in figure 6.5c appears quite constant. The absence of evidence for underpotential deposition of Cu onto polycrystalline Ir and IrO_x in figure 6.1b and the aforementioned constant charge passed, suggests that Ir grows preferentially on already formed Ir-sites, keeping the surface

area of Au relatively constant. Our high surface fraction of *ca.* 96% suggests otherwise. We can not conclude with confidence with our current data and suggest that similar studies using single crystals as the substrate would be more appropriate for these evaluations.

6.5 Conclusions

We have shown that Ir plating *via* surface limited redox replacement of Cu in a *one-pot* procedure is feasible at 70 °C in H_2SO_4 using concentrations of H_2IrCl_6 as low as $10\,\mu mol\,dm^{-3}$. The galvanic displacement reaction occurs *via* Ir(III) formation. A major fraction of the formed Ir(III) is not reduced further to Ir metal, but is lost in the bulk of the electrolyte. This results in a low yield for the procedure. The resulting deposit is Ir metal. Our results indicate that adsorption of irreducible Ir(III) species from $IrCl_3$ solutions inhibits polycrystalline gold surfaces, excluding the use of $IrCl_3$ as a precursor for the reported *one-pot* procedure electrolyte. The obtained Ir metal film apppears to be particulate in nature, with a fraction of surface atoms as high as 96%. The activity towards oxygen evolution after transformation of IrO_x is intermediate, probably owing to rapid degradation of the oxide layer at high potentials during oxygen evolution.

Chapter 7

Investigation of the Ir-Cu SLRR system

7.1 Experimental

All electrochemical experiments were performed in two almost identical glass cells, one of which was equipped with a water jacket. A polycrystalline gold rotating disc electrode (Au_{poly} RDE) (5 mm internal diameter, 15 mm outer diameter PEEK shroud; Pine), a glassy carbon rotating disc electrode (GC RDE) (5 mm internal diameter, 15 mm outer diameter PEEK shroud; Pine) modified with Au nanoparticles (Au_{np}) or a flat polycrystalline Ir electrode embedded in epoxy served as working electrodes. The electrodes were polished to a mirror finish with successively 0.3 µm and 0.05 µm alumina suspensions (Pine) on a microcloth and rinsed using DI water (Millipore, 18.2 MΩ@25 °C) prior to each experiment. The RDEs was mounted on a Pine Classic RDE/RRDE Shaft (15 mm OD PEEK shroud, stainless steel rod) attached to a Pine MSR rotator. The potentiostat used was a Gamry reference 600. The ohmic drop was determined by the built in utility, of which 85% was compensated through positive feedback compensation. The counter- and reference electrodes were a Pt-foil and a reversible hydrogen electrode (RHE), respectively. All potentials reported are versus RHE. SLRR was performed using solutions containing 0.5 mol L^{-1} H_2SO_4 (96.3%, VWR) + 1 mmol L^{-1} $CuSO_4$ (Sigma, 99.995 %) with 10 µmol dm^{-3} K_2IrCl_6 (Sigma, 99.99 %) or K_3IrCl_6 (Sigma). The electrolytes were purged using Ar(g) for at least 30 min prior to each experiment and kept under an Ar(g) atmosphere for the duration of the experiments. The electrolyte temperature was kept at either room temperature (25 ± 1) °C or (70 ± 1) °C. Heating was achieved by circulating water from a water bath through the water jacket. The concentrations were always 0.5 mol dm^{-3} for H_2SO_4, 1 mmol dm^{-3} for $CuSO_4$ and 10 µmol dm^{-3} for K_2IrCl_6 and

K_3IrCl_6.

To ensure a reproducible surface, the A_{poly} RDE was cycled between $-0.1\,V$ and $1.7\,V$ at $50\,mV\,s^{-1}$ in $0.5\,mol\,dm^{-3}$ H_2SO_4 at room temperature for 50 cycles prior to each experiment. The charge of the cathodic Au reduction peak around $1.15\,V$, Q_{Au}, was determined to normalize variations in the surface area of Au_{poly} RDE from one experiment to another.

Voltammograms of the copper underpotential deposition reaction (Cu_{UPD}) on a polished Au_{poly} electrode in $0.5\,mol\,dm^{-3}$ H_2SO_4 + $1\,mmol\,L^{-1}$ $CuSO_4$ were obtained at $50\,mV\,s^{-1}$ at room temperature and at 70 °C. The anodic potential limit was always $0.8\,V$ whereas the cathodic limit was varied from $0.7\,V$ to $0.2\,V$ in steps of $-10\,mV$.

The open circuit potential of the Au_{poly} working electrode was monitored while K_2IrCl_6 or K_3IrCl_6 was added to the H_2SO_4 + $CuSO_4$ electrolyte under Ar(g) mixing while rotating the electrode at 1600 rpm. The gas-mixing was terminated after $\approx 30\,s$.

The *one-pot* SLRR procedure was as follows; The potential of the working electrode was held for 5 s at $0.7\,V$ followed by a 2 s hold at $0.3\,V$ or $0.34\,V$. This was followed by an intermittent time at open circuit (120 s - 300 s) at open circuit, where the open circuit potential (OCP) was recorded. The procedure was repeated 10 times consequtively. The electrode rotation rate was 0 rpm, 100 rpm, 400 rpm, 900 rpm or 1600 rpm and the electrolyte was kept at room temperature or 70 °C. The electrolyte contained H_2SO_4 and K_2IrCl_6 or K_3IrCl_6 (blank experiments) or H_2SO_4, $CuSO_4$ and K_2IrCl_6 or K_3IrCl_6. The electrode was then rinsed by immersion into H_2SO_4 and DI water. These two potential holds with a following intermittent time at open circuit are refered to as one displacement event.

Au nanoparticles, Au_{np}, were prepared using a modified(inverse) Turkevich method [261] in a three neck flask equipped with a water cooled coiled condenser, placed in a heating mantle. Briefly, a small amount of an aqueous solution of $HAuCl_4$ (> 99.9 %, Sigma) was added to a refluxing solution of 75 % trisodium citrate dihydrate (≥ 99.0 %, Sigma) and 25 % citric acid (≥ 99.5 %, Sigma) under vigorous stirring. The citrate solution was refluxed for 15 min before Au precursor addition. After the solution turned wine red [262], the flask was removed from the heating mantle and the suspension cooled down to room temperature. More details regarding the preparation of Au_{np} are given in appendix E.17

Au_{np} were deposited onto a GC RDE by depositing $2 \times 20\,\mu L$ droplets of the cooled Au_{np} suspension onto the glassy carbon surface. Each droplet was dried in a heating cabinet at 60 °C while covered with a beaker for protection.

The electrodes prepared by the SLRR routine were subjected to potential cycling between 0.05 V and 1.35 V in 0.5 mol dm^{-3} H_2SO_4 at room temperature until the voltammogram did not change significantly over 10 cycles. Potential sweep rate was 50 mV. The charge of hydrogen underpotential deposition, Q_H, was determined by integrating the anodic peak between 0.05 V and 0.4 V in the first potential cycle. The potential cycling transformed any Ir deposit to IrO_x (anodically formed iridium oxide films, AIROF). The total amount of electrochemically available IrO_x, Q_t, was estimated from voltammograms obtained at potential sweep rates 5 mV s^{-1} through 500 mV s^{-1} using a methoud outlined previously in section 2.2. Briefly, the anodic charge between 0.4 V and 1.4 V in voltmmograms obtained at different potential sweep rates was extrapolated to infinite and zero potential sweep rate.

Polarization curves of the electrodes prepared by the SLRR experiments were obtained after the aformentioned potential cycling. The electrode potential was slowly increased in steps of 1 mV from 1.45 V to 1.65 V at 5 mV min^{-1} in 0.5 mol dm^{-3} H_2SO_4. The electrode was rotated at 1600 rpm unless noted differently. Voltammograms were obtained as previously described before and after the polarization curve.

An overview of the SLRR experiments conducted using a Au_{poly} RDE as the working electrode are given in table 7.1. Experiments conducted without $CuSO_4$ added to electrolyte was to evaluate to which extent Ir was reduced directly onto the electrode through reactions (1.46) to (1.48)

Table 7.1: Overview of the experiments conducted with the *one-pot* SLRR routine using a Au_{poly} RDE as the working electrode. Columns designate, from left to right, experiment no., electrode rotation rate, electrolyte temperature, the potential used to form Cu_{UPD} in a 2 s potential hold, Ir precursor salt, and whether $CuSO_4$ was present in the electrolyte.

Experiment no.	ω_{rpm}/rpm	T/°C	E_{UPD}/V	Ir precursor	$CuSO_4$
1	1600	25	0.3	K_2IrCl_6	x
2	1600	70	0.3	K_3IrCl_6	-
3	1600	70	0.3	K_3IrCl_6	x
4	1600	70	0.3	K_2IrCl_6	-
5	1600	70	0.3	K_2IrCl_6	x
6	1600	70	0.34	K_2IrCl_6	-
7	1600	70	0.34	K_2IrCl_6	x
8	0	70	0.34	K_2IrCl_6	x
9	400	70	0.34	K_2IrCl_6	x
10	900	70	0.34	K_2IrCl_6	x

An overview of the SLRR experiments conducted using a Au_{np}/GC RDE as the working electrode are given in table 7.2. Experiments 12 and 13 were indentical.

Table 7.2: Overview of the experiments conducted with the *one-pot* SLRR routine using a Au_{np}/GC RDE as the working electrode. Columns designate, from left to right, experiment no., electrode rotation rate, electrolyte temperature, the potential used to form Cu_{UPD} in a 2 s potential hold, Ir precursor salt, and whether $CuSO_4$ was present in the electrolyte.

Experiment no.	ω_{rpm}/rpm	T/°C	E_{UPD}/V	Ir precursor	$CuSO_4$
11	0	70	0.34	K_2IrCl_6	x
12	400	70	0.34	K_2IrCl_6	x
13	400	70	0.34	K_2IrCl_6	x
14	1600	70	0.34	K_2IrCl_6	x

7.2 Results

7.2.1 Underpotential deposition of copper

Figure 7.1 shows cyclic voltammograms of Au_{poly} and Au_{np} in solutions containing (a) 0.5 mol dm^{-3} H_2SO_4 and (b) 1 mmol dm^{-3} $CuSO_4$ + 0.5 mol dm^{-3} H_2SO_4 at room temperature. The currents have been normalized to the area under the Au reduction peak around 1.15 V for easier comparison.

In figure 7.1 (a), the Au_{np} oxidation wave starting at 1.3 V overlaps with oxidation of the GC substrate. Figure 7.1 (b) shows formation and stripping of Cu_{UPD} on Au_{poly} and Au_{np}, similar to what was shown earlier in figure 1.8 in section 1.5 and figure 6.1 (a) in chapter 6. The voltammogram of Cu_{UPD} on Au_{np} is superimposed with the relatively large double layer capacitance seen at $E \leq 1$ V in (a).

Figure 7.2 shows a cyclic voltammogram of a flat Ir electrode in 0.5 mol dm^{-3} H_2SO_4. The voltammogram was obtained at 5 mV s^{-1} after 500 potential cycles. AIROF are known to form a cracked-mud like structure [69, 73, 74]. Between 0.4 V and 0.05 V, H_{UPD} peaks are present, indicative that metallic Ir are still exposed to the electrolyte. The prepeak around 0.65 V and the pair of anodic and cathodic peaks around 1 V are typically associated with the transition between Ir(III) and Ir(IV) in IrO_x and incorporaton of species from the solution into the film, reactions (1.19) and (2.3) [48, 48, 70, 72, 73, 76, 77, 220–228]

Figure 7.3 (a,b) presents cyclic voltammograms of Au_{poly} in 1 mmol dm^{-3} $CuSO_4$(aq) + 0.5 mol dm^{-3} H_2SO_4(aq) at room temperature(a) and 70 °C (b). Sweep rates was

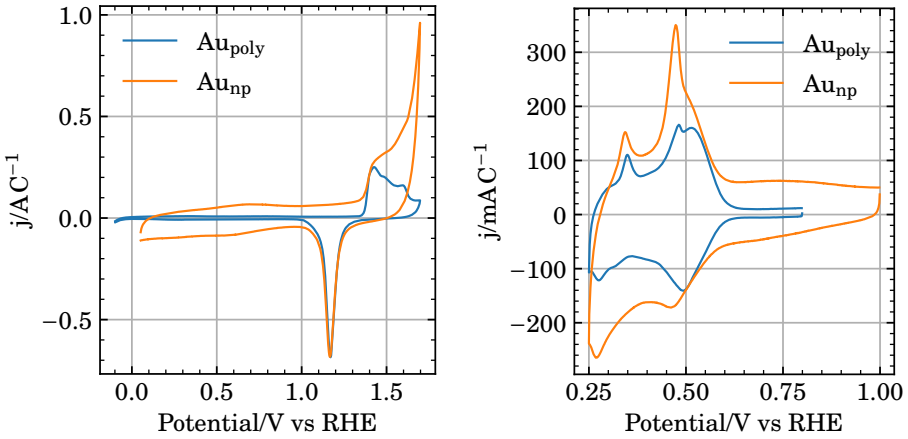

Figure 7.1: Cyclic voltammograms of Au_{poly} and Au_{np} in (a) 0.5 mol dm^{-3} H_2SO_4 and (b) in 1 mmol dm^{-3} $CuSO_4$ + 0.5 mol dm^{-3} H_2SO_4 at room temperature. Potential sweep rate was 50 mV s^{-1}. The current axes have been normalized to the area under the Au reduction peak around 1.15 V.

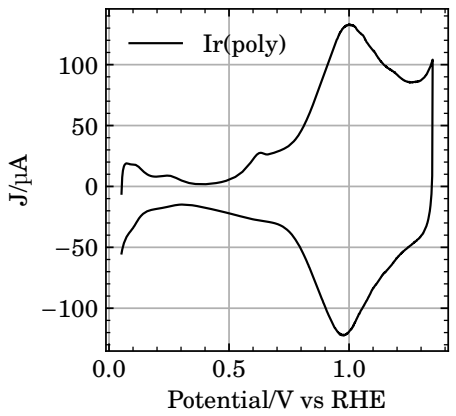

Figure 7.2: Cyclic voltammogram of a polycrystalline Ir electrode embedded in epoxy in 0.5 mol dm^{-3} H_2SO_4 at room temperature. Voltammogram was obtained at 5 mV s^{-1} after 500 potential cycles.

$50\,\mathrm{mV\,s^{-1}}$ and the electrode was rotated at 1600 rpm. The anodic limit was always 0.8 V, whilst the cathodic limited was shifted in steps of −10 mV per cycle. The voltammograms with a cathodic limit of 0.3 V and 0.34 V is highlighted i red and blue, respectively. The anodic stripping charge of each voltammogram, corrected for the double layer capacitance between 0.65 V and 0.75 V, is shown in (c).

Below 0.6 V, at potentials positive of the reversible potential for the Cu^{2+}/Cu redox couple ($E^{\mathrm{rev,25\,°C}}_{Cu^{2+}/Cu} \approx 0.25\,\mathrm{V}$), the current in the negative-going sweep became progressively more negative as the potential was swept in the cathodic direction. At room temperature (a), the current became exponentially more negative at potentials below the reversible potentials which we associate with overpotential deposition (OPD) of Cu. At 70 °C (b), the current became rapidly more negative at potentials below the *standard* potential of the Cu^{2+}/Cu redox couple, 0.34 V. A small bump in the cathodic sweeps can be seen between 0.25 V and 0.3 V, which we associate with the onset of overpotential deposition of Cu.

7.2.2 Effect of Ir precursor and UPD formation potential

Figure 7.4 (a) shows the open circuit potential transients obtained in experiments 1 through 7 in table 7.1. The transients shown from each experiment are number 1 out of 10, where all the transients obtained in each experiment are shown individually in figures E.6, E.10, E.16, E.23, E.29, E.36 and E.42. Figure 7.4 (b) shows all ten transients obtained successively in experiment 5.

Experiments 2, 4 and 6 in figure 7.4 (a) are blank experiments where no Cu_{UPD} can form due to the absence of $CuSO_4$ in the electrolyte, and any Ir deposit obtained is from direct electrolysis of K_3IrCl_6 (exp. 2) or K_2IrCl_6 (exp. 4 and 6) through reactions (1.46) to (1.48) during the 2 s potential hold at 0.3 V (exp. 2 and 4) or 0.34 V (exp. 6). The potential rapidly increased towards a steady state value around 1.05 V (exp. 4 and 6 K_2IrCl_6) or 0.7 V (exp. 2, K_3IrCl_6). This is consistent with the open circuit potential of the electrolyte 30 min after addition of K_2IrCl_6 or K_3IrCl_6, figure E.94.

When the electrolyte contained K_3IrCl_6 + $CuSO_4$ (exp. 3), the potential increased slowly from 0.35 V to 0.5 V. Within this potential range, the fractional coverage of Cu_{UPD} is non-zero, as seen in the voltammograms in figure 7.3 (b). This is consistent with our previous work using similar solutions containing $IrCl_3$ in chapter 6

With the electrolytes containing K_2IrCl_6 + $CuSO_4$ (exp. 1, 5 and 7), the potential first increased rapidly up to ≈ 0.55 V before it increased more rapidly and stabilized towards a steady value around 1.05 V. This is consistent with similar *one-pot* SLRR experiments in chapter 6 where the Ir precursor was a similar solution containing H_2IrCl_6. In experiments 5 and 7 (K_2IrCl_6 + H_2SO_4, 70 °C, 1600 rpm), the potential

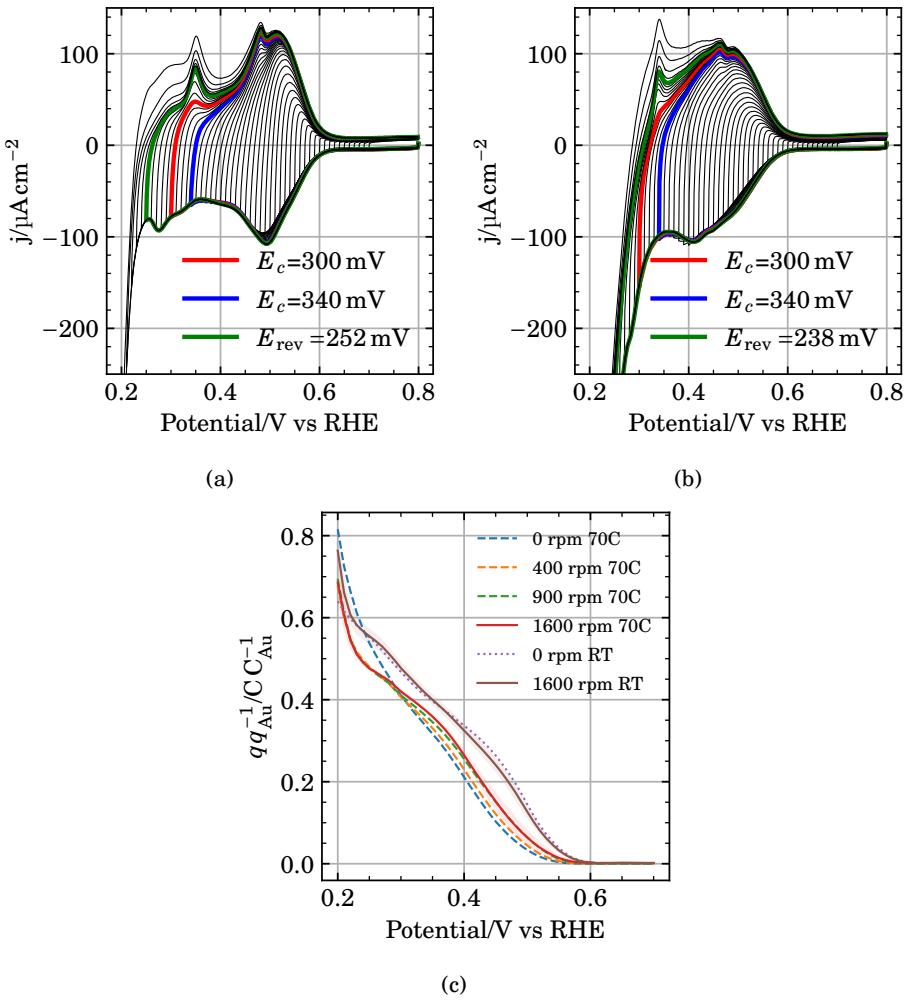

Figure 7.3: Cyclic voltammograms (a,b) of a Au(poly) RDE in 1×10^{-3} mol dm^{-3} $CuSO_4$ + 0.5 mol dm^{-3} H_2SO_4 at room temperature (a) and at 70 °C (b). Sweep rate was 50 mV s^{-1}. The electrode was rotated at 1600 rpm. The anodic limit was 0.8 V, and the cathodic limit was varied between 0.7 V and 0.2 V in steps of 10 mV. (c) is the anodic stripping charge of each voltammogram.

increased more slowly between 20 s and 100 s for each sucessive displacement event. This is seen in figures 7.4b and E.29b (exp. 5) and figure E.42b (exp. 7) where all the 10 sucessively obtained potential transients are shown.

Figure 7.5 shows the current (a) and total charge (b) passed during each potential hold at 0.3 V in experiment 5.

The reactions contributing to the total charge passed at 0.3 V are the formation of a Cu_{UPD} adlayer on Au_{poly} and reduction of the K_2IrCl_6 solution, reactions (1.46) to (1.48). In the first potential hold, there was a slight shoulder around 0.25 s. The shoulder shifted to longer times for each displacement event, and the current at the end of the potential hold increased. The cumulative charge, (b) appear to increase linearly for each consequtive displacement event. This shoulder in the current transients is only present in solutions containing $CuSO_4$ or $CuSO_4$ and K_2IrCl_6 or K_3IrCl_6 at 70 °C, figures E.2a, E.15a, E.28a, E.41a, E.48a, E.55a and E.62a. The charge passed at 0.7 V also appear to increase, although this appear not the be the case in runs 1-4 and 6-10 in figures E.6a, E.10a, E.16a, E.23a, E.36a, E.42a, E.49a, E.56a and E.63a where the charge passed at 0.7 V did not increase for each displacement event.

The voltammograms in figure 7.6 shows the first potential sweeps obtained in 0.5 mol dm^{-3} H_2SO_4 at 50 mV s^{-1} of electrodes 1-7 prepared in experiments 1 through 7 in table 7.1. The currents have been normalized to Q_{Au} (a), Q_t (b) and Q_H (c) for each electrode, respectively. Electrode 1 is not shown in (b,c) as $Q_{Ir} = 0$ and $Q_H = 0$. The voltammograms in (a) are given individually in figures E.7, E.11, E.17, E.24, E.30, E.37 and E.43. The voltammograms and extrapolations to zero- and infinite sweep rates used to determine Q_t are given in figures E.12, E.18, E.25, E.31, E.38 and E.44.

The voltammograms in figure 7.7, except electrode 1, show a cathodic wave and anodic peak between 0.05 V and 0.4 V. The anodic sweeps show a varying degree of an oxidation wave followed by a wide peak positive of 1 V in the following cathodic sweep. The cathodic wave and anodic peak between 0.05 V and 0.4 V in the first potential cycles are consistent with underpotential deposition of hydrogen on polycrystalline Ir metal [113, 210].

The voltammograms in figure 7.7 shows 50th potential sweeps obtained in 0.5 mol dm^{-3} H_2SO_4 at 50 mV s^{-1} of electrodes 1-7 prepared in experiments 1 through 7 in table 7.1. The currents have been normalized to Q_{Au} (a), Q_t (b) and Q_H (c) for each electrode, respectively. Electrode 1 is not shown in (b,c) as $Q_{Ir} = 0$ and $Q_H = 0$. The voltammograms in (a) are given individually in figures E.7, E.11, E.17, E.24, E.30, E.37 and E.43. The voltammograms and extrapolations to zero- and infinite sweep rates used to determine Q_t are given in figures E.12, E.18, E.25, E.31, E.38

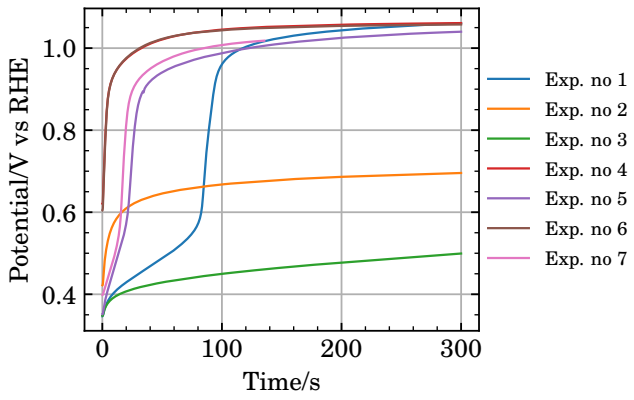

(a)

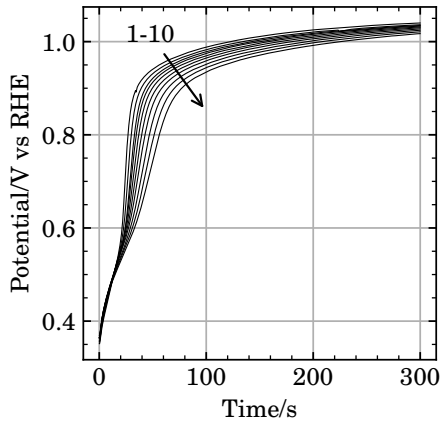

(b)

Figure 7.4: (a) Open circuit potential transients obtained in experiments 1 through 7 in table 7.1. The electrolyte was a solution containing 0.5 mol dm^{-3} H_2SO_4, 1 mmol dm^{-3} $CuSO_4$ (1,3,5,7) and 10 µmol dm^{-3} K_3IrCl_6 (2,3) or K_2IrCl_6 (1,4-7). The potential transients were obtained after a 2 s potential hold at 0.3 V (1-5) or 0.34 V (6,7). The electrolyte was kept at room temperature (1) or 70 °C (2-7). The electrode was rotated at 1600 rpm. (b) shows all ten transients obtained successively in experiment 5.

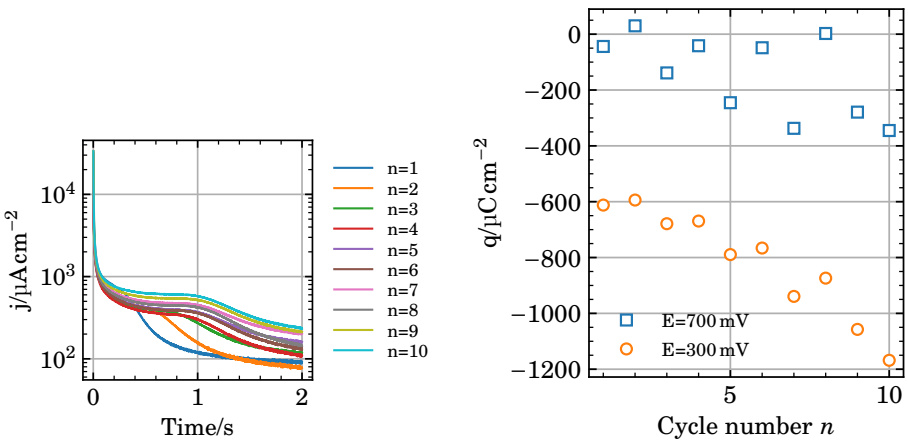

(a) (b)

Figure 7.5: (a) Current versus time during each potential hold at 0.3 V in a solution containing 0.5 mol dm^{-3} H_2SO_4, 1 mmol dm^{-3} $CuSO_4$ and 10 μmol dm^{-3} K_2IrCl_6 at 70 °C with en electrode rotation rate of 1600 rpm. (b) Total charge passed in each current transient in (a).

and E.44.

The voltammograms in figure 7.7, except electrode 1, show a pair of peaks centered around 1 V and a prepeak around 0.65 V.

The pair of peaks centered around 1 V is usually associated with AIROF in H_2SO_4, and the voltammograms in figure 7.7 (a,b,c) is similar to the voltammogram of the flat Ir electrode in figure 7.2 [48, 48, 70, 72, 73, 76, 77, 220–228].

Figure 7.8 compares the values of Q_{Au}, Q_t and Q_H of electrode 2-7 prepared in experiments 2-7 through the ratios (a) $Q_t Q_{Au}^{-1}$, (b) $Q_H Q_t^{-1}$ and (c) $Q_H Q_{Au}^{-1}$. The columns are grouped, from left to right, electrodes (2,3), (4,5) and (6,7). The ratios are only qualitative values used to compare electrodes. $Q_t Q_{Au}^{-1}$ relates the amount of eletrochemically available IrO_x to the amount of Au on the electrode surface, *i.e.* it relates the total amount of Ir deposit to the surface area of the substrate. $Q_H Q_t^{-1}$ relates the number of surface Ir atoms in the freshly prepared electrode to the total amount of IrO_x after transformation to AIROF by potential cycling, *i.e.* it relates the surface area to the volume of the Ir deposit. $Q_H Q_{Au}^{-1}$ similarly relates the number of surface Ir atoms in the freshly prepared electrode to the number of Au atoms on the electrode before deposition of Ir, *i.e.* it relates the surface area of the Ir deposit to

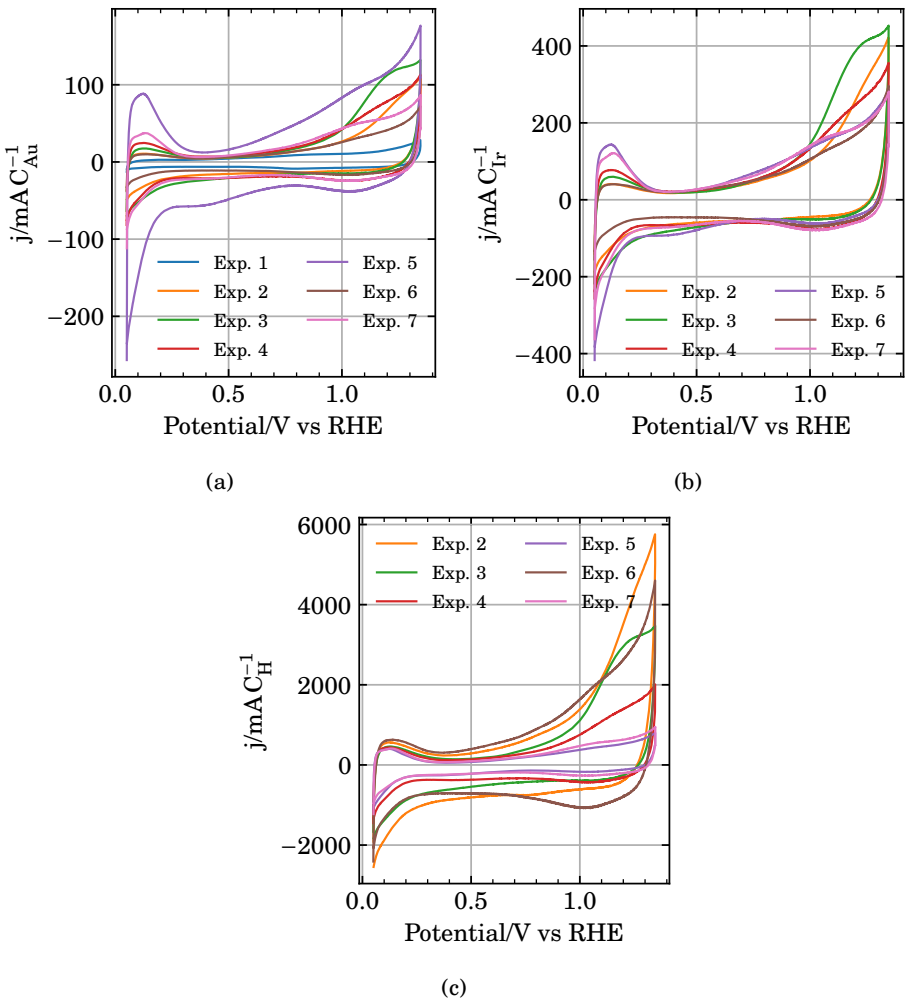

Figure 7.6: Voltammograms of electrodes 1-7 prepared in experiments 1 through 7 by the SLRR procedure. The voltammograms shown are the first potential cycle in 0.5 mol dm^{-3} H_2SO_4 at 50 mV s^{-1}. The currents have been normalized to Q_{Au} (a), Q_t (b) and Q_{H} (c) for each electrode, respectively. Electrode 1 is not shown in (b,c) as $Q_t = 0$ and $Q_{\mathrm{H}} = 0$.

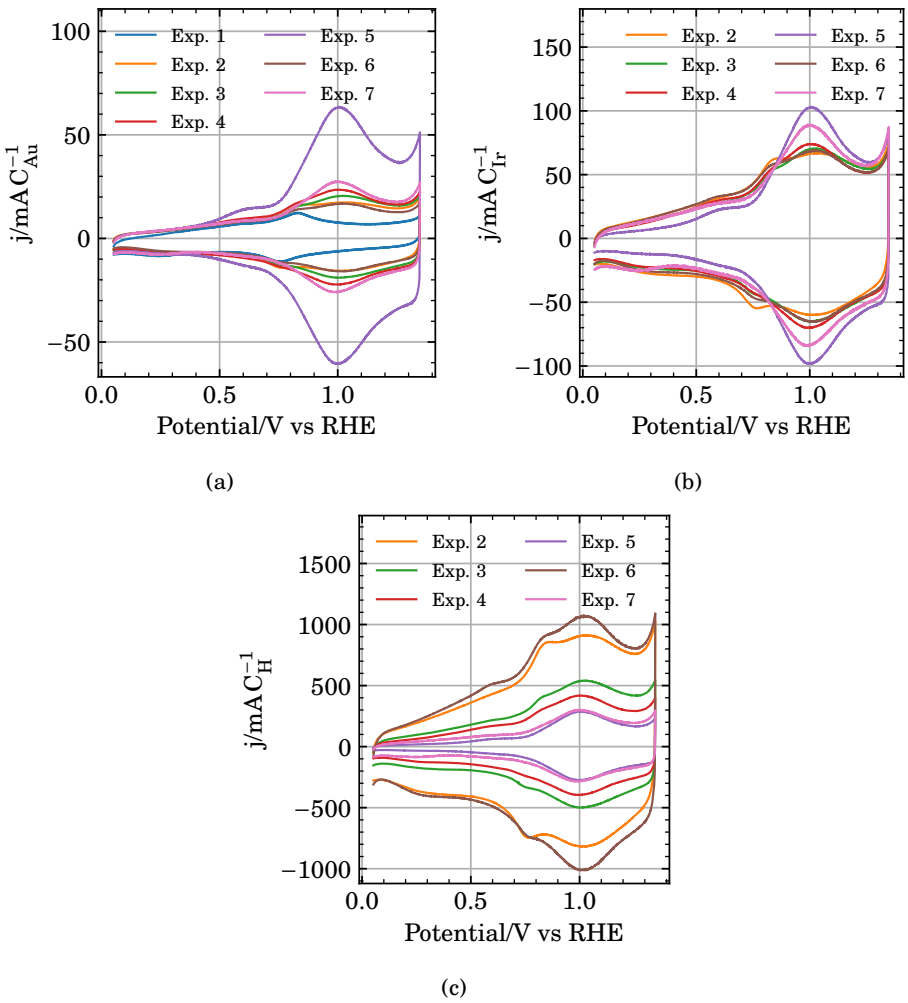

Figure 7.7: Voltammograms of electrodes 1-7 prepared in experiments 1 through 7 by the SLRR procedure. The voltammograms shown are the 50th potential cycle in 0.5 mol dm^{-3} H_2SO_4 at 50 mV s^{-1}. The currents have been normalized to Q_{Au} (a), Q_t (b) and Q_H (c) for each electrode, respectively. Electrode 1 is not shown in (b,c) as $Q_t = 0$ and $Q_H = 0$.

the surface area of the Au_{poly} substrate.

Some Ir was reduced directly onto the electrode at 0.3 V or 0.34 V at 70 °C through reactions (1.46) to (1.48) in experiments 2, 4 and 6 (blank experiments). Including $CuSO_4$ in the electrolyte increased the amount of Ir obtained in experiments 3, 5 and 7 (SLRR) when compared to the blank experiments. The yield appear to be greater when using K_2IrCl_6 compared to K_3IrCl_6.

7.2.3 Effect of electrode rotation and mass transport

Figure 7.9 shows the open circuit potential transients obtained in experiments 7 through 10 in table 7.1, at a rotating electrode for various rotation rates. The transients shown are number 1 out of 10, where all the successively obtained transients are shown individually for each experiment in figures E.42, E.49, E.56 and E.63. Experiment 7 is reprinted from figure 7.4.

The potential transients obtained from the SLRR procedure at 0 rpm, 400 rpm, 900 rpm and 1600 rpm are similar to what was shown before in figure 7.4. The potential increases more rapidly with time as the electrode rotation rate is increased. The potential where the transient starts to flatten out also appear to increase as the electrode rotation rate is increased.

The voltammograms in figure 7.10 show the first potential sweeps of electrodes 7-10 obtained in 0.5 mol dm^{-3} H_2SO_4 at 50 mV s^{-1}. The currents have been normalized to Q_{Au} (a), Q_t (b) and Q_H (c) for each electrode, respectively. Electrode 7 is reprined from figure 7.6. The voltammograms in (a) are given individually in figures E.43, E.50, E.57 and E.64. The voltammograms and extrapolations to zero- and infinite sweep rates used to determine Q_t are given in figures E.44, E.51, E.58 and E.65.

The voltammograms in figure 7.10 show a cathodic wave and anodic peak between 0.05 V and 0.4 V. The anodic sweeps show a varying degree of an oxidation wave followed by a wide peak anodically of 1 V in the cathodic direction. The cathodic wave and anodic peak between 0.05 V and 0.4 V in the first potential cycle are consistent with underpotential deposition deposition of hydrogen on polycrystalline Ir metal [113, 210].

The voltammograms in figure 7.11 show the 50th potential sweeps of electrodes 7-10 obtained in 0.5 mol dm^{-3} H_2SO_4 at 50 mV s^{-1}. The currents have been normalized to Q_{Au} (a), Q_t (b) and Q_H (c) for each electrode, respectively. Electrode 7 is reprined from figure 7.7. The voltammograms in (a) are given individually in figures E.43, E.50, E.57 and E.64. The voltammograms and extrapolations to zero- and infinite sweep rates used to determine Q_t are given in figures E.44, E.51, E.58 and E.65.

The voltammograms in figure 7.11 all show a pair of peaks centered around 1 V and

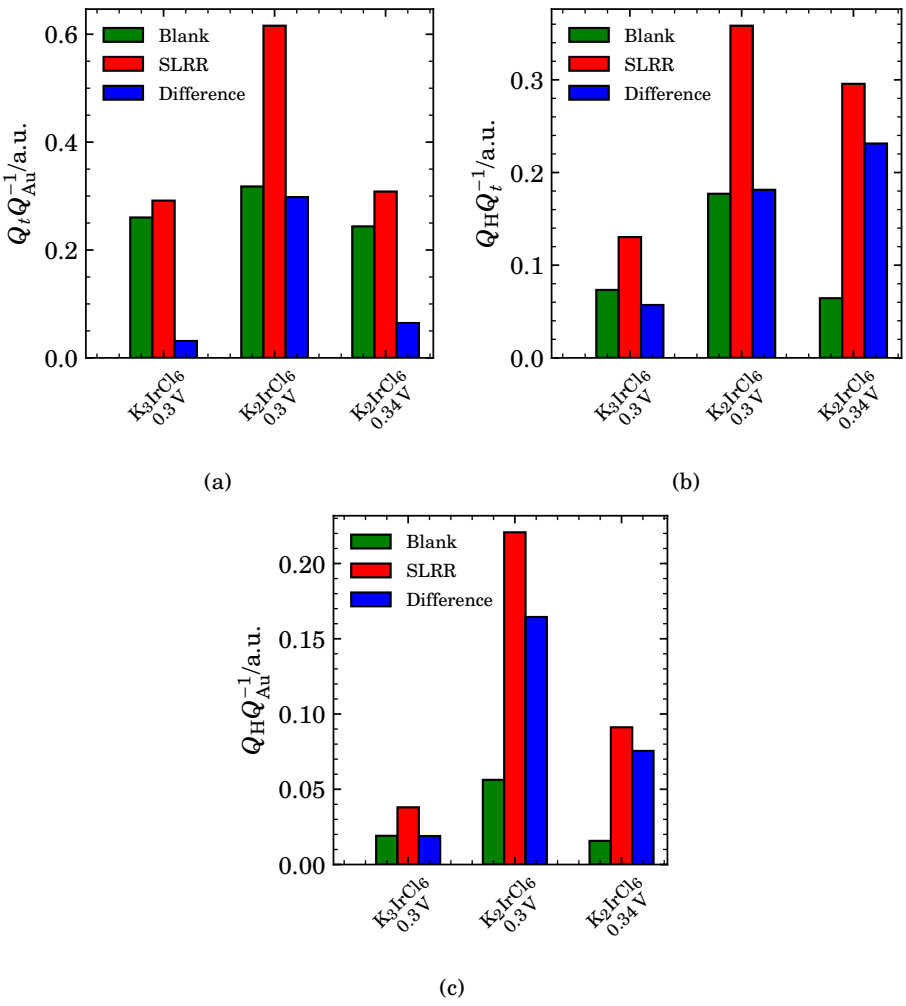

Figure 7.8: Comparisons of Q_{Au}, Q_t and Q_H from electrodes 2-7 prepared in experiments 2-7 through the ratios (a) $Q_t Q_{Au}^{-1}$, (b) $Q_H Q_t^{-1}$ and (c) $Q_H Q_{Au}^{-1}$. $Q_t Q_{Au}^{-1}$ relates the amount of eletrochemically available IrO_x to the amount of Au on the electrode surface, *i.e.* it relates the total amount of Ir deposit to the surface area of the substrate. $Q_H Q_t^{-1}$ relates the number of surface Ir atoms in the freshly prepared electrode to the total amount of IrO_x after transformation to AIROF by potential cycling, *i.e.* it relates the surface area to the volume of the Ir deposit. $Q_H Q_{Au}^{-1}$ similarly relates the number of surface Ir atoms in the freshly prepared electrode to the number of Au atoms on the electrode before deposition of Ir, *i.e.* it relates the surface area of the Ir deposit to the surface area of the Au_{poly} substrate.

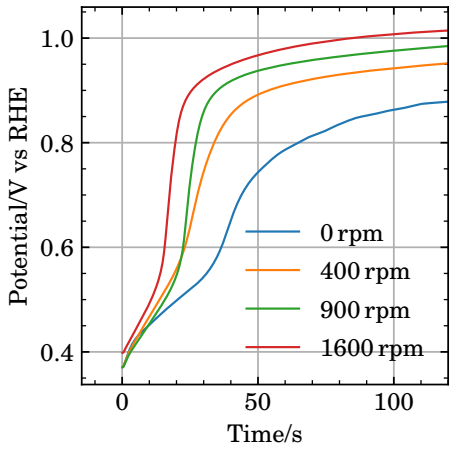

Figure 7.9: Open circuit potential transients obtained during experiments 7 through 10 in table 7.1. The electrolyte was a solution containing 0.5 mol dm^{-3} H_2SO_4, 1 mmol dm^{-3} $CuSO_4$ and 10 µmol dm^{-3} K_2IrCl_6. Potential transient was obtained after a 2 s potential hold at 0.34 V. The electrolyte was kept at 70 °C and the electrode was rotated at 0 rpm, 400 rpm, 900 rpm or 1600 rpm.

a prepeak around 0.65 V.

The pair of peaks centered around 1 V is typical for voltammgrams of AIROF in H_2SO_4, and the voltammograms in figure 7.11 are similar to the voltammogram of the polycrystalline Ir electrode in figure 7.2 and the previously shown voltammograms of electrodes 1-7 in 7.7 [48, 48, 70, 72, 73, 76, 77, 220–228].

Figure 7.12 compares the values of Q_{Au}, Q_t and Q_H from experiments 7-10 through the ratios (a) $Q_t Q_{Au}^{-1}$, (b) $Q_H Q_t^{-1}$ and (c) $Q_H Q_{Au}^{-1}$. The Ir deposits prepared in experiments 7 through 10 were obtained at a rotating electrode using various rotation rates. $Q_H Q_t^{-1}$ relates the number of surface Ir atoms in the freshly prepared electrode to the total amount of IrO_x after transformation to AIROF by potential cycling, *i.e.* it relates the surface area to the volume of the Ir deposit. $Q_t Q_{Au}^{-1}$ relates the amount of eletrochemically available IrO_x to the amount of Au originally on the electrode surface, *i.e.* it relates the total amount of Ir deposit to the surface area of the substrate. $Q_H Q_{Au}^{-1}$ similarly relates the number of surface Ir atoms in the freshly prepared electrode to the number of Au atoms on the electrode before modification with Ir, *i.e.* it relates the surface area of the Ir deposit to the surface area of the Au_{poly} substrate.

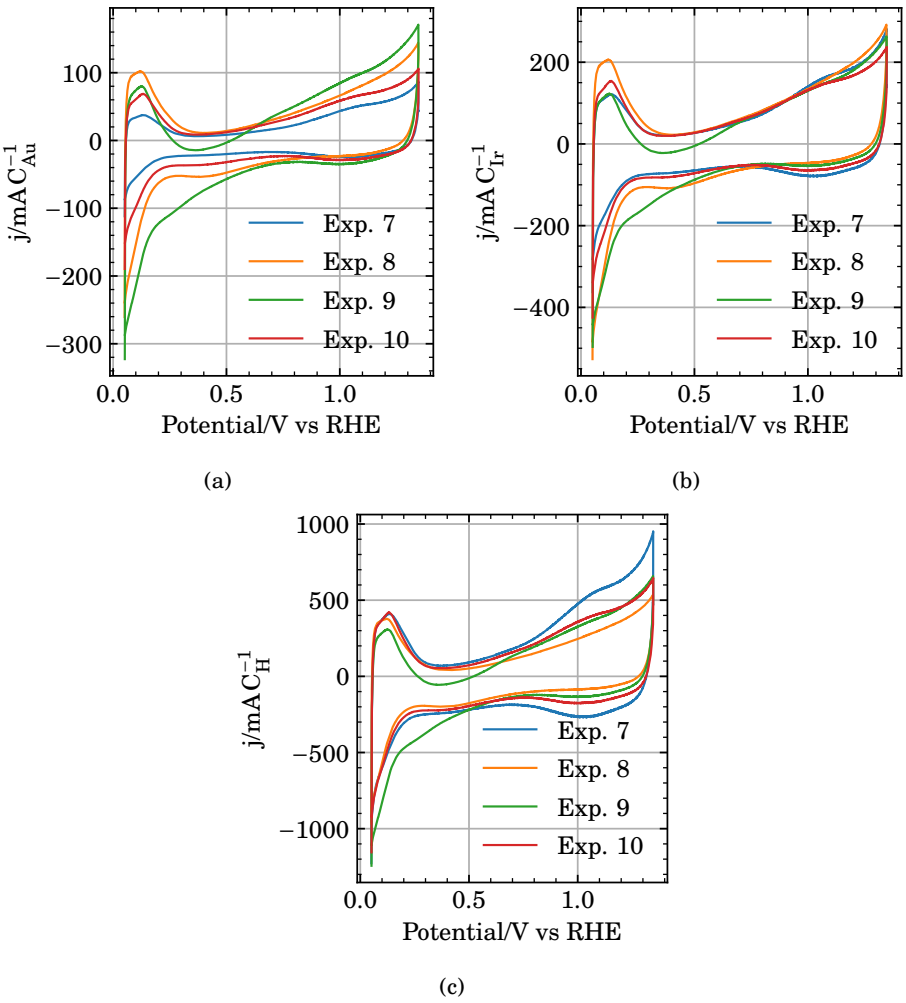

Figure 7.10: Voltammograms of electrodes 7-10 prepared in experiments 7 through 10 by the SLRR procedure. The voltammograms shown are the first potential cycle in 0.5 mol dm^{-3} H_2SO_4 at 50 mV s^{-1}. The currents have been normalized to Q_{Au} (a), Q_{Ir} (b) and Q_H (c) for each electrode, respectively.

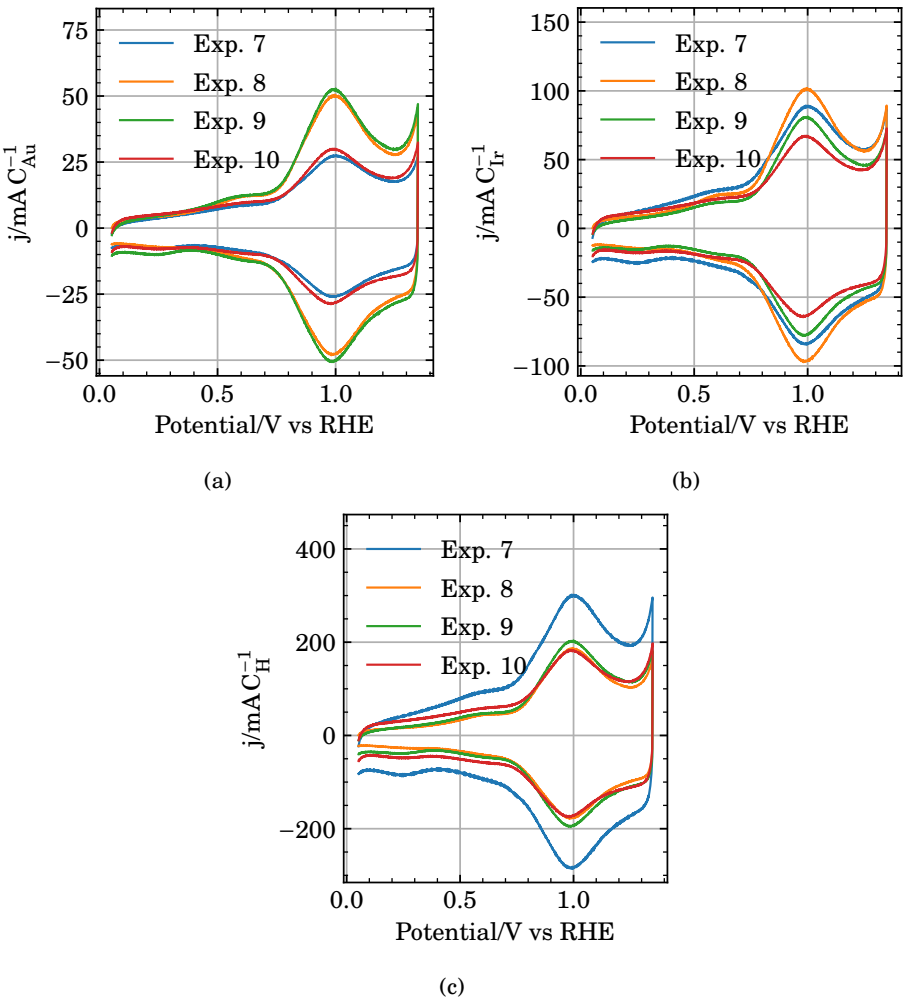

Figure 7.11: Voltammograms of electrodes 7-10 prepared in experiments 7 through 10 by the SLRR procedure. The voltammograms shown are the 50th potential cycle in 0.5 mol dm^{-3} H_2SO_4 at 50 mV s^{-1}. The currents have been normalized to Q_{Au} (a), Q_{Ir} (b) and Q_H (c) for each electrode, respectively.

The yield of the SLRR procedure, $Q_t Q_{\mathrm{Au}}^{-1}$, appear to be inversely proportional to the electrode rotation rate, with a maximum at 400 rpm. The number of surface Ir atoms in the freshly prepared electrode to the total amount of IrO_x after transformation to AIROF by potential cycling, $Q_{\mathrm{H}} Q_t^{-1}$, also appears to be inversely proportional to the electrode rotation rate. A low electrode rotation rate also appear to increase the surface area of the Ir deposit relative to the surface area of the underlying $\mathrm{Au_{poly}}$ substrate.

Figure 7.13 shows polarization curves of electrodes 3, 5 and 7 (a), and 7-10 figure 7.13b, after transformation to AIROF by potential cycling in $0.5\,\mathrm{mol\,dm^{-3}}$ H_2SO_4. The potential was increased from 1.45 V to 1.65 V at $5\,\mathrm{mV\,min^{-1}}$ in $0.5\,\mathrm{mol\,dm^{-3}}$ H_2SO_4, rotating the electrode at 1600 rpm. The currents are normalized to Q_t. The dashed lines show plots of equation (1.54), fitted as described in section 2.3. The fitting was restricted to $1.5\,\mathrm{V} \leq E \leq 1.6\,\mathrm{V}$, as we assume the upwards bend above 1.6 V is due to degradation of the electrode. The current at $E = 1.55\,\mathrm{V}$ and values of $\log_{10}(p_1)$, $\log_{10}(p_2)$ and α_2 obtained by the fitting are given in table 7.3. The values are consistent with previously reported values [17, 55].

Table 7.3: The current at $E = 1.55\,\mathrm{V}$ and values of $\log_{10}(p_1)$, $\log_{10}(p_2)$ and α_2 obtained by fitting the polarization curves in figure 7.13a to the rate expression for the electrochemical oxide path, equation (1.54) [17, 55], using the method outlined in section 2.3.

Electrode no.	$j_{1.55\mathrm{V}}/\mathrm{mA\,C^{-1}}$	$\log_{10}(p_1)$/a.u.	$\log_{10}(p_2)$/a.u.	α_2
3	84.5	−18.54	25.89	0.33
5	77.4	−6.26	26.81	0.78
7	67.0	−14.35	26.01	0.49
8	79.7	−17.14	26.04	0.38
9	61.9	−16.53	26.10	0.41
10	57.5	−15.68	26.03	0.44

Figure 7.14 shows voltammograms of an electrode prepared in experiment 7 in table 7.1. The voltammograms are similar to the voltammograms in figure 7.7 (a,b,c). 5 The voltammograms were obtained before and after the polarizaiton curves in figure 7.13, at $50\,\mathrm{mV\,s^{-1}}$ in $0.5\,\mathrm{mol\,dm^{-3}}$ H_2SO_4. Similar voltammograms of electrodes prepared in experiments 3, 5 and 7-10 before and after the polarization curves in figure 7.13 are given in figures E.20, E.33, E.46, E.53, E.60 and E.67.

The area under the anodic and cathodic peaks around 1 V were significantly reduced after exposure to potentials over 1.6 V. The double layer region below 0.4 V remained relatively constant.

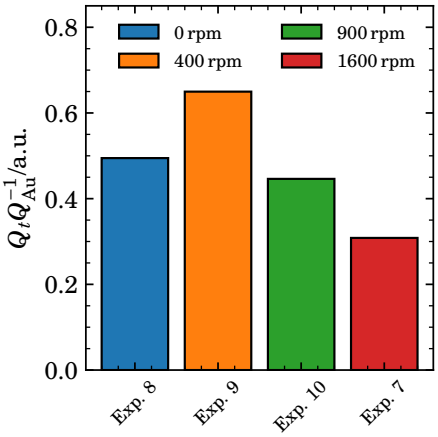

(a) IrO_x:Au

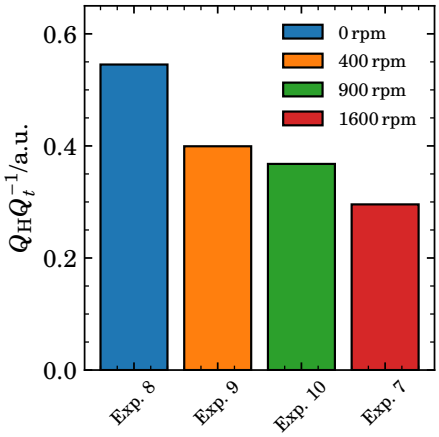

(b) Ir:IrO_x

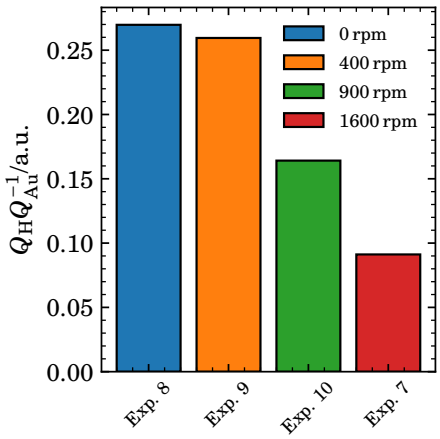

(c) Ir:Au

Figure 7.12: Comparisons of Q_{Au}, Q_t and Q_{H} from electrodes 7-10 prepared in experiments 7-10 through the ratios (a) $Q_t Q_{\mathrm{Au}}^{-1}$, (b) $Q_{\mathrm{H}} Q_t^{-1}$ and (c) $Q_{\mathrm{H}} Q_{\mathrm{Au}}^{-1}$. $Q_{\mathrm{Ir}} Q_{\mathrm{Au}}^{-1}$ relates the amount of IrO_x to amount of Au on the electrode surface. 5 $Q_{\mathrm{H}} Q_{\mathrm{Ir}}^{-1}$ relates the number of surface Ir atoms in the freshly prepared electrode to the total amount of IrO_x after transformation to AIROF by potential cycling. $Q_{\mathrm{H}} Q_{\mathrm{Au}}^{-1}$ compares the number of surface Ir atoms in the freshly prepared electrode to the number of Au atoms on the electrode before deposition of Ir.

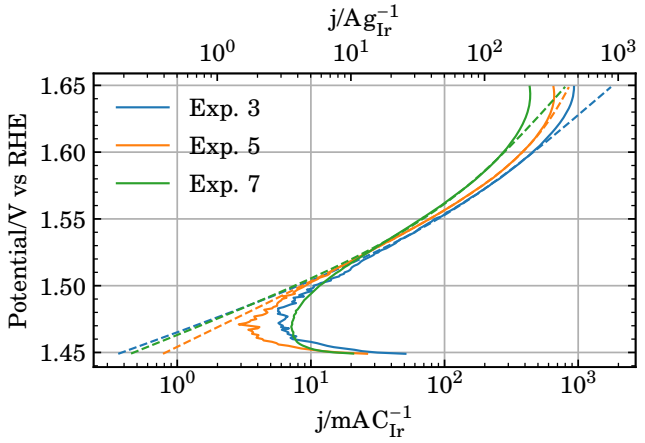

(a)

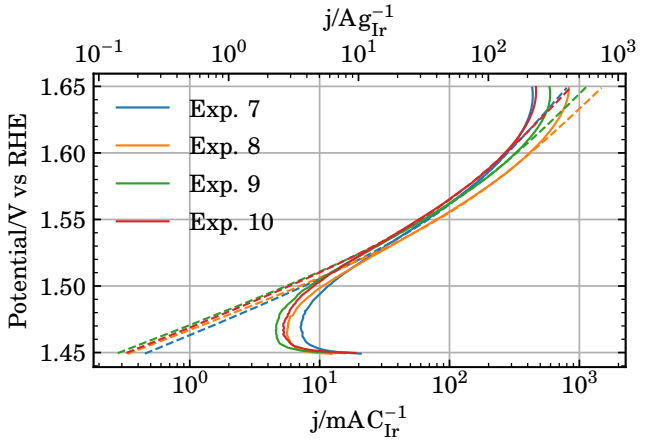

(b)

Figure 7.13: Polarizaton curves of electrodes 3, 5 and 7 (a), and 7-10 (b) after transformation to AIROF by potential cycling in 0.5 mol dm^{-3} H_2SO_4. Polarization curves were obtained by sweeping the electrode potential from 1.45 V to 1.65 V at 3 mV min^{-1} in 0.5 mol dm^{-3} H_2SO_4. The electrode was rotated at 1600 rpm. Dashed lines show fits to the rate expression of the electrochemical oxide path path [17, 55]. The current axes are normalized to the total amount of electrochemically available IrO_x, Q_{Ir}.

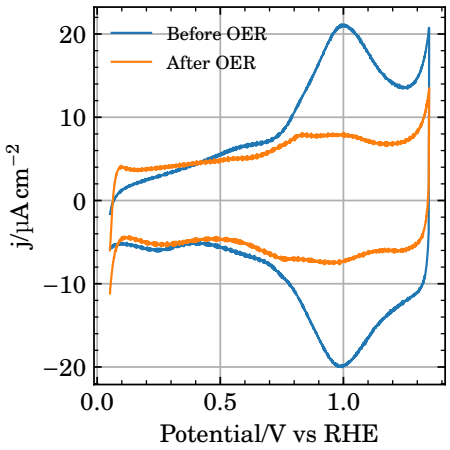

Figure 7.14: Voltammograms of an electrode prepared by the SLRR routine, experiment 7, before and after oxygen evolution. Potential sweep rate was 50 mV s^{-1} and the electrolyte was 0.5 mol dm^{-3} H_2SO_4.

7.2.4 Au nanoparticles

The value of Q_{Au} for gold nanoparticles, Au_{np}/GC, was determined by integrating the charge of the Au reduction peak around 1.15 V in voltammograms similar to figure 7.1a for electrodes of different mass loadings. This was determined as (91 ± 10) µC for an electrode loaded with 40 µL Au_{np} suspension. Charge at different loadings is given in figure E.96.

Figure 7.15 shows the open circuit potential transients obtained in experiments 11, 12/13 and 14 in table 7.2 with Au_{np}/GC as the working electrode The first (solid lines), fifth (dashed lines) and tenth (dotted lines) transients are shown, where the all the transients for each run are shown individually in figures E.70, E.77, E.84 and E.90.

The open circuit potential transients obtained with Au_{np}/GC show the same features as those obtained with the Au_{poly} electrode in figures 7.4 and 7.9. The potential transient appear to stabilize at a lower potential when the electrode rotation rate is reduced. The slope of potential versus time increases between 0.5 V and 0.6 V. The potential increases more slowly for each consequtive potential transient, and more slowly as the electrode rotation rate is reduced.

The voltammograms in figure 7.16 show the first potential sweeps obtained in 0.5 mol dm^{-3} H_2SO_4 at 50 mV s^{-1} of electrodes 11, 12/13 and 14 as prepared in

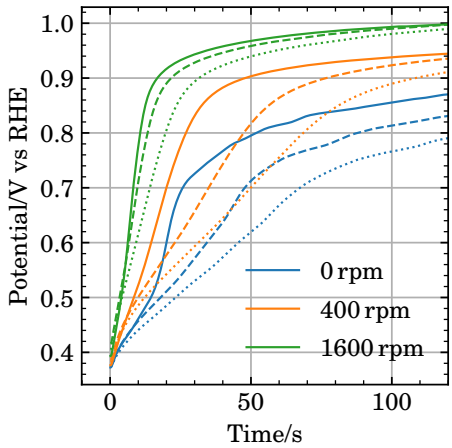

Figure 7.15: Open circuit potential transients obtained i experiments 11, 12/13 and 14 in table 7.1 with Au_{np}/GC as the working electrode. The electrolyte was a solution containing 0.5 mol dm^{-3} H_2SO_4, 1 mmol dm^{-3} $CuSO_4$ and 10 µmol dm^{-3} K_2IrCl_6. The potential transient were obtained after a 2 s potential hold at 0.34 V. The electrolyte was kept at 70 °C and the electrode was rotated at 0 rpm, 400 rpm or 1600 rpm.

esperiments 11, 12/13 and 14 in table 7.2 with Au_{np}/GC as the working electrode. The currents have been normalized to Q_{Au} (a), Q_t (b) and Q_H (c) for each electrode, respectively. The voltammograms in (a) are given individually in figures E.71, E.78, E.85 and E.91. The voltammograms and fits to zero- and infinite sweep rates used to determine Q_t are given in figures E.72, E.79, E.86 and E.92

The voltammograms in (a,b,c) show a cathodic wave and anodic peak between 0.05 V and 0.4 V.

The cathodic wave and anodic peak between 0.05 V and 0.4 V in the first potential cycle are consistent with underpotential deposition of hydrogen on polycrystalline Ir metal [113, 210].

The voltammograms in figure 7.17 show the 50th potential sweep obtained in $0.5\,\mathrm{mol\,dm^{-3}}$ H_2SO_4 at $50\,\mathrm{mV\,s^{-1}}$ of electrodes 11, 12/13 and 14 as prepared in esperiments 11, 12/13 and 14 in table 7.2 with Au_{np}/GC as the working electrode. The currents have been normalized to Q_{Au} (a), Q_t (b) and Q_H (c) for each electrode, respectively. The voltammograms in (a) are given individually in figures E.71, E.78, E.85 and E.91. The voltammograms and fits to zero- and infinite sweep rates used to determine Q_t are given in figures E.72, E.79, E.86 and E.92

The voltammograms in (a,b,c), all show a pair of peaks centered around 1 V and a prepeak around 0.65 V. The pair of peaks centered around 1 V is typical for voltammgrams of AIROF in H_2SO_4 [48, 48, 70, 72, 73, 76, 77, 220–228].

Figure 7.18 compares different ratios of Q_t, Q_H and Q_{Au} for Ir/Au_{np} electrodes 11, 12/13 and 14 prepared with the SLRR routine at 0.34 V using solutions of $0.5\,\mathrm{mol\,dm^{-3}}$ H_2SO_4, $10\,\mu\mathrm{mol\,dm^{-3}}$ K_2IrCl_6 and $1\,\mathrm{mmol\,dm^{-3}}$ $CuSO_4$ kept at 70 °C. The electrode was rotated at 0 rpm, 400 rpm or 1600 rpm during the SLRR procedure. The results are consistent with what has been presented for a polycrystalline gold electrode previously, *i.e.* there appears to be a maximum in the yield, $Q_t Q_{Au}^{-1}$, at 400 rpm.

Figure 7.19 (a) shows a polarization curve of an IrO_x/Au_{np} electrode prepared at 400 rpm, experiment 12/13, as described above. The polarizarion curve was obtained by sweeping the potential from 1.35 V to 1.65 V and back at $5\,\mathrm{mV\,min^{-1}}$ in $0.5\,\mathrm{mol\,dm^{-3}}$ H_2SO_4. The eletrode was kept stagnant. The current in the forward sweep at 1.55 V was $(79 \pm 16)\,\mathrm{mA\,C^{-1}}$. The dashed lines show the fits of equation (1.54) to the forward (dotted), reverse (dash-dots) and full (dashed) sweep. The fitted values of $\log_{10}(p_1)$, $\log_{10}(p_2)$ and α_2 in the forward sweep was $\log_{10}(p_1) = -18.97 \pm 0.23$, $\log_{10}(p_2) = 25.92 \pm 0.03$ and $\alpha_2 = 0.31 \pm 0.01$ and is consistent with previously reported values and the values obtained on the polycrystalline electrode [17, 55]. The foward sweep in figure 7.19 (a) shows an upwards bend at higher potentials. The reverse sweep does not overlap with the forward sweep.

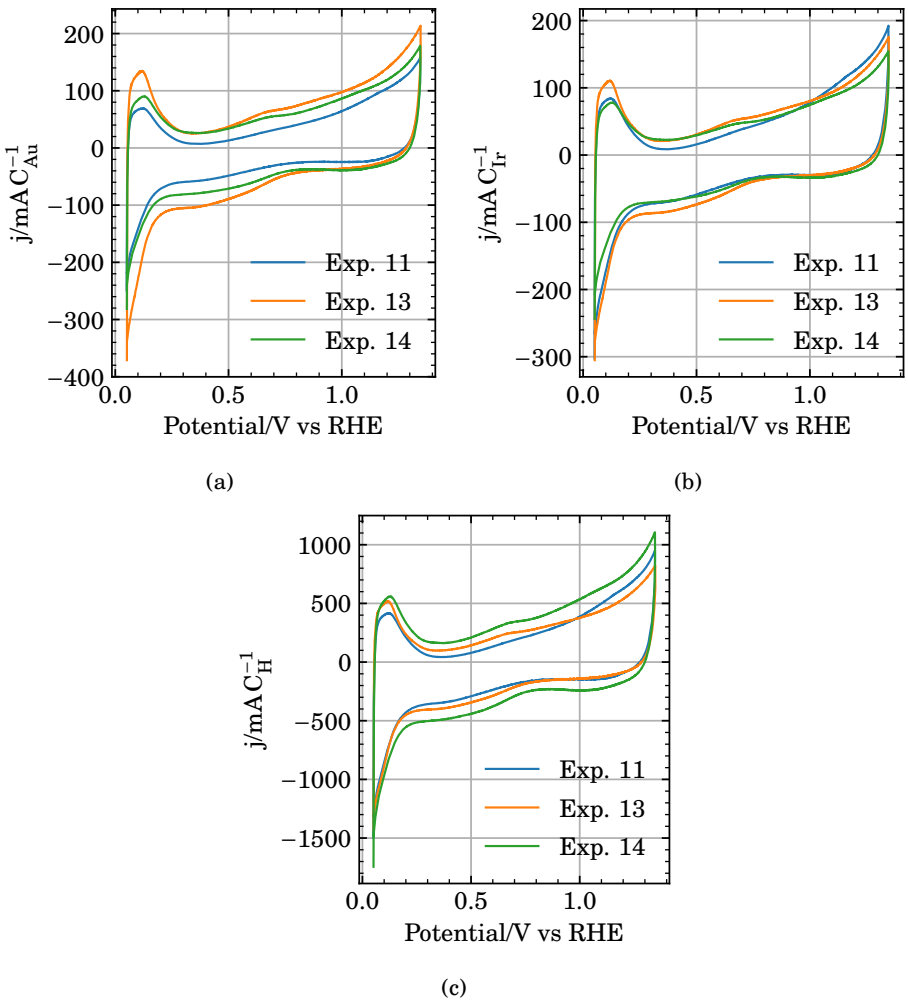

Figure 7.16: Voltammograms of electrodes 11, 12/13 and 14 prepared by the *one-pot* SLRR routine at 0 rpm, 400 rpm or 1600 rpm with Au_{np} on a GC RDE. Voltammograms shownthe first potential cycle obtained in 0.5 mol dm^{-3} H_2SO_4 at 50 mV s^{-1}. The currents have been normalized to Q_{Au} (a), Q_{Ir} (b) and Q_H (c) for each electrode, respectively.

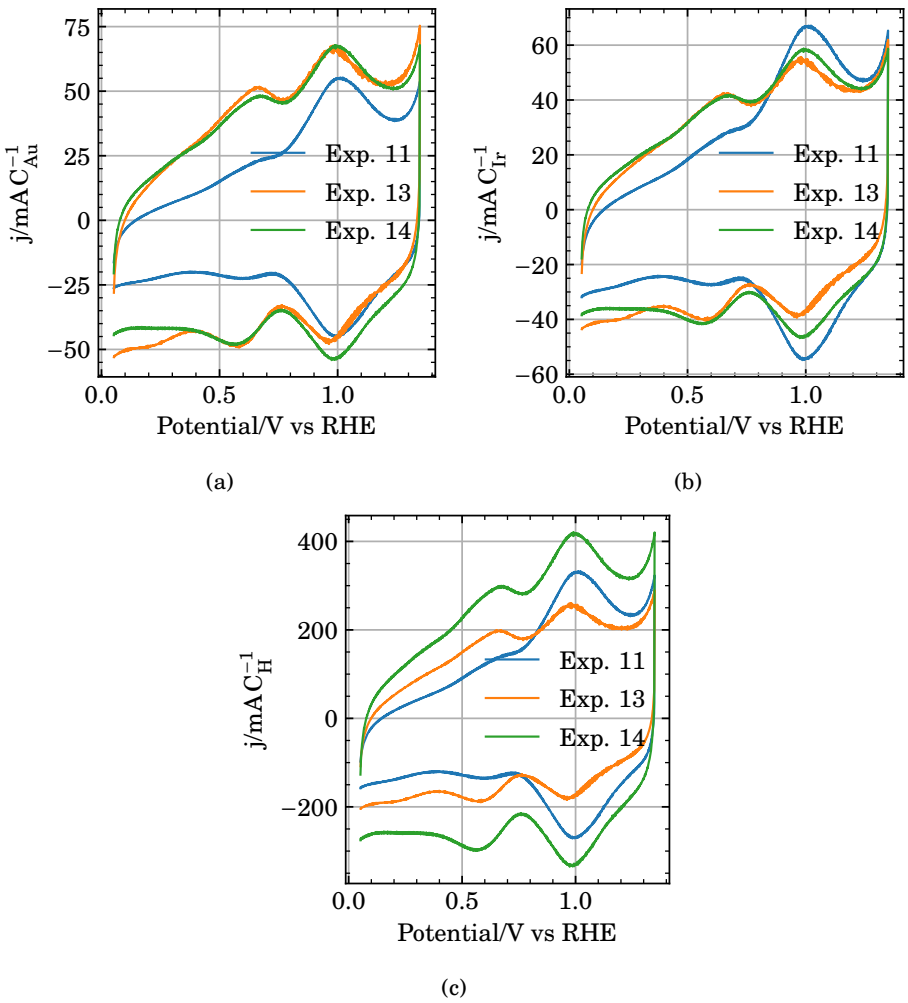

Figure 7.17: Voltammograms of electrodes 11, 12/13 and 14 prepared by the *one-pot* SLRR routine at 0 rpm, 400 rpm or 1600 rpm with Au_{np} on a GC RDE. Voltammograms shown are after potential cycling in 0.5 mol dm^{-3} H_2SO_4, which transformed any Ir deposits to IrO_x. Potential sweep rate was 50 mV s^{-1}. The currents have been normalized to Q_{Au} (a), Q_{Ir} (b) and Q_H (c) for each electrode, respectively.

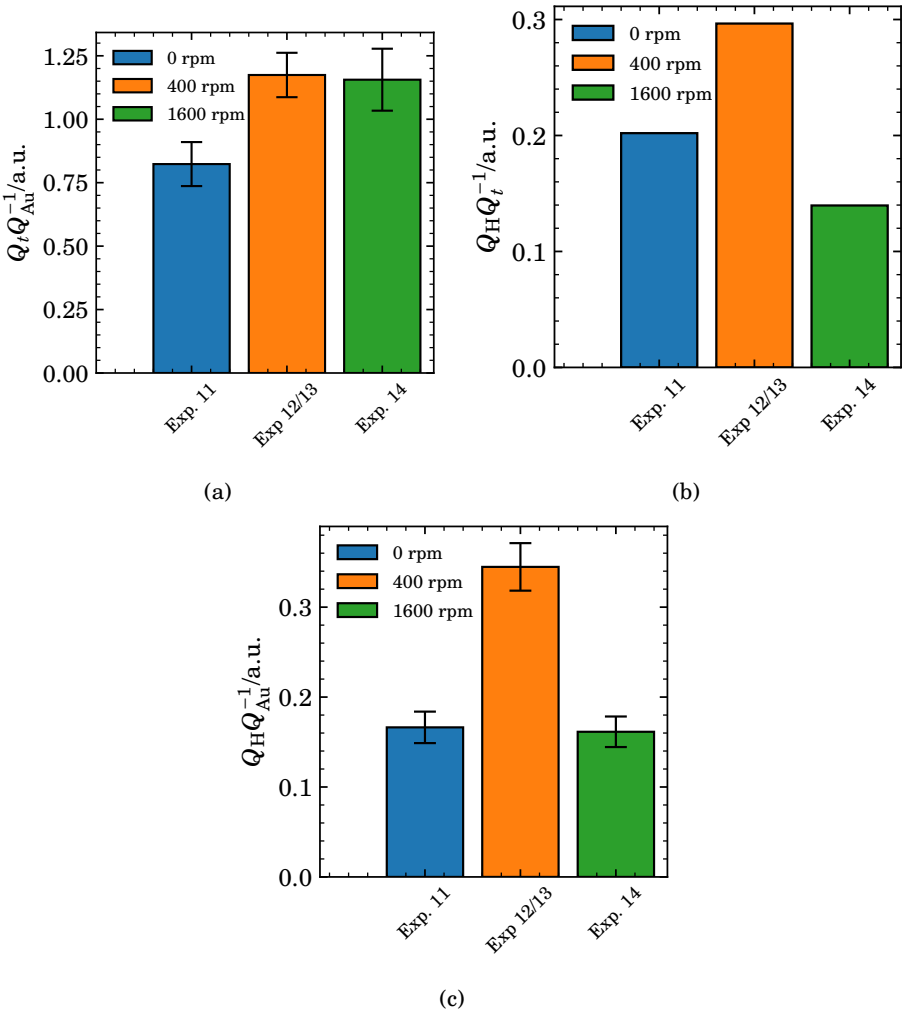

Figure 7.18: Comparisons of Q_{Au}, Q_t and Q_H from electrodes 11, 12/13 and 14 through the ratios (a) $Q_t Q_{Au}^{-1}$, (b) $Q_H Q_t^{-1}$ and (c) $Q_H Q_{Au}^{-1}$. $Q_{Ir} Q_{Au}^{-1}$ relates the amount of IrO_x to amount of Au initially present on the electrode surface. 5 $Q_H Q_{Ir}^{-1}$ relates the number of surface Ir atoms in the freshly prepared electrode to the total amount of IrO_x after transformation to AIROF by potential cycling. $Q_H Q_{Au}^{-1}$ relates the number of surface Ir atoms in the freshly prepared electrode to the number of Au atoms initially present on the electrode surface before depositon of Ir.

Figure 7.19 (b) shows voltammograms similar to those in figure 7.17 obtained before and after the polarization curve in (a). The magnitude of the main pair of peaks around 1 V in the voltammograms was significantly reduced after the slow potential cycle between 1.35 V and 1.65 V.

The yield of Ir obtained in experiments 7-10 ($Q_t Q_{\mathrm{Au}}^{-1}$, figure 7.8) was inversely proportional to the rotation rate of the electrode. The rate of consumption of Ir(III), reactions (1.47) and (1.48), is assumed to be very slow relative to the rate of formation [176], reaction (1.46). In solutions containing K_2IrCl_6, the bulk conentration of Ir(III) is close to zero. The flux of Ir(III) *away from the electrode surface*, $N_{\mathrm{Ir(III)}}$, is then given by equation (7.1),

$$N_{\mathrm{Ir(III)}} = D_{\mathrm{Ir(III)}} \frac{c^{\sigma}_{\mathrm{Ir(III)}}}{\delta_N} \tag{7.1}$$

where $D_{\mathrm{Ir(III)}}$ is the diffusion coefficient of Ir(III), $c^{\sigma}_{\mathrm{Ir(III)}}$ is the concentration at the electrode surface, and δ_N is the width of the Nernst diffusion layer [16].

δ_N is proportional to the inverse of the square root of the electrode rotation rate, $\delta_N \propto \omega^{-1/2}$, and equation (7.1) can be written as equation (7.2) [16]

$$N_{\mathrm{Ir(III)}} = 0.62 \times D_{\mathrm{Ir(III)}}^{2/3} \times \nu^{-1/6} \times c^{\sigma}_{\mathrm{Ir(III)}} \omega^{1/2} = A\omega^{1/2} \tag{7.2}$$

where ν is the kinematic viscosity of the solvent (water) and $A = 0.62 \times D_{\mathrm{Ir(III)}}^{2/3} \times \nu^{-1/6} \times c^{\sigma}_{\mathrm{Ir(III)}}$

The total flux balance of Ir(III) is then given as equation (7.3)

$$\begin{aligned} v_{\mathrm{Ir(IV)/Ir(III)}} &= v_{\mathrm{Ir(III)/Ir(0)}} + N_{\mathrm{Ir(III)}} \\ v_{\mathrm{Ir(IV)/Ir(III)}} &= v_{\mathrm{Ir(III)/Ir(0)}} + A\sqrt{\omega} \end{aligned} \tag{7.3}$$

where $v_{\mathrm{Ir(IV)/Ir(III)}}$ is the rate of formation of Ir(III) (reaction (1.46)), $v_{\mathrm{Ir(III)/Ir(0)}}$ is the rate of consumption of Ir(III) (reactions (1.47) and (1.48)) and $N_{\mathrm{Ir(III)}}$ and $A\sqrt{\omega}$ is the flux away from the electrode defined in equation (7.2).

Re-organizing and integrating each term of equation (7.3) from 0 to t, $\int_0^t v_i \, \mathrm{d}t = Q_i$ gives equation (7.4),

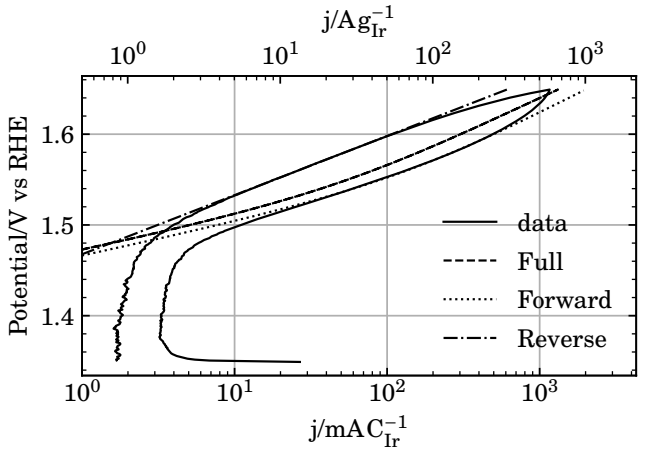

(a)

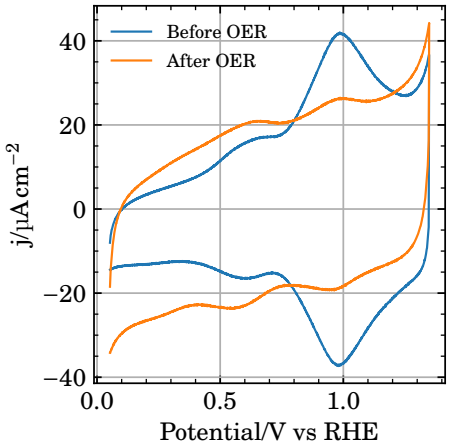

(b)

Figure 7.19: (a) Polarization curve of an IrO_x/Au_{np} electrode prepared by the SLRR routine using K_2IrCl_6 at 400 rpm and 70 °C. The polarization curve was obtained after transformation of the Ir deposit to IrO_x by potential cycling. The electrode potential was swept from 1.35 V to 1.65 V and back at 5 mV min^{-1} in 0.5 mol dm^{-3} H_2SO_4. The eletrode was kept stagnant. (b) Cyclic voltammograms of an electrode before and after the polarization curves in (a). Potential sweep rate was 50 mV s^{-1} and the electrolyte was 0.5 mol dm^{-3} H_2SO_4.

$$\int_0^t v_{\mathrm{Ir(III)/Ir(0)}}\,\mathrm{d}t = \int_0^t v_{\mathrm{Ir(IV)/Ir(III)}}\,\mathrm{d}t - \int_0^t A\sqrt{\omega}\,\mathrm{d}t$$
$$Q_{\mathrm{Ir(III)/Ir(0)}} = Q_{\mathrm{Ir(IV)/Ir(III)}} - A\sqrt{\omega}t \tag{7.4}$$

where $Q_{\mathrm{Ir(III)/Ir(0)}}$ represents Q_t as defined previously.

Figure 7.20 shows plots of $Q_t Q_{\mathrm{Au}}^{-1}$, $Q_{\mathrm{H}} Q_t^{-1}$ and $Q_{\mathrm{H}} Q_{\mathrm{Au}}^{-1}$ from figure 7.12 versus $\sqrt{\omega}$. $\omega = 0$ has been included in the figure, but equation (7.4) is not valid for $\omega_{\mathrm{rpm}} < 100\,\mathrm{rpm}$ [16]. $Q_t Q_{\mathrm{Au}}^{-1}$ versus $\sqrt{\omega}$ shows good agreement with equation (7.4). We have also included $Q_{\mathrm{H}} Q_t^{-1}$ and $Q_{\mathrm{H}} Q_{\mathrm{Au}}^{-1}$. $Q_{\mathrm{H}} Q_t^{-1}$ relates the number of Ir surface atoms in the as-prepared film to the total amount of IrO_x after potential cycling, *i.e.* it relates to surface area to the volume. $Q_{\mathrm{H}} Q_{\mathrm{Au}}^{-1}$ relates the total surface area of the as-prepared Ir deposit to the surface area of the underlying Au substrate. Both relations are inversely proportional to the electrode rotation rate.

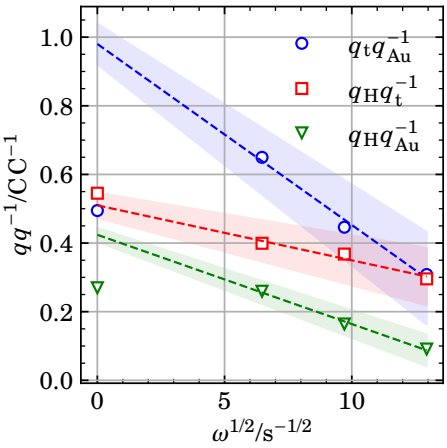

Figure 7.20: The different measures of the yield of the SLRR routine obtained in experiments 7 through 10 plotted versus the electrode rotation rate.

It is of interest to relate the total charge passed during the potential holds at 0.7 V and 0.3 V or 0.34 V in experiments 1-10 to the number of successive displacement events. In experiments 5 and 7-10, the total charge passed at 0.3 V or 0.34 V increased proportionally with the number of successive displacement events. Figure 7.21 (a) plots the total charge passed in each potential hold at 0.34 V in experiments 7 through 10. Experiments 1 thorugh 10 are given in figures E.6a, E.10a,

E.16a, E.23a, E.29a, E.36a, E.42a, E.49a, E.56a and E.63a. The total charge passed as 0.34 V appear to increased linearly with each displacement event with slope $\partial Q_{\mathrm{UPD}}/\partial n$, where the slope $\partial Q_{\mathrm{UPD}}/\partial n$ appear to be a function of the electrode rotation rate for $\omega > 0$, as seen in figure 7.21 (b). The dashed lines and colored areas show linear regressions with one standard deviation.

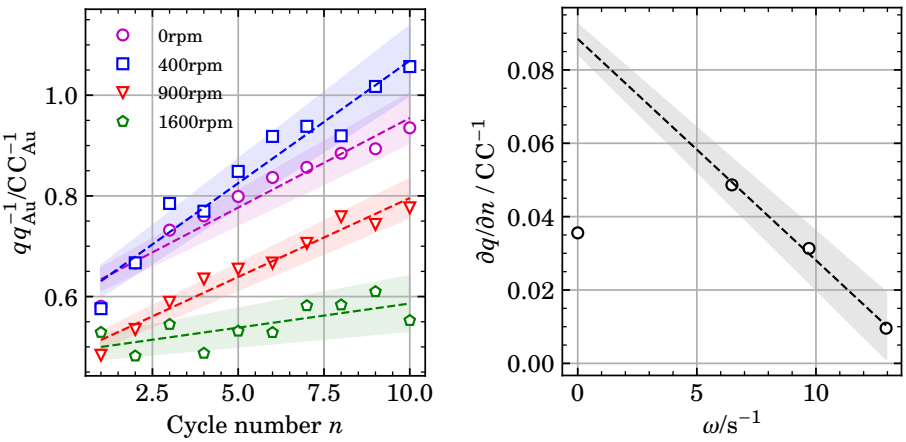

Figure 7.21: (a) The total charge passed during each potential hold at 0.34 V in experiments 7 through 10. The electrolyte contained 0.5 mol dm^{-3} H_2SO_4, 1 mmol dm^{-3} $CuSO_4$ and 10 µmol dm^{-3} K_2IrCl_6. (b) The slopes obtained from the linear regressions of the data in (a).

The slope of potential versus time in the open circuits potential transients from experiments 1, 5 and 7 through 10 in figures 7.4 and 7.9 incresed around 0.6 V. This is the same potential where the charge in the Cu_{UPD} isotherms given previously in figure 7.3c approaches zero. It is therefore of interrest to relate the time of which the slope $\partial E/\partial t$ in the open circuit potential transients of from experiments 7 through 10 (figures E.42b, E.49b, E.56b and E.63b) reaches a maximum to the number of successive displacement events. Figure 7.22a relates the time of which the slope $\partial E/\partial t$ in the open circuit potential transients of from experiments 7 through 10 (figures E.42b, E.49b, E.56b and E.63b) reached a maximum to the number of successive displacement events. There appears to be a linear correlation.

Since the two correlations above were both linear, we also plotted the aforementioned time as a function of the aforementioned charge in figure 7.23. There appears to be a linear correlation between the charge passed at 0.34 V and the time of which the slope

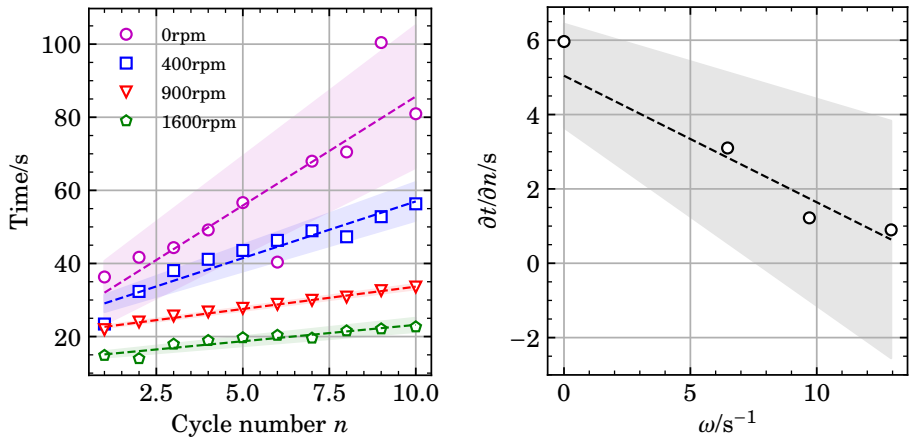

(a) (b)

Figure 7.22: (a) Time at which a maximum appeared in the slope of potential versus time, $\partial E/\partial t$ in the open circuit potential transients obtained in experimetns 7 through 10 as a function of successive displacement eventds. (b) The slopes obtained from the linear regressions of (a).

$\partial E/\partial t$ in the following open circuit potential transient reached a maximum.

7.3 Discussion

The decrease in yield with increased electrode rotation rate indicates that a reaction intermediate is transported away from the electrode. Ir(III) formed by reduction of Ir(IV) through reaction (1.46) escapes the electrode surface, lowering the overall yield of the procedure. This was argued previously when defining equation (7.4). The slow consumption of Ir(III) through reactions (1.47) and (1.48) means that more Ir(III) formed through reaction (1.46) escapes the electrode surface when the rotation rate of increassed. This is consistent with the yield of experiments 7 through 10 which was inversely proportional with the square root of the electrode rotation rate, figure 7.20 and a slow consumption of Ir(III) [176]. At room temperature, experiment 1, no Ir was obtained.

The results above suggests that the Ir(III) complexes formed through reduction of solutions containing K_2IrCl_6 (exp. 1, 4, 5 and 6-10) is different from those present in solutions containing K_3IrCl_6 (epx. 2 and 3) . More Ir was obtained from solutions containing only K_2IrCl_6 (exp. 4 and 6) than with solutions containing only K_3IrCl_6

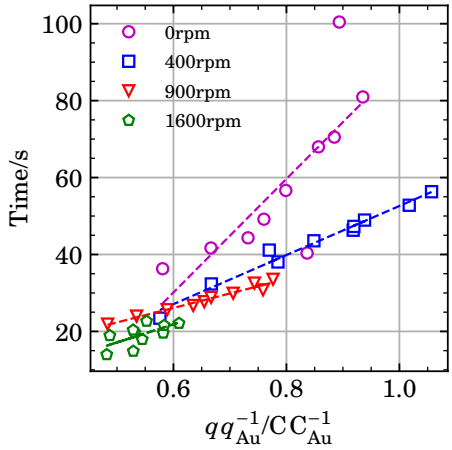

Figure 7.23: The time of which the slope $\partial E/\partial t$ in the open circuit potential transients obtained in experiments 7 through 10 reached a maximum versus the charge passed in the preceeding potential hold at 0.34 V.

(exp. 2 and 4) when considering both the total amount of IrO_x (figure 7.8 (a)) and the charge of the H_{UPD} peaks (figure 7.8 c)). The reaction mechanism for reduction of Ir(IV) could be different from that of reduction of Ir(III), but reaction (1.46) is a well known reaction with a standard reduction potential of $E^{\ominus}_{Ir(IV)/Ir(II)}$=0.86 V [19, 90, 176, 177, 180, 183]. Reactions (1.47) to (1.50) [176, 183] is also consistent with our previous argument; Ir(III) formed in reaction (1.46) appear to diffuse away from the electrode surface. With the above arguments that reduction of both Ir(III) and Ir(IV) solutions should follow reactions (1.46) to (1.48), the difference between the solutions containing Ir(III) and Ir(IV) must be the complexes formed in aqueous solutions containing $CuSO_4$ and/or H_2SO_4.

Cu_{UPD} appears to grow onto Ir metal, where the surface area of Ir increases for every displacement event. The total charge passed during each potential hold at 0.34 V in figure 7.21 (a) (exp. 7 through 10) increased with each following potential hold (figures E.42, E.49, E.56 and E.63). The electrolyte used in experiments 7 through 10 contained $CuSO_4$ and K_2IrCl_6. The charge also increased for each successive potential hold at 0.3 V in experiment 5 (figure E.29), where the electrolyte contained $CuSO_4$ and K_2IrCl_6. The charge did not increase when the electrolyte contained K_2IrCl_6 only (exp. 4 and 6, figures E.23 and E.36), K_3IrCl_6 only (exp. 2, figure E.10) or K_3IrCl_6 and $CuSO_4$ (exp. 3, figure E.16). Experiments 2 through 10 was conducted at 70 °C. The charge did not increase at room temperature when the electrolyte

contained $CuSO_4$ and K_2IrCl_6, (exp. 1, figure E.6)). The charge increased *only in experiments 5 and 7 through 10*, *i.e.* in the presence of both K_2IrCl_6 and $CuSO_4$ at 70 °C. The slope and intercept of the linear regressions of charge versus the number of consequtive potential holds was inversely proportional to the electrode rotation rate *only* in the presence of both K_2IrCl_6 and $CuSO_4$ at 70 °C. The yield of the SLRR reaction in experiments 7-10 was also inversely proportional to the electrode rotation rate (figure 7.20). This implies that the increased charge passed at 0.3 V or 0.34 V for each displacement event is not solely due to nucleation and growth of Ir, *i.e.* the charge does not increase because the surface area where reactions (1.46) to (1.48) occured increased. For each consequtive open circuit potential transient, the time of which the slope $\partial E/\partial t$ reached a maximum, figure 7.22a, was proportional to the total charge that passed in the preceeding potential hold *only* in the presence of both K_2IrCl_6 and $CuSO_4$ at 70 °C. This implies that either the kinetics of the reactions at the electrode surface was changed as more Ir was deposited onto the surface, *or* that more Cu_{UPD} was deposited onto the electrode surface as more Ir was present.

There was no apparent changes in the current transients at 0.3 V or 0.34 V in the blank experiments (2, 4 and 6) with each consecutive potential hold at 0.3 V or 0.34 V figures E.9, E.15, E.22 and E.35, so we can assume that the kinetics of reactions (1.46) to (1.48) did not change significantly when some Ir is deposited onto the surface. Furthermore, we associate the shoulder in the current transients at 0.3 V and 0.34 V (exp. 5, 7-10, figures E.28a, E.41a, E.48a, E.55a and E.62a) with the Cu_{UPD} reaction, as it is clearly visible in current transients obtained from solutions containing only H_2SO_4 + $CuSO_4$ (figure E.2) [263]. This means that the shoulder in the current transients in figures E.28a, E.41a, E.48a, E.55a and E.62a shifting to longer times for each consequtive potential pulse is due to Cu_{UPD} forming on Ir metal, of which the surface area is growing for every displacement event. It is possible that Cu_{UPD} forms onto Au and a continiously forming Ir layer during the potential holds at 0.30 V or 0.34 V.

The Ir deposits appear to be thin, or adhere poorly to the Au substrate. The upwards and backwards bend of the polarization curves in figures 7.13 and 7.19 at $E \geq 1.6$ V is indicative of the electrode degrading. The bend predicted by the reaction mechanism is seen in the dashed curves, and is much less prominent than the one observed experimentally. IrO_x is known to degrade at potentials above 1.6 V [1, 13]. This is consistent with the voltammograms obtained before and after the polarization curves, figures 7.14 and 7.19b. The pair of peaks around 1 V dissapeared after the polarization curves, while the capacitive currents in $E \leq 0.4$ V did not change significantly. This means that the active material, IrO_x, contributing to the peaks around 1 V was lost during the polarization curve. This would not be observed to a large extent for a thick film of IrO_x, because dissolution of the active material would simply expose more active material. When the IrO_x film is sufficiently thin, dissolu-

tion exposes the much less active Au substrate. This causes the total current on the electrode to decrease as the potential is increased above 1.6 V. The voltammograms obtained at different potential sweep rates normalized to the anodic peak current around 1 V, figures E.13, E.19, E.26, E.32, E.39, E.45, E.52, E.59 and E.66 show that the peak potential does not shift with sweep rate, and is indicative that the films are indeed thin [79].

The *one-pot* SLRR proceedure appear to produce Ir deposits on Au_{np} as expected from the results obtained on Au_{poly}. The open circuit potential transients measured on Au_{np}/GC in figure 7.15 show the same trends as those measured on Au_{poly} in figures E.29, E.42, E.49, E.56 and E.63 where the potential increases more slowly for each consequtive potential transient, and more slowly for lower electrode rotation rates. The current passed at Au_{np}/GC at 0.34 V in figures E.69, E.76, E.83 and E.89 appear the same as for Au_{poly} figures E.28, E.41, E.48, E.55 and E.62, where a shoulder between 0 s and 1 s shifts to longer times for each consequtive potential hold, and more charge is transferred in total after each displacement event. The voltammograms in figures 7.16a to 7.16c show an anodic peak typical for H_{UPD} between 0.4 V and 0 V and pair a of peaks around 1 V is present in figures 7.17a, 7.17b and 7.18c. This is similar to Au_{poly} in figures 7.7 and 7.11 and has been discussed previously.

The polarization curve in figure 7.19a show that the Ir/Au_{np} catalyst either degrades or dislodges from the glassy carbon surface when the potential is increases above 1.6 V. The currents on the reverse sweep does not overlap with the forward sweep and is indicative that active material has been lost. This is confirmed by the voltammograms obtained prior to- and after the polarization curve, figure 7.19b.

7.4 Conclusions

We have again showed how a *one-pot* surface limited redox replacement procedure can be used to prepare thin films of Ir on bulk and nanocrystalline Au *via* galvanic displacement of underpotentially deposited Cu. The results indicate that the yield of the procedure is inversely proportional to the degree of agitation in the electrolyte, due to transport of reaction intermediates. Contrary to intuition, the yield of the procedure is higher with Ir(IV) precursor solutions than with Ir(III) precursor solutions, likely due to differences in the Ir(III) complexes formed by reduction of Ir(IV) compared to those present in solutions allready containing Ir(III). The Ir films formed by the *one-pot* procedure is thin, and therefore degreades rapidly at potentials positive of 1.6 V in 0.5 mol dm^{-3} H_2SO_4.

Chapter 8

Ir deposition onto Pd by SLRR of Cu

8.1 Experimental

Materials and equipment

All experiments were performed in a glass cell equipped with a water jacket. A polycrystalline palladium rotating disc electrode (Pd_{poly} RDE) (5 mm internal diameter, PEEK shroud, exchangeable disc; Pine) or a glassy carbon rotating disc electrode (GC RDE) (5 mm internal diameter, PEEK shroud, fixed disc; Pine) covered with a thin film of Pd/C (10 wt% Pd on activated carbon, Alfa Aesar) served as working electrodes. The electrodes were polished to a mirror finish with successively 0.3 µm and 0.05 µm alumina suspensions (Allied) on a microcloth (Buehler) and rinsed using DI water (Millipore, 18.2 MΩ@25 °C), followed by gentle sonication of the surface and finally rinsed using DI water a second time prior to each experiment. The electrode was mounted on a Pine Classic RDE/RRDE Shaft (15 mm OD PEEK shroud, stainless steel rod) attached to a Pine MSR rotator.

The potentiostat used was a Gamry reference 600. The ohmic drop was determined by the built in utility, of which 85% was compensated through positive feedback compensation. The counter- and reference electrodes were a Pt-foil and a reversible hydrogen electrode (RHE), respectively. All potentials reported are versus RHE.

Experiments were performed using solutions containing 0.5 mol L^{-1} H_2SO_4 (96.3%, VWR), 1 mmol L^{-1} $CuSO_4$ (Sigma, 99.995 %), and 10 µmol dm^{-3} K_2IrCl_6 (Heraeus).

All electrolytes were always purged using Ar(g) for at least 30 min prior to each experiment and kept under an Ar(g) atmosphere for the duration of the experiment.

The electrolyte temperature was kept at $(70 \pm 1)\,^{\circ}\mathrm{C}$ by circulating water from a water bath through the water jacket, or room temperature $T_{\mathrm{RT}} \approx (23 \pm 1)\,^{\circ}\mathrm{C}$.

Polycrystalline palladium

The polished $\mathrm{Pd_{poly}}$ electrode was cycled at $50\,\mathrm{mV\,s^{-1}}$ between 0.2 V and 1.2 V in $0.5\,\mathrm{mol\,dm^{-3}}$ $\mathrm{H_2SO_4}$ at room temperature until the voltammogram did not change significantly over 10 cycles. A *one-pot* SLRR routine was employed as described in chapters 6 and 7. The electrolyte was a solution containing $0.5\,\mathrm{mol\,L^{-1}}$ $\mathrm{H_2SO_4}$, $1\,\mathrm{mmol\,L^{-1}}$ $\mathrm{CuSO_4}$ and $10\,\mu\mathrm{mol\,dm^{-3}}$ $\mathrm{K_2IrCl_6}$ kept at 70 °C. The electrode potential was held at 0.7 V for 5 s, followed by a 2 s hold at 0.34 V. The open circuit potential (OCP) of the electrode was then recorded for 200 s. This procedure of 2 potentials holds and time at OCP was repeated successively 10 times. The electrode was rotated at 1600 rpm.

10 wt% Pd/C

Inks were prepared with $1\,\mathrm{mg\,mL^{-1}}$ Pd/C in DI water and isopropanol (1:1 by volume) and 20 wt% Nafion to solids (5 wt% Nafion 117 Solution, Sigma).

Electrodes were prepared by pipetting 4 aliquotes of $5\,\mu\mathrm{L}$ onto a glassy carbon rotating disc electrode mounted on an inverted rotator [216–218] and allowed to dry in ambient conditions while the electrode rotation rate was slowly increased to 700 rpm. Each droplet was fully dried before the next one was applied. The electrode mass loading was $102\,\mu\mathrm{g\,cm^{-2}}$.

The as-prepared electrode was then cycled between 0.05 V and 0.4 V in $0.5\,\mathrm{mol\,dm^{-3}}$ $\mathrm{H_2SO_4}$ at $50\,\mathrm{mV\,s^{-1}}$ until the voltammogram did not change upon further cycling.

SLRR experiments were conducted at 70 °C in solutions as mentioned previously. A single displacement event was performed by adding $\mathrm{K_2IrCl_6}$ to the electrolyte after forming $\mathrm{Cu_{UPD}}$ by a potential hold at 0.34 V. Multiple displacements was performed as described for the polycrystalline electrode above.

Electrochemical characterization

The as-prepared $\mathrm{IrPd_{poly}}$ and IrPd/C electrodes were rinsed in $0.5\,\mathrm{mol\,dm^{-3}}$ $\mathrm{H_2SO_4}$ and transferred to a cell containing $0.5\,\mathrm{mol\,dm^{-3}}$ $\mathrm{H_2SO_4}$. Voltammograms were obtained in different potential regions, before any Ir-deposits was transformed to IrO_x by potential cycling between 0.05 V and 1.2 V ($\mathrm{IrPd_{poly}}$) or 1.45 V (IrPd/C).

8.2 Results

8.2.1 Polycrystalline palladium

Figure 8.1 shows voltammograms of Pd_{poly} in solutions containing (blue) 0.5 mol dm^{-3} H_2SO_4 at room temperature, and 0.5 mol dm^{-3} H_2SO_4 + 1 mmol dm^{-3} $CuSO_4$ at (orange) room temperature and (green) 70 °C. Potential sweep rate was 50 mV s^{-1}.

In only H_2SO_4 (blue line), the cathodic current increased drastically as the potential became less positive below 0.35 V. This was accompanied by an anodic peak around 0.25 V upon potential sweep reversal. This lower potential region is typically association with the formation of palladium hydride [33, 34, 36–39]. The current between 0.35 V and 0.75 V appear constant with potential, *i.e.* there is only double layer charging.

In all the voltammograms in Figure 8.1, there is an anodic wave starting at about 0.75 V, which we associate with formation of palladium oxides [26–28]. The corresponding cathodic peak around 0.75 V represents reduction of Pd oxides formed in the anodic wave.

With the addition of $CuSO_4$ at room temperature (orange line), the current in the cathodic sweep became more negative as the potential became less positive than 0.6 V. There is a small shoulder in the cathodic wave around 0.35 V. The anodic sweep shows peaks at 0.28 V, 0.38 V, 0.55 V and a shoulder around 0.62 V. We associate these extra features with underpotential deposition of copper, Cu_{UPD} [143, 264].

At 70 °C (green line), the currents related to the Cu_{UPD} reaction changed compared to room temperature. The cathodic current became negative more rapidly as the potential became less positive than 0.6 V. A cathodic peak appeared at 0.45 V. Upon scan reversal, the anodic sweep was quite symmetrical to the cathodic sweep. An anodic peak appeared around 0.47 V.

Figure 8.2 (a) shows the open circuit potential of a Pd_{poly} RDE during each displacement event in the *one-pot* SLRR routine. Each potential transient was preceded by a 5 s potential hold at 0.7 V and 2 s potential hold at 0.34 V. The sequence of 5 s at 0.7 V - 2 s at 0.34 V - and 200 s at open circuit was repeated 10 times consecutively.

Figure 8.2 (b) shows the derivative of the potential in (a) with respect to time, $(\partial E/\partial t)$.

The potential transients in figure 8.2 (a) show the same characteristics as was shown for similar experiments using a Au_{poly} RDE in chapters 6 and 7. The potential initially increased continuously, until it stabilized towards a steady state value around 0.92 V. For the increasing part, the slope $(\partial E/\partial t)$ was initially high, but then decreased before increasing again. The slopes in (b) thus show a single peak that

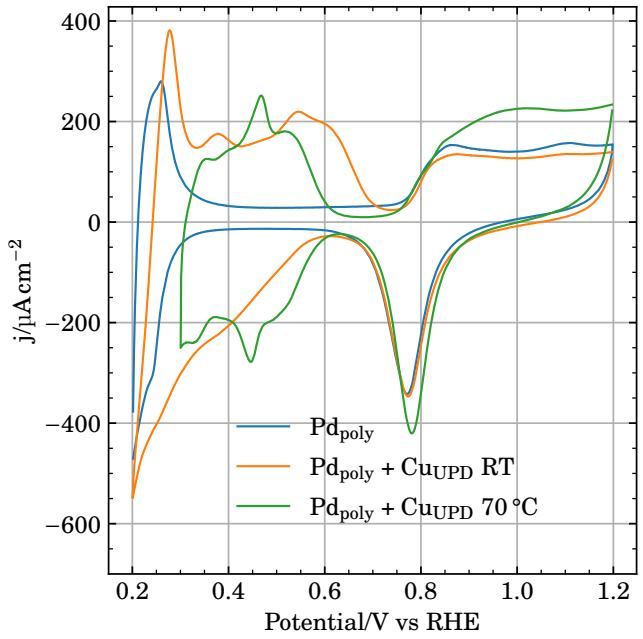

Figure 8.1: Cyclic voltammograms of Pd_{poly} in solutions containing 0.5 mol dm^{-3} H_2SO_4 at room temperature, and 0.5 mol dm^{-3} H_2SO_4 + 1 mmol dm^{-3} $CuSO_4$ at room temperature and 70 °C. Potential sweep rate was 50 mV s^{-1}.

decreases in magnitude, broadens, and is shifted to longer times for each successive displacement event.

Figure 8.3 shows the current (a,b) and charge (c,d) passed at a Pd_{poly} RDE during the potential holds at 0.7 V (a,c) and 0.34 V (b,d) in the *one-pot* SLRR routine. Each line correspond to a (a,c) 5 s potential hold at 0.7 V and a (b,d) 2 s potential hold at 0.34 V *before* each corresponding open circuit potential transient (1-10) in figure 8.2. The insets show the final (total) charge at the end of each potential hold. The dashed black line in the inset show a linear fit to the final charge as a function of potential hold number. The electrode was rotated at 1600 rpm in an electrolyte containing 0.5 mol dm^{-3} H_2SO_4, 1 mmol dm^{-3} $CuSO_4$ and 10 µmol dm^{-3} K_2IrCl_6 kept at 70 °C.

The charge and current passed during the potential holds at 0.7 V was cathodic. Formation of palladium oxides does not commence until 0.75 V. In potential holds 2-10, the potential was stepped to 0.7 V from the open circuit potential around 0.92 V

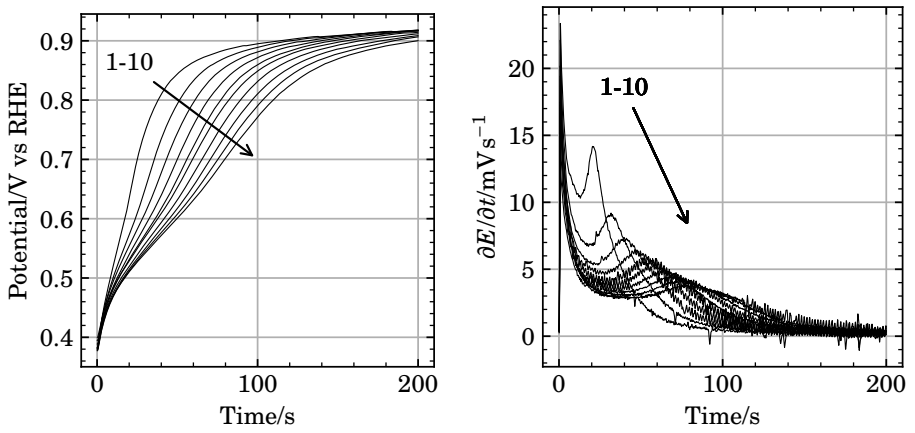

Figure 8.2: (a) 10 open circuit potential transients recorded over 200 s after holding the potential of a Pd_{poly} RDE first at 0.7 V for 5 s and then at 0.34 V for 2 s followed by 200 s at open circuit in a solution containing 0.5 mol dm^{-3} H_2SO_4, 1 mmol dm^{-3} $CuSO_4$ and 10 µmol dm^{-3} K_2IrCl_6 kept at 70 °C. The electrode was rotated at 1600 rpm. The potential holds and time at open circuit was performed successively 10 times. (b) show the derivative of the potential in (a) with respect to time.

(figure 8.2). This correspond to potentials where there are no more Cu_{UPD} left at the surface. Reaction (1.46) proceeds in the cathodic direction at 0.7 V. There appears to be no change in the charge passed with each following displacement event.

At 0.34 V, the currents and the total charge passed was one order of magnitude larger than at 0.7 V. The charge passed also increased linearly with each following displacement event. There was a shoulder in the current transient around 0.2 s that shifted to longer times for each successive displacement event

Figure 8.4 shows voltammograms of a Pd_{poly} and Ir/Pd_{poly} RDE, as prepared above. The electrolyte was 0.5 mol dm^{-3} H_2SO_4 and potential sweep rate was 50 mV s^{-1}. Pd_{poly} show the same features as described previously in figure 8.1. The first cycle in the voltammogram of Ir/Pd_{poly} shows no peaks or waves at potentials above 0.3 V. After 50 potential cycles, an anodic wave and a cathodic peak appeared, both centered around 0.75 V. Compared to Pd_{poly}, the onset of the anodic wave in the voltammogram of Ir/Pd_{poly} appears to be shifted to higher potentials and the cathodic peak is reduced in magnitude.All the voltammograms show a cathodic wave and an anodic peak between 0.2 V and 0.35 V, where the magnitude of the anodic peak

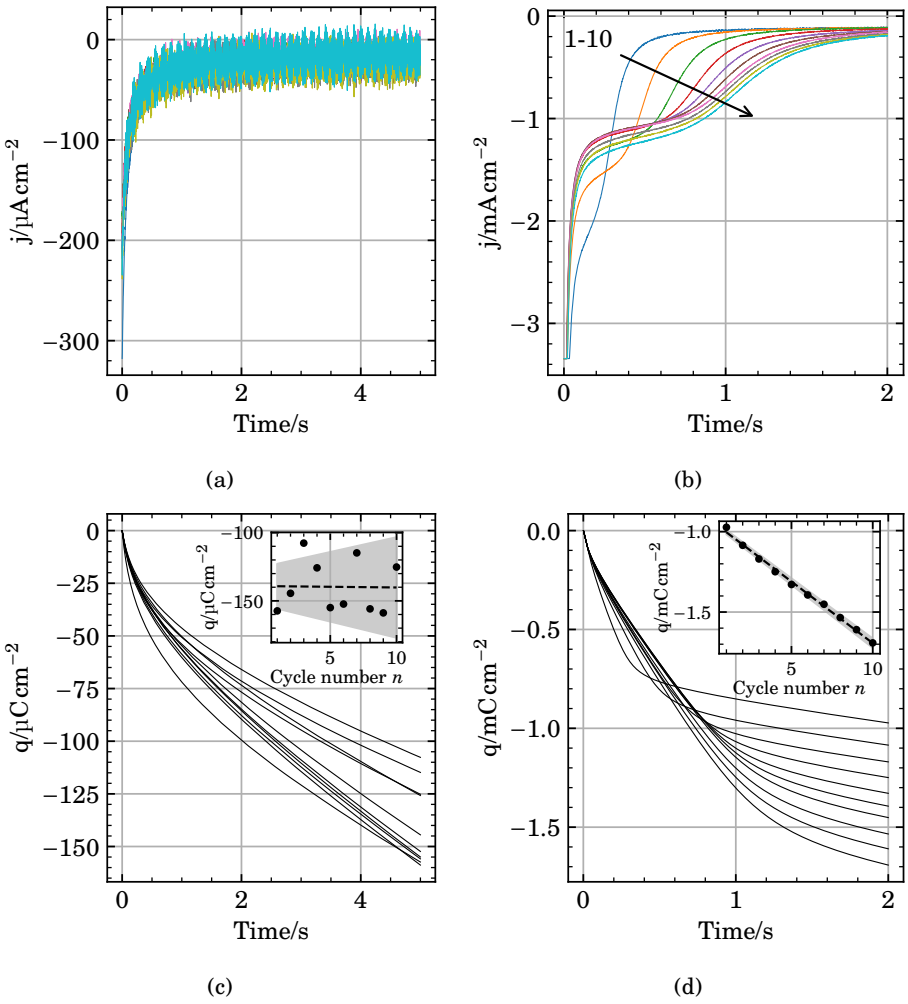

Figure 8.3: Current (a,b) and charge (c,d) passed over time at a Pd_{poly} RDE during 5 s potential holds at 0.7 V (a,c) and during 2 s potential holds at 0.34 V (b,d) in a solution containing 0.5 mol dm^{-3} H_2SO_4, 1 mmol dm^{-3} $CuSO_4$ and 10 μmol dm^{-3} K_2IrCl_6. Temperature was 70 °C and the electrode was rotated at 1600 rpm. The electrode was held at 0.7 V and then and 0.34 V. The open circuit potential of the electrode was measured for 200 s after each potential hold at 0.34 V. The potential holds at 0.7 V and 0.34 V and intermittent time at open circuit was performed successively 10 times. The insets show the final charge at the end of each potential hold.

increases in the order $\mathrm{Ir/Pd_{poly}}(n = 1) < \mathrm{Ir/Pd_{poly}}(n = 50) < \mathrm{Pd_{poly}}$.

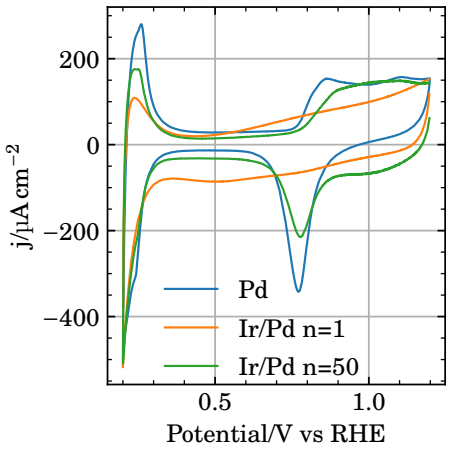

Figure 8.4: Cyclic voltammograms of $\mathrm{Pd_{poly}}$ and $\mathrm{Ir/Pd_{poly}}$ in $0.5\,\mathrm{mol\,dm^{-3}}$ $\mathrm{H_2SO_4}$. Potential sweep rate was $50\,\mathrm{mV\,s^{-1}}$. n=1, and n=50 designate potential cycle number for $\mathrm{Ir/Pd_{poly}}$.

8.2.2 10 wt% Pd/C

Figure 8.5 shows voltammograms of Pd/C in $0.5\,\mathrm{mol\,dm^{-3}}$ $\mathrm{H_2SO_4}$ and $1\,\mathrm{mmol\,dm^{-3}}$ $\mathrm{CuSO_4}$ at 70 °C. In $\mathrm{H_2SO_4}$, the cathodic current becomes more negative with potential below $E < 0.25\,\mathrm{V}$. There is a pair of anodic and cathodic peaks between 0 V and 0.05 V, and a shoulder around 0.2 V in the anodic sweep. We associate these features with formation of palladium hydrides and underpotential deposition of hydrogen [33, 34, 36–39, 113]. The voltammogram shows no noticeable features at potentials higher than 0.25 V. In $\mathrm{H_2SO_4}$ + $\mathrm{CuSO_4}$, a reduction wave appears below 0.5 V with a corresponding oxidation peak between 0.4 V and 0.5 V, which we associate with underpotential deposition of Cu [143, 264].

Single displacement event

Figure 8.6 shows the open circuit potential of a Pd/C electrode during a single displacement event of $\mathrm{Cu_{UPD}}$ by $\mathrm{K_2IrCl_6}$. The electrode was held at 0.34 V for 60 s in $0.5\,\mathrm{mol\,dm^{-3}}$ $\mathrm{H_2SO_4}$ and $1\,\mathrm{mmol\,dm^{-3}}$ $\mathrm{CuSO_4}$ kept at 70 °C while rotating the electrode at 1600 rpm. $\mathrm{K_2IrCl_6}$ was then added so that the final concentration of $\mathrm{K_2IrCl_6}$ was $10\,\mathrm{\mu mol\,dm^{-3}}$. After a few seconds of mixing by the joint action of bubbling of Ar gas through the solution and rotating the electrode, the frit through which the gas

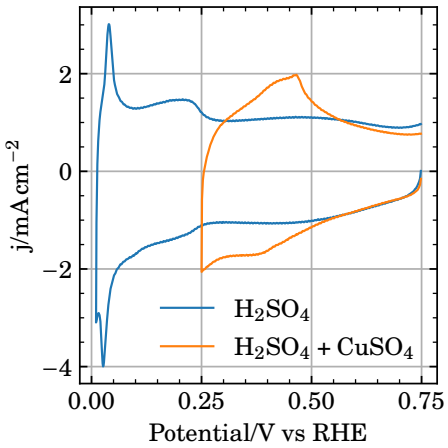

Figure 8.5: Voltammmograms of Pd/C in an electrolyte containing 0.5 mol dm^{-3} H_2SO_4 or 0.5 mol dm^{-3} H_2SO_4 and 1 mmol dm^{-3} $CuSO_4$. The electrolyte was kept at 70 °C and the electrode was rotated at 1600 rpm. Potential sweep rate was 50 mV s^{-1}.

was supplied was lifted out of the electrolyte and kept above it. The electrode rotation was stopped. This resulted in a small dent in the potential transient around $t = 20$ s. The electrode, denoted Ir_1Pd/C, was then kept at open circuit for 450 s, emmersed from the electrolyte, rinsed in 0.5 mol dm^{-3} H_2SO_4 and transferred to a separate cell containing 0.5 mol dm^{-3} H_2SO_4 kept at room temperature. The horizontal lines show the stable open circuit potential of Pd/C and Ir_1Pd/C in 0.5 mol dm^{-3} H_2SO_4 after the transfer and at room temperature. The open circuit potential increased slowly from 0.34 V to about 0.75 V, with no notable features.

Figure 8.7 (a,b) shows cyclic voltammograms of Pd/C and Ir_1Pd/C obtained at 50 mV s^{-1} in 0.5 mol dm^{-3} H_2SO_4. The anodic potential limit was either 0.4 V (a) or 1.45 V (b). Figure 8.7 (a) shows voltammgrams of Pd/C and Ir_1Pd/C between 10 mV and 400 mV. Both voltammograms show a pair of peaks centered around 50 mV, where the peaks are sharper and less separated for Ir_1Pd/C. Pd/C display a pair of peaks around 250 mV, which are not present for Ir_1Pd/C. Figure 8.7 (b) was obtained in a wider potential range. The voltammograms of Pd/C and Ir_1Pd/C both display an anodic wave starting around 0.8 V and a corresponding cathodic peak around 0.65 V. Both voltammograms also show anodic and cathodic features at potentials below 0.3 V, as described previously for (a). An anodic peak appeared on Ir_1/Pd around 0.6 V after 40 cycles. This is usually associated with the carbon support [237]. The corresponding cathodic peak overlaps with the previously mentioned

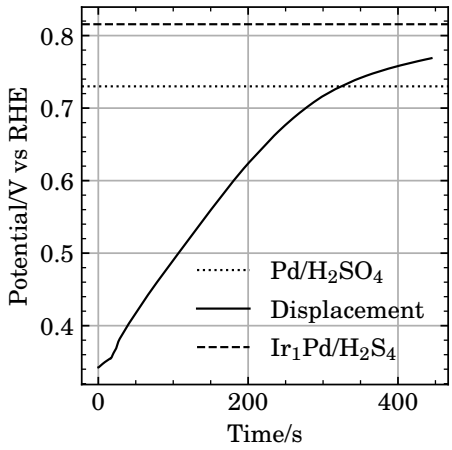

Figure 8.6: Open circuit potential transient of a Pd/C electrode during a single displacement of Cu_{UPD} by K_2IrCl_6. The electrode potential was held at 0.34 V for 60 s prior to the displacement. The electrolyte during the potential hold contained 0.5 mol dm^{-3} H_2SO_4 and 1 mmol dm^{-3} $CuSO_4$. The electrolyte during the displacement also contained 10 µmol dm^{-3} K_2IrCl_6, which was added between $t = 0$ s and $t = 20$ s. The electrolyte was kept at under an Ar(g) atmosphere and at 70 °C. The electrode was kept stagnant. The horizontal lines anodically of 0.7 V and 0.8 V are the open circuit potential for the Pd/C and Ir1Pd/C samples, respectively after transfer to an electrolyte containing 0.5 mol dm^{-3} H_2SO_4 at room temperature.

peak corresponding to reduction of palladium oxide.

3 successive *one-pot* displacements

Figure 8.8 shows the charge (a) and potential transients (b) obtained during 3 successive displacement events using the same *one-pot* method as described earlier for Pd_{poly}. A Pd/C electrode was immersed in a solution containing 0.5 mol dm^{-3} H_2SO_4, 1 mmol dm^{-3} $CuSO_4$ and 10 µmol dm^{-3} K_2IrCl_6 kept at 70 °C at under an Ar (g) atmosphere. The potential was successively kept at 0.7 V for 5 s and 0.34 V for 2 s followed by 900 s at open circuit. This was repeated three times. The electrode was rotated at 1600 rpm. Figure 8.8a (a) shows the charge passed at 0.34 V, where the inset shows the final charge at $t = 2$ s as a function of number of potential pulses. Figure 8.8 (b) shows the open circuit potential transients obtained after each potential holds at 0.34 V.

Figure 8.9 shows cyclic voltammograms of Pd/C, Ir_1Pd/C, Ir_2Pd/C and Ir_3Pd/C in

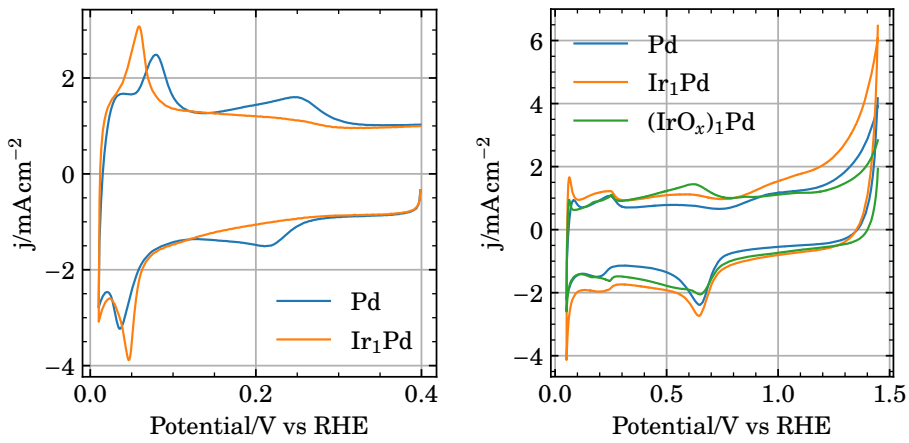

Figure 8.7: Cyclic voltammograms of Pd/C and Ir_1Pd/C. (a) was obtained before (b), where $(IrO_x)_1Pd$/C is Ir_1d/C after 50 potential cycles. Voltammograms obtained at room temperature in 0.5 mol dm^{-3} H_2SO_4 at 50 mV s^{-1}.

0.5 mol dm^{-3} H_2SO_4 in a narrow (a) and wide (d,c) potential region. Some electrode material appear to have been physically lost the first time the electrode was moved between electrolytes, as the double layer region ($E > 0.3$ V) of Ir_1Pd/C, Ir_2Pd/C and Ir_3Pd/C in (a) is lower in magnitude than for Pd/C. The double layer current was not decreased in figure 8.7 (and other similar voltammograms in chapter 9), although the Pd/C electrode was prepared using the same electrode, method and materials. We therefore assume the decrease in double layer current was due to loss of active material. Figure 8.9 (b) therefore shows the same voltammograms as figure 8.9a, but normalized to the anodic currents at $E = 0.35$ V for easier comparison.

The voltammogram of Pd/C in figures 8.9a and 8.9b shows a pair of peaks centered around 0.25 V which is not present for Ir_nPd/C. The voltammograms of Ir_nPd/C show a pair of peaks around 0.1 V - 0.15 V which appears to grow with each displacement event. The pair of anodic peaks between 0 V and 0.1 V shown by Pd/C are replaced by a single peak around 0.05 V for Ir_nPd/C.

Figure 8.9 (d, c) shows voltammograms similar to (a), but with the anodic potential limit increased from 0.4 V to 1.45 V. Potential cycling between 0.05 V and 1.45 V in 0.5 mol dm^{-3} H_2SO_4 is a destructive test for Pd nanoparticles, as some Pd is dissolved for each potential cycle [26, 28, 265–270]. This is clear from the wide voltammogram of Pd/C, figure 8.9 (d). The peaks below 0.4 V related to formation and oxidation of

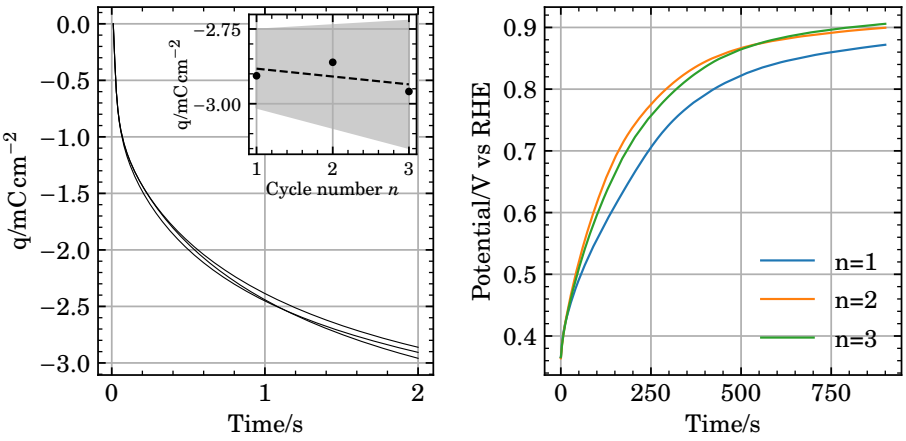

(a) (b)

Figure 8.8: Charge (a) and open circuit potential transients (b) obtained during 3 successive displacement events using the *one-pot* SLRR routine with a Pd/C working electrode. A Pd/C electrode was immersed in a solution containing 0.5 mol dm^{-3} H_2SO_4, 1 mmol dm^{-3} $CuSO_4$ and 10 µmol dm^{-3} K_2IrCl_6 kept at 70 °C at under an Ar (g) atmosphere. The potential was successively kept at 0.7 V for 5 s and 0.34 V for 2 s followed by 900 s at open circuit. This was repeated three times. The electrode was rotated at 1600 rpm.

H_{UPD} and PdH_x are lost after 20 potential cycles. The Pd oxidation wave above 0.6 V and reduction peak at 0.65 V also disappeared with potential cycling. Only a pair of peaks centered around 0.6 V associated with the carbon support was left [237].

In the voltammogram of Ir_3Pd/C, figure 8.9 (c), the Pd reduction peak at 0.65 V is never present, but an anodic H_{UPD} peak is clearly seen at potentials lower than 0.3 V. An additional pair of peaks around 1 V can bee seen after 50 potential cycles. This pair of peak peaks was not seen for the pure Pd/C. Similarly to (a,b), the H_{UPD} area, $E < 0.4$ V, is characterized by peaks around 0.25 V and 0.05 V for Pd/C and only 0.05 V for Ir_3Pd/C.

8.3 Discussion

The *one-pot* SLRR procedure appears to have successfully modified a polycrystalline Pd electrode with Ir. The charge-time curves and potential transients in figures 8.2 and 8.3 bear a strong resemblance to what has been shown for almost identical

experiments on a polycrystalline Au electrode in chapters 6 and 7. The potential transients in figure 8.2 (a) goes towards a potential where solutions of K_2IrCl_6 are not reduced to metallic iridium [161, 176, 177, 180, 182].

The Ir deposit obtained on Pd_{poly} likely covered most of the Pd surface. The first voltammogram of Ir/Pd_{poly} in figure 8.4 did not show any anodic waves or cathodic peaks around 0.75 V related to formation and reduction of palladium oxides. After potential cycling, the Ir deposit is transformed to IrO_x/AIROF which usually formes a cracked-mud like structure [69, 73, 74]. This would expose the underlying Pd substrate to the electrolyte. This is consistent with the emergence of an anodic wave and a cathodic peak at 0.75 V after potential cycling. IrO_x/AIROF is also a proton conductor. The magnitude of the anodic peak around 0.25 V for Ir/Pd_{poly} increased after potential cycling. This is consistent with more of the underlying Pd substrate being exposed to protons.

Cu_{UPD} appears to grow onto Ir. The open circuit potential transients obtained from the *one-pot* SLRR routine with the polycrystalline palladium electrode are consistent with what we observed with seemingly identical experiments in chapters 6 and 7 using a Au_{poly} working electrode. A more detailed discussion can be found in chapter 7. Briefly, the potential in the open circuit potential transients in figure 8.2 shifting to longer times for each successive displacement event and the charge passed during the potential hold at 0.34 V increasing for each successive displacement event is consistent with Cu_{UPD} growing onto a growing Ir deposit.

The following points are consistent with galvanic displacement of Cu_{UPD} by $IrCl_6^{2}$(aq); *(i)* The peaks of $(\partial E/\partial t)$ in figure 8.2 (b) shifts to longer times with a decreased magnitude for each displacement event. *(ii)* The potential in the transients in figure 8.2 (a) increase more slowly for each displacement event. *(iii)* The potential in figure 8.2 (a) corresponding to the time of each peak in figure 8.2 (b) is consistent with the onset of Cu_{UPD} formation in figure 8.1. Suppression of the anodic wave- and cathodic peak related to formation and reduction of Pd oxide around 0.7 V in figure 8.4 is as expected for a palladium surface covered with Ir [113]. Further potential cycling in H_2SO_4 dissolves- and re-deposits some Pd for each cycle [26, 28, 265–270]. This effectively brings the Ir sub-surface while the Pd oxide features re-emerges [113].

The Pd/C catalyst was successfully modified with Ir by the SLRR routine. The voltammogram of Ir_3Pd/C in figure 8.9c contains a single peak related to H_{UPD} around 0.1 V even in the absence of peaks related to Pd above 0.5 V. This single peak is also different from the pair of peaks shown by Pd/C in figure 8.9d. This indicates that metallic Ir was present at the surface. This is consistent with a pair of peak emerging around 1 V after potential cycling. This is consistent with IrO_x in H_2SO_4 and our previous work on Ir deposition onto Au by SLRR of Cu_{UPD} in chapters 6

and 7 [48, 48, 70, 72, 73, 76, 77, 220–228]. The open circuit potential of Ir_1Pd/H_2SO_4 in H_2SO_4 in figure 8.6 was almost 100 mV higher than Pd/C at room temperature in H_2SO_4. This is consistent with the standard reduction potential of Ir^{3+}/Ir being higher than Pd^{2+}/Pd, and is thus consistent with Ir present at the surface [19].

8.4 Conclusions

It appears that the previously *one-pot* SLRR routine can be utilized to modify Pd nanoparticles with Ir. This is not of direct importance for water electrolysis, as a Pd/Ir core/shell catalyst would not be long-term stable due to Ir dissolution exposing the Pd core. This is important because it should allow for *in-situ* and *ex-situ* XAS and EXAFS studies of the galvanic displacement reaction between Cu_{UPD} and solutions of K_2IrCl_6 and other Ir-precursors.

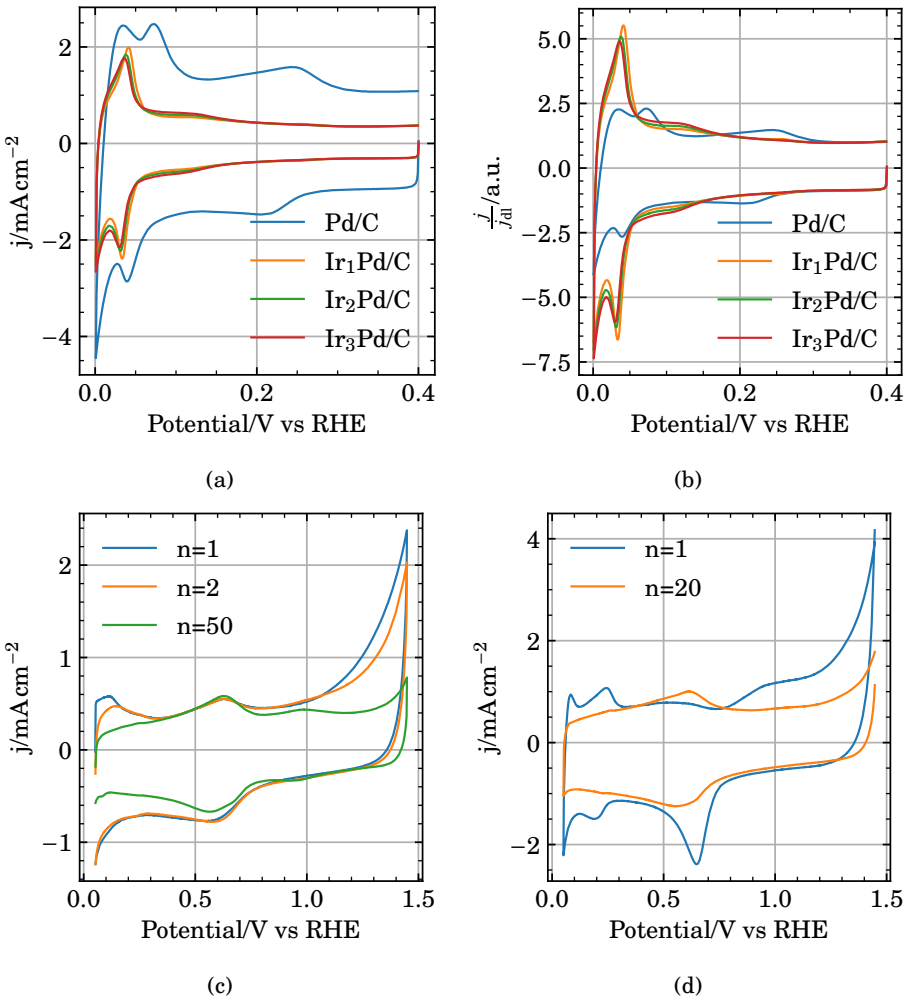

Figure 8.9: Cyclic voltammograms of (a, b) Pd/C, Ir_1Pd/C, Ir_2Pd/C and Ir_3Pd/C, (c) of Ir_3Pd/C and (d) of Pd/C where n designate potential cycle number. Potential sweep rate was 50 mV s^{-1} and the electrolyte was 0.5 mol dm^{-3} H_2SO_4.

Chapter 9

Ir deposition onto Pd by galvanic displacement of PdH_x

9.1 Introduction

Replacing the underpotentially deposited metal (Cu, Pb, etc) in the *one-pot* SLRR method [103,106,107,134,137,144] with underpotentially deposited hydrogen, H_{UPD}, provides one distinct advantage; The preparation of noble metal films free of mediator metal impurities [102,144].

Palladium hydride (PdH_x) has been previously used both as an electron source for Pb_{UPD} formation [104] and as a reduction agent directly [144,151,152].

Ambrozik and Dimitrov [104] used a palladium hydride (PdH_x) electrode *in liu* of a potentiostat for Pt deposition on Au by surface limited redox replacement of Pb. In this work, the PdH_x phase was not the reduction agent directly, but rather served as an electron source to form Pb_{UPD} on Au.

Achari, Ambrozik and Dimitrov [144] noted that during displacement of H_{UPD} by Pd on Au and Pd_{nML}, both adsorbed *and absorbed* H_{UPD} participated in the displacement reaction when $n > 2$. In other words; Pd growth by H_{UPD} displacement was restricted by the amount of hydrogen on the surface of H_{UPD}/Au and H_{UPD}/Pd_{nML}/Au when $n = 1,2$. During H_{UPD} formation on H_{UPD}/Pd_{nML}/Au with $n > 2$, a PdH_x phase was formed which provided additional hydrogen to act as a reduction agent for the growing Pd film.

Zolfaghari and Conway [151] reported electroless deposition of Pt onto a PdH_x reference electrode by galvanic displacement of PdH_x. Pt dissolved as $PtCl_6^{2-}$ and $PtCl_4^{2-}$ in a Cl^-(aq) containing electrolyte during voltammetric cycling had reacted

with the PdH_x reference electrode and covered the surface in Pt.

Cappillino, Robinson and coworkers [152] introduced a facile scalable approach to atomic layer deposition much similar to surface limited redox replacement. PdH_α was formed by bubbling dilute H_2(g) in N_2(g) through a suspension of Pd/C. Subsequent addition of Rh- or Pt-salt allowed the α-hydride phase to serve as the reduction agent for a growing adlayer. This method carries two distinct advantages over the SLRR method. *(i)* The amount of adlayer obtained in a single displacement event is not limited solely by the stoichiometry of the displacement reaction, which is a limiting factor during Ir(IV) plating by Cu displacement. *(ii)* Formation of the material to be oxidized, *i.e.* the α-hydride phase, is a more facile procedure as it only requires a H_2(g) stream.

Palladium hydride can be formed both physically [32–35] and electrochemically [33, 34, 36–39] at room temperature. The α phase, which is actually a solid solution, forms at low H_2(g) partial pressures before a phase transition to the hydride β phase takes place. The minimum and maximum values of α and β in PdH_α and PdH_β is particle size dependent [34, 37]. Electrochemically, the α phase is formed at $< 300\,\mathrm{mV}$. The PdH_β forms at potential less positive than PdH_α, right before the onset of hydrogen evolution, around 40 mV [36–39].

A simple scheme describing formation of palladium hydride is given in reactions (9.1) and (9.2) [39], although the actual mechanisms involved in the formation of the α- and $\beta-$ phases are more complex [40].

$$H^+(aq) + Pd_{surface} + e^- \rightleftharpoons PdH_{ads} \tag{9.1}$$

$$PdH_{ads} + Pd_{subsurface} \rightleftharpoons Pd_{surface}\,PdH_{abs} \tag{9.2}$$

A typical voltammogram of polycrystalline Pd in H_2SO_4 is given in figure 9.1. It is visually very similar to that of Pt above 0.4 V. Palladium simultaneously starts to form oxides and dissolve around 0.75 V in the anodic scan, and is reduced in the cathodic scan, where the cathodic peak potential depends on the upper potential limit used in the voltammogram [27, 28]. Below 0.4 V, hydrogen is adsorbed and absorbed as H_{UPD} and the aforementioned PdH_x phases.

Reactions between $IrCl_6^{(z-6)}$(aq) and adsorbed hydrogen, H_{ads}, or Cu_{UPD} is given in reactions (9.3) and (9.4), where $z = 3$ or $z = 4$.

$$IrCl_6^{(z-6)}(aq) + zH_{ads} \rightleftharpoons Ir(s) + zH^+(aq) + 6\,Cl^-(aq) \tag{9.3}$$

$$IrCl_6^{(z-6)}(aq) + \frac{z}{2}Cu_{UPD} \rightleftharpoons Ir(s) + \frac{z}{2}Cu^{2+}(aq) + 6\,Cl^-(aq) \tag{9.4}$$

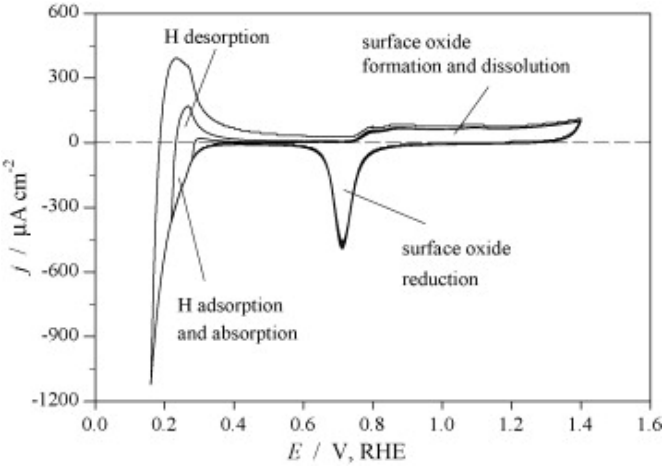

Figure 9.1: Typical voltammograms of a polycrystalline palladium disc electrode in $0.5\,\mathrm{mol\,dm^{-3}}$ H_2SO_4 at 298 K recorded at $50\,\mathrm{mV\,s^{-1}}$. Reprinted from [26] with permission.

We can reasonably expect Ir-chloro complexes such as those formed in aqueous solutions of K_2IrCl_6 and K_3IrCl_6 to be reduced by the hydrogen in PdH_x at temperatures lower than 70 °C. H_{UPD} and PdH_x is stable at potentials less positive than Cu_{UPD}, $< 0.4\,\mathrm{V}$, hence the electrochemical driving force of reaction (9.3) is expected to be stronger than reaction (9.4). This should allow reaction (9.3) to proceed at a lower temperature than reaction (9.4). Ideally at room temperature.

The use of PdH_x as a reduction agent carries a second advantage over Cu_{UPD}; It may be possible to achieve full coverage of Ir on the Pd substrate. At most, a 2/3 coverage can be achieved in a single displacement event of Cu_{UPD} by Ir(III) [113], as is obvious from the stoichiometry in reaction (9.4) when $z = 3$. Charge storage in PdH_x is not restricted to only the surface, and the Ir coverage will vary with x in PdH_x. The electroless procedure introduced by Cappillino, Robinson and coworkers [152] is simple and scaleable, and thus Ir deposition by displacement of hydrogen absorbed in palladium should be explored.

9.2 Experimental

Materials and equipment

All electrochemical experiments were performed in glass cells, one equipped with a water jacket. The working electrode was a glassy carbon rotating disc electrode

(GC RDE) (15 mm outer diameter, 5 mm internal diameter, PEEK shroud; Pine) or a change-disc electrode with a palladium disc insert (15 mm outer diameter, 5 mm disc diameter, PEEK shroud; Pine). The electrodes were polished to a mirror finish with successively 0.3 µm and 0.05 µm alumina suspensions (Allied) on a microcloth (Buehler) and rinsed using DI water (Millipore, 18.2 MΩ@25 °C) prior to each experiment. The electrodes were mounted on a Pine Classic RDE/RRDE Shaft (15 mm outer diameter PEEK shroud, stainless steel rod) attached to a Pine MSR rotator. The potentiostat used was a Gamry reference 600. The ohmic drop was determined by the built in utility, of which 85% was compensated through positive feedback compensation. The counter- and reference electrodes were Pt-foil and a reversible hydrogen electrode (RHE), respectively. The counter electrode was separated from the main electrolyte by a porous glass frit. All potentials reported are versus RHE. The electrolytes were purged using Ar(g) for at least 30 min prior to each experiment and kept under an Ar(g) atmosphere for the duration of the experiments. The electrolyte temperature was kept at either room temperature (23 ± 1) °C or (50 ± 1) °C by circulating water from a water bath through the water jacket.

Polycrystalline Pd RDE

A Pd(poly) RDE (Pd_{poly}) was prepared as described above. The potential of the electrode was swept between 0.3 V and 1.45 V in 0.5 mol dm^{-3} H_2SO_4 at room temperature until the voltammogram did not change significantly from one cycle to the next. PdH_x was then formed either by a potential hold ar −0.1 V or a slow potential scan from 0.7 to −0.1 V. After formation of PdH_x, the electrode was quickly transferred to a separate cell containing 0.5 mol dm^{-3} H_2SO_4 and 10 µmol dm^{-3} K_2IrCl_6 kept at either room temperature or 50 °C. The electrode was rotated at 1600 rpm while the open circuit potential was measured. The electrode was then rinsed in DI water and transferred back to a cell containing H_2SO_4, where the PdH_x phase was removed by a long potential hold at 0.5 V. The $IrPd_{poly}$ deposits was then transformed to IrO_xPd_{poly} by potential cycling between 0.3 V and 1.45 V in 0.5 mol dm^{-3} H_2SO_4, as described later.

The surface of the Pd_{poly} working electrode was imaged using a Hitatchi S-3400N scanning electron microscope equipped with an Oxford instruments Aztec EDS system.

Carbon supported palladium catalysts

Two different sources of Pd supported on carbon was used. Pd/C (10 wt% Pd on activated carbon, Alfa Aesar) and Pd/KB (40 wt% Pd on carbon Ketjenblack 300. Prepared by Dr. Jørgen Svendby in a different project).

Inks were prepared using 1 mg mL^{-1} Pd/C or Pd/KB DI water and isopropanol (1:1 by volume) and 20 wt% Nafion to solids (5 wt% Nafion 117 Solution, Sigma).

2 (Pd/KB) or 4 (Pd/C) aliquotes of 5 µL was pipetted onto a glassy carbon rotating disc electrode mounted on an inverted rotator [216–218] and allowed to dry in ambient conditions while the electrode rotation rate was slowly increased to 500 rpm. The electrode mass loading was 51 µg cm^{-2} (Pd/KB) or 102 µg cm^{-2} (Pd/C).

The as-prepared electrode was then cycled between 0.01 V (Pd/C) or 0.05 V (Pd/KB) and 0.4 V in 0.5 mol dm^{-3} H_2SO_4 at 50 mV s^{-1} until the voltammogram did not change upon further cycling.

PdH_x was formed with a potential sweep from 0.4 V to −0.1 V at 5 mV s^{-1} while rotating the electrode at 1600 rpm.

The electrode was then quickly transferred to a separate cell containing 0.5 mol dm^{-3} H_2SO_4 and 10 µmol dm^{-3} K_2IrCl_6 kept at room temperature or 50 °C, where the open circuit potential was measured while rotating the electrode at 1600 rpm.

When the open circuit potential had increased to *ca* 0.72 V, the electrode was emmersed from the solution, rinsed in 0.5 mol dm^{-3} H_2SO_4 and transferred back to the cell containing only H_2SO_4.

A voltammogram in the double-layer and PdH_x region, 0.01 V (Pd/C) or 0.05 V (Pd/KB) to 0.4 V, was then obtained at 50 mV s^{-1}.

This procedure of PdH_x formation and displacement with K_2IrCl_6(aq) followed up by a voltammogram of the PdH_x region was repeated five times.

Charge-potential curves of Pd/C and Ir_5Pd/C were obtained by integrating the anodic charge of voltammograms performed at 5 mV s^{-1} from 0.4 V with the cathodic limit being varied from 0.35 V to 0.01 V in −10 mV steps.

Transformation to IrO_x

The final $IrPd_{poly}$, Ir_5Pd/C and Ir_5Pd/KB deposits were transformed to IrO_x/Pd by potential cycling between 0.3 V (polycrystalline Pd) or 0.05 V (Pd/C and Pd/KB) and 1.45 V 0.5 mol dm^{-3} H_2SO_4 at 50 mV s^{-1} until there was no apparent changes from one voltammogram to the next. The samples were then named IrO_xPd_{poly} IrO_xPd/C and IrO_xPd/KB.

The amount of electrochemically available IrO_x was evaluated from voltammograms obtained at different potential sweep rates, 5 mV s^{-1} through 500 mV s^{-1} in 0.5 mol dm^{-3} H_2SO_4 after transformation to IrO_x using a method outlined previously in section 2.2 [212]. Briefly, the anodic charge between 0.4 V and 1.4 V in voltammograms obtained at different potential sweep rates was extrapolated to zero and

infinite potential sweep rate in order to estimate the total amount and surface area of IrO_x.

9.3 Results

Polycrystalline palladium disc electrode

Figure 9.2 show the potential of a polycrystalline PdH_x electrode rotated at 1600 rpm in a solution containing H_2SO_4(aq) + K_2IrCl_6(aq) at room temperature. PdH_x had been formed by a 5 min potential hold at −0.1 V in H_2SO_4. After 3.5 h, the electrode was rinsed in DI water, transferred to a different cell containing H_2SO_4 only, and the Ir deposit was transformed to IrO_x by potential cycling as decribed previously. The hydride phase was recharged as before and the electrode was again left in H_2SO_4(aq) + K_2IrCl_6(aq) for an additional ≈ 15 h. The electrode was then emmersed from the solution, rinsed in DI water and transferred to a different cell containing H_2SO_4 only where the Ir deposit was transformed to IrO_x by potential cycling as decribed previously. The Ir deposits obtained after 3.5 h and 15 h are labelled $IrPd_{poly}$:3 and $IrPd_{poly}$:15, respectively. After transformation to IrO_x by potential cycling, the electrodes are labelled IrO_xPd_{poly}:3 and IrO_xPd_{poly}:15

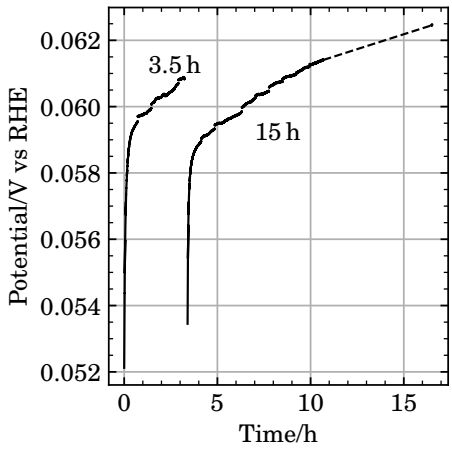

Figure 9.2: Open circuit potential of a polycrystalline PdH_x immersed in a solution of 0.5 mol dm^{-3} H_2SO_4 and 10 µmol dm^{-3} K_2IrCl_6 at room temperature ((23 ± 1) °C). The electrode was rotated at 1600 rpm.

Figure 9.3 shows voltammograms of Pd_{poly}, IrO_xPd_{poly}:3 and IrO_xPd_{poly}:15 at 50 mV s^{-1} in 0.5 mol dm^{-3} H_2SO_4. The voltammogram of Pd_{poly} exhibit a large reduction peak

at 0.7 V, and an oxidation wave starting at 0.7 V. This corresponds to formation- and reduction of palladium oxides [26–28]. After 3.5 h of displacement, the voltammogram of IrO_xPd_{poly}:3 appear as that of Pd_{poly}, except a small ill-defined wide cathodic peak around 0.9 V, but with no clear corresponding anodic peak. The surface area appear to have increased, as the overall volume of the voltammogram increased, but the size of the palladium reduction peak appear to be approximately the same as for Pd_{poly}. After 15 h of displacement, a pair of peaks around 0.9 V appeared in the voltammogram of IrO_xPd_{poly}:15, and the Pd reduction peak was reduced in magnitude. This pair of peaks around 0.9 V-1 V are typical for deposits of Ir transformed to IrO_x by potential cycling in H_2SO_4, and have been shown numerous times previously in chapters 3 and 5 to 8 [48, 48, 70, 72, 73, 76, 77, 220–228].

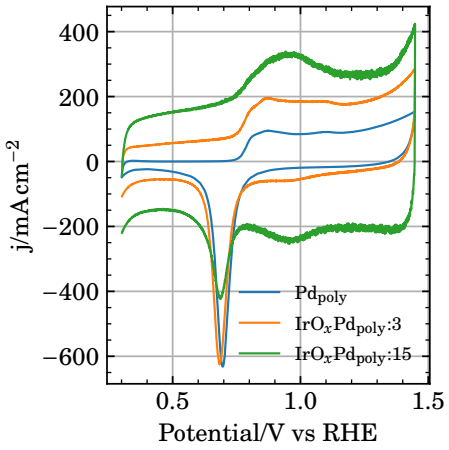

Figure 9.3: Cyclic voltammograms of a Pd(poly) RDE before and after immersion into 0.5 mol dm^{-3} H_2SO_4 + 10 µmol dm^{-3} K_2IrCl_6 for 3.5 h and an additional 15 h at room temperature, (23 ± 1) °C, while rotating the electrode at 1600 rpm. The voltammograms were obtained at 50 mV s^{-1} in 0.5 mol dm^{-3} H_2SO_4 after transformation of any Ir deposits to IrO_x by potential cycling.

Figure 9.4 shows the potential of a polycrystalline PdH_x electode immersed in a solution containing 0.5 mol dm^{-3} H_2SO_4(aq) + 10 µmol dm^{-3} K_2IrCl_6(aq) at 50 °C for 1 h. The electrode was rotated at 1600 rpm. PdH_x had been formed by a 5 mV s^{-1} potential scan from 0.7 V to −0.1 V in 0.5 mol dm^{-3} H_2SO_4, rotating the electrode at 1600 rpm. The resulting electrode is labelled $IrPd_{poly}$:50 before and IrO_xPd_{poly}:50 after transformation to IrO_x by potential cycling in H_2SO_4, as outlined previously.

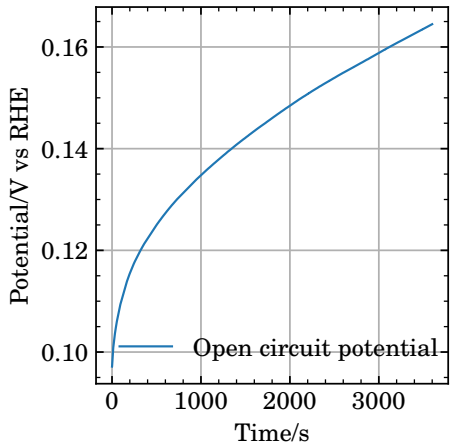

Figure 9.4: Open circuit potential of a polycrystalline PdH_x electrode immersed in a solution of 0.5 mol dm^{-3} H_2SO_4 and 10 µmol dm^{-3} K_2IrCl_6 at 50 °C. The electrode was rotated at 1600 rpm.

Figure 9.5 shows voltammograms Pd_{poly} and IrO_xPd_{poly}:50. Voltammograms shown were obtained in 0.5 mol dm^{-3} H_2SO_4 at 50 mV s^{-1} after transforming the obtained iridium deposit to iridium oxide by potential cycling until the voltammogram did not change significantly between cycles. At 0.7 V, there is a cathodic peak present in both voltammograms. This corresponds to reduction of Pd oxidized at potentials above 0.7 V and appear to be of the same magnitude in both voltammograms. Pd_{poly} also show an oxidation wave starting around 0.7 V. IrO_xPd_{poly}:50 show a pair of wide peaks around 0.95 V. This pair of peaks is typical for AIROF in H_2SO_4 [48, 48, 70, 72, 73, 76, 77, 220–228]. The capacitance of IrO_xPd_{poly}:50 appear to be much larger than Pd_{poly}.

Figure 9.6 displays SEM micrographs of $IrPd_{poly}$:50 before (a) and after (b) transformation to IrO_x. $IrPd_{poly}$:50 was covered in a contiguous layer of Ir, comprised of smaller particles (more images in figure F.2). It does not appear as a dense, protective film, but rather as particles that have grown homogeneously across the surface. After transformation to IrO_x, the surface had a cracked-mud like structure, typical for AIROF [73, 74].

The total amount of electrochemically active IrO_x in IrO_xPd_{poly}:50, figures 9.5 and 9.6, was estimated from the voltammograms in figure F.1 by the method outlined earlier[ardizzone] [212]. The total, surface bound and inner charge was determined to as $q_t = 17.9\,\mathrm{mC\,cm^{-2}}$, $q_s = 14.5\,\mathrm{mC\,cm^{-2}}$ and $q_i = 3.5\,\mathrm{mC\,cm^{-2}}$. This gives a frac-

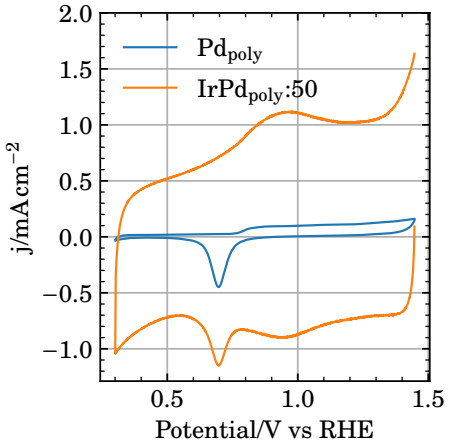

Figure 9.5: Cyclic voltammogram of Pd_{poly} and $IrPd_{poly}$:50 obtained at 50 mV s^{-1} in 0.5 mol dm^{-3} H_2SO_4. The voltammograms were obtained after potential cycling until the voltammogram did not change significantly upon further cycling. $IrPd_{poly}$:50 was prepared by charging Pd_{poly} with hydrogen, PdH_x, using a 5 mV s^{-1} potential scan from 0.7 V to −0.1 volt in 0.5 mol dm^{-3} H_2SO_4 and an electrode rotation rate of 1600 rpm. The charged PdH_x electrode was then immersed at open circuit in 0.5 mol dm^{-3} H_2SO_4(aq) + 10 µmol dm^{-3} K_2IrCl_6(aq) at 50 °C for 1 h while rotating at 1600 rpm.

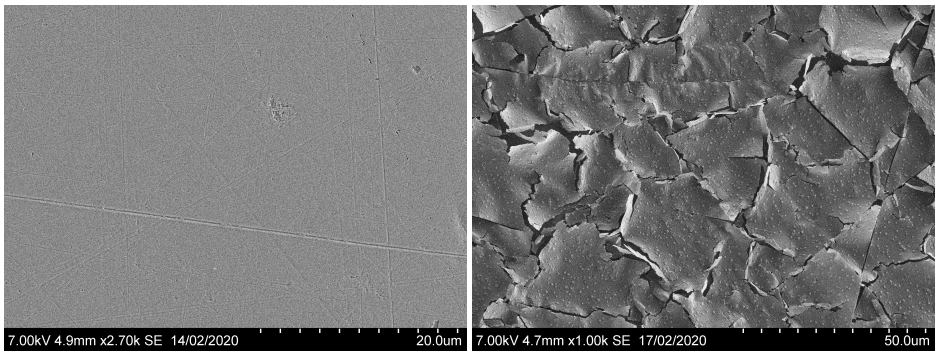

(a) (b)

Figure 9.6: SEM images of $IrPd_{poly}$:50 before (a) and after (b) transformation to IrO_x.

tion of iridium atoms in some sense close the surface of 0.81. Taking the thickness of an AIROF film to be $14\,\mathrm{nm\,mC^{-1}\,cm^2}$ [74], this corresponds to a thickness of 251.3 nm for our film.

Carbon suppported palladium

Figure 9.7 displays the current on (a) Ir_nPd/C and (b) Ir_nPd/KB during $5\,\mathrm{mV\,s^{-1}}$ linear sweeps from 0.4 V to −0.1 V in $0.5\,\mathrm{mol\,dm^{-3}}$ H_2SO_4. The working electrode was rotated at 1600 rpm. Large H_2(g) bubbles was observed at the working electrode at negative potentials. The HER+PdH_x current increased after each displacement event with iridium, indicative of modification of the surface. This is consistent with the higher activity towards HER of iridium to that of palladium [271].

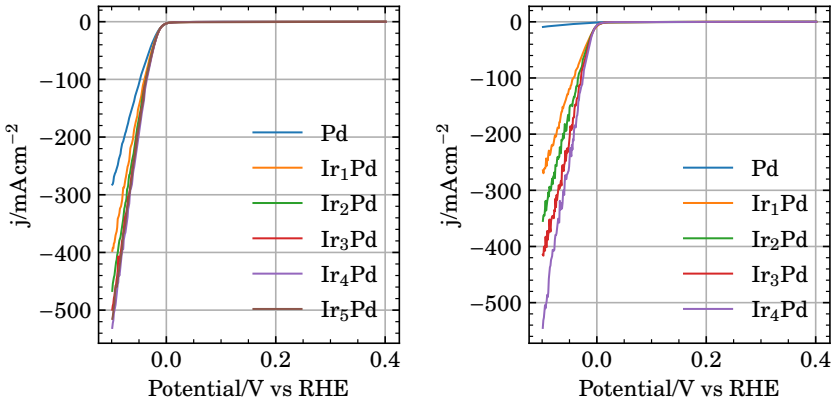

Figure 9.7: $5\,\mathrm{mV\,s^{-1}}$ linear sweeps from 0.4 V to −0.1 V in $0.5\,\mathrm{mol\,dm^{-3}}$ H_2SO_4. Working electrode was a glassy carbon rotating disc electrode with a thin film of (a) Ir_nPd/C or (b) Ir_nPd/KB rotated at 1600 rpm.

figure 9.8 displays voltammograms of the H-UPD and PdH_x region of (a) Ir_nPd/C and (b) Ir_nPd/KB working electrodes after each successive displacement event at 50 °C. Voltammograms were obtained in $0.5\,\mathrm{mol\,dm^{-3}}$ H_2SO_4 at $50\,\mathrm{mV\,s^{-1}}$.

The oxidation peaks around 50 mV on Ir_nPd/C (a) was shifted to less positive potentials after the first displacement event. This potential shift is consistent with submonolayers of Ir on Pd nanoparticles [113]. The potential of the corresponding reduction peak remained constant at *ca* 0.05 V. A pair of reduction- and oxidation waves appeared at *ca* 0.1 V and increased in magnitude for each displacement. The

PdH_α peak at *ca* 0.25 V was reduced in magnitude after the first displacement event and remained constant thereafter.

The PdH_α peak at *ca* 0.25 V on Ir_nPd/KB (b) was reduced in magnitude after the first displacement event and remained constant thereafter. The cathodic and anodic waves at potentials below 0.2 V increased in magnitude for each displacement event.

Figure 9.9 shows the anodic charge of the H-UPD/PdH_x-region, 0.01 V to 0.4 V, as a function of the cathodic potential limit in voltammograms of Pd/C and Ir_5Pd/C in figure F.6. The charge was obtained by integrating the anodic part of the voltammograms and removing the double layer capacitance between 0.35 V and 0.4 V. The voltammograms were obtained as the ones in figure 9.8 above, but with the cathodic limit being made more negative by steps of −10 mV for each voltammogram, starting at 350 mV and ending at 10 mV. The anodic limit was always 400 mV. The charge-potential curves appear identical at potentials positive of 250 mV. Between 0.12 V and 0.25 V, less hydrogen appear to adsorb+absorb onto Ir_5Pd/C compared to Pd/C. At potentials negative of 0.12 V, more hydrogen adsorption+absorption appear to be enhanced on Ir_5Pd/C compared to Pd/C. The right axis indicates the fraction of hydrogen- to palladium atoms, based on the electrode mass loading and the adsorption+absorption charge.

Figure 9.10 displays voltammograms of (a) Pd/C and Ir_5Pd/C, and Pd/KB and (b) Ir_5Pd/C obtained at 50 mV s^{-1} in 0.5 mol dm^{-3} H_2SO_4. Ir_5Pd/C and Ir_5Pd/KB was transformed to $(IrO_x)_5$Pd/C and $(IrO_x)_5$Pd/KB by 20 potential cycles between 0.05 V and 1.45 V. This is evident from the pair of peaks centered at *ca* 0.95 V, similar to those on the iridium-modified polycrystalline palladium electrode in figure 9.5. Modification of the surface is also indicated by the increased currents in the H-UPD region below 0.3 V. The Pd-reduction peak around 0.65 V in figure 9.10 (a) was shifted to slightly less positive potentials after modifying the surface with iridium. Upon potential cycling of Ir_5Pd, the palladium reduction peak in figure 9.10 (a) disappeared. We associate the broad peaks that emerged around 0.6 V with the carbon support [237]. The palladium reduction peak in figure 9.10 (b) increased somewhat in magnitude after the transformation of Ir_5Pd/KB to $(IrO_x)_5$Pd/KB, and the voltammogram appear as that of Ir_5Pd/KB with the additional IrO_x peaks around 0.95 V.

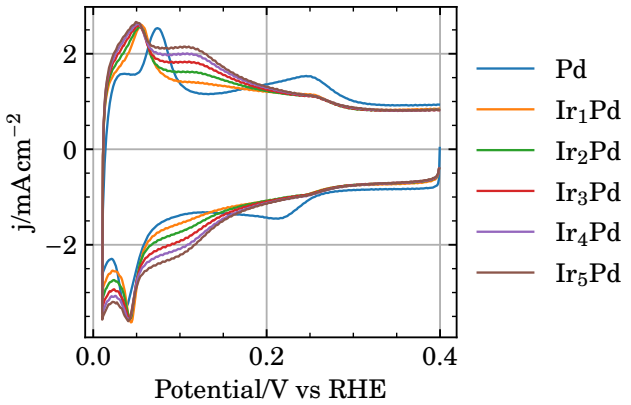

(a)

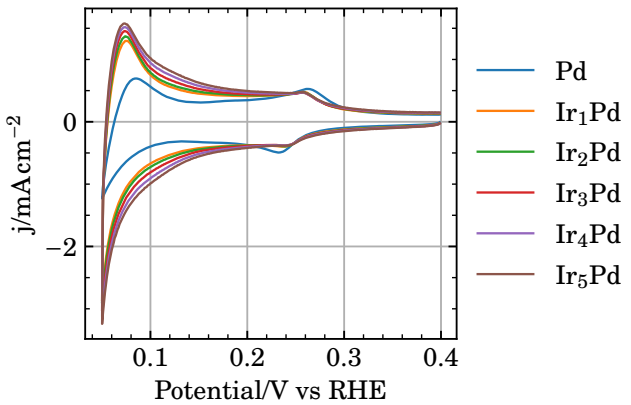

(b)

Figure 9.8: Cyclic voltammograms of Ir_nPd/C (a) and Ir_nPd/C (b) during H-UPD and PdH_x formation and oxidation, and after 1, 2, 3, 4 and 5 displacement events in 10 µmol dm^{-3} K_2IrCl_6 and 0.5 mol dm^{-3} H_2SO_4 at 50 °C. Voltammograms were obtained at 50 mV s^{-1} in 0.5 mol dm^{-3} H_2SO_4.

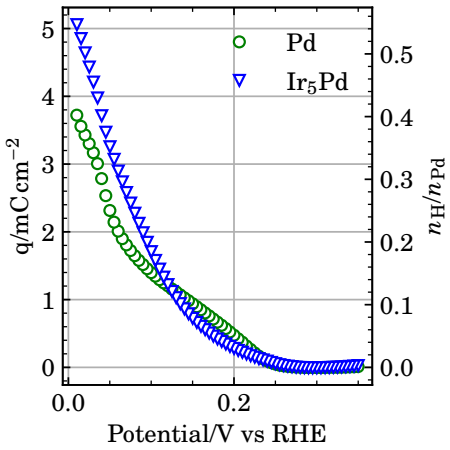

Figure 9.9: Charge-potential curves of Pd/C and Ir_5Pd/C obtained by integration of the anodic parts of voltammograms obtained at 5 mV s^{-1} in 0.5 mol dm^{-3} H_2SO_4. The cathodic limit of the voltammograms were decreased in steps of −10 mV, from 0.35 to 0.01 V. The anodic limit was always 0.4 V.

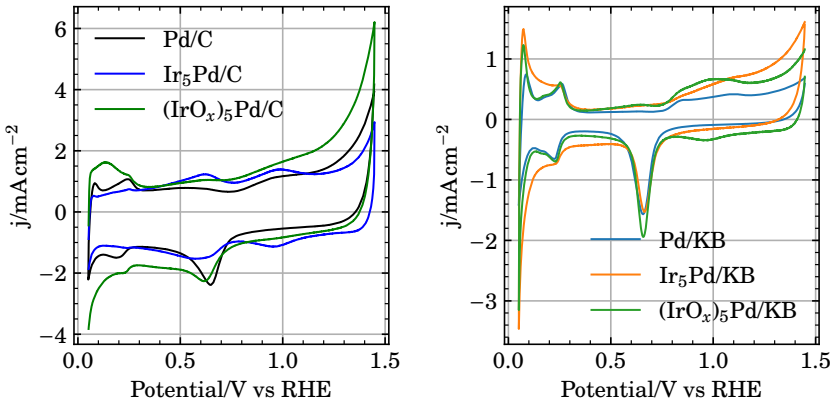

(a) (b)

Figure 9.10: Cyclic voltammograms of (a) Pd/C and Ir_5Pd/C and Pd/KB and (b) Ir_5Pd/C before and after transformation to IrO_xPd by 20 potentials cycles between 0.05 V and 1.45 V at 50 mV s^{-1} in 0.5 mol dm^{-3} H_2SO_4. Voltammograms were obtained at 50 mV s^{-1} in 0.5 mol dm^{-3} H_2SO_4.

9.4 Discussion

Polycrystalline Pd

The apparent capacitance in the voltammograms of $IrPd_{poly}$:3, $IrPd_{poly}$:15 and $IrPd_{poly}$:50 was larger compared to that of Pd_{poly} in figures 9.3 and 9.5. This is attributed to the Ir deposit, as the height of the Pd reduction peak at 0.7 V does not appear to increase in any of the voltammograms. The increased capacitance can be attributed to two sources;

- The total surface area increased. The (relatively) thick, cracked film of IrO_x on $IrPd_{poly}$:50 in figure 9.6b exposes the underlying Pd substrate. The voltammogram of $IrPd_{poly}$:50 in figure 9.5 is then the voltammograms of IrO_x and Pd superimposed.
- Protons intercalate into IrO_x, as according to reactions (1.19) and (2.3), which makes the volume, *i.e.* thickness, of the film contribute to the currents in the voltammogram.

The slow reaction at room temperature gave a denser, more uniform Ir film than the faster reaction at 50 °C. The reduced height of the Pd reduction peak in $IrPd_{poly}$:15 and the apparent increased capacitance suggests that some of the Pd was protected from the electrolyte, while the increased capacitance suggests the same as mentioned above.

It appears as though the cracked IrO_x film on $IrPd_{poly}$:50 in figures 9.6 and F.2 may consist of multiple layers. A rough estimate of 60 nm for a single layer may be estimated from figure F.2 (c,d). This is consistent with the apparent particle diameter in figure F.2 (b). Multiple layers of 60 nm with a total average height of 251 nm equals four layers.

Effect of temperature

The displacement rate at room temperature was very slow. This is clear from the small amount of iridium obtained after more than 15 hours of displacement at room temperature, figure 9.3, relative to what was obtained at 50 °C in one hour, figure 9.5. This is consistent with thermal activation of K_3IrCl_6 reduction [180] followed by formation of an unstable Ir(I) intermediate [183] and our previous work on displacement of underpotential deposited copper on polycrystalline gold electrodes from similar solutions of H_2IrCl_6, $IrCl_3$, K_2IrCl_6 and K_3IrCl_6 in chapters 6 and 7. A comparison of displacement experiments using Pd/KB at room temperature and 50 °C can be seen in figures F.3 to F.5, but the results were somewhat inconclusive as to whether the palladium nanoparticles were modified at room temperature.

Carbon supported Pd catalysts

Both Pd/C and Pd/KB was successfully modified with Ir by the PdH_x displacement procedure at 50 °C. The emerging H-UPD wave centered at 0.1 V in figure 9.8 and cathodic shift of the main H_{UPD} peak are consistent with a mixed Ir/Pd surface [113]. The emergence of a pair of peaks around 0.95 V after transformation to IrO_x in figure 9.10 is typical for IrO_x in H_2SO_4, as has already been argued earlier for the polycrystalline samples. The voltammgrams in figure 9.8a and charge-potential curves in figure 9.9 of Pd/C and Ir_5Pd/C implies that total adsorpion+absorption of hydrogen is initially suppressed at potentials positive of 120 mV by an Ir overlayer, and is enhanced at potentials negative of 120 mV. This is likely due to an increase in the total surface area from the Ir deposit and an increased contribution from H_{UPD}.

The largest modification of the Pd surface was after the first displacement event. The large change in the H_{UPD}/PdH_x region in the voltammogram of Ir_5Pd/C in figure 9.8 (b) after the first displacement event was followed by small, incremental changes with successive displacement events. This indicates that the larges modification of the surface was obtained in the first displacement. This is supported by the HER currents in figure 9.7 (b) increasing in the same manner.

After transformation of Ir_5Pd/KB to $(IrO_x)_5Pd/KB$, the Pd-reduction peak at 0.65 V in figure 9.10 (b) increased in magnitude. This is likely due to oxidation- and re-deposition of palladium during cycling, as some Pd is expected to dissolve during potential cycling in H_2SO_4 [26, 28, 265–270].

9.5 Conclusions

We have shown how PdH_x can be used as a reduction agent to reduce a solution of K_2IrCl_6 onto a palladium surface as metallic Ir, and that the reaction proceeds even at room temperature. This is a significant advantage over the *one-pot* SLRR procedure presented in chapters 6 to 8 where Cu_{UPD} acts as the reduction agent because; *(i)* The possibility of Cu contaminants in the resulting Ir film is eliminated [102, 144], and *(ii)* The amount of electrons available to reduce Ir onto the surface is determined by the bulk volume of the Pd core, and not by the surface charge of Cu_{UPD} on the core, and *(iii)* The procedure can be conducted at room temperature, although the kinetics are significantly improved at 50 °C.

This work was intended to culminate in preparation of larger batches of IrPd/C by using hydrogen gas to form the PdH_x phase, but the work was cut short due to the Covid-19 lockdown. The intended procedure is outlined in [152]. PdH_x can be formed by bubbling H_2(g) through a suspension of Pd/C. Subsequent addition of an

Ir precursor solution allows reaction (9.3) to proceed. If the amount of precursor solution is chosen so that the hydride phase is in excess, this procedure can be performed successively so that no Ir is reduced by hydrogen in the bubbling step. The process should then self terminate if a protective Ir shell is formed in the Pd cores. This can be monitored by keeping an electrode with a Pd/C film, as used in this work, immersed in the suspension at open circuit.

Chapter 10

Simulation of SLRR reactions

In this chapter we address some shortcomings in the existing mathematical description of surface-limited redox replacement (SLRR) reactions in the literature. In particular, we introduce *i)* detailed rate equations for both the oxidation of the sacrificial metal and the reduction of the noble-metal precursor, and *ii)* the effects of mass transfer.

10.1 Description of Cu underpotential deposition

It has been shown on Au(111) that underpotential deposition of copper (Cu_{UPD}) from aqueous solutions containing $CuSO_4$ and H_2SO_4 involves two charge transfer steps at distinctly different potentials with well defined peaks in cyclic voltammograms [272]. On polycrystalline gold, the the current contribution from each step are usually more convoluted [263]. The first step involves both charge- and mass transfer [273] and can be described through a Langmuir-type adsorption isotherm [263] and may be well explained by reaction (10.1). The second step occurring at less positive potentials then the first step involves charge transfer only, and can hence be described by reaction (10.2). It should be noted that second step, reaction (10.2), has been described as *surprisingly slow* [274].

$$Cu^{2+}(aq) + e^- \underset{k_{-1}}{\overset{k_{+1}}{\rightleftharpoons}} Cu^+(ads) \tag{10.1}$$

$$Cu^+(ads) + e^- \underset{k_{-2}}{\overset{k_{+2}}{\rightleftharpoons}} Cu(ads) \tag{10.2}$$

The rate of reactions (10.1) and (10.2) is expressed as follows by equations (10.3) and (10.4),

$$v_1 = k_{+1}\Gamma_i\theta_s c_1 - k_{-1}\Gamma_i\theta_1 \tag{10.3}$$
$$v_2 = k_{+2}\Gamma_i\theta_1 - k_{-2}\Gamma_i\theta_2 \tag{10.4}$$

where c_1 is the concentration[1] of Cu^{2+}(aq), θ_s is the total fractional coverage of surface sites at which Cu^{-}(ads) be be reduced and θ_1 and θ_2 are the fractional coverage of Cu^{+}(ads) and Cu(ads) at the surface.

The rate constants $k_{\pm 1}$ and $k_{\pm 2}$ are given in equations (10.5) and (10.6),

$$k_{+l} = k^{\circ}_{+l} \exp\left[-\alpha_l \frac{F}{RT}E - \alpha_l \sum_i f_{l,i}\theta_i\right] \qquad l = 1,2 \tag{10.5}$$
$$k_{-l} = k^{\circ}_{-l} \exp\left[(1-\alpha_l)\frac{F}{RT}E + (1-\alpha_l)\sum_i f_{l,i}\theta_i\right] \qquad l = 1,2 \tag{10.6}$$

where subscript i denotes any specie present at the surface and the Temkin parameter $f_{l,i}$ accounts for interactions between surface species.

10.2 Reduction of Ir precursors

We assume that reduction of Ir from hexachloro-complexes in aqueous solution proceeds through reactions (10.7) to (10.9)

$$IrCl_6^{2-}(aq) + e^- \underset{k_{-3}}{\overset{k_{+3}}{\rightleftharpoons}} IrCl_6^{3-}(aq) \tag{10.7}$$
$$IrCl_6^{3-}(aq) \underset{k_{-4}}{\overset{k_{+4}}{\rightleftharpoons}} IrCl_6^{3-}(ads) \tag{10.8}$$
$$IrCl_6^{3-}(ads) + 3e^- \underset{k_{-5}}{\overset{k_{+5}}{\rightleftharpoons}} Ir(s) + 6Cl^-(aq) \tag{10.9}$$

where reaction (10.7) is well known [176, 177].

Further reaction steps from Ir(III) to Ir(0) are less clear. Sawy and Birss argued that the reduction goes *via* slow adsorption of $IrCl_6^{3-}$(aq). From electroplating of Ir onto polycrystalline Au from H_2IrCl_6 solutions, they reported a reduction in current efficiency when forced convection was introduced or if the H_2IrCl_6 concentration was increased. This was consistent with formed $IrCl_6^{3-}$(aq) going away from the electrode.

[1] We assume that the activity coefficients of all species are approximately equal to one

An adsorption step is also consistent with Le-Vot *et. al* [161, 182] who reported a high overpotential for nucleation of Ir onto glassy carbon electrodes compared to one with pre-existing Ir or Pt nuclei.

Nie *et al.* (1992) suggested the reduction of H_2IrCl_6 to Ir(s) by hydrogen gas to proceed through Ir(I), with reduction of Ir(III) to Ir(I) as the slow step [183]. They supported this with an observed reaction order with respect to the Ir precursor concentration and partial pressure of hydrogen both to be equal to one. After the initial nucleation stage, hydrogen adsorbed dissociatively on metallic iridium transferred an electron to the central iridium ion in the $IrCl_6^{3-}$ complexes though a chloride bridge. In other words; atomic hydrogen acted as the reduction agent, which has been suggested by others as well [176, 180, 182]. This is consistent with previous reports on Ir electrodeposition, where the potential needs to be brought down to the H-UPD area for the reaction to proceed at room temperature [161,176,177,182].

The corresponding rate expressions for reactions (10.7) to (10.9) are expressed as equations (10.10) to (10.12)

$$v_3 = k_{+3}\Gamma_i\theta_a c_3 - k_{-3}\Gamma_i\theta_a c_4 \tag{10.10}$$

$$v_4 = k_{+4}\Gamma_i\theta_s^* c_4 - k_{-4}\Gamma_i\theta_3 \tag{10.11}$$

$$v_5 = k_{+5}(\Gamma_i\theta_3)^{\Omega_3} - k_{-5}(\Gamma_i\theta_4)^{\Omega_4} \tag{10.12}$$

where c_2 and c_3 are the concentrations of $IrCl_6^{2-}$(aq) and $IrCl_6{}^{3-}$(aq), respectively. θ_a is the total fractional coverage of sites at the surface where charge transfer may occur and θ_s^* is the total fractional coverage of sites where $IrCl_6^{3-}$(aq) may adsorb onto. θ_3 and θ_4 are the fractional coverage of $IrCl_6^3$(ads) and Ir(s) at the surface. Ω_3 and Ω_4 are the reaction orders of equation (10.12) with respect to θ_3 and θ_4, respectively[2].

We assume that the rate constants for equations (10.10) to (10.12) are given as equations (10.13) to (10.18),

[2]Strictly speaking, the reaction orders are potential dependent, so this is formally wrong.

$$k_{+3} = k_{+3}^{\circ} \exp\left[-\alpha_3 \frac{F}{RT} E - \alpha_3 \sum_i f_{3,i}\theta_i\right] \tag{10.13}$$

$$k_{-3} = k_{-3}^{\circ} \exp\left[(1-\alpha_3) \frac{F}{RT} E + (1-\alpha_3) \sum_i f_{3,i}\theta_i\right] \tag{10.14}$$

$$k_{+4} = k_{+4}^{\circ} \exp\left[-\frac{E_{+a}}{RT} - \sum_i f_{4,i}\theta_i\right] \tag{10.15}$$

$$k_{-4} = k_{-4}^{\circ} \exp\left[-\frac{E_{-a}}{RT} + \sum_i f_{4,i}\theta_i\right] \tag{10.16}$$

$$k_{+5} = k_{+5}^{\circ} \exp\left[-\alpha_{5,c} \frac{F}{RT} E - \alpha_{5,c} \sum_i f_{5,i}\theta_i\right] \tag{10.17}$$

$$k_{-5} = k_{-5}^{\circ} \exp\left[\alpha_{5,a} \frac{F}{RT} E + \alpha_{5,a} \sum_i f_{5,i}\theta_i\right] \tag{10.18}$$

where $E_{\pm a}$ are the adsorption and desorption activation energies of reaction (10.8). $\alpha_{5,c}$ and $\alpha_{5,a}$ need not obey $\alpha_a + \alpha_c = 1$ as reaction (10.9) does not represent an elementary step. The other constants have previously been defined.

10.3 General model for galvanic displacement of Cu_{UPD} by Ir

We tabulate the species presented earlier in table 10.1 for easy reference.

Table 10.1: Overview of the symbols used to represent the different species in the model.

Symbol	Specie
c_1	Cu^{2+}(aq)
c_2	$IrCl_6^{2-}$(aq)
c_3	$IrCl_6^{3-}$(aq)
θ_1	Cu^{+}(ads)
θ_2	Cu(upd)
θ_3	$IrCl_6^{3-}$(ads)
$\theta_{4,ext}$	Ir(s)
θ_4	$1-\exp\left(-\theta_{4,ext}\right)$

We also define θ_s, θ_a and θ_s^* from equations (10.3), (10.10) and (10.11) as

$$\theta_s = 1 - \theta_1 - \theta_2 - \theta_3 \tag{10.19}$$
$$\theta_a = 1 \tag{10.20}$$
$$\theta_s^* = 1 - \theta_1 - \theta_2 - \theta_3 \tag{10.21}$$

The first and last relation prevents Ir from growing onto Cu, which is something we have not taken into account in our model, but Cu and Ir may deposit onto Ir[3]. The above relations defines $\theta_s^* = \theta_s$.

This defines the general rate expressions in equations (10.3), (10.4) and (10.10) to (10.12) more accurately as equations (10.22) to (10.26)

$$v_1 = k_{+1}\Gamma_i(1 - \theta_1 - \theta_2 - \theta_3)c_1 - k_{-1}\Gamma_i\theta_1 \tag{10.22}$$
$$v_2 = k_{+2}\Gamma_i\theta_1 - k_{-2}\Gamma_i\theta_2 \tag{10.23}$$
$$v_3 = k_{+3}\Gamma_i c_3 - k_{-3}\Gamma_i c_4 \tag{10.24}$$
$$v_4 = k_{+4}\Gamma_i(1 - \theta_1 - \theta_2 - \theta_3)c_4 - k_{-4}\Gamma_i\theta_3 \tag{10.25}$$
$$v_5 = k_{+5}(\Gamma_i\theta_3)^{\Omega_3} - k_{-5}(\Gamma_i\theta_4)^{\Omega_4} \tag{10.26}$$

Γ_i is present in all the rate expressions to remain consistent with the notation $c_{Cu_{UPD}} = \Gamma_i\theta_{Cu_{UPD}}$.

The governing equations describing change of θ_i over time are given in equations (10.27) to (10.30)

$$\Gamma_i\frac{\partial\theta_1}{\partial t} = v_1 - v_2 \tag{10.27}$$
$$\Gamma_i\frac{\partial\theta_2}{\partial t} = v_2 \tag{10.28}$$
$$\Gamma_i\frac{\partial\theta_3}{\partial t} = v_4 - v_5 \tag{10.29}$$
$$\Gamma_i\frac{\partial\theta_4}{\partial t} = v_5 \tag{10.30}$$

The total current density at the electrode surface is given in equation (10.31)

[3]This is primarily of importance if one is to simulate multiple successive displacement experiments

$$j = j_1 + j_2 + j_3 + j_5 + j_{dl} \tag{10.31}$$

where $j_i = -z_i F v_i$ and j_{dl} is given in equation (10.32)

$$j_{dl} = C_{dl} \frac{\partial E}{\partial t} \tag{10.32}$$

where C_{dl} is the double layer capacity, of which we have assumed is constant through all potential ranges (typically $1\,\mu\mathrm{F\,cm^{-2}}$).[4]

Inserting equation (10.32) and the above definition of j_i with $z_{1,2,3} = 1$ and $z_5 = 3$ into equation (10.31) gives equation (10.33) which describes the total current density at the electrode.

$$j = -F(v_1 + v_2 + v_3 + 3v_5) + C_{dl} \frac{\partial E}{\partial t} \tag{10.33}$$

Assuming the electrolyte is well supported and that electroneutrality is fulfilled at all times, the change in concentration of an aqueous specie is given by the mass transport expression for a rotation disc electrode, equation (10.34) [15]

$$\frac{\partial c_i}{\partial t} = D_i \frac{\partial^2 c_i}{\partial x^2} + Bx^2 \frac{\partial c_i}{\partial x} \tag{10.34}$$

Where $B = 0.51 \nu^{-\frac{1}{2}} \omega^{\frac{3}{2}}$, x is the distance perpendicular to the electrode surface, ω is the radial rotation rate of the electrode and ν is the kinematic viscosity of the solvent. D_i is the diffusion coefficient of specie c_i from table 10.1.

We assume no change in concentration at some very-far away distance from the electrode

$$\lim_{x \to \infty} c_i = c_i(t = 0) = c_i^{\infty} \tag{10.35}$$

The width of the Nernst diffusion layer, δ_N, is defined for a rotating disc electrode, when $\omega \geq 10.5\,\mathrm{s^{-1}}$, as equation (10.36) [16]

[4] This creates a capacitor with infinite capacity. This is formally wrong, but sufficient for our formulation.

$$\delta_N = 1.61 D^{1/3} \omega^{-1/2} \nu^{1/6} \tag{10.36}$$

and equation (10.35) is imposed at some distance outside δ_N and is implicitly taken into account through the last term on the right-hand side of equation (10.34).

The flux of c_i at the electrode surface, $x = 0$, is defined by the relevant reaction rates involving c_i. For c_1, c_2 and c_3, this is given as equations (10.37) to (10.39)

$$D_1 \frac{\partial c_1}{\partial x}|_{x=0} = v_1 \tag{10.37}$$

$$D_2 \frac{\partial c_2}{\partial x}|_{x=0} = v_3 \tag{10.38}$$

$$D_3 \frac{\partial c_3}{\partial x}|_{x=0} = v_4 - v_3 \tag{10.39}$$

where everything has been defined previously.

This sums up a set of equations, equations (10.22) to (10.30), (10.34), (10.35) and (10.37) to (10.39)

which may be used to model reactions (10.1), (10.2) and (10.7) to (10.9) at a rotating disc electrode. If modelling a galvanostatic experiment, *i.e.* constant current, equation (10.33) is added to the system.

10.4 Dimensionless variables

Before discretizing the system, we introduce the dimensionless variables

$$\Psi = \frac{F}{RT}E \quad \rightarrow \text{Potential} \tag{10.40}$$

$$\mathscr{C}_{dl} = \frac{RT}{\Gamma_i F^2}C_{dl} \quad \rightarrow \text{Capacitance} \tag{10.41}$$

$$C_i = \frac{r_e}{\Gamma_i}c_i \quad \rightarrow \text{Concentration} \tag{10.42}$$

$$\tau = \frac{D^*}{r_e^2}t \quad \rightarrow \text{Time} \tag{10.43}$$

$$\Phi = \frac{E_a}{RT} \quad \rightarrow \text{Activation energy} \tag{10.44}$$

$$\xi_i = \frac{D_i}{D^*} \quad \rightarrow \text{Diffusion coefficient} \tag{10.45}$$

$$X = 1 - \exp\left(-2\frac{x}{r_e}\ln 2\right) \quad \rightarrow \text{Space/Distance} \tag{10.46}$$

$$V_1 = v_i\frac{r_e^2}{\Gamma_i D^*} \quad \rightarrow \text{Reaction rate} \tag{10.47}$$

$$J_i = j_i\frac{r_e^2}{F\Gamma_i D^*} = z_i V_i \quad \rightarrow \text{Current density} \tag{10.48}$$

where r_e is the disc radius on the rotating disc electrode and $D^* = D_1 = 1\times10^{-5}\,\mathrm{cm^2\,s^{-1}}$. Equation (10.46) elegantly transforms the coordinate map $x \in [0,\infty]$ to $X \in [0,1]$ [275, 276]. Γ_i typically has a value of $1\times10^{-9}\,\mathrm{mol\,cm^{-2}}$.

This transforms the reaction rates v_l in equations (10.22) to (10.26) to V_l in equations (10.49) to (10.53)

$$V_1 = K_{+1}(1-\theta_1-\theta_2-\theta_3)C_1 - K_{-1}\theta_1 \tag{10.49}$$

$$V_2 = K_{+2}\theta_1 - K_{-2}\theta_2 \tag{10.50}$$

$$V_3 = K_{+3}C_2 - K_{-3}C_3 \tag{10.51}$$

$$V_4 = K_{+4}(1-\theta_1-\theta_2-\theta_3)C_3 - K_{-4}\theta_3 \tag{10.52}$$

$$V_5 = K_{+5}\theta_3^{\Omega_3} - K_{-5}\theta_4^{\Omega_4} \tag{10.53}$$

where the rate constants $k_{\pm l}$ in equations (10.5), (10.6) and (10.13) to (10.18) are transformed to $K_{\pm l}$ in equations (10.54) to (10.63)

$$K_{+1} = k^{\diamond}_{+1} \frac{\Gamma_i r_e}{D^{\diamond}} \exp\left[-\alpha_1 \Psi - \alpha_1 \sum_{i=1}^{4} f_{1,i} \theta_i \right] \tag{10.54}$$

$$K_{-1} = k^{\diamond}_{-1} \frac{r_e^2}{D^{\diamond}} \exp\left[(1-\alpha_1) \Psi + (1-\alpha_1) \sum_{i=1}^{4} f_{1,i} \theta_i \right] \tag{10.55}$$

$$K_{+2} = k^{\diamond}_{+2} \frac{r_e^2}{D^{\diamond}} \exp\left[-\alpha_2 \Psi - \alpha_2 \sum_{i=1}^{4} f_{2,i} \theta_i \right] \tag{10.56}$$

$$K_{-2} = k^{\diamond}_{-2} \frac{r_e^2}{D^{\diamond}} \exp\left[(1-\alpha_2) \Psi + (1-\alpha_2) \sum_{i=1}^{4} f_{2,i} \theta_i \right] \tag{10.57}$$

$$K_{+3} = k^{\diamond}_{+3} \frac{\Gamma_i r_e}{D^{\diamond}} \exp\left[-\alpha_3 \Psi - \alpha_3 \sum_{i=1}^{4} f_{3,i} \theta_i \right] \tag{10.58}$$

$$K_{-3} = k^{\diamond}_{-3} \frac{\Gamma_i r_e}{D^{\diamond}} \exp\left[(1-\alpha_3) \Psi + (1-\alpha_3) \sum_{i=1}^{4} f_{3,i} \theta_i \right] \tag{10.59}$$

$$K_{+4} = k^{\diamond}_{+4} \frac{\Gamma_i r_e}{D^{\diamond}} \exp\left[-\Phi_+ - \sum_{i=1}^{4} f_{4,i} \theta_i \right] \tag{10.60}$$

$$K_{-4} = k^{\diamond}_{-4} \frac{r_e^2}{D^{\diamond}} \exp\left[-\Phi_- + \sum_{i=1}^{4} f_{4,i} \theta_i \right] \tag{10.61}$$

$$K_{+5} = k^{\diamond}_{+5} \frac{r_e^2}{D^{\diamond}} \Gamma_i^{(\Omega_3 - 1)} \exp\left[-\alpha_{c,5} \Psi - \alpha_{c,5} \sum_{i=1}^{4} f_{5,i} \theta_i \right] \tag{10.62}$$

$$K_{-5} = k^{\diamond}_{-5} \frac{r_e^2}{D^{\diamond}} \Gamma_i^{(\Omega_4 - 1)} \exp\left[\alpha_{c,5} \Psi + \alpha_{c,5} \sum_{i=1}^{4} f_{5,i} \theta_i \right] \tag{10.63}$$

$$\tag{10.64}$$

The governing equations for θ_i, equations (10.27) to (10.30), are thus transformed to equations (10.65) to (10.68)

$$\frac{\partial \theta_1}{\partial \tau} = V_1 - V_2 \tag{10.65}$$

$$\frac{\partial \theta_2}{\partial \tau} = V_2 \tag{10.66}$$

$$\frac{\partial \theta_3}{\partial \tau} = V_4 - V_5 \tag{10.67}$$

$$\frac{\partial \theta_4}{\partial \tau} = V_5 \tag{10.68}$$

and the inner boundary conditions for c_i at $x = 0$, equations (10.37) to (10.39) are transformed to equations (10.69) to (10.71).

$$\xi_1 \frac{\partial C_1}{\partial X}(1-X)(2\ln 2)|_{X=0} = V_1 \tag{10.69}$$

$$\xi_2 \frac{\partial C_2}{\partial X}(1-X)(2\ln 2)|_{X=0} = V_3 \tag{10.70}$$

$$\xi_3 \frac{\partial C_3}{\partial X}(1-X)(2\ln 2)|_{X=0} = V_4 - V_3 \tag{10.71}$$

The outer boundary far away from the electrode at $x \to \infty$, equation (10.35), is simply transformed to equation (10.72) at $X = 1$.

$$\lim_{X \to 1} C_i = C_i(\tau = 0) = C_i^{X=1} \tag{10.72}$$

The main transport equation of c_i, equation (10.34), is transformed to equation (10.73).

$$\frac{\partial C_i}{\partial \tau} = \xi_i \frac{\partial^2 C_i}{\partial X^2}(1-X)^2(2\ln 2)^2 + \beta \frac{\ln(1-X)^2}{(2\ln 2)} \frac{\partial C_i}{\partial X}(1-X) \tag{10.73}$$

Where $\beta = B\frac{r_e^3}{D^*}$.

Additionally, the current density at the electrode, equations (10.31) and (10.33) is transformed to equation (10.74)

$$\mathcal{J} = V_1 + V_2 + V_3 + 3V_5 + \mathscr{C}_{dl} \frac{\partial \Psi}{\partial \tau} \tag{10.74}$$

where $\mathcal{J} = \frac{j}{F} \times \frac{r_e^2}{\Gamma_i D^*}$ and each reaction rate v_i was transformed as $V_i = v_i \frac{r_e^2}{\Gamma_i D^*}$.

The total set of equations in the model are then defined as equations (10.49) to (10.53) and (10.65) to (10.73)

with equation (10.74) also included if a galvanostatic experiment is modelled.

10.5 Solution procedure

The time- and space-derivatives in equations (10.65) to (10.71) and (10.73) were discretized and organized as a set of linear equations, as explained in Appendix

sections G.1.1 and G.1.2, respectively. A program solving the set was written in Python, where the code is available upon request. The pseudocode is given in appendix G.2.

The dimensionless transformations was performed inside the model program. The program accepted real inputs, performed the calculations using dimensionless parameters, and returned both dimensionless and real values of concentrations, θ_i, potential, current and reaction rates. The program then had the capability to accept experimentally obtained values of time, potential or current, and return the corresponding simulation.

The values listed in table 10.2 were hard coded as constants in the model program.

Table 10.2: Hard coded constants used in the model program.

Symbol	Description	Value	Units
D_i	Diffusion constant of specie i	1×10^{-5}	$\mathrm{cm^2\,s^{-1}}$
Γ_i	Initial surface excess	1×10^{-9}	$\mathrm{mol\,cm^{-2}}$
r_e	Typical radius of a rotating disc electrode	0.25	cm
ν	Kinematic viscosity of water	1×10^{-2}	$\mathrm{cm^2\,s^{-1}}$
F	Faraday's constant	96485	$\mathrm{C\,mol^{-1}}$
R	Universal gas constant	8.314	$\mathrm{J\,K^{-1}\,mol}$
nj	Number of steps in space	101	-

We first attempted to fit simulations to experimentally obtained surface limited redox replacement (SLRR) data. In short, SLRR is the process where an adlayer of an underpotentially deposited metal is oxidized by a more noble metal cation in solution. The cations of the more noble metal is in turn reduced onto the electrode. The open circuit potential of the working electrode is typically recorded during such experiments. At open circuit, the net current at the working electrode is zero. In this text, we use the term SLRR also for reactions where the more noble metal cation is reduced to a lower oxidation state, but remains in solution.

In chapter 7 (Experiment 1 in table 7.1, figure 7.4 (a) and figure E.6 (b)), we presented SLRR transients where a Au rotating disc electrode initially covered in a $\mathrm{Cu_{UPD}}$ layer is kept at open circuit in a solution containing $\mathrm{K_2IrCl_6}$ at room temperature. We previously concluded that reduction of Ir(III) species, reactions (6.3) and (6.4), is negligible at potentials positive of 300 mV at 25 °C (chapter 7). We could therefore assume $k_{\pm l} = 0$ for $l = 4,5$ at 25 °C. The model program was then used to fit the values of $\log_{10}\left(k^{\circ}_{\pm l}\right)$ for $l = 1,2,3$, $\log_{10}(C_{dl})$, $f_{1,i}$ and $f_{2,i}$ to a SLRR transient obtained in chapter 7 (Experiment 1 in table 7.1, figure 7.4 (a) and figure E.6 (b)). In the

real experiment, a Au rotating disc electrode was first held at 0.7 V for 5 s. The potential was then stepped to 0.3 V for 2 s where Cu_{UPD} was formed, and then the open circuit potential of the electrode was recorded for 300 s. The electrolyte contained 0.5 mol dm^{-3} H_2SO_4, 1 mmol dm^{-3} $CuSO_4$ and 10 µmol dm^{-3} K_2IrCl_6 and was kept at room temperature. The electrode was rotated as 1600 rpm. This is shown schematically in figure 10.1.

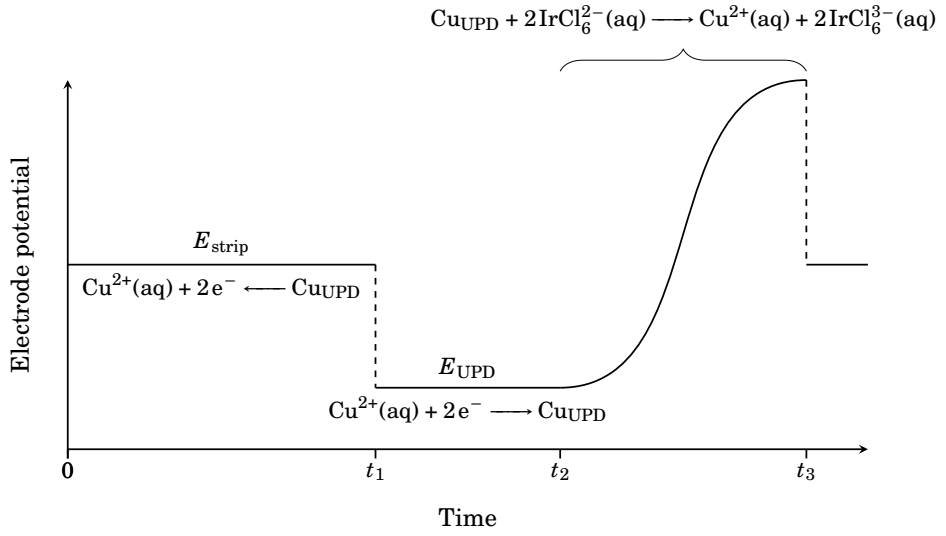

Figure 10.1: Schematic representation of the SLRR procedure. The first step between $t = 0$ and $t_:1$ ensures the electrode to be free of Cu_{UPD}, where a Cu_{UPD} adlayer is formed in the second step between t_1 and t_2. In the third step, between t_2 and t_3, the open circuit potential of the electrode is recorded.

During the time at open circuit, the Cu_{UPD} adlayer was oxidized by the K_2IrCl_6 solution. Ir(IV) was reduced to Ir(III) while Cu_{UPD} was oxidized to Cu(II).

Fitting of the model to the experimental values was performed through the Trust Region Reflective algorithm [213] as implemented in the curve fitting procedure included in the optimization module of Scipy [214][5]. The curve fitting procedure was used with the standard implemented settings, where the initial guess and lower and upper bounds of the fitted parameters are given in table 10.3. The curve fitting objective function was on the form $0.5\sum_i^N \left(y_{\mathrm{exp,i}} - y_{\mathrm{sim,i}}\right)^2$, which was minimized with

[5]We also attempted to use other global minimization algorithms such as simulated annealing, but this proved to be too computationally expensive given our implementation of the code and available hardware.

ones used as weighting factors. The curve fitting program was written so as to represent the experiment where the experimental data was obtained. The program first simulated a 5 s potential hold at 0.7 V. The output was used as initial values for a 2 s potential hold at $E_2 = 0.3$ V, where the output again was used as initial values to simulate an open circuit potential transient, of which was returned to the curve fitting algorithm. The above fitting was done twice, once by holding $f_{1,i} = 0$ and $f_{2,i} = 0$, and once by refining also these values as described above.

The values used in the curve fitting program are listed in table 10.3

Table 10.3: Overview of the input given to the model in the curve fitting procedure

Parameter	Fitting 1	Fitting 2	Initial guess	Lower/upper bound	Units
k°_{+1}	Fitted	Fitted	9	5/15	$\mathrm{cm^3\,s^{-1}}$
k°_{-1}	Fitted	Fitted	-4	-8/5	$\mathrm{s^{-1}}$
k°_{+2}	Fitted	Fitted	7	-2/10	$\mathrm{s^{-1}}$
k°_{-2}	Fitted	Fitted	1	-8/2	$\mathrm{s^{-1}}$
k°_{+3}	Fitted	Fitted	12	-8/20	$\mathrm{cm^3\,s^{-1}}$
k°_{-3}	Fitted	Fitted	-1	-5/5	$\mathrm{cm^3\,s^{-1}}$
$k_{\pm 4}$	0	0	-	-	$\mathrm{cm^3\,s^{-1}}$
k°_{+5}	0	0	-	-	$\mathrm{mol^{1-\Omega_3}\,cm^{-\Omega_3}\,s^{-1}}$
k°_{-5}	0	0	-	-	$\mathrm{mol^{1-\Omega_4}\,cm^{-\Omega_4}\,s^{-1}}$
C_{dl}	Fitted	Fitted	-6	-10/-3	$\mathrm{F\,cm^{-2}}$
$f_{1,i}$	0	Fitted	0	-20/50	a.u.
$f_{2,i}$	0	Fitted	0	-20/50	a.u.
$f_{4,i}$	0	0	-	-	a.u.
$f_{5,i}$	0	0	-	-	a.u.
c_1	1×10^{-6}	1×10^{-6}	-	-	$\mathrm{mol\,cm^{-3}}$
c_2	1×10^{-8}	1×10^{-8}	-	-	$\mathrm{mol\,cm^{-3}}$
c_3	1×10^{-12}	1×10^{-12}	-	-	$\mathrm{mol\,cm^{-3}}$
α_l	0.5	0.5	-	-	a.u.
ω_{rpm}	1600	1600	-	-	rpm
T	298.15	298.15	-	-	K
E_2	0.3	0.3	-	-	V

We then used the values of $\log_{10}\left(k^{\circ}_{\pm l}\right)$ for $l = 1,2,3$ and $\log_{10}(C_{dl})$ obtained in the first fitting and simulated SLRR transients and cyclic voltammograms in three sets in order to investigate the sensitivity to $k^{\circ}_{\pm 3}$ and c^b_3, as well as the effect of ω_{rpm}.

The SLRR transients were simulated as before; the program first simulated a 5 s potential hold at 0.7 V. The output was used as initial values for a 2 s potential

hold at E_2, where the output again was used as initial values to simulate an SLRR transient.

Voltammograms were simulated at $50\,\mathrm{mV\,s^{-1}}$ between 1.5 V and 0 V.

The values of ω_{rpm}, $k^{\circ}_{\pm 3}$ and $c_3$were systematically varied, while keeping $k^{\circ}_{+3}/k^{\circ}_{-3}$ and all other parameters constant.

Table 10.4 presents an overview over the values used in the simulations where some parameters were varied, as describe above. * Indicate that the value was obtained by the curve fitting procedure described before. ω_{rpm} was set to either set to 1600 rpm (SLRR transients), 0 rpm (Voltammogram) or varied.

Table 10.4: Overview of the inputs given the model when simulating open circuit potential transients and voltammograms. * Indicate that the value was obtained from the first previous curve fitting. SLRR potential transients were simulated at 1600 rpm and voltammograms at 0 rpm.

Parameter	Runs 1	Runs 2	Runs 3	Units
k°_{+1}	*	*	*	$\mathrm{cm^3\,s^{-1}}$
k°_{-1}	*	*	*	$\mathrm{s^{-1}}$
$k^{\circ}_{\pm 2}$	*	*	*	$\mathrm{s^{-1}}$
$k^{\circ}_{\pm 3}$	$* \times \left[\mathbf{10^{-1} - 10^{5}}\right]$	*	*	$\mathrm{cm^3\,s^{-1}}$
$k_{\pm 4}$	0	0	0	$\mathrm{cm^3\,s^{-1}}$
k°_{+5}	0	0	0	$\mathrm{mol^{(1-\Omega_3)}\,cm^{-\Omega_3}\,s^{-1}}$
k°_{-5}	0	0	0	$\mathrm{mol^{(1-\Omega_4)}\,cm^{-\Omega_4}\,s^{-1}}$
C_{dl}	*	*	*	$\mathrm{F\,cm^{-2}}$
$f_{1,i}$	0	0	0	a.u.
$f_{2,i}$	0	0	0	a.u.
$f_{4,i}$	0	0	0	a.u.
$f_{5,i}$	0	0	0	a.u.
c_1	1×10^{-6}	1×10^{-6}	1×10^{-6}	$\mathrm{mol\,cm^{-3}}$
c_2	1×10^{-8}	1×10^{-8}	1×10^{-8}	$\mathrm{mol\,cm^{-3}}$
c_3	1×10^{-12}	$\mathbf{1 \times 10^{-15} - 1 \times 10^{-8}}$	1×10^{-12}	$\mathrm{mol\,cm^{-3}}$
α_l	0.5	0.5	0.5	a.u.
ω_{rpm}	1600/0	1600/0	**100-5000**	rpm
T	298.15	298.15	298.15	K
E_2	0.3	0.3	0.3	V

10.6 Results

Figure 10.2 shows an experimentally obtained SLRR transient (black circles) obtained by displacement of Cu_{UPD} by K_2IrCl_6 at room temperature, in an electrolyte containing $0.5\,\mathrm{mol\,dm^{-3}}$ H_2SO_4, $1\,\mathrm{mmol\,dm^{-3}}$ $CuSO_4$ and $10\,\mu\mathrm{mol\,dm^{-3}}$ K_2IrCl_6. The data is reprinted from chapter 7 (Experiment 1 in figure 7.4 (a) and figure E.6 (b)). The red and blue lines show simulated transients obtained by fitting the values of (blue) $\log_{10}(k_{\pm l})$, $l = 1,2,3$ and $\log_{10}(C_{dl})$ or (red) $\log_{10}(k_{\pm l})$, $l = 1,2,3$, $\log_{10}(C_{dl})$, $f_{1,i}$ and $f_{2,i}$, $i = 1,2$ until a best fit was obtained to the experimentally obtained SLRR transient.

The simulated transients show an excellent agreement with the experimental data, regardless if the Temkin parameters $f_{l,i}$ is kept at zero or included in the fitting. The fitted values of $f_{l,i}$ was sensitive to the initial guess provided to the minimizer algorithm, but the simulated SLRR transient appeared to be insensitive to $f_{l,i}$.

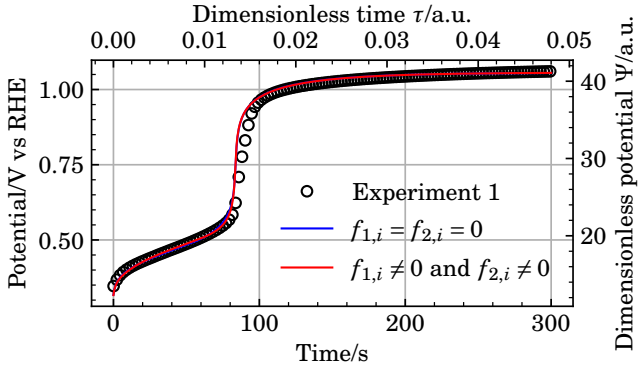

Figure 10.2: Experimentally obtained (black circles) and simulated (blue and red lines) SLRR transients of CuUPD and K_2IrCl_6 at room temperature while rotating the electrode at 1600 rpm.

Table 10.5 shows the fitted values of $\log_{10}(k_{\pm l})$, $l = 1,2,3$, $\log_{10}(C_{dl})$, $f_{1,i}$ and $f_{2,i}$, $i = 1,2$ after fitting the simulations to experimental data. $k^{\circ}_{\pm 3}$ appear to be fairly insensitive to whether $f_{1,i}$ and $f_{2,i}$ is set to 0 or included in the fitting. The standard reduction potential of reaction (6.2) calculated from $k^{\circ}_{\pm 3}$, E°_3, is fairly consistent with literature values [19]. E°_1 represents the onset potential of Cu_{UPD} when $c_1 = 1$. Calculating $E_1^{c_1=1\,\mathrm{mmol\,dm^{-3}}} = 0.622\,\mathrm{V}$ is consistent with voltammograms of Cu_{UPD} on Au_{poly} in a solution containing $0.5\,\mathrm{mol\,dm^{-3}}$ H_2SO_4 and $1\,\mathrm{mmol\,dm^{-3}}$ $CuSO_4$ at room temperature in chapter 7, figure 7.3 (a).

Table 10.5: The converged values after fitting $\log_{10}(k_{\pm l})$, $l = 1,2,3$, $\log_{10}(C_{dl})$, $f_{1,i}$ and $f_{2,i}$, $i = 1,2$ to an SLRR transient obtained experimentally at room temperature.

Parameter	Fitting 1	Fitting 2
$\log_{10}\left(k^{\circ}_{+1}\right)$	9.157	9.700
$\log_{10}\left(k^{\circ}_{-1}\right)$	−4.488	−3.878
$\log_{10}\left(k^{\circ}_{+2}\right)$	7.948	9.148
$\log_{10}\left(k^{\circ}_{-2}\right)$	1.235	0.712
$\log_{10}\left(k^{\circ}_{+3}\right)$	10.394	10.401
$\log_{10}\left(k^{\circ}_{-3}\right)$	−2.455	−2.455
$\log_{10}(C_{dl})$	−7.394	−7.379
$f_{1,1}$	0.000	3.966
$f_{1,2}$	0.000	1.739
$f_{2,1}$	0.000	2.702
$f_{2,2}$	0.000	4.074
E°_1/V	0.807	0.803
$E_2^{\theta_i \to 0.5}$/V	0.397	0.299
E°_3/V	0.760	0.761

Figure 10.3 shows the same simulated potential transients as in figure 10.2, with the values of θ_1 and θ_2 as a function of time. The slope $\partial\Psi/\partial\tau$ appears to increase rapidly when θ_1 goes towards zero.

The simulations show that while the potential transients are fairly identical, $\theta_i(\tau)$ is affected by $f_{1,i}$ and $f_{2,i}$. With $f_{1,i} = f_{2,i} = 0$ in figure 10.3 (a), θ_2 decreases monotonically and goes towards zero around $\tau = 0.0075$. θ_1 increases initially, until it reaches $\theta_1 > 0.6$ and decreases monotonically towards zero, which is reached around $\tau = 0.0125$.

With $f_{1,i} \neq 0$ and $f_{2,i} \neq 0$ in figure 10.3 (b), θ_2 also decreases monotonically until it reaches zero around $\tau = 0.0125$. θ_1 increases initially, but starts to decrease again after reaching about $\theta_1 = 0.2$ and goes toward zero about the same time as θ_2.

Figure 10.4 shows the concentration profile of C_2, Ir(IV), across the grid at selected dimensionless potentials during the simulated SLRR transients in figure 10.3. Figure 10.4 (a) corresponds to $f_{1,i} = f_{2,i} = 0$ in figure 10.3 (a) and figure 10.2. Figure 10.4 (b) corresponds to $f_{1,i} \neq 0$ and $f_{2,i} \neq 0$ in figure 10.3 (b) and figure 10.2.

At $\Psi = 15$, the surface concentration is about $0.4 \times C_2^{X=1}$. At $\Psi = 20$, the surface concentration is close to the bulk concentration. This means that reduction of Ir(IV) to Ir(III), reaction (6.2), is not diffusion controlled in these simulations.

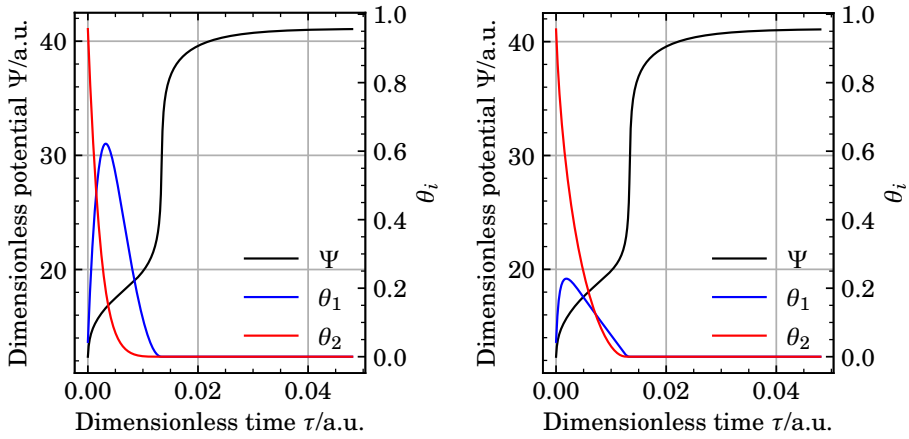

(a) $f_{1,i} = f_{2,i} = 0$ (b) $f_{1,i} \neq 0$ and $f_{2,i} \neq 0$

Figure 10.3: (Simulated SLRR transients obtained by fitting the simulations to experimental data, along with θ_1 and θ_2 as a function of time during the simulations.

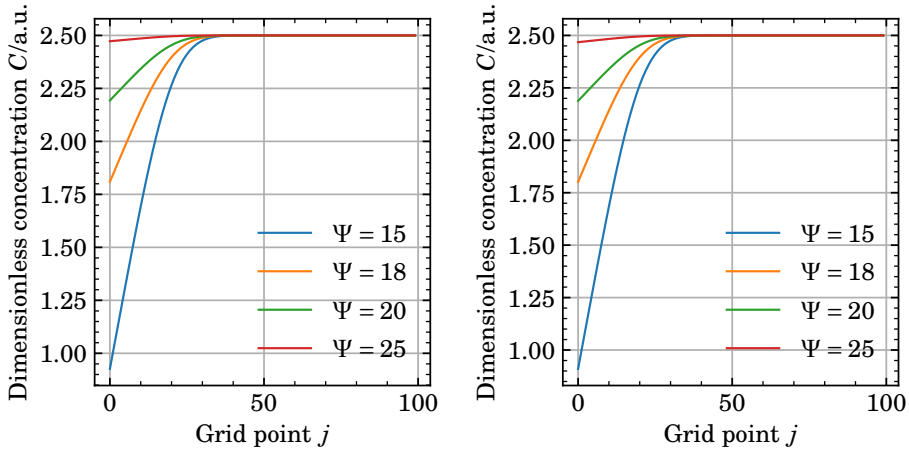

(a) $f_{1,i} = f_{2,i} = 0$ (b) $f_{1,i} \neq 0$ and $f_{2,i} \neq 0$

Figure 10.4: Concentration profile of C_2 over the discretized grid at selected potentials from the SLRR simulations in figure 10.3.

Figure 10.5 shows the current densities of reactions (6.2), (10.1) and (10.2) and equation (10.32), J_1, J_2, J_3 and J_{dl} (magnified) during the simulated SLRR transients in figure 10.3. Figure 10.5 (a) correspond to $f_{1,i} = f_{2,i} = 0$ in figure 10.3 (a) and figure 10.2. Figure 10.5 (b) correspond to $f_{1,i} \neq 0$ and $f_{2,i} \neq 0$ in figure 10.3 (b) and figure 10.2.

J_3 is fairly identical in figure 10.5 (a) and (b) and goes towards zero quite monotonically. In both figure 10.5 (a, $f_{1,i} = f_{2,i} = 0$) and (b, $f_{1,i} \neq 0$ and $f_{2,i} \neq 0$), J_2 decreases monotonically. J_1 initially increases before it decreases again.

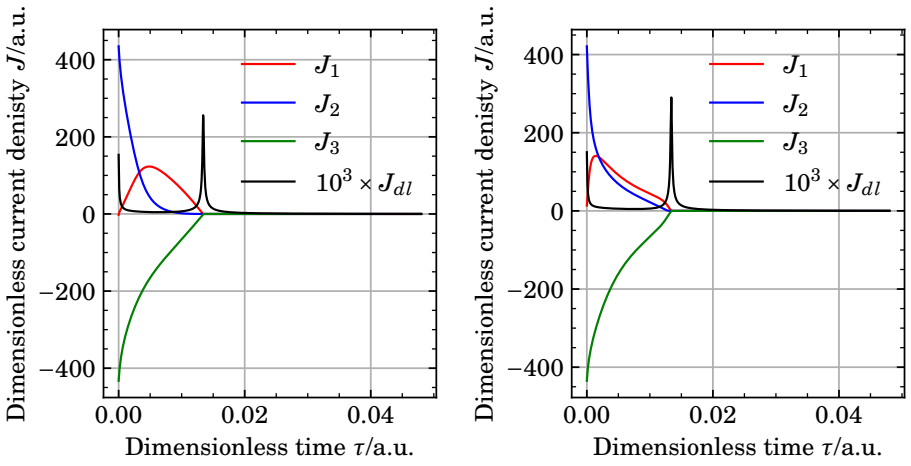

(a) $f_{1,i} = f_{2,i} = 0$ (b) $f_{1,i} \neq 0$ and $f_{2,i} \neq 0$

Figure 10.5: Currents J_1, J_2, J_3 and J_{dl} (magnified) during the simulated SLRR transients in figure 10.3.

Figure 10.6 shows simulated voltammograms of reactions (10.1) and (10.2) (J_1 and J_2) and reaction (6.2) (J_3) simulated at $50\,\mathrm{mV\,s^{-1}}$ and $\omega_{\mathrm{rpm}} = 1600\,\mathrm{rpm}$ where other physical constants were identical to the simulated SLRR transients in figure 10.3. The important results from this simulation is the current density J_3 (green line). This represents reduction of Ir(IV) to Ir(III), reaction (6.2). J_3 is diffusion controlled at potentials $\Psi < 10$ and under mixed kinetic and mass transfer control at potentials positive of $\Psi > 10$. This is consistent with the concentration gradients shown in figure 10.4 and indicates that the rate of the simulated SLRR transients are *not* purely controlled by diffusion of Ir(IV) through the diffusion layer. This is not consistent with our results in chapters 6 and 7 which indicated that reaction (6.2) was diffusion controlled at potentials where $\theta_{\mathrm{Cu_{UPD}}} > 0$.

We also attempted to fit only $\log_{10}(k_{\pm l})$, $l = 1,2$ and $\log_{10}(C_{dl})$ with $\log_{10}\left(k^{\circ}_{+3}\right) = 16$, $\log_{10}\left(k^{\circ}_{-3}\right) = 0$ and $f_{1,i} = f_{2,i} = 0$ to ensure that J_3 would be diffusion controlled through the simulation, but an acceptable fit could not be achieved.

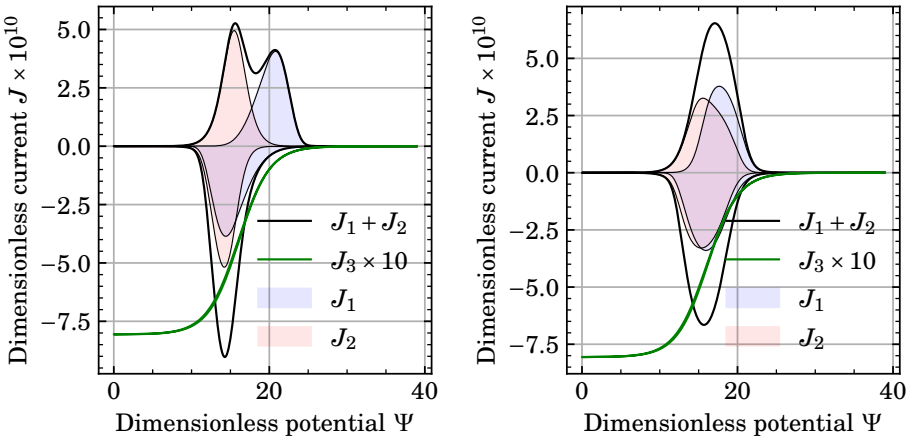

(a) $f_{1,i} = f_{2,i} = 0$ (b) $f_{1,i} \neq 0$ and $f_{2,i} \neq 0$

Figure 10.6: Simulated voltammograms of reactions (10.1) and (10.2) (J_1 and J_2) and reaction (6.2) (J_3) at $50\,\mathrm{mV\,s^{-1}}$ and $\omega_{\mathrm{rpm}} = 1600\,\mathrm{rpm}$. All other parameters were identical to figures 10.2 and 10.3.

Figure 10.7 (a) shows simulated SLRR transients with the same inputs as the simulations presented previously in figure 10.3, except ω_{rpm} was varied between 100 rpm and 5000 rpm.

Figure 10.7 (b) shows the time τ at which the slope $\partial\Psi/\partial\tau$ in figure 10.7 (a) reached a maximum, as a function of $\omega_{\mathrm{rpm}}^{-1/2}$. The time τ at which the slope $\partial\Psi/\partial\tau$ reached a maximum is clearly linearly dependent on $\omega_{\mathrm{rpm}}^{-1/2}$.

Figure 10.8 (a) shows simulated SLRR transients with the same inputs as the simulations presented previously in figure 10.3, except $k^{\circ}_{\pm 3}$ was scaled between $10^{-1} \times k^{\circ}_{\pm 3}$ and $10^{3} \times k^{\circ}_{\pm 3}$, while keeping the ratio $k^{\circ}_{+3}/k^{\circ}_{-3}$ constant. The inset axis shows the same data as the main axis, except the time τ has been normalized to the time τ at which the slope $\partial\Psi/\partial\tau$ reached a maximum. Figure 10.8 (b) shows the time τ at which the slope $\partial\Psi/\partial\tau$ in figure 10.8 (a) reached a maximum, as a function of the factor of which $k^{\circ}_{\pm 3}$ was scaled, $x_{k^{\circ}_{\pm 3}}$.

The time τ at which the slope $\partial\Psi/\partial\tau$ in figure 10.8 (a) reached a maximum appear to scale with $x^{-1}_{k^{\circ}_{\pm 3}}$ when $x_{k^{\circ}_{\pm 3}} < 10$ and to become independent of $x_{k^{\circ}_{\pm 3}}$ for $x_{k^{\circ}_{\pm 3}} > 10$.

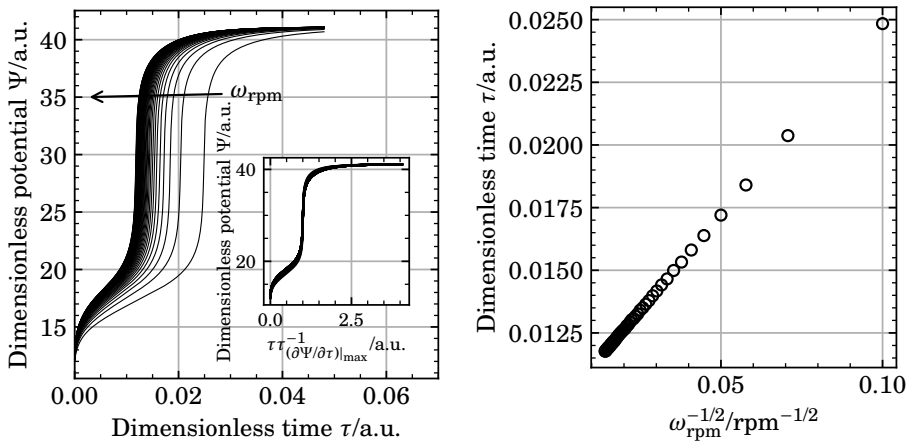

Figure 10.7: (a) Simulated SLRR transients with the same inputs as the simulations presented previously in figure 10.3. ω_{rpm} was varied between 100 rpm and 5000 rpm. (b) The time τ at which the slope $\partial\Psi/\partial\tau$ in (a) reached a maximum, as a function of $\omega_{\mathrm{rpm}}^{-1/2}$

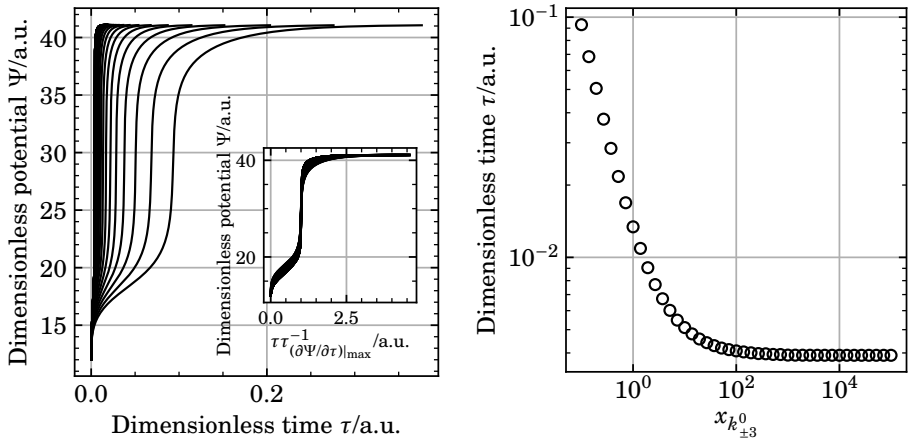

(a) (b)

Figure 10.8: (a) Simulated SLRR transients with the same inputs as the simulations presented previously in figure 10.3. $k^{\circ}_{\pm 3}$ was scaled between $10^{-1} \times k^{\circ}_{\pm 3}$ and $10^{3} \times k^{\circ}_{\pm 3}$, while keeping the ratio $k^{\circ}_{+3}/k^{\circ}_{-3}$ constant. (b) The time τ at which the slope $\partial\Psi/\partial\tau$ in (a) reached a maximum, as a function of the factor of which $k^{\circ}_{\pm 3}$ was scaled, $x_{k^{\circ}_{\pm 3}}$

Figure 10.9 shows the concentration profile of C_2, Ir(IV), across the grid at selected dimensionless potentials during a simulated SLRR transient in figure 10.8 (a) where $x_{k^\circ_{\pm 3}} = 10^4$. The concentration profiles corresponding to $x_{k^\circ_{\pm 3}} = 10^0$ are shown previously in figure 10.4a

The surface concentration of C_2 is close to zero at $\Psi = 15$ through $\Psi = 26$, and starts to increase between $\Psi = 26$ and $\Psi = 28$. This correspond to the part of the potential transients in figure 10.8a where the slope $\partial\Psi/\partial\tau$ is high. The surface concentration is close to the bulk concentration at $\Psi \geq 33$. This means that reduction of Ir(IV) to Ir(III), reaction (6.2), is diffusion controlled in these simulations.

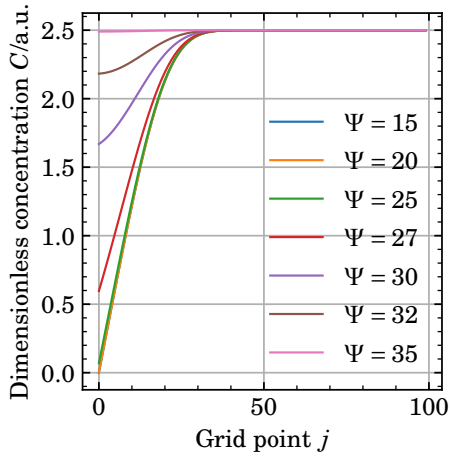

Figure 10.9: Concentration profile of C_2 over the discretized grid at selected potentials from the SLRR simulation in figure 10.8a where $x_{k^\circ_{\pm 3}} = 10^4$.

Figure 10.10 shows the current densities of reaction (10.1) (J_1,a), reaction (10.2) (J_2,b) and reaction (6.2) (J_3,c) during the SLRR simulations in figure 10.8 (a) at selected values of $x_{k^\circ_{\pm 3}}$. The x-axes has been normalized to the time which the slope $\partial\Psi/\partial\tau$ in figure 10.8 (a) reached a maximum. At $x_{k^\circ_{\pm 3}} \geq 10^2$, reaction (6.2) ($J_3$,c) appear to become constant with time at $\tau\tau^{-1}_{(\partial\Psi/\partial\tau)|_{\max}}$. This mean the rate of the SLRR reaction was controlled by diffusion of Ir(IV) when the rate constants $k^\circ_{\pm 3}$ was scaled by a factor larger than 10^2.

Figure 10.11 shows simulated SLRR transients with the same inputs as the simulations presented previously in figure 10.3, except c_3 was varied between $1 \times 10^{-15}\,\mathrm{mol\,cm^{-3}}$ and $1 \times 10^{-18}\,\mathrm{mol\,cm^{-3}}$.

The first part of the SLRR transients, before the sharp increase in potential, appears

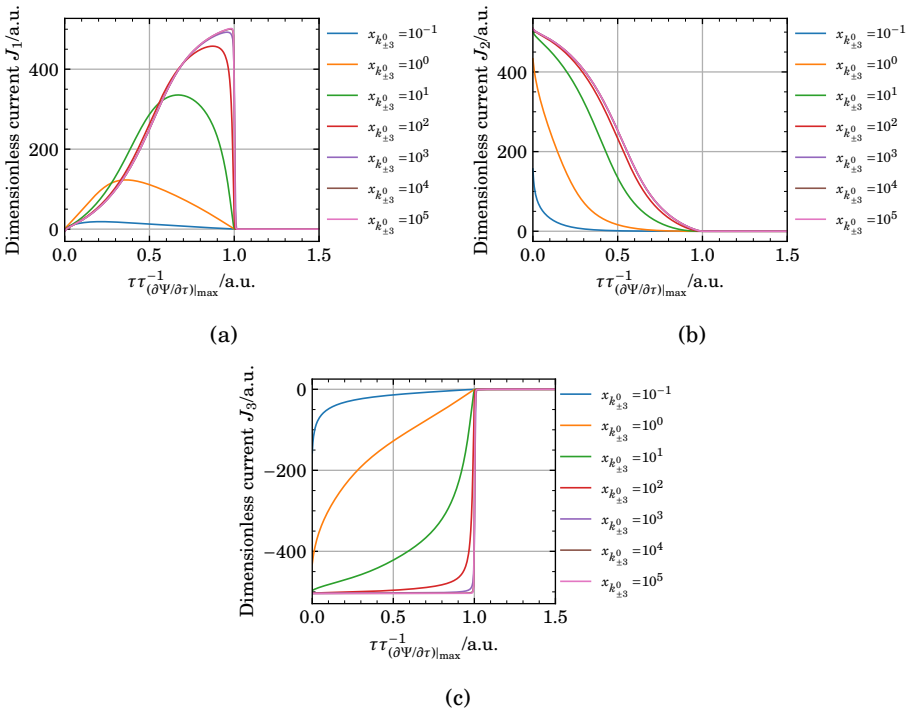

Figure 10.10: Current densities of reaction (10.1) (J_1,a), reaction (10.2) (J_2,b) and reaction (6.2) (J_3,c) during the SLRR simulations in figure 10.8 (a) at selected values of $x_{k^*_{\pm 3}}$.

be insensitive to the concentration of C_3 in the bulk. Only the steady state potential of which the potential transient appears to converge towards appears to be affected by the concentration of C_3 in the bulk of the electrolyte.

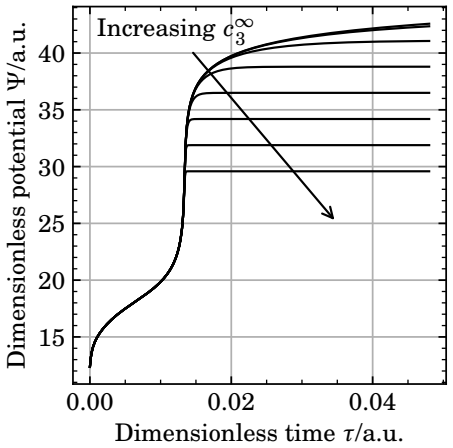

Figure 10.11: Simulated SLRR transients with the same inputs as the simulations presented previously in figure 10.3. c_3 was varied between $1 \times 10^{-15}\,\mathrm{mol\,cm^{-3}}$ and $1 \times 10^{-8}\,\mathrm{mol\,cm^{-3}}$.

10.7 Discussion

We have demonstrated how open circuit potential transients obtained through SLRR experiments can be simulated by microkinetic simulations and fitted to experimentally obtained data.

The results indicate that the rate of oxidation Cu_{UPD} by K_2IrCl_6 in solutions containing $0.5\,\mathrm{mol\,dm^{-3}}$ H_2SO_4, $1\,\mathrm{mmol\,dm^{-3}}$ $CuSO_4$ and $10\,\mu\mathrm{mol\,dm^{-3}}$ K_2IrCl_6 is controlled by mixed kinetics and mass transport of Ir(IV) to Ir(III) at room temperature:

i The concentration profiles of Ir(IV) in figure 10.4 and voltammograms in figure 10.6 show that reduction of Ir(IV) to Ir(III) is not only diffusion controlled in the potential range where Cu_{UPD} is oxidised, and

ii The time τ of which the slope $\partial\Psi/\partial\tau$ reached a maximum increased linearly with $\omega_{\mathrm{rpm}}^{-1}$.

iii When $k^{\circ}_{\pm 3}$ was scaled by a factor of 10^{-1} through 10^{5}, the rate of reaction (6.2) transitioned from mixed control to diffusion control.

The time of which the slope $\partial\Psi/\partial\tau$ in figure 10.8 (a) reached a maximum scaled with $x^{-1}_{k^{\circ}_{\pm 3}}$ for $x_{k^{\circ}_{\pm 3}} < 10$. This is consistent with the rate of the SLRR reaction being controlled by reaction (6.2) under mixed control, where the kinetic contribution is multiplied by $x_{k^{\circ}_{\pm 3}}$ until the reaction becomes limited by mass transport.

The time of which the slope $\partial\Psi/\partial\tau$ in figure 10.8 (a) reached a maximum became independent of $x_{k^{\circ}_{\pm 3}}$ for $x_{k^{\circ}_{\pm 3}} > 10$. This is consistent with the rate of the SLRR reaction initially being determined by reaction (6.2) under mixed control, where the kinetic contribution is increased to such an extent to that mass transport becomes limiting.

The overall shape of the simulated SLRR transients seems to be insensitive to whether the total rate is determined by mixed kinetics and mass transport, or mass transport only. The insets in figure 10.8 (a) appear to overlap, even though the overall rate transitions from mixed control to pure mass transport control.

We have previously, in chapter 7, argued that reduction of Ir(IV) to Ir(III) is diffusion controlled if the time of which the slope of $\partial\Psi/\partial\tau$ reaches a maximum is linearly dependent with $\omega^{-1/2}_{\text{rpm}}$. The above results show that this is necessarily true. A linear relation is also observed for reactions under mixed kinetic and diffusion control.

10.8 Conclusions

We have demonstrated how potential transients obtained through surface limited redox replacement can be simulated using microkinetic simulations, which can serve as a valuable tool when evaluating the kinetics and reaction mechanisms of SLRR experiments.

We compared simulations to experimentally obtained potential transients, where simulations could be fitted to the experimentally obtained values with excellent results. Also comparing simulations to voltammograms and potentiostatic current transients coupled with in-situ methods such as reflectivity [106], EQCM [101] and EXAFS/XANES [122] would arguably provide more extensive insight into the surface processes occuring during the experiments.

Summary and outlook

The work in this thesis has shown how galvanic displacement is a powerful tool for preparing thin films of noble metals onto suitable substrates. Through galvanic displacement of Ni and Cu with Ir, we have shown how active catalysts can be prepared in simple procedures, which holds great potential if optimized. The use of Cu in particular is promising as some of the challenges related to use of Ni is mitigated.

In order to perform a rational optimization of a galvanic displacement procedure, it is of great importance to known the mechanism of each reaction involved. Through galvanic displacement of Cu monolayers on Au electrodes and Au nanoparticles, we show that the yield of the galvanic displacement reaction appears to reach an optimium at low electrolyte agitation, and that the yield is, conterintuitively, larger with Ir(IV) precursor solutions than with Ir(III) precursor solutions.

Last, we demonstrate how microkinetic simulations can be used to model both the kinetics and the mass transport in such reactions.

Due to the highly corrosive conditions at PEMWE anodes, the Ir catalyst prepared slowly corroded. A thin layer of Ir on a core/shell catalyst will only expose the core earlier than a corresponding thick layer of Ir. Perhaps it would be more rational to first focus on increasing the *stability* of catalysts for PEM water electrolyzer anodes, and then to minimize the loading of such a catalyst through the use of porous and core/shell structures.

Catalyst stability aside, we suggest a method for preparation of larger batches of oxide supported Ir-based core/shell catalysts. If one prepares a MO_x/Au core/shell substrate where MO_x is a stable conducting oxide such as antimony doped tin oxide (ATO), the methods presented in this thesis can be used to prepare MO_x/Au/Ir electrocatalysts. Exposing an agitated suspension of MO_x/Au to an electrode held at a suitable potential, or a Cu sheet, in a solution containing Cu^{2+}(aq) should cause an underpotentially deposited layer of Cu_{UPD} to form on the Au surface. Subsequent removal of the electrode or Cu sheet and addition of an Ir precursor solution to the

suspension should then cause galvanic displacement of Cu_{UPD} by Ir. Repeating this procedure as many times as necesarry has potential for preparing Ir based core/shell catalyst for oxygen evolution on PEMWE anodes.

Bibliography

[1] Qi Feng, Xiao-Zi Yuan, Gaoyang Liu, Bing Wei, Zhen Zhang, Hui Li, and Haijiang Wang. A review of proton exchange membrane water electrolysis on degradation mechanisms and mitigation strategies. *Journal of Power Sources*, 366:33–55, October 2017.

[2] J. M. Carrasco, L. G. Franquelo, J. T. Bialasiewicz, E. Galvan, R. C. PortilloGuisado, M. A. M. Prats, J. I. Leon, and N. Moreno-Alfonso. Power-Electronic Systems for the Grid Integration of Renewable Energy Sources: A Survey. *IEEE Transactions on Industrial Electronics*, 53(4):1002–1016, June 2006.

[3] Exposed: Child labour behind smart phone and electric car batteries.

[4] S. Shiva Kumar and V. Himabindu. Hydrogen production by PEM water electrolysis – A review. *Materials Science for Energy Technologies*, 2(3):442–454, December 2019.

[5] Marcelo Carmo, David L. Fritz, Jürgen Mergel, and Detlef Stolten. A comprehensive review on PEM water electrolysis. *International Journal of Hydrogen Energy*, 38(12):4901–4934, April 2013.

[6] Gordon Aylward and Tristan Findlay. *SI Chemical Data*. John Wiley and Sons Ltd, sixth edition, 2008.

[7] A. Hauch, R. Küngas, P. Blennow, A. B. Hansen, J. B. Hansen, B. V. Mathiesen, and M. B. Mogensen. Recent advances in solid oxide cell technology for electrolysis. *Science*, 370(6513), October 2020.

[8] Libin Lei, Jihao Zhang, Zhihao Yuan, Jianping Liu, Meng Ni, and Fanglin Chen. Progress Report on Proton Conducting Solid Oxide Electrolysis Cells. *Advanced Functional Materials*, 29(37):1903805, 2019.

[9] Jh Russell, Lj Nuttal, and Ap Fickett. Hydrogen Generation by Solid Polymer Electrolyte Water Electrolysis. *Abstracts of Papers of the American Chemical Society*, (AUG26):2–2, 1973.

[10] J. Ahn and R. Holze. Bifunctional electrodes for an integrated water-electrolysis and hydrogen-oxygen fuel cell with a solid polymer electrolyte. *Journal of Applied Electrochemistry*, 22(12):1167–1174, December 1992.

[11] M. H. Miles, E. A. Klaus, B. P. Gunn, J. R. Locker, W. E. Serafin, and S. Srinivasan. The oxygen evolution reaction on platinum, iridium, ruthenium and their alloys at 80°C in acid solutions. *Electrochimica Acta*, 23(6):521–526, June 1978.

[12] Jakob Kibsgaard and Ib Chorkendorff. Considerations for the scaling-up of water splitting catalysts. *Nature Energy*, 4(6):430–433, June 2019.

[13] Zhenbin Wang, Ya-Rong Zheng, Ib Chorkendorff, and Jens K. Nørskov. Acid-Stable Oxides for Oxygen Electrocatalysis. *ACS Energy Letters*, 5(9):2905–2908, September 2020.

[14] Keith B. Oldham, Jan C. Myland, and Alan M. Bond. *Electrochemical Science and Technology*. John Wiley & Sons Inc, 2011.

[15] John Newman and Karen E. Thomas-Alyea. *Electrochemical Systems*. John Wiley & Sons Inc, third edition, 2004.

[16] D. Pletcher, R. Greff, R. Peat, L. M. Peter, and R. Robinson. *Instrumental Methods in Electrochemistry - 1st Edition*. Woodheat Publishing Limited, 2001.

[17] Anita Hamar Reksten, Heidi Thuv, Frode Seland, and Svein Sunde. The oxygen evolution reaction mechanism at IrxRu1-xO2 powders produced by hydrolysis synthesis. *Journal of Electroanalytical Chemistry*, April 2018.

[18] L. D. Burke and P. F. Nugent. The electrochemistry of gold: I the redox behaviour of the metal in aqueous media. *Gold Bulletin*, 30(2):43–53, June 1997.

[19] Allen J. Bard, Roger Parsons, and Joseph Jordan. *Standard Potentials in Aqueous Solution*. CRC Press, August 1985.

[20] G. Tremiliosi-Filho, L. H. Dall'Antonia, and G. Jerkiewicz. Growth of surface oxides on gold electrodes under well-defined potential, time and temperature conditions. *Journal of Electroanalytical Chemistry*, 578(1):1–8, April 2005.

[21] Z. Shi, J. Lipkowski, M. Gamboa, P. Zelenay, and A. Wieckowski. Investigations of SO42- adsorption at the Au(111) electrode by chronocoulometry and radiochemistry. *Journal of Electroanalytical Chemistry*, 366(1):317–326, March 1994.

[22] Gregory J. Edens, Xiaoping Gao, and Michael J. Weaver. The adsorption of sulfate on gold(111) in acidic aqueous media: Adlayer structural inferences from infrared spectroscopy and scanning tunneling microscope. *Journal of Electroanalytical Chemistry*, 375(1):357–366, September 1994.

[23] Zenonas Jusys and Stanley Bruckenstein. Electrochemical Quartz Crystal Microgravimetry of Gold in Perchloric and Sulfuric Acid Solutions. *Electrochemical and Solid-State Letters*, 1(2):74, June 1998.

[24] B. Madry, K. Wandelt, and M. Nowicki. Deposition of copper multilayers on Au(111) in sulfuric acid solution: An electrochemical scanning tunneling microscopy study. *Surface Science*, 637-638:77–84, July 2015.

[25] B. Madry, K. Wandelt, and M. Nowicki. Deposition of copper and sulfate on Au(111): New insights. *Applied Surface Science*, 388:678–683, December 2016.

[26] Michal Grdeń, Mariusz Łukaszewski, Gregory Jerkiewicz, and Andrzej Czerwiński. Electrochemical behaviour of palladium electrode: Oxidation, electrodissolution and ionic adsorption. *Electrochimica Acta*, 53(26):7583–7598, November 2008.

[27] L. H. Dall'Antonia, G. Tremiliosi-Filho, and G. Jerkiewicz. Influence of temperature on the growth of surface oxides on palladium electrodes. *Journal of Electroanalytical Chemistry*, 502(1):72–81, April 2001.

[28] K. Juodkazis, J. Juodkazytė, B. Šebeka, G. Stalnionis, and A. Lukinskas. Anodic Dissolution of Palladium in Sulfuric Acid: An Electrochemical Quartz Crystal Microbalance Study. *Russian Journal of Electrochemistry*, 39(9):954–959, September 2003.

[29] J. W. Simons and Ted B. Flanagan. Absorption Isotherms of Hydrogen in the α-Phase of the Hydrogen-Palladium System. *The Journal of Physical Chemistry*, 69(11):3773–3781, November 1965.

[30] J. F. Lynch and Ted B. Flanagan. Dynamic equilibrium between chemisorbed and absorbed hydrogen in the palladium/hydrogen system. *The Journal of Physical Chemistry*, 77(22):2628–2634, October 1973.

[31] T B Flanagan and W A Oates. The Palladium-Hydrogen System. *Annual Review of Materials Science*, 21(1):269–304, 1991.

[32] H. Conrad, G. Ertl, and E. E. Latta. Adsorption of hydrogen on palladium single crystal surfaces. *Surface Science*, 41(2):435–446, February 1974.

[33] Gregory Jerkiewicz and Alireza Zolfaghari. Comparison of Hydrogen Electroadsorption from the Electrolyte with Hydrogen Adsorption from the Gas Phase. *Journal of the Electrochemical Society*, 143(4):1240, April 1996.

[34] Stéphane Bastide, Claudia Zlotea, Michel Laurent, Michel Latroche, and Christine Cachet-Vivier. Direct assessment from cyclic voltammetry of size effect on the hydrogen sorption properties of Pd nanoparticle/carbon hybrids. *Journal of Electroanalytical Chemistry*, 706:33–39, October 2013.

[35] R. Lässer and K. H. Klatt. Solubility of hydrogen isotopes in palladium. *Physical Review B*, 28(2):748–758, July 1983.

[36] Abigail Rose, Stephanie Maniguet, Rebecca J. Mathew, Claire Slater, Jun Yao, and Andrea E. Russell. Hydride phase formation in carbon supported palladium nanoparticle electrodes investigated using in situ EXAFS and XRD. *Physical Chemistry Chemical Physics*, 5(15):3220–3225, July 2003.

[37] C. Gabrielli, P. P. Grand, A. Lasia, and H. Perrot. Investigation of Hydrogen Adsorption and Absorption in Palladium Thin Films II. Cyclic Voltammetry. *Journal of The Electrochemical Society*, 151(11):A1937–A1942, November 2004.

[38] Hugues Duncan and Andrzej Lasia. Separation of hydrogen adsorption and absorption on Pd thin films. *Electrochimica Acta*, 53(23):6845–6850, October 2008.

[39] Ramesh Kumar Singh, Rahul Ramesh, Ruttala Devivaraprasad, Arup Chakraborty, and Manoj Neergat. Hydrogen Interaction (Electrosorption and Evolution) Characteristics of Pd and Pd3Co Alloy Nanoparticles: An In-situ Investigation with Electrochemical Impedance Spectroscopy. *Electrochimica Acta*, 194:199–210, March 2016.

[40] Hugues Duncan and Andrzej Lasia. Mechanism of hydrogen adsorption/absorption at thin Pd layers on Au(111). *Electrochimica Acta*, 52(21):6195–6205, June 2007.

[41] E. L. MacNamara. The Electrodeposition of Iridium. *Journal of The Electrochemical Society*, 109(1):61–63, January 1962.

[42] T. Jones. Iridium plating. *Metal Finishing*, 102(6):87–103, June 2004.

[43] A. A. F Grupioni, E Arashiro, and T. A. F Lassali. Voltammetric characterization of an iridium oxide-based system: The pseudocapacitive nature of the Ir0.3Mn0.7O2 electrode. *Electrochimica Acta*, 48(4):407–418, December 2002.

[44] Dong-Qiang Liu, Sung-Hun Yu, Se-Wan Son, and Seung-Ki Joo. Electrochemical Performance of Iridium Oxide Thin Film for Supercapacitor Prepared by Radio Frequency Magnetron Sputtering Method. *ECS Transactions*, 16(1):103, December 2008.

[45] Yi-Ting Shih, Kuei-Yi Lee, and Ying-Sheng Huang. Characterization of iridium dioxide–carbon nanotube nanocomposites grown onto graphene for supercapacitor. *Journal of Alloys and Compounds*, 619:131–137, January 2015.

[46] Youngwoo Jung, Jaeyoung Lee, and Yongsug Tak. Electrochromic Mechanism of IrO2 Prepared by Pulsed Anodic Electrodeposition. *Electrochemical and Solid-State Letters*, 7(2):H5, December 2003.

[47] S Gottesfeld, J D E McIntyre, G Beni, and J L Shay. Electrochromism in anodic iridium oxide films. *Appl. Phys. Lett.*, 33:4, 1978.

[48] S. Gottesfeld and J. D. E. McIntyre. Electrochromism in Anodic Iridium Oxide Films II . pH Effects on Corrosion Stability and the Mechanism of Coloration and Bleaching. *Journal of The Electrochemical Society*, 126(5):742–750, May 1979.

[49] Wen-Ding Huang, Hung Cao, Sanchali Deb, Mu Chiao, and J. C. Chiao. A flexible pH sensor based on the iridium oxide sensing film. *Sensors and Actuators A: Physical*, 169(1):1–11, September 2011.

[50] Patrick Steegstra and Elisabet Ahlberg. In situ pH measurements with hydrous iridium oxide in a rotating ring disc configuration. *Journal of Electroanalytical Chemistry*, 685:1–7, October 2012.

[51] Jongman Park, Moonhee Kim, and Shinseon Kim. Surface renewable nano-iridium oxide polymeric composite pH electrodes. *Sensors and Actuators B: Chemical*, 204:197–202, December 2014.

[52] Tae Yong Kim and Sung Yang. Fabrication method and characterization of electrodeposited and heat-treated iridium oxide films for pH sensing. *Sensors and Actuators B: Chemical*, 196:31–38, June 2014.

[53] S. C Mailley, M Hyland, P Mailley, J. M McLaughlin, and E. T McAdams. Electrochemical and structural characterizations of electrodeposited iridium oxide thin-film electrodes applied to neurostimulating electrical signal. *Materials Science and Engineering: C*, 21(1):167–175, September 2002.

[54] Daniel F. Abbott, Dmitry Lebedev, Kay Waltar, Mauro Povia, Maarten Nachtegaal, Emiliana Fabbri, Christophe Copéret, and Thomas J. Schmidt. Iridium Oxide for the Oxygen Evolution Reaction: Correlation between Particle Size,

Morphology, and the Surface Hydroxo Layer from Operando XAS. *Chemistry of Materials*, 28(18):6591–6604, September 2016.

[55] Anita Reksten. *Iridium-Based Electrocatalysts for the Oxygen Evolution Reaction*. Doctoral thesis, Norwegian University of Science and Technology, 2016.

[56] S. Siracusano, V. Baglio, S. A. Grigoriev, L. Merlo, V. N. Fateev, and A. S. Aricò. The influence of iridium chemical oxidation state on the performance and durability of oxygen evolution catalysts in PEM electrolysis. *Journal of Power Sources*, 366(Supplement C):105–114, October 2017.

[57] P. Lettenmeier, J. Majchel, L. Wang, V. A. Saveleva, S. Zafeiratos, E. R. Savinova, J.-J. Gallet, F. Bournel, A. S. Gago, and K. A. Friedrich. Highly active nano-sized iridium catalysts: Synthesis and operando spectroscopy in a proton exchange membrane electrolyzer. *Chemical Science*, 9(14):3570–3579, 2018.

[58] Marc Ledendecker, Simon Geiger, Katharina Hengge, Joohyun Lim, Serhiy Cherevko, Andrea M. Mingers, Daniel Göhl, Guilherme V. Fortunato, Daniel Jalalpoor, Ferdi Schüth, Christina Scheu, and Karl J. J. Mayrhofer. Towards maximized utilization of iridium for the acidic oxygen evolution reaction. *Nano Research*, 12(9):2275–2280, September 2019.

[59] Robert Tang-Kong, Chrisopher E. D. Chidsey, and Paul C. McIntyre. Reversible Decay of Oxygen Evolution Activity of Iridium Catalysts. *Journal of The Electrochemical Society*, 166(14):H712–H717, January 2019.

[60] E. Fabbri, A. Habereder, K. Waltar, R. Kötz, and T. J. Schmidt. Developments and perspectives of oxide-based catalysts for the oxygen evolution reaction. *Catalysis Science & Technology*, 4(11):3800–3821, October 2014.

[61] Sergio Trasatti. Physical electrochemistry of ceramic oxides. *Electrochimica Acta*, 36(2):225–241, January 1991.

[62] Thierry Pauporté, Daniel Aberdam, Jean-Louis Hazemann, René Faure, and Robert Durand. X-ray absorption in relation to valency of iridium in sputtered iridium oxide films. *Journal of Electroanalytical Chemistry*, 465(1):88–95, April 1999.

[63] A. Robert Hillman, Magdalena A. Skopek, and Stephen J. Gurman. X-Ray spectroscopy of electrochemically deposited iridium oxide films: Detection of multiple sites through structural disorder. *Physical Chemistry Chemical Physics*, 13(12):5252–5263, March 2011.

[64] N. R. Elezović, P. Zabinski, U. Č. Lačnjevac, M. N. Krstajić Pajić, and V. D. Jović. Electrochemical deposition and characterization of iridium oxide films

on Ti2AlC support for oxygen evolution reaction. *Journal of Solid State Electrochemistry*, 25(1):351–363, January 2021.

[65] Egil Rasten, Georg Hagen, and Reidar Tunold. Electrocatalysis in water electrolysis with solid polymer electrolyte. *Electrochimica Acta*, 48(25):3945–3952, November 2003.

[66] E. Mayousse, F. Maillard, F. Fouda-Onana, O. Sicardy, and N. Guillet. Synthesis and characterization of electrocatalysts for the oxygen evolution in PEM water electrolysis. *International Journal of Hydrogen Energy*, 36(17):10474–10481, August 2011.

[67] S. Siracusano, N. Van Dijk, E. Payne-Johnson, V. Baglio, and A. S. Aricò. Nanosized IrOx and IrRuOx electrocatalysts for the O2 evolution reaction in PEM water electrolysers. *Applied Catalysis B: Environmental*, 164(Supplement C):488–495, March 2015.

[68] Anita Hamar Reksten, Andrea E. Russell, Peter W. Richardson, Stephen J. Thompson, Karina Mathisen, Frode Seland, and Svein Sunde. An in situ XAS study of high surface-area IrO2 produced by the polymeric precursor synthesis. *Physical Chemistry Chemical Physics*, 22(34):18868–18881, September 2020.

[69] V. Birss, R. Myers, H. Angerstein-Kozlowska, and B. E. Conway. Electron Microscopy Study of Formation of Thick Oxide Films on Ir and Ru Electrodes. *Journal of The Electrochemical Society*, 131(7):1502–1510, July 1984.

[70] J. Mozota and B. E. Conway. Surface and bulk processes at oxidized iridium electrodes—I. Monolayer stage and transition to reversible multilayer oxide film behaviour. *Electrochimica Acta*, 28(1):1–8, January 1983.

[71] D.N. Buckley, L.D. Burke, and J.K. Mulcahy. The oxygen electrode. Part 7.-Influence of some electrical and electrolyte variables on the charge capacity of iridium in the anodic region. *Journal of the Chemical Society, Faraday Transactions 1: Physical Chemistry in Condensed Phases*, 72:1896–1902, 1976.

[72] Peter G. Pickup and V. I. Birss. A model for anodic hydrous oxide growth at iridium. *Journal of Electroanalytical Chemistry and Interfacial Electrochemistry*, 220(1):83–100, March 1987.

[73] Peter G. Pickup and Viola I. Birss. The Influence of the Aqueous Growth Medium on the Growth Rate, Composition, and Structure of Hydrous Iridium Oxide Films. *Journal of The Electrochemical Society*, 135(1):126–133, January 1988.

[74] C. Bock and V. I. Birss. Irreversible Decrease of Ir Oxide Film Redox Kinetics. *Journal of The Electrochemical Society*, 146(5):1766–1772, May 1999.

[75] D.N. Buckley and L.D. Burke. The oxygen electrode. Part 5. - Enhancement of charge capacity of an iridium surface in the anodic region. *Journal of the Chemical Society, Faraday Transactions 1: Physical Chemistry in Condensed Phases*, 71:1447–1459, 1975.

[76] Lars-Erik Owe, Mikhail Tsypkin, and Svein Sunde. The effect of phosphate on iridium oxide electrochemistry. *Electrochimica Acta*, 58:231–237, December 2011.

[77] V.i. Birss, C Bock, and H. Elzanowska. Hydrous Ir oxide films: The mechanism of the anodic prepeak reaction. *Canadian Journal of Chemistry*, 75(11):1687–1693, November 1997.

[78] Liudmila Ilyukhina, Svein Sunde, and Richard G. Haverkamp. Electronic Structure and Growth of Electrochemically Formed Iridium Oxide Films. *Journal of The Electrochemical Society*, 164(14):F1662–F1670, January 2017.

[79] Peter G. Pickup and Viola I. Birss. The kinetics of charging and discharging of iridium oxide films in aqueous and non-aqueous media. *Journal of Electroanalytical Chemistry and Interfacial Electrochemistry*, 240(1):185–199, January 1988.

[80] Nolwenn Mayet, Karine Servat, K. Boniface Kokoh, and Teko W. Napporn. Probing the Surface of Noble Metals Electrochemically by Underpotential Deposition of Transition Metals. *Surfaces*, 2(2):257–276, June 2019.

[81] D. M. Kolb, M. Przasnyski, and H. Gerischer. Underpotential deposition of metals and work function differences. *Journal of Electroanalytical Chemistry and Interfacial Electrochemistry*, 54(1):25–38, July 1974.

[82] S. Swathirajan and Stanley Bruckenstein. Thermodynamics and kinetics of underpotential deposition of metal monolayers on polycrystalline substrates. *Electrochimica Acta*, 28(7):865–877, July 1983.

[83] Stephen W. T. Price, Jonathon D. Speed, Prabalini Kannan, and Andrea E. Russell. Exploring the First Steps in Core–Shell Electrocatalyst Preparation: In Situ Characterization of the Underpotential Deposition of Cu on Supported Au Nanoparticles. *Journal of the American Chemical Society*, 133(48):19448–19458, December 2011.

[84] Athanasios Papaderakis, Ioanna Mintsouli, Jenia Georgieva, and Sotiris Sotiropoulos. Electrocatalysts Prepared by Galvanic Replacement. *Catalysts*, 7(3):80, March 2017.

[85] Geon Dae Moon, Sungwook Ko, Yuho Min, Jie Zeng, Younan Xia, and Unyong Jeong. Chemical transformations of nanostructured materials. *Nano Today*, 6(2):186–203, April 2011.

[86] A. Touni, A. Papaderakis, D. Karfaridis, A. Banti, I. Mintsouli, D. Lambropoulou, and S. Sotiropoulos. Oxygen evolution at IrO2-modified Ti anodes prepared by a simple galvanic deposition method. *Journal of Electroanalytical Chemistry*, 855:113485, December 2019.

[87] Lourdes Vázquez-Gómez, Sandro Cattarin, Paolo Guerriero, and Marco Musiani. Hydrogen evolution on porous Ni cathodes modified by spontaneous deposition of Ru or Ir. *Electrochimica Acta*, 53(28):8310–8318, November 2008.

[88] Matteo Duca, Edoardo Guerrini, Alessandra Colombo, and Sergio Trasatti. Activation of Nickel for Hydrogen Evolution by Spontaneous Deposition of Iridium. *Electrocatalysis*, 4(4):338–345, August 2013.

[89] A. Papaderakis, N. Pliatsikas, Ch. Prochaska, G. Vourlias, P. Patsalas, D. Tsiplakides, S. Balomenou, and S. Sotiropoulos. Oxygen Evolution at IrO2 Shell–Ir-Ni Core Electrodes Prepared by Galvanic Replacement. *The Journal of Physical Chemistry C*, 120(36):19995–20005, September 2016.

[90] Sophia R. Mellsop, Alister Gardiner, and Aaron T. Marshall. Spontaneous Deposition of Iridium onto Nickel Substrates for the Oxygen Evolution Reaction. *Electrocatalysis*, 7(3):226–234, May 2016.

[91] A. Papaderakis, N. Pliatsikas, P. Patsalas, D. Tsiplakides, S. Balomenou, A. Touni, and S. Sotiropoulos. Hydrogen evolution at Ir-Ni bimetallic deposits prepared by galvanic replacement. *Journal of Electroanalytical Chemistry*, 808(Supplement C):21–27, January 2018.

[92] Shaun M. Alia, Sarah Shulda, Chilan Ngo, Svitlana Pylypenko, and Bryan S. Pivovar. Iridium-Based Nanowires as Highly Active, Oxygen Evolution Reaction Electrocatalysts. *ACS Catalysis*, 8(3):2111–2120, March 2018.

[93] Seungyeon Baek, Kwang Hwan Kim, Myung Jun Kim, and Jae Jeong Kim. Morphology control of noble metal catalysts from planar to dendritic shapes by galvanic displacement. *Applied Catalysis B: Environmental*, 217:313–321, November 2017.

[94] Melissa F. Mrozek, Yong Xie, and Michael J. Weaver. Surface-Enhanced Raman Scattering on Uniform Platinum-Group Overlayers: Preparation by Redox Replacement of Underpotential-Deposited Metals on Gold. *Analytical Chemistry*, 73(24):5953–5960, December 2001.

[95] N. Dimitrov, R. Vasilic, and N. Vasiljevic. A Kinetic Model for Redox Replacement of UPD Layers. *Electrochemical and Solid-State Letters*, 10(7):D79–D83, July 2007.

[96] L. T. Viyannalage, R. Vasilic, and N. Dimitrov. Epitaxial Growth of Cu on Au(111) and Ag(111) by Surface Limited Redox ReplacementAn Electrochemical and STM Study. *The Journal of Physical Chemistry C*, 111(10):4036–4041, March 2007.

[97] Chandru Thambidurai, Youn-Geun Kim, and John L. Stickney. Electrodeposition of Ru by atomic layer deposition (ALD). *Electrochimica Acta*, 53(21):6157–6164, September 2008.

[98] M. Fayette, Y. Liu, D. Bertrand, J. Nutariya, N. Vasiljevic, and N. Dimitrov. From Au to Pt via Surface Limited Redox Replacement of Pb UPD in One-Cell Configuration. *Langmuir*, 27(9):5650–5658, May 2011.

[99] Dincer Gokcen, Sang-E. Bae, and Stanko R. Brankovic. Kinetics of Metal Deposition via Surface-Limited Redox Replacement Reaction. *ECS Transactions*, 35(21):11–22, October 2011.

[100] Dincer Gokcen, Sang-Eun Bae, and Stanko R. Brankovic. Reaction kinetics of metal deposition via surface limited red-ox replacement of underpotentially deposited metal monolayers. *Electrochimica Acta*, 56(16):5545–5553, June 2011.

[101] C. Mitchell, M. Fayette, and N. Dimitrov. Homo- and hetero-epitaxial deposition of Au by surface limited redox replacement of Pb underpotentially deposited layer in one-cell configuration. *Electrochimica Acta*, 85:450–458, December 2012.

[102] J. Nutariya, M. Fayette, N. Dimitrov, and N. Vasiljevic. Growth of Pt by surface limited redox replacement of underpotentially deposited hydrogen. *Electrochimica Acta*, 112:813–823, December 2013.

[103] S. Ambrozik, B. Rawlings, N. Vasiljevic, and N. Dimitrov. Metal deposition via electroless surface limited redox replacement. *Electrochemistry Communications*, 44:19–22, July 2014.

[104] S. Ambrozik and N. Dimitrov. The Deposition of Pt via Electroless Surface Limited Redox Replacement. *Electrochimica Acta*, 169:248–255, July 2015.

[105] Zakiya Al Amri, Michael P. Mercer, and Natasa Vasiljevic. Surface Limited Redox Replacement Deposition of Platinum Ultrathin Films on Gold: Thickness and Structure Dependent Activity towards the Carbon Monoxide and Formic Acid Oxidation reactions. *Electrochimica Acta*, 210:520–529, August 2016.

[106] Ela Bulut, Dongjun Wu, Nikhil Dole, Hasan Kilic, and Stanko R. Brankovic. Editors' Choice—Reaction Kinetics of Metal Deposition via Surface Limited Redox Replacement of Underpotentially Deposited Monolayer Studied by Surface Reflectivity and Open Circuit Potential Measurements. *Journal of The Electrochemical Society*, 164(4):D159–D168, January 2017.

[107] Johannes Dornhof, Gerald A. Urban, and Jochen Kieninger. Deposition of Copper Nanofilms by Surface-Limited Redox Replacement of Underpotentially Deposited Lead on Polycrystalline Gold. *Journal of The Electrochemical Society*, 166(1):D3001, August 2018.

[108] Aliya S. Lapp, Zhiyao Duan, Graeme Henkelman, and Richard M. Crooks. Combined Experimental and Theoretical Study of the Structure of AuPt Nanoparticles Prepared by Galvanic Exchange. *Langmuir*, 35(50):16496–16507, December 2019.

[109] S. R. Brankovic, J. X. Wang, and R. R. Adžić. Metal monolayer deposition by replacement of metal adlayers on electrode surfaces. *Surface Science*, 474(1–3):L173–L179, March 2001.

[110] J. Zhang, Y. Mo, M. B. Vukmirovic, R. Klie, K. Sasaki, and R. R. Adzic. Platinum Monolayer Electrocatalysts for O2 Reduction: Pt Monolayer on Pd(111) and on Carbon-Supported Pd Nanoparticles. *The Journal of Physical Chemistry B*, 108(30):10955–10964, July 2004.

[111] Dincer Gokcen, Sang-Eun Bae, and Stanko R. Brankovic. Stoichiometry of Pt Submonolayer Deposition via Surface-Limited Redox Replacement Reaction. *Journal of The Electrochemical Society*, 157(11):D582–D587, November 2010.

[112] Mohsen Khosravi and Mohammad K. Amini. Carbon paper supported Pt/Au catalysts prepared via Cu underpotential deposition-redox replacement and investigation of their electrocatalytic activity for methanol oxidation and oxygen reduction reactions. *International Journal of Hydrogen Energy*, 35(19):10527–10538, October 2010.

[113] Seth L. Knupp, Miomir B. Vukmirovic, Pradeep Haldar, Jeffrey A. Herron, Manos Mavrikakis, and Radoslav R. Adzic. Platinum Monolayer Electrocatalysts for O2 Reduction: Pt Monolayer on Carbon-Supported PdIr Nanoparticles. *Electrocatalysis*, 1(4):213–223, December 2010.

[114] Tumaini S. Mkwizu, Mkhulu K. Mathe, and Ignacy Cukrowski. Electrodeposition of Multilayered Bimetallic Nanoclusters of Ruthenium and Platinum via Surface-Limited Redox-Replacement Reactions for Electrocatalytic Applications. *Langmuir*, 26(1):570–580, January 2010.

[115] Kotaro Sasaki, Hideo Naohara, Yun Cai, Yong Man Choi, Ping Liu, Miomir B. Vukmirovic, Jia X. Wang, and Radoslav R. Adzic. Core-Protected Platinum Monolayer Shell High-Stability Electrocatalysts for Fuel-Cell Cathodes. *Angewandte Chemie International Edition*, 49(46):8602–8607, November 2010.

[116] K. Sasaki, J. X. Wang, H. Naohara, N. Marinkovic, K. More, H. Inada, and R. R. Adzic. Recent advances in platinum monolayer electrocatalysts for oxygen reduction reaction: Scale-up synthesis, structure and activity of Pt shells on Pd cores. *Electrochimica Acta*, 55(8):2645–2652, March 2010.

[117] Wei-Ping Zhou, Kotaro Sasaki, Dong Su, Yimei Zhu, Jia X. Wang, and Radoslav R. Adzic. Gram-Scale-Synthesized Pd2Co-Supported Pt Monolayer Electrocatalysts for Oxygen Reduction Reaction. *The Journal of Physical Chemistry C*, 114(19):8950–8957, May 2010.

[118] Minhua Shao, Amra Peles, and Krista Shoemaker. Electrocatalysis on Platinum Nanoparticles: Particle Size Effect on Oxygen Reduction Reaction Activity. *Nano Letters*, 11(9):3714–3719, September 2011.

[119] Michael P. Humbert, Brandon H. Smith, Qi Wang, Steven N. Ehrlich, and Minhua Shao. Synthesis and Characterization of Palladium-Platinum Core-Shell Electrocatalysts for Oxygen Reduction. *Electrocatalysis*, 3(3-4):298–303, December 2012.

[120] Kurian A. Kuttiyiel, Kotaro Sasaki, YongMan Choi, Dong Su, Ping Liu, and Radoslav R. Adzic. Bimetallic IrNi core platinum monolayer shell electrocatalysts for the oxygen reduction reaction. *Energy & Environmental Science*, 5(1):5297–5304, January 2012.

[121] Kotaro Sasaki, Hideo Naohara, YongMan Choi, Yun Cai, Wei-Fu Chen, Ping Liu, and Radoslav R. Adzic. Highly stable Pt monolayer on PdAu nanoparticle electrocatalysts for the oxygen reduction reaction. *Nature Communications*, 3, 2012.

[122] Stephen W. T. Price, Jennifer M. Rhodes, Laura Calvillo, and Andrea E. Russell. Revealing the Details of the Surface Composition of Electrochemically Prepared Au@Pd Core@Shell Nanoparticles with in Situ EXAFS. *The Journal of Physical Chemistry C*, 117(47):24858–24865, November 2013.

[123] Dincer Gokcen, Qiuyi Yuan, and Stanko R. Brankovic. Nucleation of Pt Monolayers Deposited via Surface Limited Redox Replacement Reaction. *Journal of The Electrochemical Society*, 161(7):D3051–D3056, January 2014.

[124] Tumaini S. Mkwizu and Ignacy Cukrowski. Physico–chemical Modelling of Adlayer Phase Formation via Surface–limited Reactions of Copper in Relation

to Sequential Electrodeposition of Multilayered Platinum on Crystalline Gold. *Electrochimica Acta*, 147:432–441, November 2014.

[125] Ali Abdelhafiz, Adam Vitale, Corey Joiner, Eric Vogel, and Faisal M. Alamgir. Layer-by-Layer Evolution of Structure, Strain, and Activity for the Oxygen Evolution Reaction in Graphene-Templated Pt Monolayers. *ACS Applied Materials & Interfaces*, 7(11):6180–6188, March 2015.

[126] Haoxiong Nan, Xinlong Tian, Lijun Yang, Ting Shu, Huiyu Song, and Shijun Liao. A Platinum Monolayer Core-shell Catalyst with a Ternary Alloy Nanoparticle Core and Enhanced Stability for the Oxygen Reduction Reaction. *J. Nanomaterials*, 2015:5:5–5:5, January 2015.

[127] Xuejiao Yan, Haiyan Xiong, Qingguo Bai, Jan Frenzel, Conghui Si, Xiaoting Chen, Gunther Eggeler, and Zhonghua Zhang. Atomic layer-by-layer construction of Pd on nanoporous gold via underpotential deposition and displacement reaction. *RSC Advances*, 5(25):19409–19417, February 2015.

[128] Yu Dai and Shengli Chen. AuPt core-shell electrocatalysts for oxygen reduction reaction through combining the spontaneous Pt deposition and redox replacement of underpotential-deposited Cu. *International Journal of Hydrogen Energy*, 41(48):22976–22982, December 2016.

[129] Kaushik Jagannathan, David M. Benson, David B. Robinson, and John L. Stickney. Hydrogen Sorption Kinetics on Bare and Platinum-Modified Palladium Nanofilms, Grown by Electrochemical Atomic Layer Deposition (E-ALD). *Journal of The Electrochemical Society*, 163(12):D3047–D3052, 2016.

[130] Siddique Khateeb, Sandra Guerreo, Dong Su, Robert M. Darling, Lesia V. Protsailo, and Minhua Shao. Fuel Cell Performance of Palladium-Platinum Core-Shell Electrocatalysts Synthesized in Gram-Scale Batches. *Journal of The Electrochemical Society*, 163(7):F708–F713, January 2016.

[131] Shangqian Zhu, Jeffrey Yue, Xueping Qin, Zidong Wei, Zhixiu Liang, Radoslav R. Adzic, Stanko R. Brankovic, Zheng Du, and Minhua Shao. The Role of Citric Acid in Perfecting Platinum Monolayer on Palladium Nanoparticles during the Surface Limited Redox Replacement Reaction. *Journal of The Electrochemical Society*, 163(12):D3040–D3046, 2016.

[132] David M. Benson, Chu F. Tsang, Joshua D. Sugar, Kaushik Jagannathan, David B. Robinson, Farid El Gabaly, Patrick J. Cappillino, and John L. Stickney. Enhanced Kinetics of Electrochemical Hydrogen Uptake and Release by Palladium Powders Modified by Electrochemical Atomic Layer Deposition. *ACS Applied Materials & Interfaces*, 9(21):18338–18345, May 2017.

[133] Daisuke Takimoto, Tomohiro Ohnishi, Jeerapat Nutariya, Zhongrong Shen, Yusuke Ayato, Dai Mochizuki, Arnaud Demortière, Adrien Boulineau, and Wataru Sugimoto. Ru-core@Pt-shell nanosheet for fuel cell electrocatalysts with high activity and durability. *Journal of Catalysis*, 345:207–215, January 2017.

[134] Innocent Achari, Stephen Ambrozik, and Nikolay Dimitrov. Electrochemical Atomic Layer Deposition by Surface Limited Redox Replacement of Pd Thin Films in One-Cell Configuration Using Cu UPD Layers: Interrupting Mass-Transport Limited Growth. *Journal of The Electrochemical Society*, 165(15):J3074–J3082, January 2018.

[135] Liang Song, Zhixiu Liang, Miomir B. Vukmirovic, and Radoslav R. Adzic. Enhanced Oxygen Reduction Reaction Activity on Pt-Monolayer-Shell PdIr/Ni-Core Catalysts. *Journal of The Electrochemical Society*, 165(15):J3288–J3294, January 2018.

[136] Qiuyi Yuan, Yuki Wakisaka, Yohei Uemura, Takahiro Wada, Hiroko Ariga-Miwa, Satoru Takakusagi, Kiyotaka Asakura, and Stanko R. Brankovic. Reaction Stoichiometry and Mechanism of Pt Deposition via Surface Limited Redox Replacement of Copper UPD Layer on Au(111). *The Journal of Physical Chemistry C*, 122(29):16664–16673, July 2018.

[137] Naoya Aoki, Hideo Inoue, Takashi Okawa, Yuta Ikehata, Akira Shirai, Hideo Daimon, Takayuki Doi, Yuki Orikasa, Yoshiharu Uchimoto, Hiroshi Jinnai, Shin Inamoto, Yuji Otsuka, and Minoru Inaba. Enhancement of Oxygen Reduction Reaction Activity of Pd Core-Pt Shell Structured Catalyst on a Potential Cycling Accelerated Durability Test. *Electrocatalysis*, 9(2):125–138, March 2018.

[138] Deyu Qu, Chan-Yong Jung, Chi-Woo Lee, and Kohei Uosaki. Pt Monolayer Creation on a Au Surface via an Underpotentially Deposited Cu Route. *The Journal of Physical Chemistry C*, 123(5):2872–2881, February 2019.

[139] A. C. Mkhohlakali, X. Fuku, R. M. Modibedi, L. E. Khotseng, S. C Ray, and M. K. Mathe. Electrosynthesis and characterization of PdIr using electrochemical atomic layer deposition for ethanol oxidation in alkaline electrolyte. *Applied Surface Science*, 502:144158, February 2020.

[140] Fatima Haidar, Mathieu Maas, Andrea Piarristeguy, Annie Pradel, Sara Cavaliere, and Marie-Christine Record. Ultra-Thin Platinum Deposits by Surface-Limited Redox Replacement of Tellurium. *Nanomaterials*, 8(10), 2018.

[141] Ijjada Mahesh and A. Sarkar. Scale-Up Process of Core@Shell Monolayer Catalyst without Active Potential Control through Electroless Underpotential Deposition Galvanic Replacement. *ChemistrySelect*, 3(41):11622–11626, 2018.

[142] J. S. Fang, H. M. Wang, C. H. Hsu, Y. L. Cheng, and G. S. Chen. Growth of a Cu(Co) film by underpotential deposition of Co and controlling the time of the surface-limited redox replacement of Cu. *International Journal of Electrochemical Science*, 14(6):5143–5153, June 2019.

[143] Jia X. Wang, Hiromi Inada, Lijun Wu, Yimei Zhu, YongMan Choi, Ping Liu, Wei-Ping Zhou, and Radoslav R. Adzic. Oxygen Reduction on Well-Defined Core-Shell Nanocatalysts: Particle Size, Facet, and Pt Shell Thickness Effects. *Journal of the American Chemical Society*, 131(47):17298–17302, December 2009.

[144] Innocent Achari, Stephen Ambrozik, and Nikolay Dimitrov. Electrochemical Atomic Layer Deposition of Pd Ultrathin Films by Surface Limited Redox Replacement of Underpotentially Deposited H in a Single Cell. *The Journal of Physical Chemistry C*, 121(8):4404–4411, March 2017.

[145] Jeerapat Nutariya, Eri Kuroiwa, Daisuke Takimoto, Zhongrong Shen, Dai Mochizuki, and Wataru Sugimoto. Model electrode study of Ru@Pt core-shell nanosheet catalysts: Pure two-dimensional growth via surface limited redox replacement. *Electrochimica Acta*, 283:826–833, September 2018.

[146] Ryo Shirai, Masaru Irita, Tomohiro Kurose, Natasa Vasiljevic, and Masanori Hayase. A Miniature Fuel Cell with Monolithically Fabricated Si Electrodes: Application of Au-Pd-Pt Multilayer Catalyst. *Journal of The Electrochemical Society*, 166(15):D834–D842, 2019.

[147] Miomir B. Vukmirovic, Stoyan T. Bliznakov, Kotaro Sasaki, Jia X. Wang, and Radoslav R. Adzic. Electrodeposition of Metals in Catalyst Synthesis: The Case of Platinum Monolayer Electrocatalysts. *The Electrochemical Society Interface*, 20(2):33, January 2011.

[148] R. Vasilic and N. Dimitrov. Epitaxial Growth by Monolayer-Restricted Galvanic Displacement. *Electrochemical and Solid-State Letters*, 8(11):C173, September 2005.

[149] Nikolay Dimitrov. Recent Advances in the Growth of Metals, Alloys, and Multilayers by Surface Limited Redox Replacement (SLRR) Based Approaches. *Electrochimica Acta*, 209:599–622, August 2016.

[150] Hong Zhu, Ming-Chuan Luo, Ye-Zheng Cai, Zhao-Nan Sun, Hong Zhu, Ming-Chuan Luo, Ye-Zheng Cai, and Zhao-Nan Sun. Core-Shell Structured Elec-

trocatalysts for the Cathodic Oxygen Reduction Reaction in Proton Exchange Membrane Fuel Cells, Core-Shell Structured Electrocatalysts for the Cathodic Oxygen Reduction Reaction in Proton Exchange Membrane Fuel Cells. *Acta Physico-Chimica Sinca*, 32(10):2462–2474, June 2016.

[151] Alireza Zolfaghari and Brian E. Conway. Electroless deposition of Pt at a Pd electrode by reaction with sorbed H in Pd/H. *Journal of Electroanalytical Chemistry*, 488(2):151–153, July 2000.

[152] Patrick J. Cappillino, Joshua D. Sugar, Farid El Gabaly, Trevor Y. Cai, Zhi Liu, John L. Stickney, and David B. Robinson. Atomic-Layer Electroless Deposition: A Scalable Approach to Surface-Modified Metal Powders. *Langmuir*, 30(16):4820–4829, April 2014.

[153] Ingeborg A. Poulsen and Clifford S. Garner. A Thermodynamic and Kinetic Study of Hexachloro and Aquopentachloro Complexes of Iridium(III) in Aqueous Solutions. *Journal of the American Chemical Society*, 84(11):2032–2037, June 1962.

[154] James C. Chang and Clifford S. Garner. Kinetics of Aquation of Aquopentachloroiridate(III) and Chloride Anation of Diaquotetrachloroiridate(III) Anions. *Inorganic Chemistry*, 4(2):209–215, February 1965.

[155] Abbas A. El-Awady, Edwin J. Bounsall, and Clifford S. Garner. Kinetics of aquation of cis- and trans-diaquotetrachloroiridate(III) anions and chloride anation of 1,2,6-triaquotrichloroiridium(III). *Inorganic Chemistry*, 6(1):79–86, January 1967.

[156] W.J. Van Ooy and J.P.W. Houtman. Ligand Exchange in Iridium Hexahalocomplexes: Part 1. Behaviour of Complexes of Trivalent Iridium in Aqueous Solutions. *Radiochimica Acta*, 7(2-3):115–119, 1967.

[157] W.J. Van Ooy and J.P.W. Houtman. Ligand Exchange in Iridium Hexahalocomplexes Part 2. Influence of the pH on the Reactions of the Hexachloroiridite and Hexachloroiridate Ions in Aqueous Solutions. *Radiochimica Acta*, 20(1-2):47–50, 1973.

[158] En Sloth and Cs Garner. Exchange of Radioiridium Between Hexachloroiridate(iii) and Hexachloroiridate(iv) Ions. *Journal of the American Chemical Society*, 77(6):1440–1444, 1955.

[159] Ernest H Lyons. Electronic Configuration in Electrodeposition from Aqueous Solutions. *JOURNAL OF THE ELECTROCHEMICAL SOCIETY*, page 14, 1954.

[160] P. J. Ovenden. An Iridium Plating Solution. *Nature*, 179(4549):39–39, January 1957.

[161] Steven Le Vot, Lionel Roué, and Daniel Bélanger. Synthesis of Pt–Ir catalysts by coelectrodeposition: Application to ammonia electrooxidation in alkaline media. *Journal of Power Sources*, 223:221–231, February 2013.

[162] C. J. Tyrrell. The Electrodeposition of Iridium. *Transactions of the IMF*, 43(1):161–168, January 1965.

[163] C. J. Tyrrell. The Electrodeposition of Platinum-Iridium Alloys. *Transactions of the IMF*, 45(1):53–57, January 1967.

[164] Martin Mathews, B. D. LaFerriere, L. R. Pederson, and E. W. Hoppe. Plating of iridium for use as high purity electrodes in the assay of ultrapure copper. *Journal of Radioanalytical and Nuclear Chemistry*, 307(3):2577–2585, March 2016.

[165] Takashi Ohsaka, Motohiro Isaka, Katsuhiko Hirano, and Tomoji Ohishi. Effect of ultrasound sonication on electroplating of iridium. *Ultrasonics Sonochemistry*, 15(4):283–288, April 2008.

[166] Wangping Wu, Zhizhi Wang, Peng Jiang, and Zhipeng Tang. Effect of Electroplating Variables on Electrodeposition of Ni Rich Ni-Ir Alloys from Citrate Aqueous Solutions. *Journal of The Electrochemical Society*, 164(14):D985–D993, January 2017.

[167] G. Sheela, P. Malathy, and S. Pushpavanam. Electrodeposition of iridium. *Bulletin of Electrochemistry*, 15:208–210, 1999.

[168] Dunja Čukman and Marijan Vuković. Electrochemical behaviour of an electrodeposited iridium electrode in acid solution. *Journal of Electroanalytical Chemistry and Interfacial Electrochemistry*, 279(1):283–290, February 1990.

[169] G. Sheela, Malathy Pushpavanam, and S. Pushpavanam. A Modified Process for Iridium Electrodeposition. *Transactions of the IMF*, 78(5):191–193, January 2000.

[170] A. G. Muñoz and H. J. Lewerenz. Electroplating of Iridium onto Single-Crystal Silicon: Chemical and Electronic Properties of n-Si(111)/Ir Nanojunctions. *Journal of The Electrochemical Society*, 156(5):D184–D187, May 2009.

[171] Lourdes Vázquez-Gómez, Sandro Cattarin, Rosalba Gerbasi, Paolo Guerriero, and Marco Musiani. Activation of porous Ni cathodes towards hydrogen evolution by electrodeposition of Ir nuclei. *Journal of Applied Electrochemistry*, 39(11):2165, November 2009.

[172] Takashi Ohsaka, Katsuhiko Hirano, and Shin-ichiro Imabayashi. Bath-Life Extension of Iridium Electroplating by Separating Anode and Cathode Compartments with Ion-Exchange Membrane. *Electrochemical and Solid-State Letters*, 13(8):D65, May 2010.

[173] Yueh-Yuan Fang, Yi-Cheng Hsieh, and Chii-Wann Lin. Electroplating of Nanostructured Pt, Ir and Pt-Ir at Room Temperature. *Journal of The Electrochemical Society*, 159(9):D518, August 2012.

[174] Yasser Sheasha, Khaled A. Soliman, Shi-Gang Sun, Timo Jacob, and Ludwig A. Kibler. Electrochemical Fabrication of Well-Defined Spherical Iridium Nanoparticles and Electrocatalytic Activity towards Carbon Monoxide Adlayer Oxidation. *Electrocatalysis*, 6(4):365–372, July 2015.

[175] J. Näther, F. Köster, R. Freudenberger, C. Schöberl, and T. Lampke. Electrochemical deposition of iridium and iridium-nickel-alloys. *IOP Conference Series: Materials Science and Engineering*, 181(1):012041, 2017.

[176] Ehab N. El Sawy and Viola I. Birss. Nano-porous iridium and iridium oxide thin films formed by high efficiency electrodeposition. *Journal of Materials Chemistry*, 19(43):8244–8252, October 2009.

[177] Ehab N. El Sawy and Viola I. Birss. A Comparative Study of the Electrodeposition of Nanoporous Ir and Pt Thin Films. *Journal of The Electrochemical Society*, 160(9):D386–D393, January 2013.

[178] Ehab N. El Sawy, Hebert M. Molero, and Viola I. Birss. Methanol Oxidation at Porous Co-Electrodeposited Pt-Ir Thin Films. *Electrochimica Acta*, 117:202–210, January 2014.

[179] Ehab N. El Sawy and V. I. Birss. Electrodeposited Pt-Ir Thin Films as DMFC Anode Materials. *ECS Transactions*, 28(23):195, October 2010.

[180] Sang Hyun Ahn, Haiyan Tan, Mareike Haensch, Yihua Liu, Leonid A. Bendersky, and Thomas P. Moffat. Self-terminated electrodeposition of iridium electrocatalysts. *Energy & Environmental Science*, 8(12):3557–3562, November 2015.

[181] N. R. Elezović, G. Branković, P. Zabinski, M. Marzec, and V. D. Jović. Ultra-thin layers of iridium electrodeposited on Ti2AlC support as cost effective catalysts for hydrogen production by water electrolysis. *Journal of Electroanalytical Chemistry*, 878:114575, December 2020.

[182] Steven Le Vot, Lionel Roué, and Daniel Bélanger. Electrodeposition of iridium onto glassy carbon and platinum electrodes. *Electrochimica Acta*, 59:49–56, January 2012.

[183] Xiansheng Nie, Jing Chen, and Qinglin Tan. Kinetics of iridium reduction by hydrogen in hydrochloric acid solution. *Metallurgical Transactions B*, 23(6):737–745, December 1992.

[184] P. J. Mayne. Reduction of iridium in solution. *Polyhedron*, 3(8):1013–1015, January 1984.

[185] J. Rossmeisl, Z. W. Qu, H. Zhu, G. J. Kroes, and J. K. Nørskov. Electrolysis of water on oxide surfaces. *Journal of Electroanalytical Chemistry*, 607(1):83–89, September 2007.

[186] Reza B. Moghaddam, Chao Wang, Jason B. Sorge, Michael J. Brett, and Steven H. Bergens. Easily prepared, high activity Ir-Ni oxide catalysts for water oxidation. *Electrochemistry Communications*, 60:109–112, November 2015.

[187] Tobias Reier, Zarina Pawolek, Serhiy Cherevko, Michael Bruns, Travis Jones, Detre Teschner, Sören Selve, Arno Bergmann, Hong Nhan Nong, Robert Schlögl, Karl J. J. Mayrhofer, and Peter Strasser. Molecular Insight in Structure and Activity of Highly Efficient, Low-Ir Ir–Ni Oxide Catalysts for Electrochemical Water Splitting (OER). *Journal of the American Chemical Society*, 137(40):13031–13040, October 2015.

[188] C. P. De Pauli and S. Trasatti. Electrochemical surface characterization of IrO2 + SnO2 mixed oxide electrocatalysts. *Journal of Electroanalytical Chemistry*, 396(1):161–168, October 1995.

[189] Xu Wu, Jyoti Tayal, Suddhasatwa Basu, and Keith Scott. Nano-crystalline RuxSn1-xO2 powder catalysts for oxygen evolution reaction in proton exchange membrane water electrolysers. *International Journal of Hydrogen Energy*, 36(22):14796–14804, November 2011.

[190] Nicté J. Pérez-Viramontes, Virginia H. Collins-Martínez, Ismailia L. Escalante-García, José R. Flores-Hernández, Marisol Galván-Valencia, and Sergio M. Durón-Torres. Ir-Sn-Sb-O Electrocatalyst for Oxygen Evolution Reaction: Physicochemical Characterization and Performance in Water Electrolysis Single Cell with Solid Polymer Electrolyte. *Catalysts*, 10(5):524, May 2020.

[191] Michael Bernicke, Denis Bernsmeier, Benjamin Paul, Roman Schmack, Arno Bergmann, Peter Strasser, Erik Ortel, and Ralph Kraehnert. Tailored mesoporous Ir/TiOx: Identification of structure-activity relationships for an efficient oxygen evolution reaction. *Journal of Catalysis*, 376:209–218, August 2019.

[192] Ailton J. Terezo, Juan Bisquert, Ernesto C. Pereira, and Germà Garcia-Belmonte. Separation of transport, charge storage and reaction processes of

porous electrocatalytic IrO2 and IrO2/Nb2O5 electrodes. *Journal of Electroanalytical Chemistry*, 508(1):59–69, July 2001.

[193] Ch. Comninellis and G. P. Vercesi. Characterization of DSA®-type oxygen evolving electrodes: Choice of a coating. *Journal of Applied Electrochemistry*, 21(4):335–345, April 1991.

[194] Masatsugu Morimitsu, Ryuichi Otogawa, and Morio Matsunaga. Effects of cathodizing on the morphology and composition of IrO2/Ta2O5/Ti anodes. *Electrochimica Acta*, 46(2):401–406, November 2000.

[195] Hong Nhan Nong, Lin Gan, Elena Willinger, Detre Teschner, and Peter Strasser. IrOx core-shell nanocatalysts for cost- and energy-efficient electrochemical water splitting. *Chemical Science*, 5(8):2955–2963, June 2014.

[196] Hong Nhan Nong, Hyung-Suk Oh, Tobias Reier, Elena Willinger, Marc-Georg Willinger, Valeri Petkov, Detre Teschner, and Peter Strasser. Oxide-Supported IrNiOx Core–Shell Particles as Efficient, Cost-Effective, and Stable Catalysts for Electrochemical Water Splitting. *Angewandte Chemie International Edition*, 54(10):2975–2979, March 2015.

[197] Brian M. Tackett, Wenchao Sheng, Shyam Kattel, Siyu Yao, Binhang Yan, Kurian A. Kuttiyiel, Qiyuan Wu, and Jingguang G. Chen. Reducing Iridium Loading in Oxygen Evolution Reaction Electrocatalysts Using Core–Shell Particles with Nitride Cores. *ACS Catalysis*, 8(3):2615–2621, March 2018.

[198] Wei Hu, Shengli Chen, and Qinghua Xia. IrO2/Nb–TiO2 electrocatalyst for oxygen evolution reaction in acidic medium. *International Journal of Hydrogen Energy*, 39(13):6967–6976, April 2014.

[199] Chuanpu Hao, Hong Lv, Cangen Mi, Yukun Song, and Jianxin Ma. Investigation of Mesoporous Niobium-Doped TiO2 as an Oxygen Evolution Catalyst Support in an SPE Water Electrolyzer. *ACS Sustainable Chemistry & Engineering*, 4(3):746–756, March 2016.

[200] Petr Mazúr, Jakub Polonský, Martin Paidar, and Karel Bouzek. Non-conductive TiO2 as the anode catalyst support for PEM water electrolysis. *International Journal of Hydrogen Energy*, 37(17):12081–12088, September 2012.

[201] Binghong Han, Marcel Risch, Samuel Belden, Seonggyu Lee, Domnik Bayer, Eva Mutoro, and Yang Shao-Horn. Screening Oxide Support Materials for OER Catalysts in Acid. *Journal of The Electrochemical Society*, 165(10):F813–F820, January 2018.

[202] Fatemeh Karimi and Brant A. Peppley. Metal Carbide and Oxide Supports for Iridium-Based Oxygen Evolution Reaction Electrocatalysts for Polymer-Electrolyte-Membrane Water Electrolysis. *Electrochimica Acta*, 246:654–670, August 2017.

[203] Hyung-Suk Oh, Hong Nhan Nong, Tobias Reier, Manuel Gliech, and Peter Strasser. Oxide-supported Ir nanodendrites with high activity and durability for the oxygen evolution reaction in acid PEM water electrolyzers. *Chemical Science*, 6(6):3321–3328, May 2015.

[204] Hyung-Suk Oh, Hong Nhan Nong, Tobias Reier, Arno Bergmann, Manuel Gliech, Jorge Ferreira de Araújo, Elena Willinger, Robert Schlögl, Detre Teschner, and Peter Strasser. Electrochemical Catalyst–Support Effects and Their Stabilizing Role for IrOx Nanoparticle Catalysts during the Oxygen Evolution Reaction. *Journal of the American Chemical Society*, 138(38):12552–12563, September 2016.

[205] Vinod Kumar Puthiyapura, Mohammed Mamlouk, Sivakumar Pasupathi, Bruno G. Pollet, and Keith Scott. Physical and electrochemical evaluation of ATO supported IrO2 catalyst for proton exchange membrane water electrolyser. *Journal of Power Sources*, 269:451–460, December 2014.

[206] Nemanja Danilovic, Ramachandran Subbaraman, Kee Chul Chang, Seo Hyoung Chang, Yijin Kang, Joshua Snyder, Arvydas Paul Paulikas, Dusan Strmcnik, Yong Tae Kim, Deborah Myers, Vojislav R. Stamenkovic, and Nenad M. Markovic. Using Surface Segregation To Design Stable Ru-Ir Oxides for the Oxygen Evolution Reaction in Acidic Environments. *Angewandte Chemie International Edition*, 53(51):14016–14021, 2014.

[207] Serhiy Cherevko, Simon Geiger, Olga Kasian, Andrea Mingers, and Karl J. J. Mayrhofer. Oxygen evolution activity and stability of iridium in acidic media. Part 2. – Electrochemically grown hydrous iridium oxide. *Journal of Electroanalytical Chemistry*, 774:102–110, August 2016.

[208] Carl H. Hamann, Andrew Hamnett, and Wolf Vielstich. *Electrochemistry*. Wiley-VCH Verlag GmbH & Co. KGaA, second edition, 2007.

[209] B. E. Conway, H. Angerstein-Kozlowska, W. B. A. Sharp, and E. E. Criddle. Ultrapurification of water for electrochemical and surface chemical work by catalytic pyrodistillation. *Analytical Chemistry*, 45(8):1331–1336, July 1973.

[210] R. Woods. Hydrogen adsorption on platinum, iridium and rhodium electrodes at reduced temperatures and the determination of real surface area. *Journal of Electroanalytical Chemistry and Interfacial Electrochemistry*, 49(2):217–226, January 1974.

[211] Piotr Ochal, Jose Luis Gomez de la Fuente, Mikhail Tsypkin, Frode Seland, Svein Sunde, Navaneethan Muthuswamy, Magnus Rønning, De Chen, Sergio Garcia, Selim Alayoglu, and Bryan Eichhorn. CO stripping as an electrochemical tool for characterization of Ru@Pt core-shell catalysts. *Journal of Electroanalytical Chemistry*, 655(2):140–146, June 2011.

[212] S. Ardizzone, G. Fregonara, and S. Trasatti. "Inner" and "outer" active surface of RuO2 electrodes. *Electrochimica Acta*, 35(1):263–267, January 1990.

[213] Mary Ann Branch, Thomas F. Coleman, and Yuying Li. A Subspace, Interior, and Conjugate Gradient Method for Large-Scale Bound-Constrained Minimization Problems. *SIAM Journal on Scientific Computing*, 21(1):1–23, January 1999.

[214] Pauli Virtanen, Ralf Gommers, Travis E. Oliphant, Matt Haberland, Tyler Reddy, David Cournapeau, Evgeni Burovski, Pearu Peterson, Warren Weckesser, Jonathan Bright, Stéfan J. van der Walt, Matthew Brett, Joshua Wilson, K. Jarrod Millman, Nikolay Mayorov, Andrew R. J. Nelson, Eric Jones, Robert Kern, Eric Larson, C. J. Carey, İlhan Polat, Yu Feng, Eric W. Moore, Jake VanderPlas, Denis Laxalde, Josef Perktold, Robert Cimrman, Ian Henriksen, E. A. Quintero, Charles R. Harris, Anne M. Archibald, Antônio H. Ribeiro, Fabian Pedregosa, and Paul van Mulbregt. SciPy 1.0: Fundamental algorithms for scientific computing in Python. *Nature Methods*, 17(3):261–272, March 2020.

[215] Elena S. Davydova, Maidhily Manikandan, Dario Dekel, and Svein Sunde. Effect of the synthetic method on the properties of Ni-based hydrogen oxidation catalysts. 2021.

[216] Shyam S. Kocha, Kazuma Shinozaki, Jason W. Zack, Deborah J. Myers, Nancy N. Kariuki, Tammi Nowicki, Vojislav Stamenkovic, Yijin Kang, Dongguo Li, and Dimitrios Papageorgopoulos. Best Practices and Testing Protocols for Benchmarking ORR Activities of Fuel Cell Electrocatalysts Using Rotating Disk Electrode. *Electrocatalysis*, 8(4):366–374, July 2017.

[217] Yannick Garsany, Irwin L. Singer, and Karen E. Swider-Lyons. Impact of film drying procedures on RDE characterization of Pt/VC electrocatalysts. *Journal of Electroanalytical Chemistry*, 662(2):396–406, November 2011.

[218] Yannick Garsany, Junjie Ge, Jean St-Pierre, Richard Rocheleau, and Karen Swider-Lyons. Analytical Procedure for Accurate Comparison of Rotating Disk Electrode Results for the Oxygen Reduction Activity of Pt/C. *Journal of The Electrochemical Society*, 161:F628–F640, March 2014.

[219] Hong Nhan Nong, Hoang Phi Tran, Camillo Spöri, Malte Klingenhof, Lorenz Frevel, Travis E. Jones, Thorsten Cottre, Bernhard Kaiser, Wolfram Jaegermann, Robert Schlögl, Detre Teschner, and Peter Strasser. The Role of Surface Hydroxylation, Lattice Vacancies and Bond Covalency in the Electrochemical Oxidation of Water (OER) on Ni-Depleted Iridium Oxide Catalysts. *Zeitschrift für Physikalische Chemie*, 234(5):787–812, May 2020.

[220] S. Gottesfeld and S. Srinivasan. Electrochemical and optical studies of thick oxide layers on iridium and their electrocatalytic activities for the oxygen evolution reaction. *Journal of Electroanalytical Chemistry and Interfacial Electrochemistry*, 86(1):89–104, January 1978.

[221] S. Motoo and N. Furuya. Effect of anions on hydrogen and oxygen adsorption on iridium single cyrstal surfaces. *Journal of Electroanalytical Chemistry and Interfacial Electrochemistry*, 181(1):301–305, December 1984.

[222] Inês T. E. Fonseca, M. Irene Lopes, and M. Teresa C. Portela. A comparative voltammetric study of the ir ¦ h2so4 and ir ¦ hclo4 aqueous interfaces. *Journal of Electroanalytical Chemistry*, 415(1):89–96, October 1996.

[223] D. Michell, D. A. J. Rand, and R. Woods. Analysis of the anodic oxygen layer on iridium by X-ray emission, electron diffraction and electron microscopy. *Journal of Electroanalytical Chemistry and Interfacial Electrochemistry*, 84(1):117–126, November 1977.

[224] T. M. Silva, A. M. P. Simões, M. G. S. Ferreira, M. Walls, and M. Da Cunha Belo. Electronic structure of iridium oxide films formed in neutral phosphate buffer solution. *Journal of Electroanalytical Chemistry*, 441(1):5–12, January 1998.

[225] Lars-Erik Owe, Ingrid Anne Lervik, Mikhail Tsypkin, Marie Vardenær Syre, and Svein Sunde. Electrochemical Behavior of Iridium Oxide Films in Trifluoromethanesulfonic Acid. *Journal of The Electrochemical Society*, 157(11):B1719–B1725, November 2010.

[226] Shimshon Gottesfeld, Antonio Redondo, Israel Rubinstein, and Stephen W. Feldberg. Resistance-induced peaks in cyclic voltammograms of systems that can be switched electrochemically between an insulating and conductive state. *Journal of Electroanalytical Chemistry and Interfacial Electrochemistry*, 265(1):15–22, June 1989.

[227] V. I. Birss, H. Elzanowska, and S. Gottesfeld. Quartz crystal microbalance measurements during oxidation/reduction of hydrous Ir oxide electrodes. *Journal of Electroanalytical Chemistry and Interfacial Electrochemistry*, 318(1):327–333, November 1991.

[228] B. E. Conway and J. Mozota. Surface and bulk processes at oxidized iridium electrodes—II. Conductivity-switched behaviour of thick oxide films. *Electrochimica Acta*, 28(1):9–16, January 1983.

[229] Aikaterini Touni, Athanasios Papaderakis, Dimitrios Karfaridis, Georgios Vourlias, and Sotiris Sotiropoulos. Oxygen Evolution Reaction at IrO2/Ir(Ni) Film Electrodes Prepared by Galvanic Replacement and Anodization: Effect of Precursor Ni Film Thickness. *Molecules*, 24(11):2095, January 2019.

[230] Jean Pierre Jolivet. *Metal Oxide Chemistry and Synthesis*. John Wiley & Sons Inc, 2000.

[231] Lothar Wöhler and W. Witzmann. Die Oxyde des Iridiums. *Zeitschrift für anorganische Chemie*, 57(1):323–352, 1908.

[232] Masayuki Yagi, Emi Tomita, and Takayuki Kuwabara. Remarkably high activity of electrodeposited IrO2 film for electrocatalytic water oxidation. *Journal of Electroanalytical Chemistry*, 579(1):83–88, May 2005.

[233] Yixin Zhao, Emil A. Hernandez-Pagan, Nella M. Vargas-Barbosa, Jennifer L. Dysart, and Thomas E. Mallouk. A High Yield Synthesis of Ligand-Free Iridium Oxide Nanoparticles with High Electrocatalytic Activity. *The Journal of Physical Chemistry Letters*, 2(5):402–406, March 2011.

[234] Di Xu, Peng Diao, Tao Jin, Qingyong Wu, Xiaofang Liu, Xin Guo, Hongyu Gong, Fan Li, Min Xiang, and Yu Ronghai. Iridium Oxide Nanoparticles and Iridium/Iridium Oxide Nanocomposites: Photochemical Fabrication and Application in Catalytic Reduction of 4-Nitrophenol. *ACS applied materials & interfaces*, 7(30):16738–16749, August 2015.

[235] Ida Wadseng. IrNix Core-Shell Nanocatalysts for the Oxygen Evolution Reaction. Master's thesis, Norwegian University of Science and Technology, Norway, 2019.

[236] Hong Nhan Nong, Tobias Reier, Hyung-Suk Oh, Manuel Gliech, Paul Paciok, Thu Ha Thi Vu, Detre Teschner, Marc Heggen, Valeri Petkov, Robert Schlögl, Travis Jones, and Peter Strasser. A unique oxygen ligand environment facilitates water oxidation in hole-doped IrNiO x core–shell electrocatalysts. *Nature Catalysis*, 1(11):841–851, November 2018.

[237] Youngmi Yi, Gisela Weinberg, Marina Prenzel, Mark Greiner, Saskia Heumann, Sylvia Becker, and Robert Schlögl. Electrochemical corrosion of a glassy carbon electrode. *Catalysis Today*, 295:32–40, October 2017.

[238] J. R. Smith, F. C. Walsh, and R. L. Clarke. Electrodes based on Magnéli phase titanium oxides: The properties and applications of Ebonex® materials. *Journal of Applied Electrochemistry*, 28(10):1021–1033, October 1998.

[239] E. Antolini and E. R. Gonzalez. Ceramic materials as supports for low-temperature fuel cell catalysts. *Solid State Ionics*, 180(9):746–763, May 2009.

[240] J. E. Ferrer and Ll. Victori. Study of the oxygen evolution reaction on the iridium electrode in acid medium by eis. *Electrochimica Acta*, 39(5):667–672, April 1994.

[241] Simon Geiger, Olga Kasian, Buddha R. Shrestha, Andrea M. Mingers, Karl J. J. Mayrhofer, and Serhiy Cherevko. Activity and Stability of Electrochemically and Thermally Treated Iridium for the Oxygen Evolution Reaction. *Journal of The Electrochemical Society*, 163(11):F3132–F3138, January 2016.

[242] Navaneethan Muthuswamy, Jose Luis Gomez de la Fuente, Dung T. Tran, John Walmsley, Mikhail Tsypkin, Steinar Raaen, Svein Sunde, Magnus Rønning, and De Chen. Ru@Pt core–shell nanoparticles for methanol fuel cell catalyst: Control and effects of shell composition. *International Journal of Hydrogen Energy*, 38(36):16631–16641, December 2013.

[243] Svetlana Štrbac, Irina Srejić, and Zlatko Rakočević. Electrocatalysis of Hydrogen Evolution Reaction on Au(111) by Spontaneously Deposited Iridium in Acid Solution. *Journal of The Electrochemical Society*, 165(15):J3335–J3341, January 2018.

[244] Stefan Kania and Rudolf Holze. Surface enhanced Raman spectroscopy of anions adsorbed on foreign metal modified gold electrodes. *Surface Science*, 408(1):252–259, June 1998.

[245] Alexander Vaskevich, Fabrice Sinapi, Zineb Mekhalif, Joseph Delhalle, and Israel Rubinstein. Underpotential Deposition of Nickel on {111}-Textured Gold Electrodes in Dimethyl Sulfoxide. *Journal of The Electrochemical Society*, 152(11):C744–C750, November 2005.

[246] A. Gündel, L. Cagnon, C. Gomes, A. Morrone, J. Schmidt, and P. Allongue. In-situ magnetic measurements of electrodeposited ultrathin Co, Ni and Fe/Au(111) layers. *Physical Chemistry Chemical Physics*, 3(16):3330–3335, January 2001.

[247] J. L. Bubendorff, L. Cagnon, V. Costa-Kieling, J. P. Bucher, and P. Allongue. Anion promoted Ni-underpotential deposition on Au(111). *Surface Science*, 384(1):L836–L843, July 1997.

[248] Jiajing Pei, Junjie Mao, Xin Liang, Chen Chen, Qing Peng, Dingsheng Wang, and Yadong Li. Ir–Cu nanoframes: One-pot synthesis and efficient electrocatalysts for oxygen evolution reaction. *Chemical Communications*, 52(19):3793–3796, February 2016.

[249] Chao Wang, Yongming Sui, Guanjun Xiao, Xinyi Yang, Yingjin Wei, Guangtian Zou, and Bo Zou. Synthesis of Cu–Ir nanocages with enhanced electrocatalytic activity for the oxygen evolution reaction. *Journal of Materials Chemistry A*, 3(39):19669–19673, 2015.

[250] Donghwan Yoon, Sulgi Bang, Jongsik Park, Jongchan Kim, Hionsuck Baik, Haesik Yang, and Kwangyeol Lee. One pot synthesis of octahedral {111} CuIr gradient alloy nanocrystals with a Cu-rich core and an Ir-rich surface and their usage as efficient water splitting catalyst. *CrystEngComm*, 17(36):6843–6847, September 2015.

[251] Jongsik Park, Young Jin Sa, Hionsuck Baik, Taehyun Kwon, Sang Hoon Joo, and Kwangyeol Lee. Iridium-Based Multimetallic Nanoframe@Nanoframe Structure: An Efficient and Robust Electrocatalyst toward Oxygen Evolution Reaction. *ACS Nano*, 11(6):5500–5509, June 2017.

[252] Lin Han, Pengfei Wang, Hui Liu, Qiangqiang Tan, and Jun Yang. Balancing the galvanic replacement and reduction kinetics for the general formation of bimetallic CuM (M = Ru, Rh, Pd, Os, Ir, and Pt) hollow nanostructures. *Journal of Materials Chemistry A*, 4(47):18354–18365, 2016.

[253] Sulgi Bang, Donghwan Yoon, Jongchan Kim, Hionsuck Baik, Haesik Yang, and Kwangyeol Lee. Formation of double layer hollow nanostars of Pd/CuIr by utilizing a Kirkendall effect and a facile Cu atom movement along twinning boundaries and their usage as efficient water splitting catalysts. *CrystEngComm*, 17(22):4084–4088, May 2015.

[254] Taehyun Kwon, Hyeyoun Hwang, Young Jin Sa, Jongsik Park, Hionsuck Baik, Sang Hoon Joo, and Kwangyeol Lee. Cobalt Assisted Synthesis of IrCu Hollow Octahedral Nanocages as Highly Active Electrocatalysts toward Oxygen Evolution Reaction. *Advanced Functional Materials*, 27(7):1604688, February 2017.

[255] René Winand. Electrodeposition of metals and alloys—new results and perspectives. *Electrochimica Acta*, 39(8):1091–1105, June 1994.

[256] S. H. Glarum and J. H. Marshall. The A-C Response of Iridium Oxide Films. *Journal of The Electrochemical Society*, 127(7):1467–1474, July 1980.

[257] Sebastian Henning, Juan Herranz, and Hubert A. Gasteiger. Bulk-Palladium and Palladium-on-Gold Electrocatalysts for the Oxidation of Hydrogen in Alkaline Electrolyte. *Journal of The Electrochemical Society*, 162:178–189, December 2014.

[258] J. O'm. Bockris. Kinetics of Activation Controlled Consecutive Electrochemical Reactions: Anodic Evolution of Oxygen. *The Journal of Chemical Physics*, 24(4):817–827, April 1956.

[259] A. Damjanovic, A. Dey, and J. O'm Bockris. Electrode Kinetics of Oxygen Evolution and Dissolution on Rh, Ir, and Pt-Rh Alloy Electrodes. *Journal of The Electrochemical Society*, 113(7):739–746, July 1966.

[260] Byung-Seok Lee, Sang Hyun Ahn, Hee-Young Park, Insoo Choi, Sung Jong Yoo, Hyoung-Juhn Kim, Dirk Henkensmeier, Jin Young Kim, Sehkyu Park, Suk Woo Nam, Kwan-Young Lee, and Jong Hyun Jang. Development of electrodeposited IrO2 electrodes as anodes in polymer electrolyte membrane water electrolysis. *Applied Catalysis B: Environmental*, 179(Supplement C):285–291, December 2015.

[261] Florian Schulz, Torge Homolka, Neus G. Bastús, Victor Puntes, Horst Weller, and Tobias Vossmeyer. Little Adjustments Significantly Improve the Turkevich Synthesis of Gold Nanoparticles. *Langmuir*, 30(35):10779–10784, September 2014.

[262] Carla Daruich De Souza, Beatriz Ribeiro Nogueira, and Maria Elisa C. M. Rostelato. Review of the methodologies used in the synthesis gold nanoparticles by chemical reduction. *Journal of Alloys and Compounds*, 798:714–740, August 2019.

[263] M. Palomar-Pardavé, E. Garfias-García, M. Romero-Romo, M. T. Ramírez-Silva, and N. Batina. Influence of the substrate's surface structure on the mechanism and kinetics of the electrochemical UPD formation of a copper monolayer on gold. *Electrochimica Acta*, 56(27):10083–10092, November 2011.

[264] Ashok Kumar and Daniel A. Buttry. Size-Dependent Underpotential Deposition of Copper on Palladium Nanoparticles. *The Journal of Physical Chemistry C*, 119(29):16927–16933, July 2015.

[265] C. L. Perdriel, E. Custidiano, and A. J. Arvia. Modifications of palladium electrode surfaces produced by periodic potential treatments. *Journal of Electroanalytical Chemistry and Interfacial Electrochemistry*, 246(1):165–180, May 1988.

[266] L. D. Burke and M. B. C. Roche. An electrochemical investigation of monolayer and multilayer oxide films on palladium in aqueous media. *Journal of Electroanalytical Chemistry and Interfacial Electrochemistry*, 186(1):139–154, May 1985.

[267] A. E. Bolzán and A. J. Arvia. The electrochemical behaviour of hydrous palladium oxide layers formed at high positive potentials in different electrolyte solutions. *Journal of Electroanalytical Chemistry*, 322(1):247–265, January 1992.

[268] L. D. Burke and J. K. Casey. An Examination of the Electrochemical Behavior of Palladium Electrodes in Acid. *Journal of The Electrochemical Society*, 140(5):1284, May 1993.

[269] L. D. Burke and J. K. Casey. The electrocatalytic behaviour of palladium in acid and base. *Journal of Applied Electrochemistry*, 23(6):573–582, June 1993.

[270] J. F. Llopis, J. M. Gamboa, and L. Victori. Radiochemical study of the anodic behaviour of palladium. *Electrochimica Acta*, 17(12):2225–2230, December 1972.

[271] Julien Durst, Christoph Simon, Frédéric Hasché, and Hubert A. Gasteiger. Hydrogen Oxidation and Evolution Reaction Kinetics on Carbon Supported Pt, Ir, Rh, and Pd Electrocatalysts in Acidic Media. *Journal of The Electrochemical Society*, 162(1):F190, December 2014.

[272] M. H. Hölzle, U. Retter, and D. M. Kolb. The kinetics of structural changes in Cu adlayers on Au(111). *Journal of Electroanalytical Chemistry*, 371(1):101–109, June 1994.

[273] Gary L. Borges, K. Keiji Kanazawa, Joseph G. Gordon, Kevin Ashley, and Jocelyn Richer. An in-situ electrochemical quartz crystal microbalance study of the underpotential deposition of copper on Au(111) electrodes. *Journal of Electroanalytical Chemistry*, 364(1):281–284, January 1994.

[274] Toshinori Hachiya, Hidetoshi Honbo, and Kingo Itaya. Detailed underpotential deposition of copper on gold(III) in aqueous solutions. *Journal of Electroanalytical Chemistry and Interfacial Electrochemistry*, 315(1):275–291, October 1991.

[275] Venkat R. Subramanian and Ralph E. White. A Semianalytical Method for Predicting Primary and Secondary Current Density Distributions: Linear and Nonlinear Boundary Conditions. *Journal of The Electrochemical Society*, 147(5):1636, May 2000.

[276] Morten Tjelta and Svein Sunde. Current-distribution effects on the impedance of porous electrodes and electrodes covered with films. *Journal of Electroanalytical Chemistry*, 737:65–77, January 2015.

[277] Peter Atkins and Julio de Paula. *Atkins' Physical Chemistry*. OUP Oxford, ninth edition, 2010.

[278] John J. Watkins and Henry S. White. The Role of the Electrical Double Layer and Ion Pairing on the Electrochemical Oxidation of Hexachloroiridate(III) at Pt Electrodes of Nanometer Dimensions. *Langmuir*, 20(13):5474–5483, June 2004.

[279] John Turkevich, Peter Cooper Stevenson, and James Hillier. A study of the nucleation and growth processes in the synthesis of colloidal gold. *Discussions of the Faraday Society*, 11(0):55–75, January 1951.

[280] John Turkevich. Colloidal gold. Part I. *Gold Bulletin*, 18(3):86–91, September 1985.

Part IV

Supplementary information

Appendix A

Galvanic displacement of carbon supported Ni by Ir

Figure A.1 shows S(T)EM images of Ni_{100}/C.

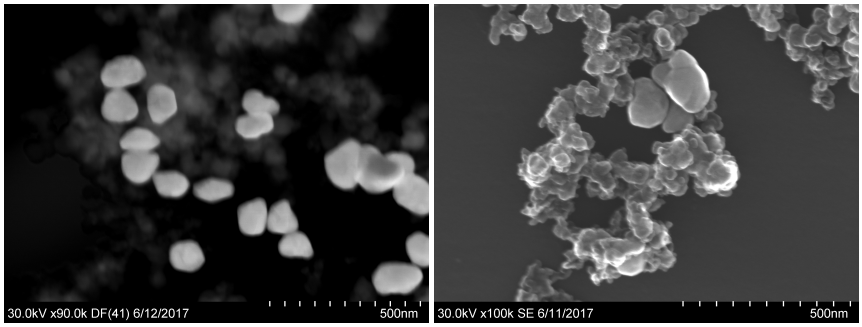

(a) (b)

Figure A.1: S(T)EM images of Ni_{100}/C. Images provided by Dr. Maidhily Manikandan

Figure A.2 show voltammograms of $IrNi_{100}$C:T60 (a) and $IrNi_{100}$C:T85 (b) after transformation to IrO_x by potential cycling. Potential cycling was done in $0.5\,\mathrm{mol\,dm^{-3}}$ H_2SO_4 at $50\,\mathrm{mV\,s^{-1}}$. Sweeprates in the shown voltammograms are $10\,\mathrm{mV\,s^{-1}}$ through $500\,\mathrm{mV\,s^{-1}}$.

Figures A.3 and A.4 show the anodic charge between 0.3 V and 1.3 V in figure A.2 as a function of potential sweep rate, linearized to zero- and infinite sweep rate as per the method outlined previously[ref] [212].

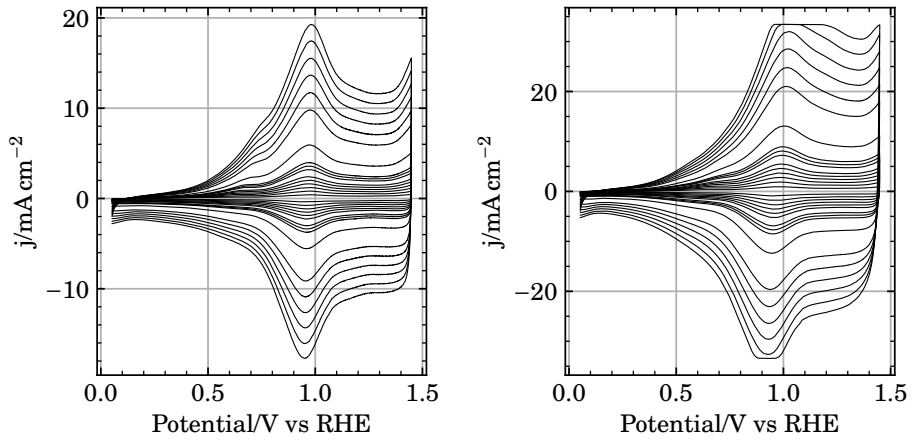

(a) $IrNi_{100}C$:T60 (b) $IrNi_{100}C$:T85

Figure A.2: Cyclic voltammograms of $IrNi_{100}C$:T60 (a), and $IrNi_{100}C$:T85 (b). Voltammograms were obtained at sweep rates ranging from $10\,mV\,s^{-1}$ to $500\,mV\,s^{-1}$ after transforming the Ir deposit to IrO_x by potential cycling in $0.5\,mol\,dm^{-3}$ H_2SO_4 at $50\,mV\,s^{-1}$.

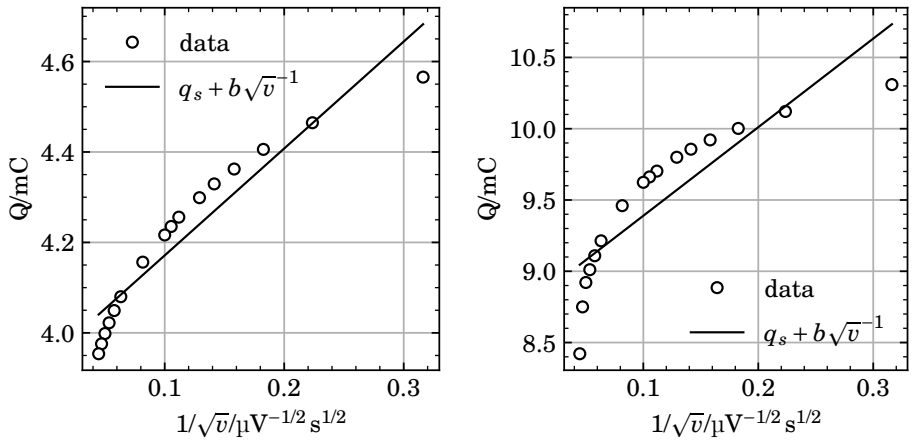

(a) $IrNi_{100}C$:T60 (b) $IrNi_{100}C$:T85

Figure A.3: Anodic charge of the voltammograms in figure A.2 and linear fit to $q = q_s + b\sqrt{v}^{-1}$

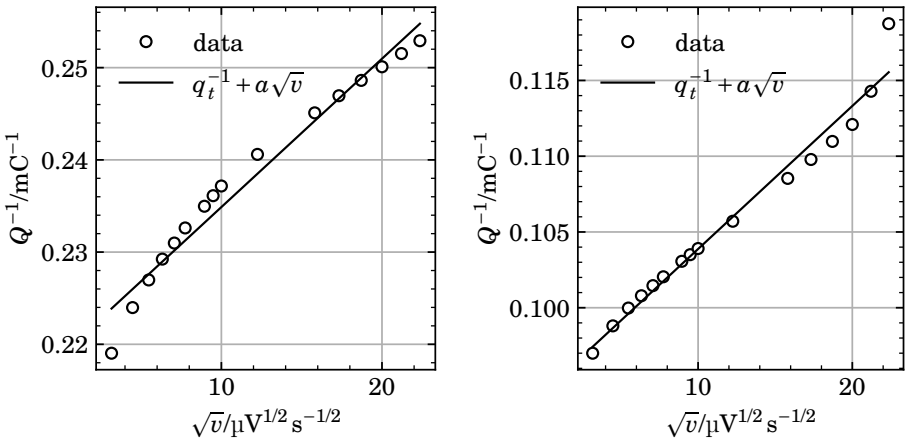

(a) $IrNi_{100}C$:T60

(b) $IrNi_{100}C$:T85

Figure A.4: Anodic charge of the voltammograms in figure A.2 and linear fit to $q^{-1} = q_t^{-1} + a\sqrt{v}$

Appendix B

Galvanic displacement of Cu by Ir

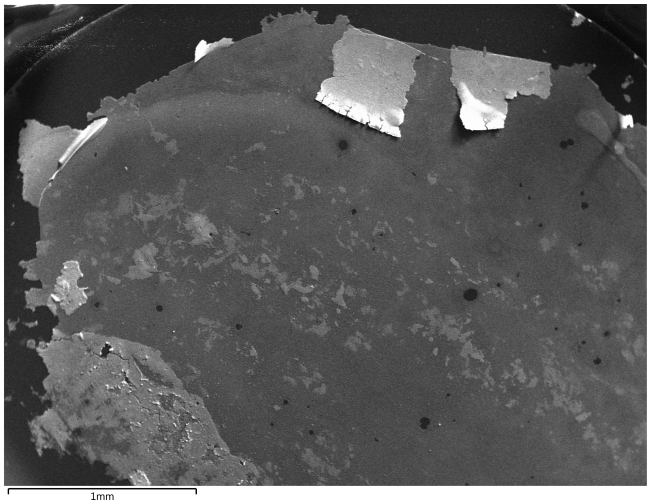

Figure B.1: A cracked film of (Ir-Cu) on glassy carbon. After displacement of a continious Cu@GC film with 1 mmol dm^{-3} H_2SO_4 for 1 h at 70 °C, the formed (Ir-Cu)@GC film cracked during immersion in DI water, an large pieces was seen falling off.

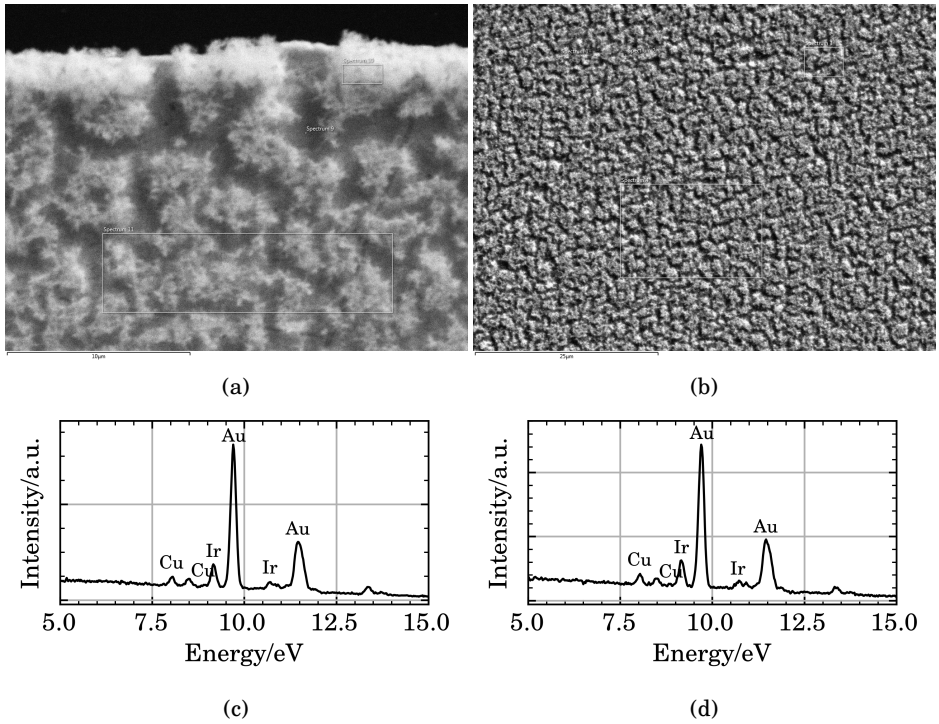

Figure B.2

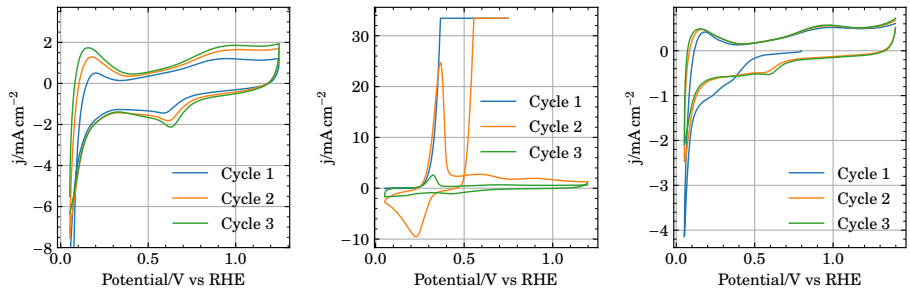

Figure B.3: Cyclic voltammograms of (Ir-Cu/Au)$_r$ (a), (Ir-Cu/Au)$_s$ (b) and (Ir-Cu)/GC (c. Voltammograms were obtained 50 mV s^{-1} in 0.5 mol dm^{-3} H_2SO_4 at 50 mV s^{-1}. The first three cycles of the as-prepared electrode are shown.

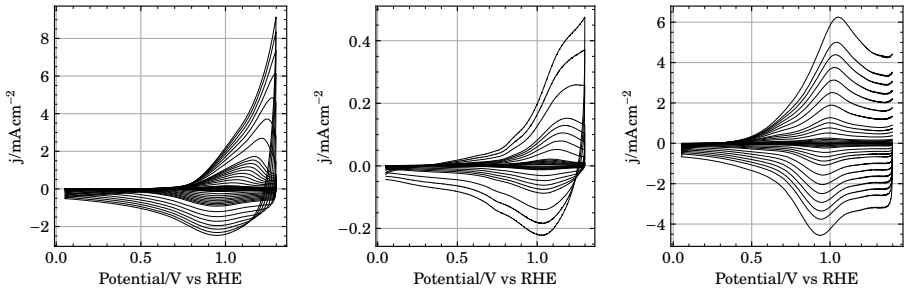

(a) $(Ir\text{-}Cu/Au)_r$ (b) $(Ir\text{-}Cu/Au)_s$ (c) (Ir-Cu/GC)

Figure B.4: Cyclic voltammograms of $(Ir\text{-}Cu/Au)_r$ (a), $(Ir\text{-}Cu/Au)_s$ (b) and (Ir-Cu)/GC (c. Voltammograms were obtained at sweep rates ranging from $2\,mV\,s^{-1}$ to $500\,mV\,s^{-1}$ after transforming the Ir deposit to IrO_x by potential cycling in $0.5\,mol\,dm^{-3}$ H_2SO_4 at $50\,mV\,s^{-1}$.

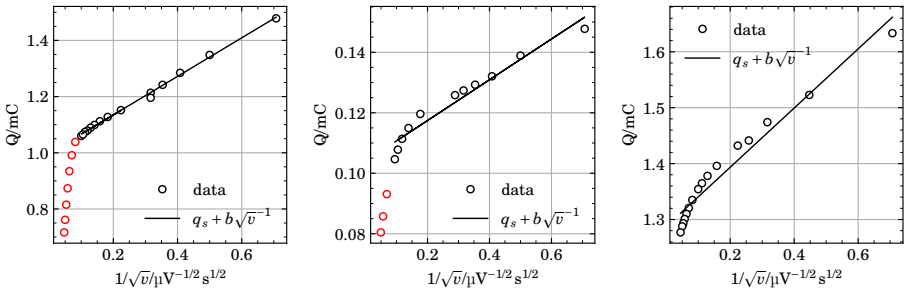

(a) $(Ir\text{-}Cu/Au)_r$ (b) $(Ir\text{-}Cu/Au)_s$ (c) (Ir-Cu/GC)

Figure B.5: Anodic charge of the voltammograms in figure B.4 and linear fit to $q = q_s + b\sqrt{v}^{-1}$

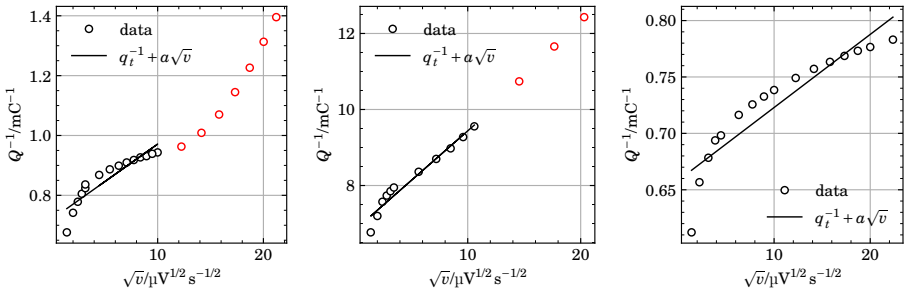

(a) (Ir-Cu/Au)$_r$ (b) (Ir-Cu/Au)$_s$ (c) (Ir-Cu/GC)

Figure B.6: Anodic charge of the voltammograms in figure B.4 and linear fit to $q^{-1} = q_t^{-1} + a\sqrt{v}$

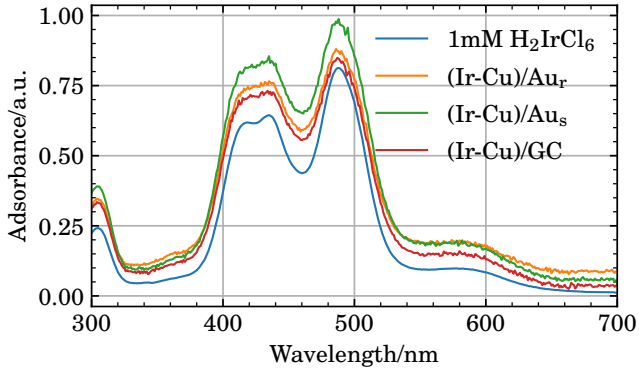

Figure B.7: UV-Vis adsorption spectra of a 1 mmol dm^{-3} solution of H_2IrCl_6 before and after galvanic displacement of Cu deposits on Au and GC rotating disc electrodes.

Appendix C

Galvanic displacement of Cu and Ni on titanium oxides by Ir

Figure C.2 is a cyclic voltammogram of (Ir−Cu)@TiO_2mixed 50wt% with carbon black. The voltammogram did not change significantly over 100 cycles between 0.05 V and 1.4 V exhibits a pair of broad peaks centered around 0.6 V, which is commonly associatiated with the carbon support.

The maximum possible Ir content is given by

$$x_{\mathrm{Ir}} = \frac{m_{\mathrm{Ir}}}{m_{\mathrm{ox}} + m_{\mathrm{Ir}}} \tag{C.1}$$

$$m_{\mathrm{Ir}} = n_{\mathrm{Ir}} M_{\mathrm{Ir}} \tag{C.2}$$

$$m_{\mathrm{ox}} = m_{\mathrm{cat}}(1 - x_{\mathrm{M}}) \tag{C.3}$$

$$n_{\mathrm{Ir}} = \frac{n_{\mathrm{M}}}{2} \tag{C.4}$$

$$n_{\mathrm{M}} = \frac{x_{\mathrm{M}} m_{\mathrm{cat}}}{M_{\mathrm{M}}} \tag{C.5}$$

$$x_{\mathrm{Ir}} = \frac{\frac{x_{\mathrm{M}} m_{\mathrm{cat}}}{2M_{\mathrm{M}}} M_{\mathrm{Ir}}}{m_{\mathrm{cat}}(1 - x_{\mathrm{M}}) + \frac{x_{\mathrm{M}} m_{\mathrm{cat}}}{2M_{\mathrm{M}}} M_{\mathrm{Ir}}} \tag{C.6}$$

$$x_{\mathrm{Ir}} = \frac{x_{\mathrm{M}} m_{\mathrm{cat}} \frac{M_{\mathrm{Ir}}}{M_{\mathrm{M}}}}{2m_{\mathrm{cat}}(1 - x_{\mathrm{M}}) + x_{\mathrm{M}} m_{\mathrm{cat}} \frac{M_{\mathrm{Ir}}}{M_{\mathrm{M}}}} \tag{C.7}$$

$$x_{\mathrm{Ir}} = \frac{x_{\mathrm{M}} \frac{M_{\mathrm{Ir}}}{M_{\mathrm{M}}}}{2 - 2x_{\mathrm{M}} + x_{\mathrm{M}} \frac{M_{\mathrm{Ir}}}{M_{\mathrm{M}}}} \tag{C.8}$$

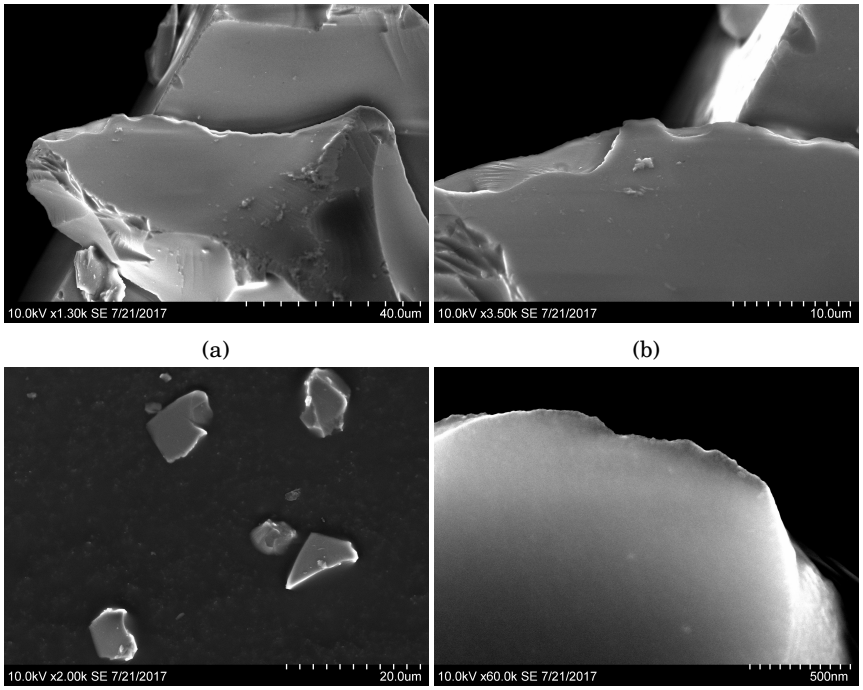

Figure C.1: S(T)EM Images of $CuNb_xTiO_2$, beforefore heat treatment in hydrogen. Images provided by Dr. Julian Tolchard

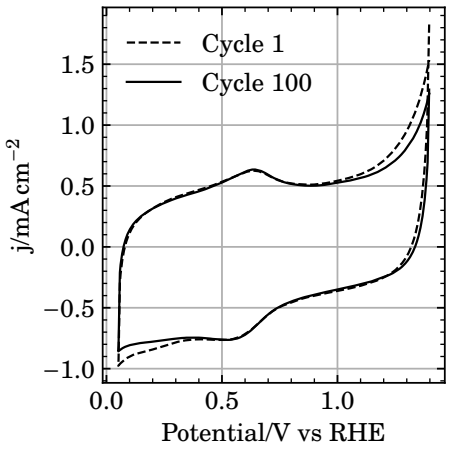

Figure C.2: Cyclic voltammograms of (Ir−Cu)@TiO_2 mixed 50 wt% with carbon black. Voltammograms were obtained at in 0.5 mol dm^{-3} H_2SO_4 with a sweeprate of 50 mV s^{-1}

$$x_{\mathrm{Ir}}(4\,\mathrm{wt\%\ Cu}) = \frac{0.04\frac{192.2\,\mathrm{g\,mol^{-1}}}{63.55\,\mathrm{g\,mol^{-1}}}}{2-0.08+0.04\frac{192.2\,\mathrm{g\,mol^{-1}}}{63.55\,\mathrm{g\,mol^{-1}}}} = 0.0593 = 5.9\,\mathrm{wt\%} \tag{C.9}$$

$$x_{\mathrm{Ir}}(5\,\mathrm{wt\%\ Cu}) = \frac{0.05\frac{192.2\,\mathrm{g\,mol^{-1}}}{63.55\,\mathrm{g\,mol^{-1}}}}{2-0.1+0.05\frac{192.2\,\mathrm{g\,mol^{-1}}}{63.55\,\mathrm{g\,mol^{-1}}}} = 0.0737 = 7.4\,\mathrm{wt\%} \tag{C.10}$$

$$x_{\mathrm{Ir}}(4\,\mathrm{wt\%\ Ni}) = \frac{0.04\frac{192.2\,\mathrm{g\,mol^{-1}}}{58.69\,\mathrm{g\,mol^{-1}}}}{2-0.08+0.04\frac{192.2\,\mathrm{g\,mol^{-1}}}{58.69\,\mathrm{g\,mol^{-1}}}} = 0.0639 = 6.4\,\mathrm{wt\%} \tag{C.11}$$

Appendix D

Ir deposition by galvanic displacement of Cu in a one-pot configuration

Figure D.1 presents voltammograms of the Ir/Au-deposit produced by SLRR depicted in figure 6.16b performed at sweep rates from 10 $mV s^{-1}$ 10 $mV s^{-1}$, 25, 50, 100, 150, 200, 250, 300, 350 and 500 $mV s^{-1}$.

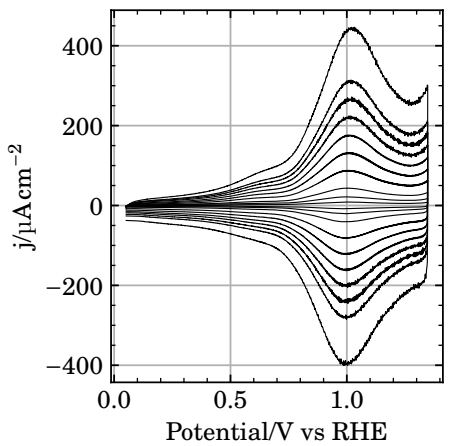

Figure D.1: Voltammograms of Ir(SLRR)/Au in 0.5 $mol dm^{-3}$ H_2SO_4. Sweep rates was 10 $mV s^{-1}$, 25, 50, 100, 150, 200, 250, 300, 350 and 500 $mV s^{-1}$.

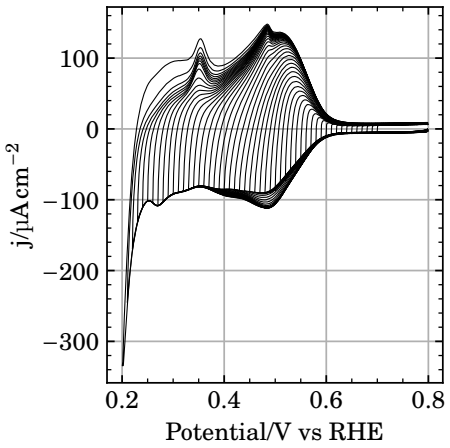

Figure D.2: Cyclic voltammograms of the Au(poly) RDE in a solution containing 1×10^{-3} mol dm^{-3} $CuSO_4$ and 0.5 mol dm^{-3} H_2SO_4 at 25 °C. The sweep rate was 50 mV s^{-1}. The electrode potential was swept from 0.8 V in each cycle, whereas the reversal potential was made more negative for each cycle.

D.1 Limiting current of $Ir_6^{2-} + e^- \rightleftharpoons IrCl_6^{3-}$

The formation of Ir(III) and further reduction to Ir(0) occurs in parallel on the surface. The maximum flux of Ir(IV) can be estimated using Fick's 1st law [16], equation (D.1);

$$J_i = -D_i \frac{\mathrm{d}c_i}{\mathrm{d}x} \tag{D.1}$$

Expressed for a rotating disc electrode [16], the flux of Ir(IV) becomes equation (D.2) when we assume the concentration of Ir(IV) at the surface to be zeroequal to the initial concentration in the bulk. It was assumed that $D_{\mathrm{Ir(IV)}} = D_{\mathrm{Ir(III)}}$.

$$J_{\mathrm{Ir(IV)}} = -0.62 \frac{D_{\mathrm{Ir(IV)}}^{2/3} \omega^{1/2}}{\nu^{1/6}} c^{\circ}_{\mathrm{Ir(IV)}} \tag{D.2}$$

The viscosity of water, η was found using equations (D.3) to (D.5) [277] where T is temperature in °C and $\eta_{20} = 0.891 \times 10^{-3}$ kg m^{-1} s^{-1}

$$\log\left(\frac{\eta_{20}}{\eta}\right) = \frac{A}{B} \tag{D.3}$$

$$A = 1.37023(T-20) + 8.36\cdot 10^{-4}(T-20)^2 \tag{D.4}$$

$$B = 109 + T \tag{D.5}$$

The diffusion coefficient, $D_{\mathrm{Ir(IV)}}$, was adjusted for temperature using the Stokes-Einstein relation [277] in equation (D.6) with $T^{\circ} = 293.15\,\mathrm{K}$ as the reference temperature, $D(T^{\circ}) = 8.3\times 10^{-6}\,\mathrm{cm^2\,s^{-1}}$ [278] and η° as aforementioned.

$$D(T) = D(T^{\circ})\left(\frac{T}{T^{\circ}}\right)\left(\frac{\eta^{\circ}}{\eta(T)}\right) \tag{D.6}$$

ω was the radial rotation rate given by equation (D.7) where Ω is the rotation rate in rpm

$$\omega = \frac{2\pi}{60}\Omega \tag{D.7}$$

The flux was found using $D_{\mathrm{Ir(IV)}}(T = 70\,^{\circ}\mathrm{C}) = 2.41\times 10^{-5}\,\mathrm{cm^2\,s^{-1}}$, $\omega = 167.6\,\mathrm{s^{-1}}$ and $c^{\circ}_{\mathrm{Ir(IV)}} = 1\times 10^{-8}\,\mathrm{mol\,cm^{-3}}$. ν was calculated from $\nu(T) = \frac{\eta(T)}{\rho} = 3.614\times 10^{-3}\,\mathrm{cm^2\,s^{-1}}$ where $999.07\,\mathrm{kg\,m^{-3}}$ was used for the density of water, ρ. $J_{\mathrm{Ir(IV)}}$ was estimated to $J_{\mathrm{Ir(IV)}} = -1.71\times 10^{-10}\,\mathrm{mol\,cm^{-2}\,s^{-1}}$. Multiplying with F gives the limiting current for Ir(IV) reduction- and Ir(III) formation, reaction (6.2), which equaled to $-16.5\,\mu\mathrm{A\,cm^{-2}}$. This is consistent with the voltammogram in figure D.4.

D.2 Adjustment for background currents

In step experiments where the electrode was taken from e.g. 0.7 V to 0.34 V, the current did not relax to zero, but rather a small, negligible background current. We attribute this to difficulty in achieving a 100 % O_2(g) free electrolyte, reduction of Ir(IV), reaction (6.2), formation Cu(I) and noise. In the chronocoulometry plot in figure D.3 showing charge passed versus time, this small current manifests as a linear tail in the plot. We used linear regression over the last 0.5 s and subtracted the linear part from the dataset, $q_{\mathrm{adj}} = q - slope * t$.

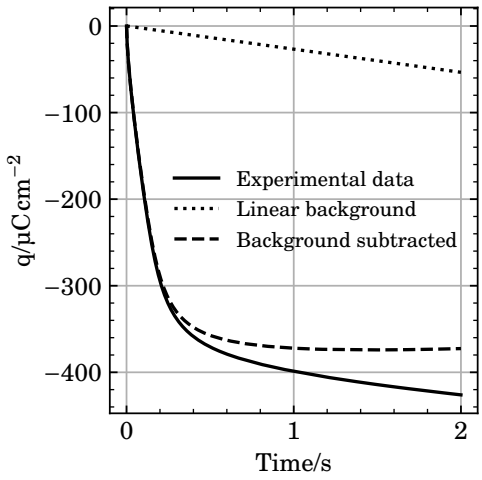

Figure D.3: Charge passed over time after stepping the potential of a Au(poly) RDE from 0.7 V to 0.34 V in 0.5 mol dm^{-3} H_2SO_4 + 1 mmol dm^{-3} $CuSO_4$ at 70 °C.

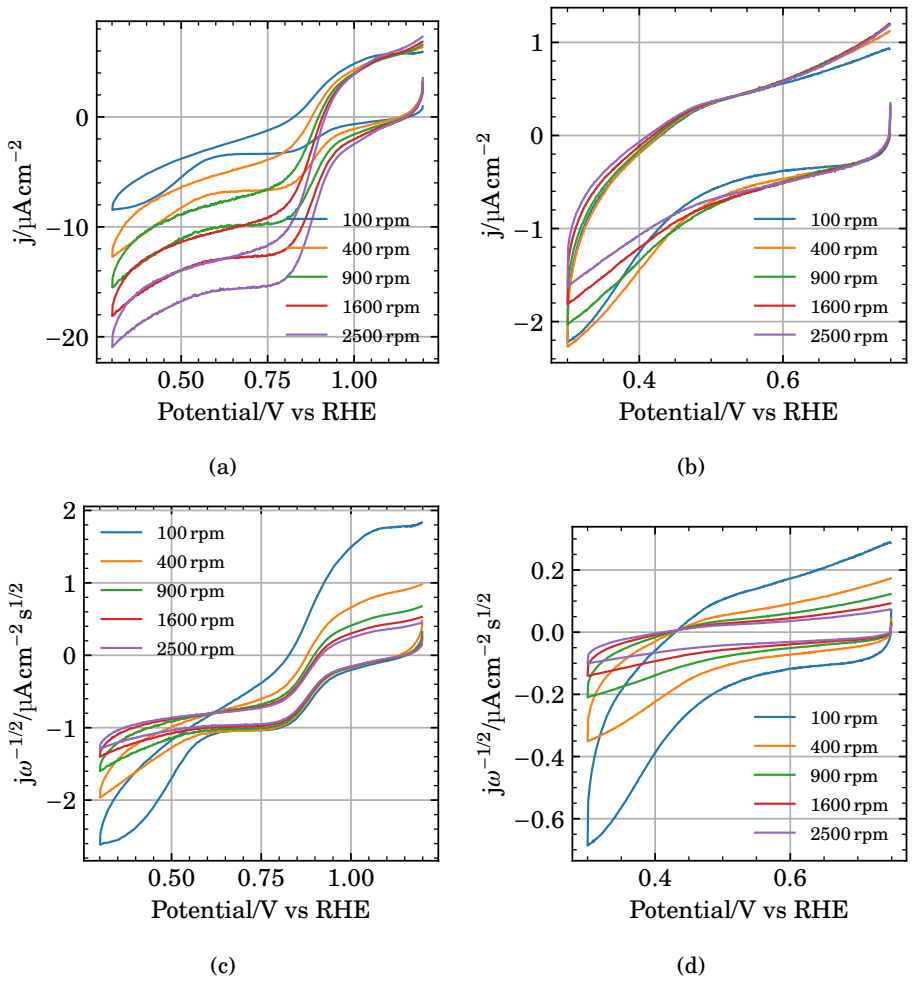

Figure D.4: Cyclic voltammograms of 0.5 mol dm^{-3} H_2SO_4 + 10 µmol dm^{-3} H_2IrCl_6, figures D.4a and D.4c or $IrCl_3$, figures D.4b and D.4d. Sweeps was performed at 5 mV s^{-1} at 70 °C using a Au(poly) RDE. figures D.4a and D.4b are normalized to the electrode geometrical surface area. Figures D.4c and D.4d are also normalized to the square root of the electrode rotation rate, in s^{-1}

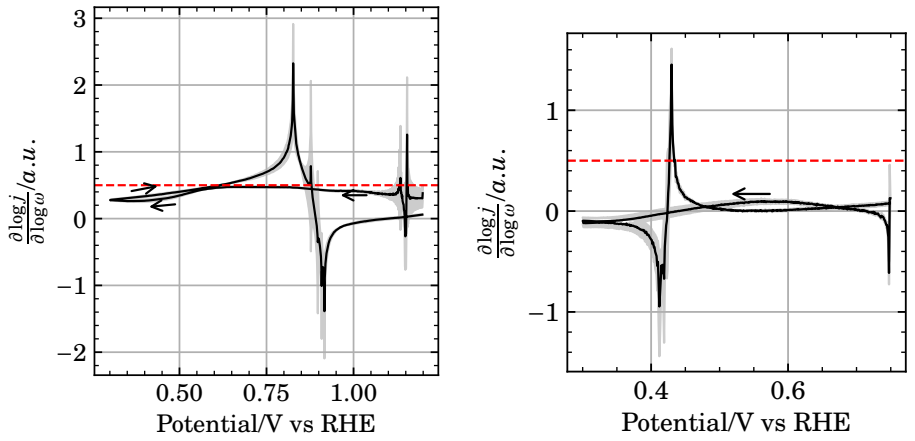

(a) (b)

Figure D.5: Value of b by linear regression of $j(E,\omega) = a + b\log(\omega)$ for the voltammograms shown in figure D.4 for H_2IrCl_6 in figure D.5a and $IrCl_3$ in figure D.5b. A value of $b \approx 0.5$ indicates a current limited by the mass transport towards the rotating electrode.

Appendix E

Investigation of the Ir-Cu SLRR system

E.1 Cu UPD

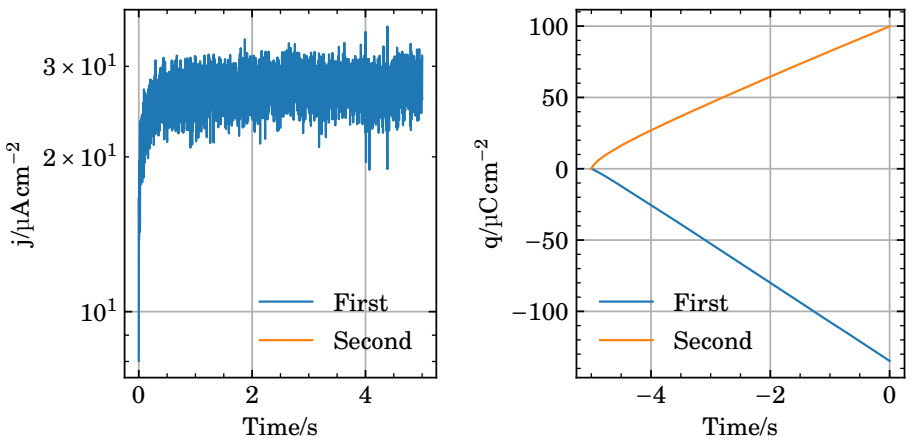

(a) (b)

Figure E.1: Current (a) and charge (b) versus time during two potential holds at 0.7 V. The working electrode was a Au_{poly} RDE. The electrolyte contained 0.5 mol dm^{-3} H_2SO_4 and 1 mmol dm^{-3} $CuSO_4$ at 70 °C. The electrode was rotated at 1600 rpm.

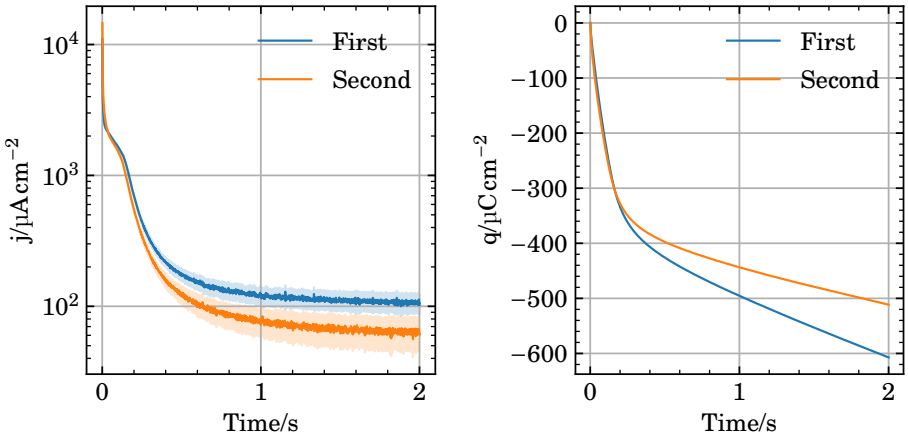

Figure E.2: Current (a) and charge (b) versus time during two potential holds at 0.3 V. The working electrode was a Au_{poly} RDE. The electrolyte contained 0.5 mol dm^{-3} H_2SO_4 and 1 mmol dm^{-3} $CuSO_4$ at 70 °C. The electrode was rotated at 1600 rpm.

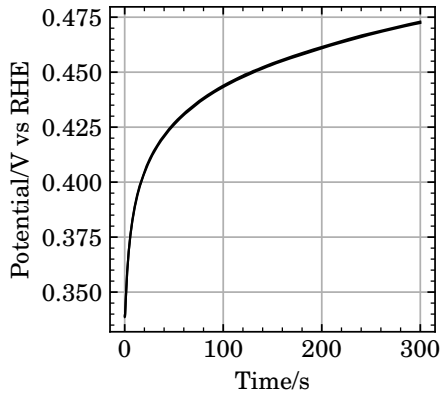

Figure E.3: Open circuit potential of a Au_{poly} RDE after a potential hold at 0.3 V in an electrolyte containing 0.5 mol dm^{-3} H_2SO_4 and 1 mmol dm^{-3} $CuSO_4$ at 70 °C. The electrode was rotated at 1600 rpm.

E.2 Experiment 1

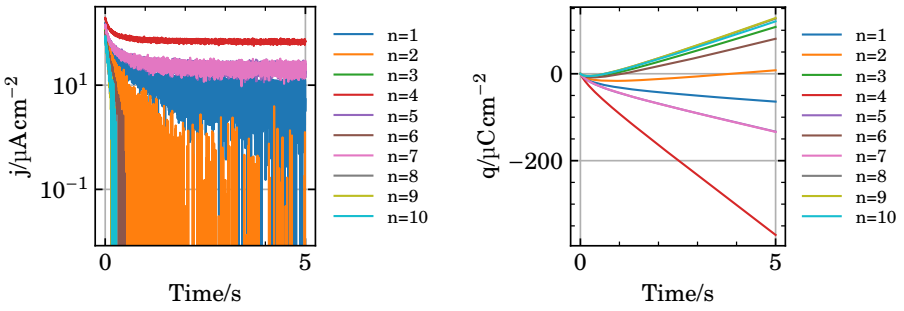

(a) (b)

Figure E.4: Current (a) and charge (b) versus time during each potential hold at 0.7 V in experiment 1.

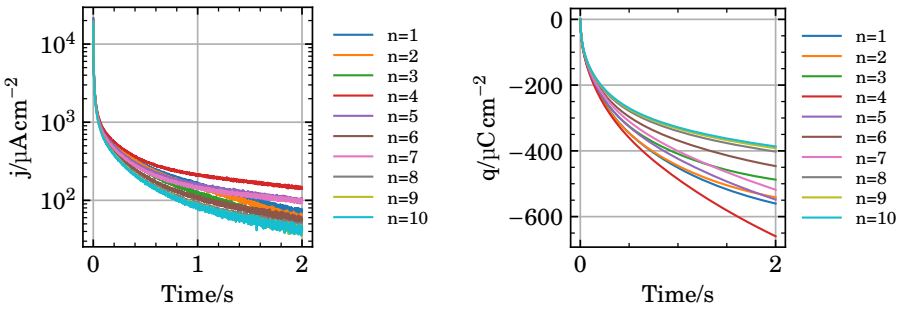

(a) (b)

Figure E.5: Current (a) and charge (b) versus time during each potential hold at 0.34 V in experiment 1.

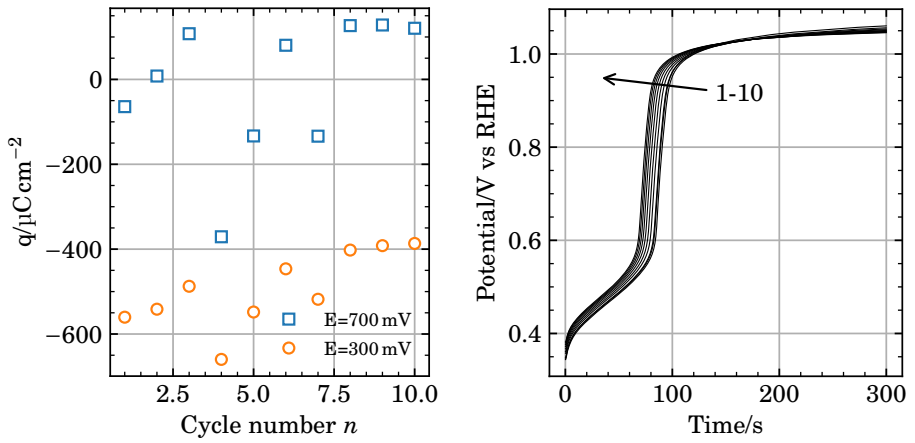

(a) (b)

Figure E.6: (a) is the total charge at at the end of the potential holds in (blue squares) figure E.4 and figure E.5 (orange circles). (b) is the open circuit potential of the electrode after each potential hold in figure E.5. The figure correspond to experiment 1.

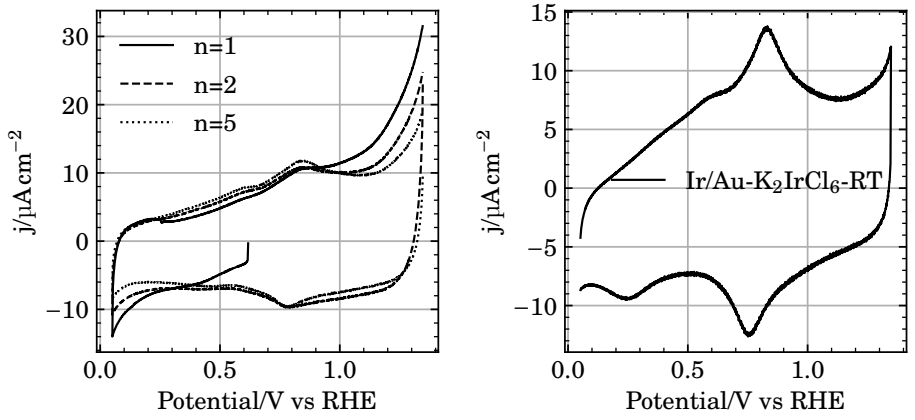

(a) (b)

Figure E.7: Voltammograms of the electrode prepared in experiment 1, obtained in 0.5 mol dm^{-3} H_2SO_4 ar 50 mV s^{-1}. (a) is the first, second and fifth potential cycle. (b) is the voltammogram obtained after extensive potential cycling. Ususally 50 cycles.

E.3 Experiment 2

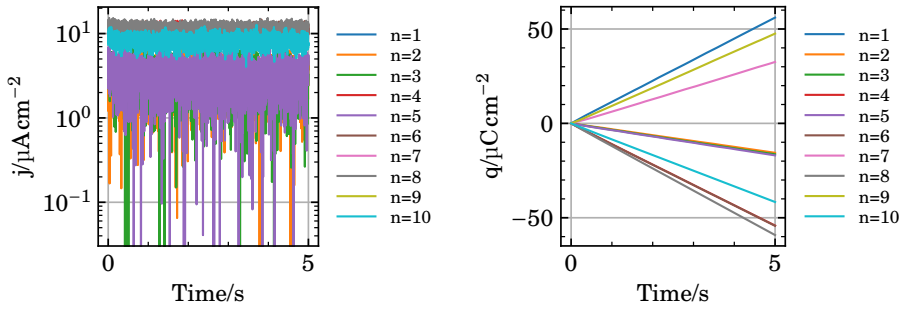

(a) (b)

Figure E.8: Current (a) and charge (b) versus time during each potential hold at 0.7 V in experiment 2.

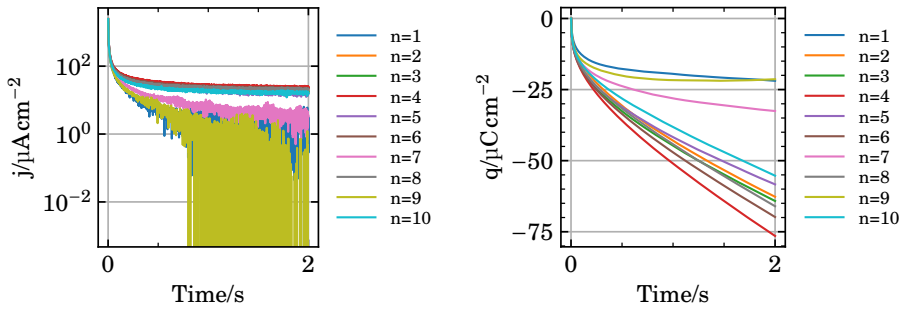

(a) (b)

Figure E.9: Current (a) and charge (b) versus time during each potential hold at 0.3 V in experiment 2.

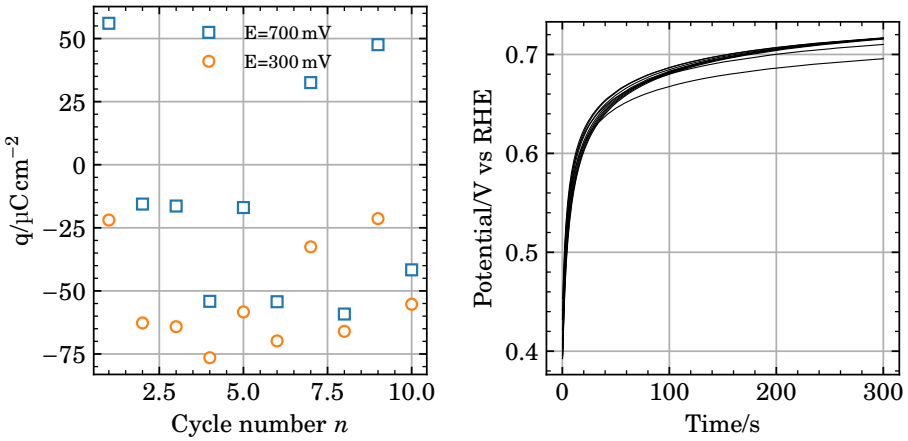

(a) (b)

Figure E.10: (a) is the total charge at the end of each potential hold at 0.7 V or 0.3 V in (blue squares) figure E.8 and (orange circles) figure E.9. (b) is the open circuit potential of the electrode after each potential hold at 0.3 V in figure E.9. The figure correspond to experiment 2.

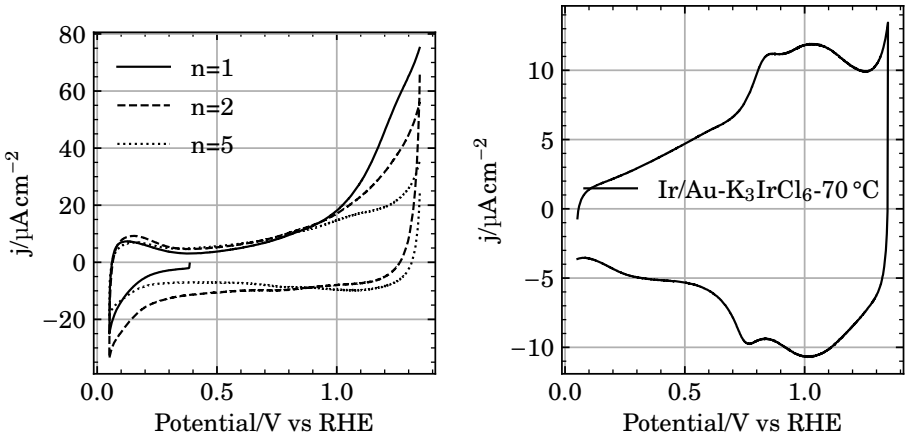

(a) (b)

Figure E.11: Voltammograms of the electrode prepared in experiment 2, obtained in 0.5 mol dm^{-3} H_2SO_4 ar 50 mV s^{-1}. (a) is the first, second and fifth potential cycle. (b) is the voltammogram obtained after extensive potential cycling. Ususally 50 cycles.

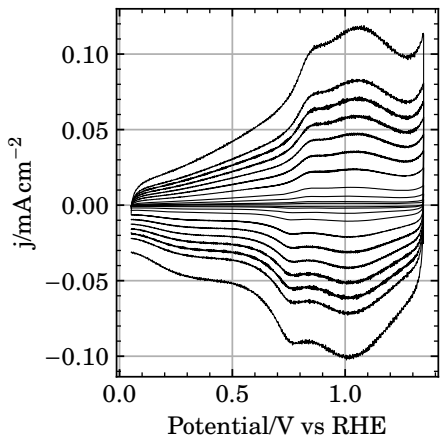

(a) CV charge from run 2

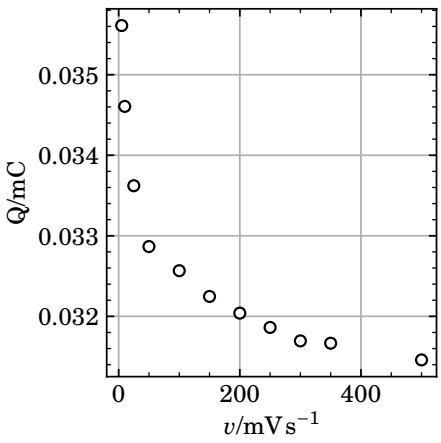

(b) Q vs v 2

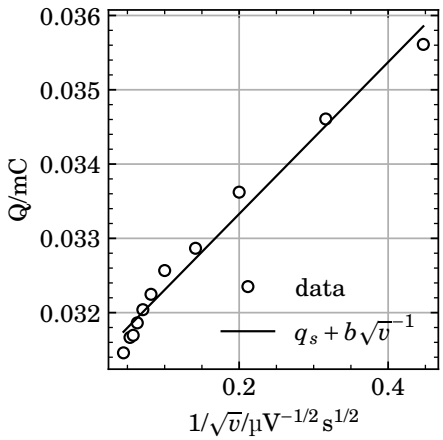

(c) CV charge from run 2

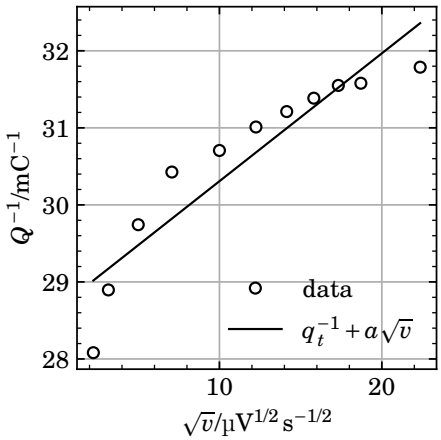

(d) CV charge from run 2

Figure E.12: (a) Voltammograms of an electrode prepared in experiment 2 performed at different potential sweep rates in 0.5 mol dm^{-3} H_2SO_4. (b) Anodic charge of the voltammograms between 0.4 V and 1.3 V versus potential sweep rate. (c) Anodic charge extrapolated to infinite potential sweep rate. (d) Anodic charge extrapolated to zero potential sweep rate.

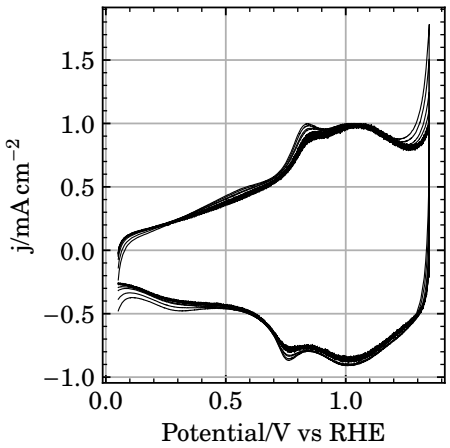

Figure E.13: The voltammograms from figure E.12 (a) normalized to the anodic peak current around 1 V.

E.4 Experiment 3

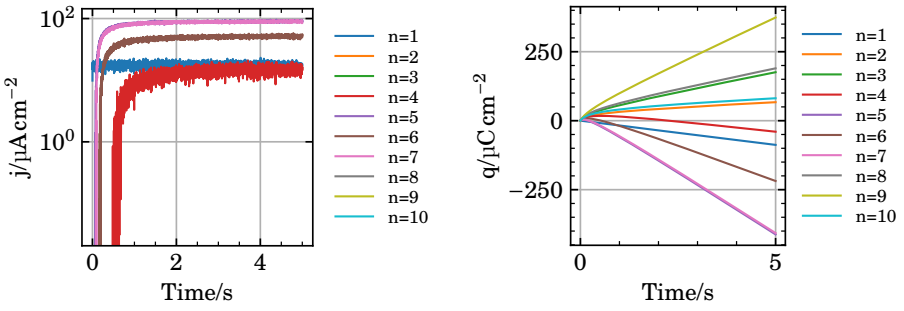

(a) (b)

Figure E.14: Current (a) and charge (b) versus time during each potential hold at 0.7 V in experiment 3.

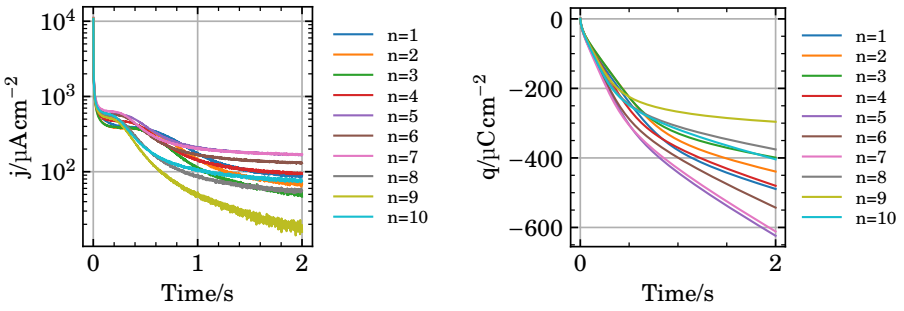

(a) (b)

Figure E.15: Current (a) and charge (b) versus time during each potential hold at 0.3 V in experiment 3.

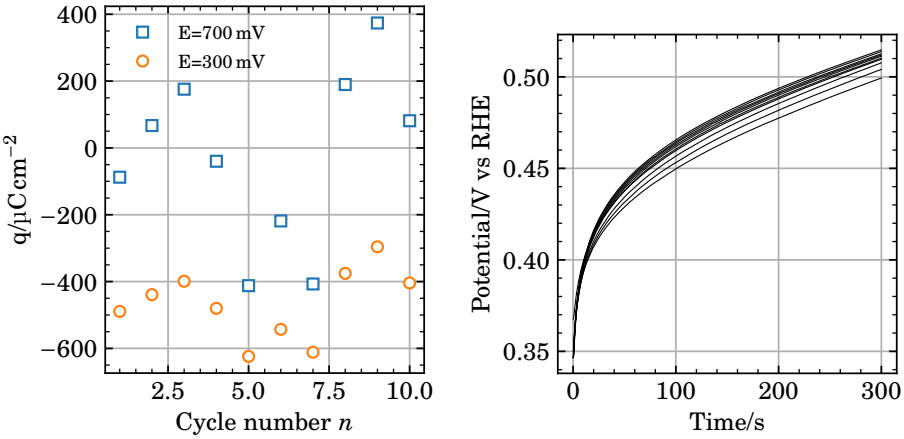

(a) (b)

Figure E.16: (a) is the total charge at the end of each potential hold at 0.7 V or 0.3 V in (blue squares) figure E.14 and (orange circles) figure E.15. (b) is the open circuit potential of the electrode after each potential hold at 0.3 V in figure E.15. The figure correspond to experiment 3.

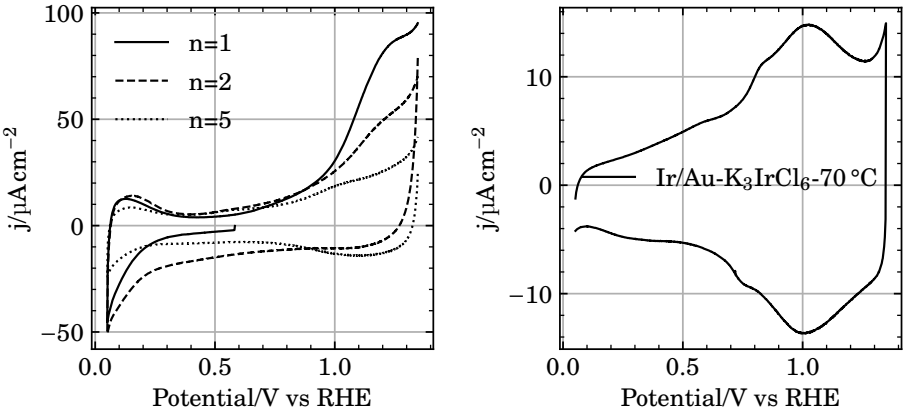

(a) (b)

Figure E.17: Voltammograms of the electrode prepared in experiment 3, obtained in 0.5 mol dm^{-3} H_2SO_4 ar 50 mV s^{-1}. (a) is the first, second and fifth potential cycle. (b) is the voltammogram obtained after extensive potential cycling. Ususally 50 cycles.

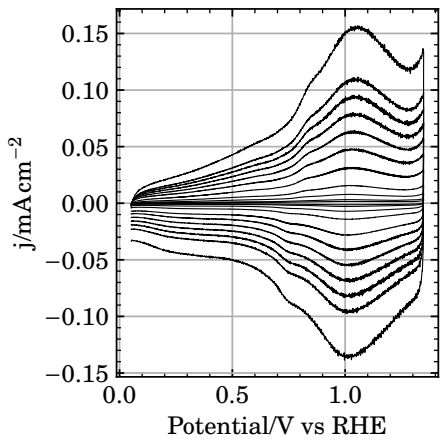

(a) CV charge from run 3

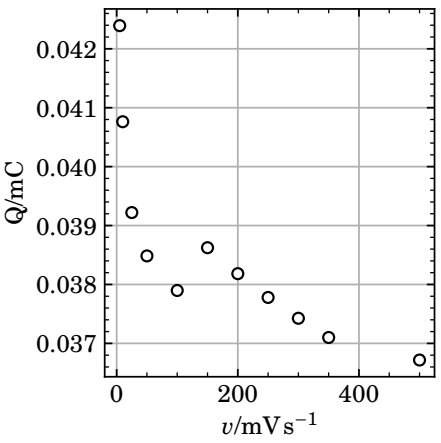

(b) Q vs v 3

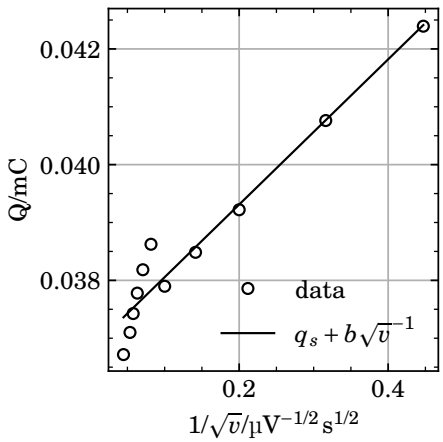

(c) CV charge from run 3

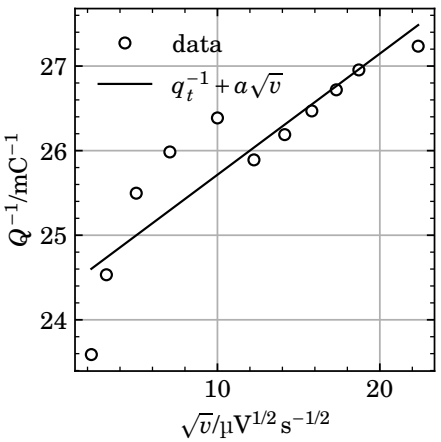

(d) CV charge from run 3

Figure E.18: (a) Voltammograms of an electrode prepared in experiment 3 performed at different potential sweep rates in 0.5 mol dm^{-3} H_2SO_4. (b) Anodic charge of the voltammograms between 0.4 V and 1.3 V versus potential sweep rate. (c) Anodic charge extrapolated to infinite potential sweep rate. (d) Anodic charge extrapolated to zero potential sweep rate.

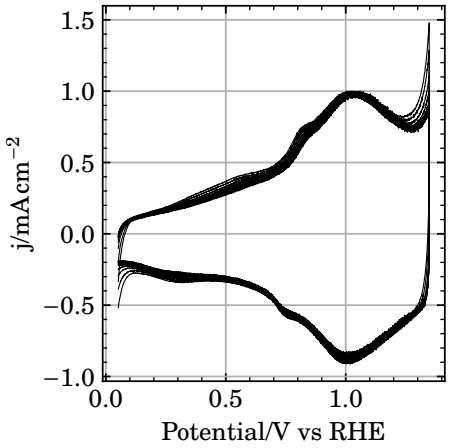

Figure E.19: The voltammograms from figure E.18 (a) normalized to the anodic peak current around 1 V.

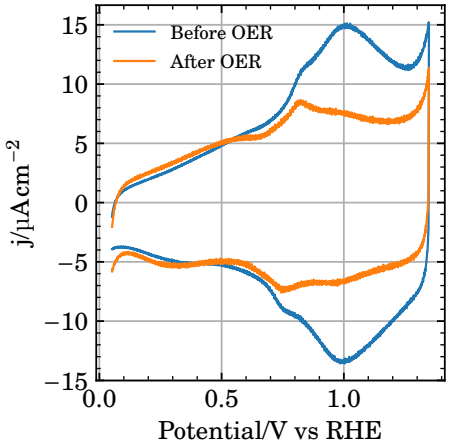

Figure E.20: Voltammograms of an electrode prepared in experiment 3 by the SLRR routine, before and after oxygen evolution. Voltammograms were obtained in 0.5 mol dm^{-3} H_2SO_4 at 50 mV s^{-1}.

E.5 Experiment 4

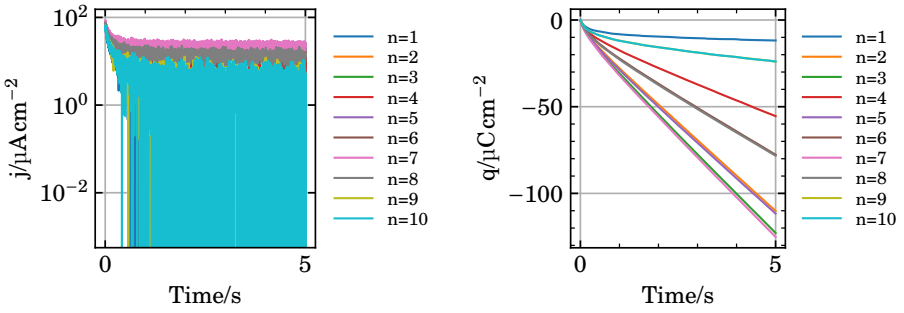

(a) (b)

Figure E.21: Current (a) and charge (b) versus time during each potential hold at 0.7 V in experiment 4.

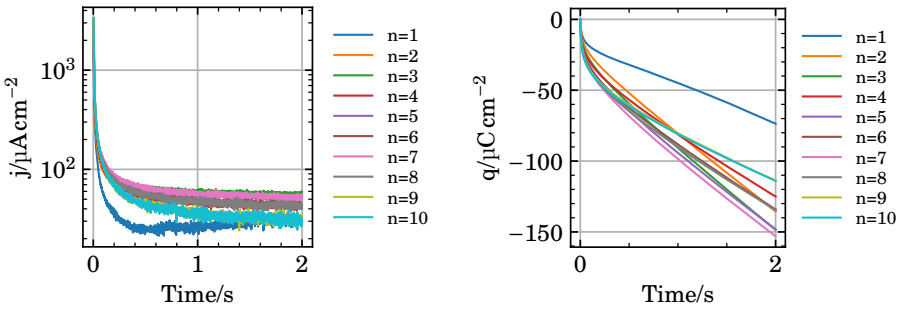

(a) (b)

Figure E.22: Current (a) and charge (b) versus time during each potential hold at 0.3 V in experiment 4.

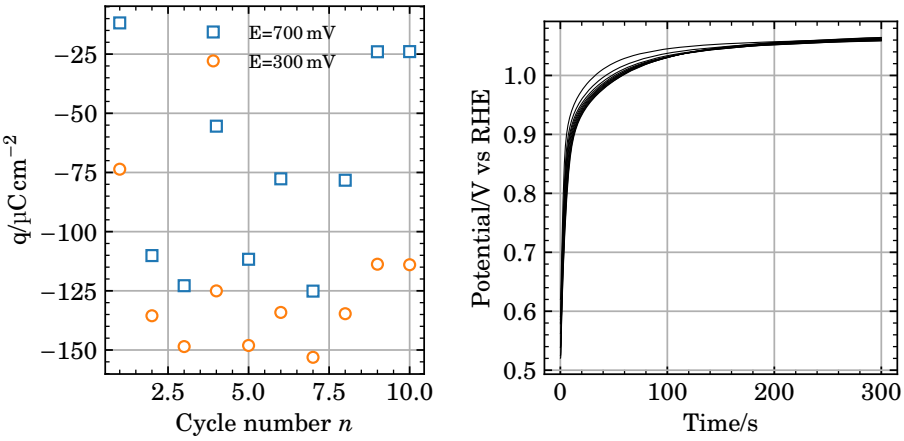

(a) (b)

Figure E.23: (a) is the total charge at the end of each potential hold at 0.7 V or 0.3 V in (blue squares) figure E.21 and (orange circles) figure E.22. (b) is the open circuit potential of the electrode after each potential hold at 0.3 V in figure E.22. The figure correspond to experiment 4.

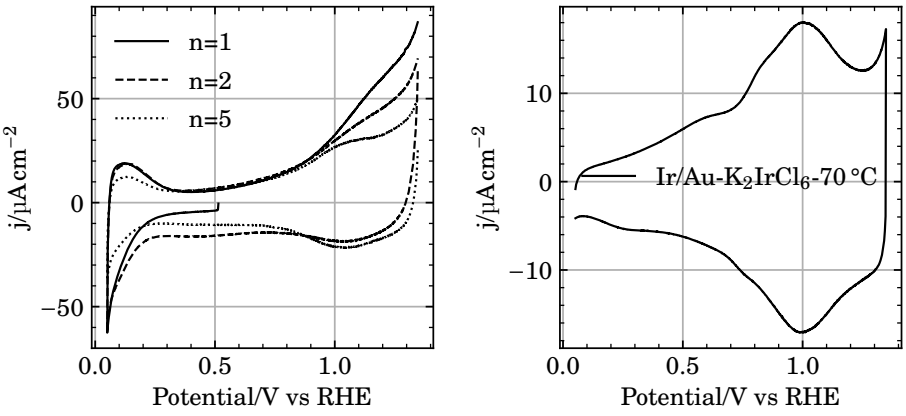

(a) (b)

Figure E.24: Voltammograms of the electrode prepared in experiment 4, obtained in 0.5 mol dm^{-3} H_2SO_4 ar 50 mV s^{-1}. (a) is the first, second and fifth potential cycle. (b) is the voltammogram obtained after extensive potential cycling. Ususally 50 cycles.

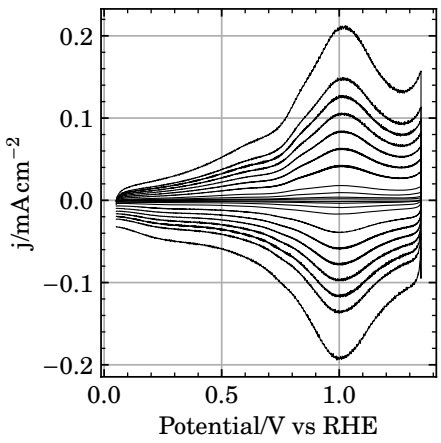

(a) CV charge from run 4

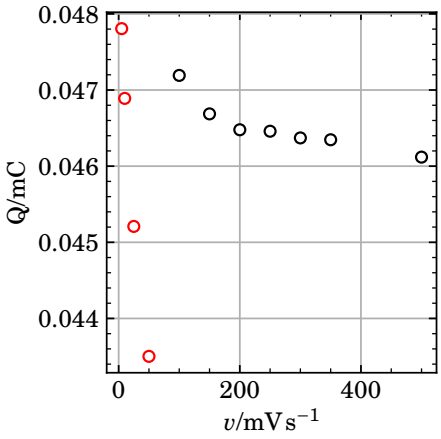

(b) Q vs v 4

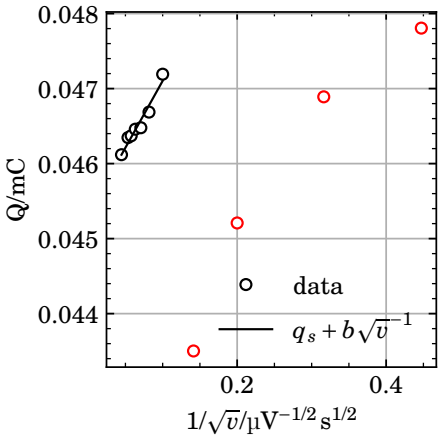

(c) CV charge from run 4

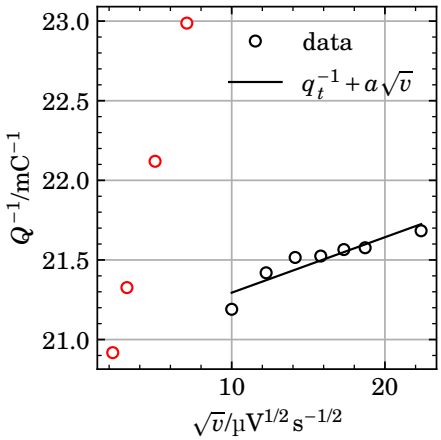

(d) CV charge from run 4

Figure E.25: (a) Voltammograms of an electrode prepared in experiment 4 performed at different potential sweep rates in 0.5 mol dm^{-3} H_2SO_4. (b) Anodic charge of the voltammograms between 0.4 V and 1.3 V versus potential sweep rate. (c) Anodic charge extrapolated to infinite potential sweep rate. (d) Anodic charge extrapolated to zero potential sweep rate.

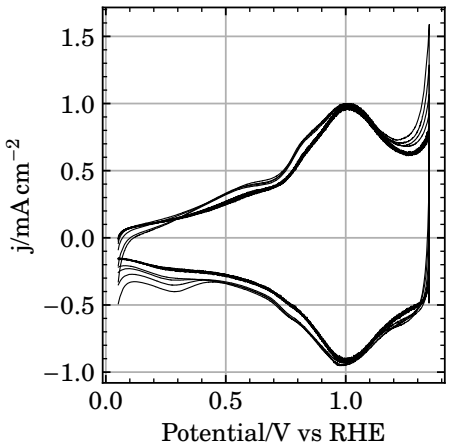

Figure E.26: The voltammograms from figure E.25 (a) normalized to the anodic peak current around 1 V.

E.6 Experiment 5

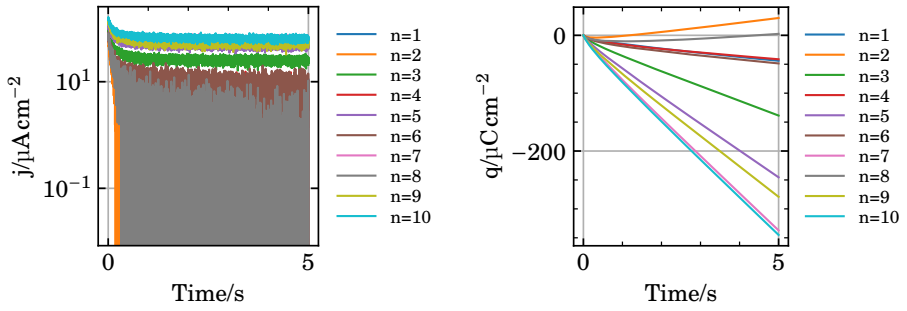

(a) (b)

Figure E.27: Current (a) and charge (b) versus time during each potential hold at 0.7 V in experiment 5.

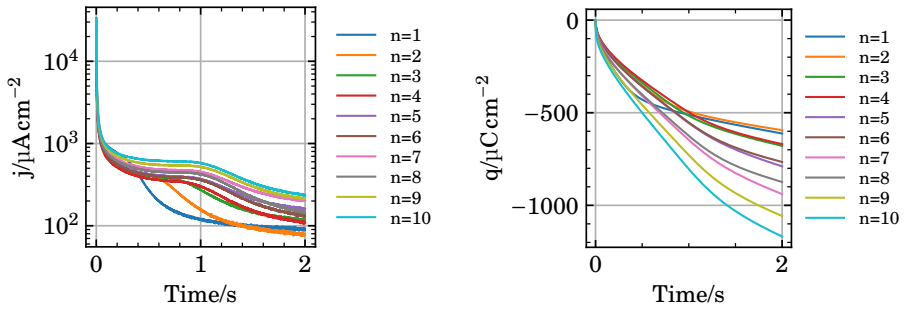

(a) (b)

Figure E.28: Current (a) and charge (b) versus time during each potential hold at 0.3 V in experiment 5.

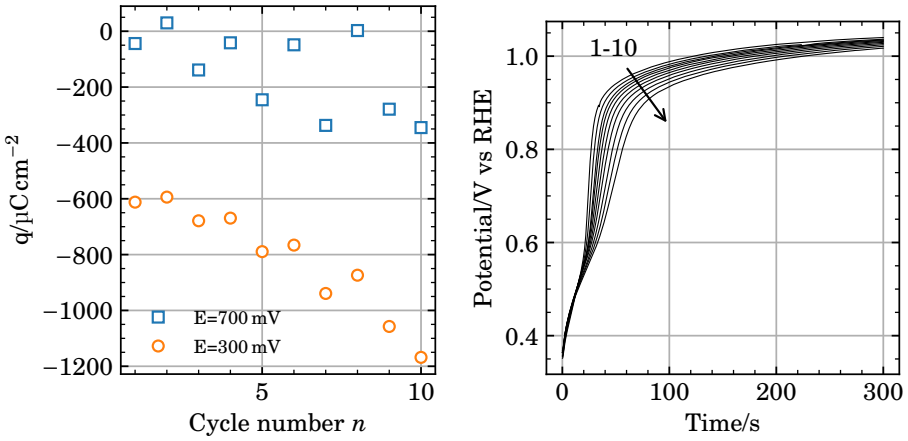

(a) (b)

Figure E.29: (a) is the total charge at the end of each potential hold at 0.7 V or 0.3 V in (blue squares) figure E.27 and (orange circles) figure E.28. (b) is the open circuit potential of the electrode after each potential hold at 0.3 V in figure E.28. The figure correspond to experiment 5.

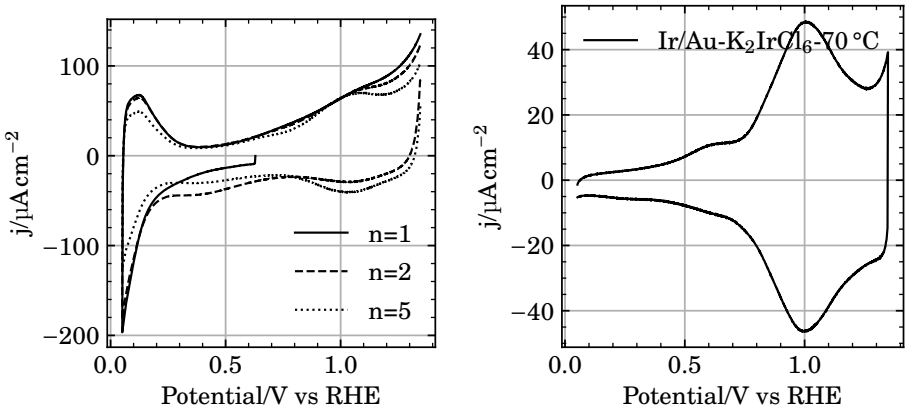

(a) (b)

Figure E.30: Voltammograms of the electrode prepared in experiment 5, obtained in 0.5 mol dm^{-3} H_2SO_4 ar 50 mV s^{-1}. (a) is the first, second and fifth potential cycle. (b) is the voltammogram obtained after extensive potential cycling. Ususally 50 cycles.

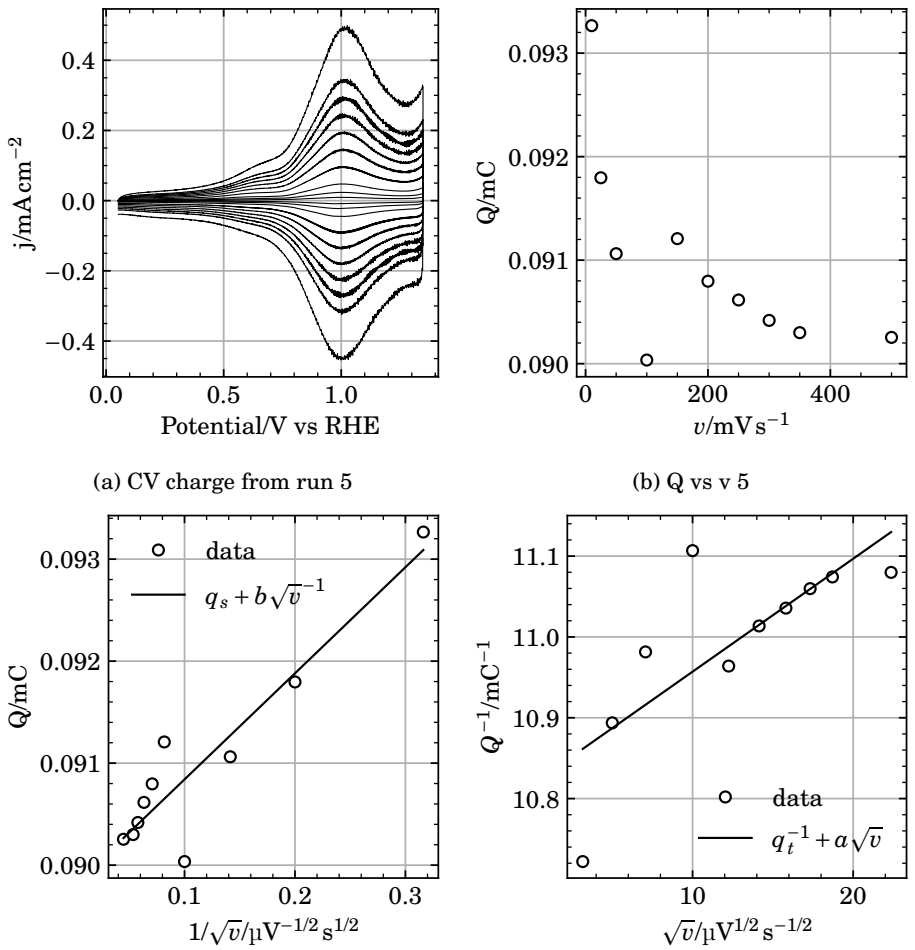

(a) CV charge from run 5

(b) Q vs v 5

(c) CV charge from run 5

(d) CV charge from run 5

Figure E.31: (a) Voltammograms of an electrode prepared in experiment 5 performed at different potential sweep rates in 0.5 mol dm^{-3} H_2SO_4. (b) Anodic charge of the voltammograms between 0.4 V and 1.3 V versus potential sweep rate. (c) Anodic charge extrapolated to infinite potential sweep rate. (d) Anodic charge extrapolated to zero potential sweep rate.

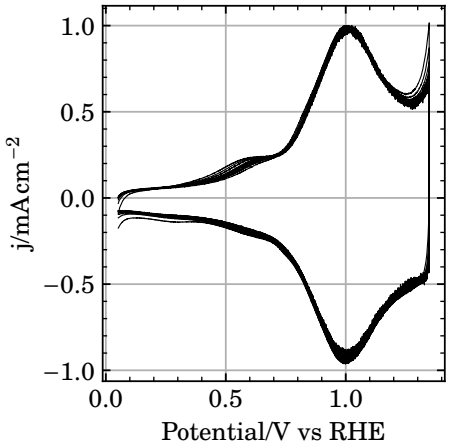

Figure E.32: The voltammograms from figure E.31 (a) normalized to the anodic peak current around 1 V.

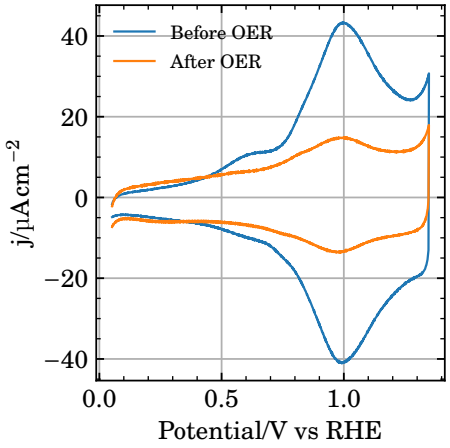

Figure E.33: Voltammograms of an electrode prepared in experiment 5 by the SLRR routine, before and after oxygen evolution. Voltammograms were obtained in 0.5 mol dm^{-3} H_2SO_4 at 50 mV s^{-1}.

E.7 Experiment 6

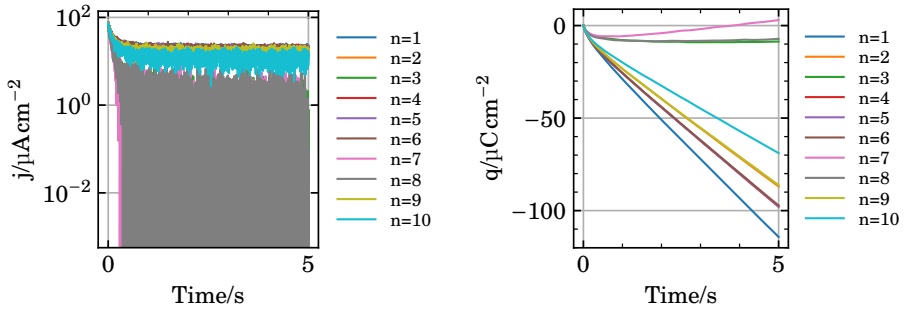

(a) (b)

Figure E.34: Current (a) and charge (b) versus time during each potential hold at 0.7 V in experiment 6.

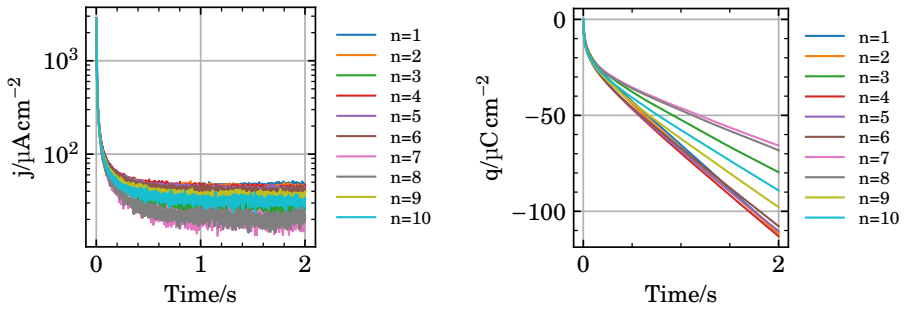

(a) (b)

Figure E.35: Current (a) and charge (b) versus time during each potential hold at 0.34 V in experiment 6.

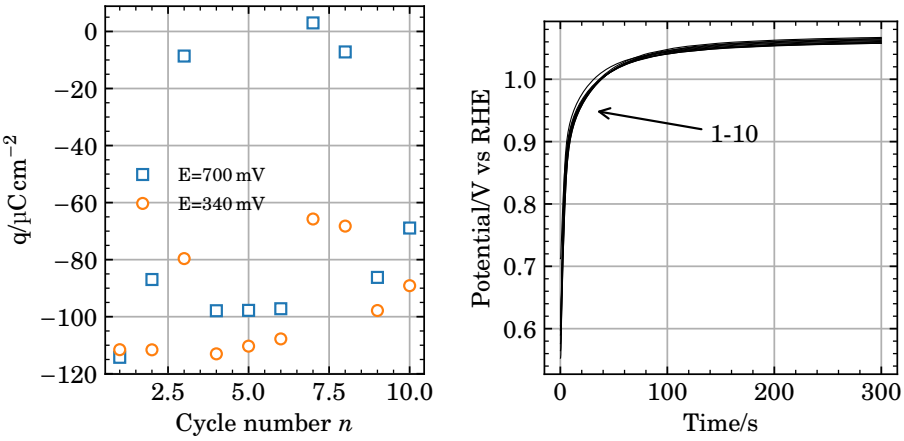

(a) (b)

Figure E.36: (a) is the total charge at the end of each potential hold at 0.7 V or 0.34 V in (blue squares) figure E.34 and (orange circles) figure E.35. (b) is the open circuit potential of the electrode after each potential hold at 0.34 V in figure E.35. The figure correspond to experiment 6.

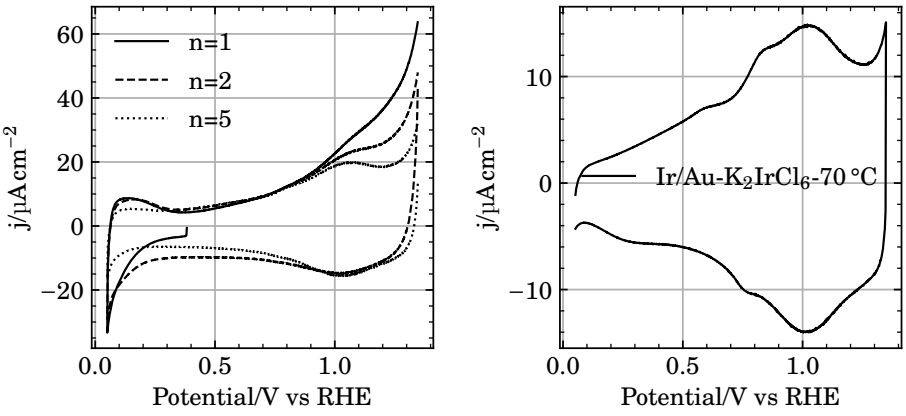

(a) (b)

Figure E.37: Voltammograms of the electrode prepared in experiment 6, obtained in 0.5 mol dm^{-3} H_2SO_4 ar 50 mV s^{-1}. (a) is the first, second and fifth potential cycle. (b) is the voltammogram obtained after extensive potential cycling. Ususally 50 cycles.

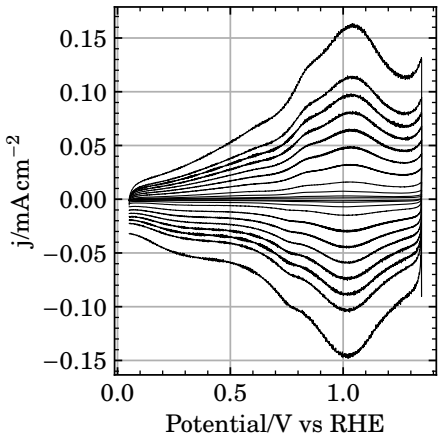

(a) CV charge from run 6

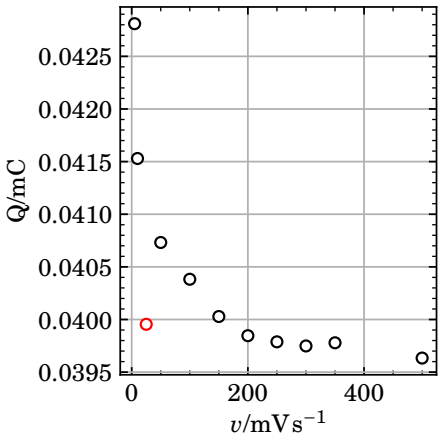

(b) Q vs v 6

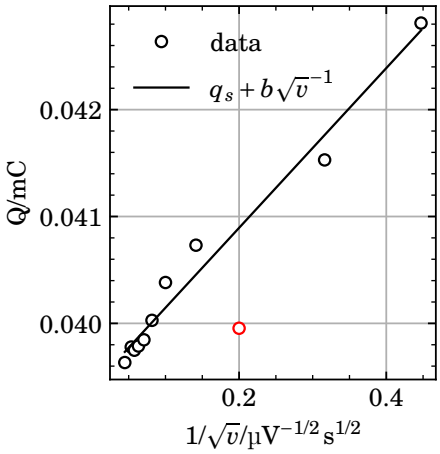

(c) CV charge from run 6

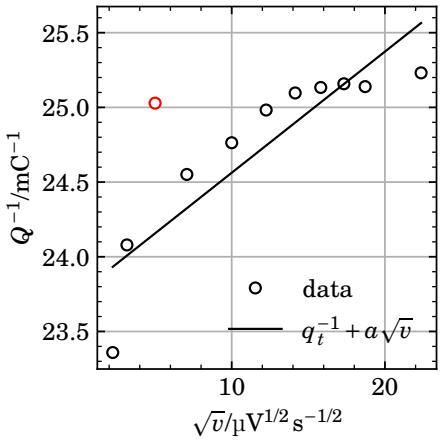

(d) CV charge from run 6

Figure E.38: (a) Voltammograms of an electrode prepared in experiment 6 performed at different potential sweep rates in 0.5 mol dm^{-3} H_2SO_4. (b) Anodic charge of the voltammograms between 0.4 V and 1.3 V versus potential sweep rate. (c) Anodic charge extrapolated to infinite potential sweep rate. (d) Anodic charge extrapolated to zero potential sweep rate.

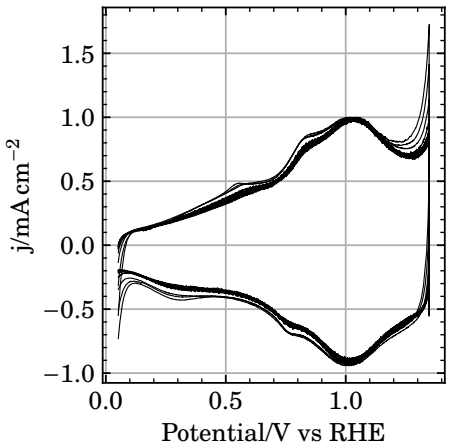

Figure E.39: The voltammograms from figure E.38 (a) normalized to the anodic peak current around 1 V.

E.8 Experiment 7

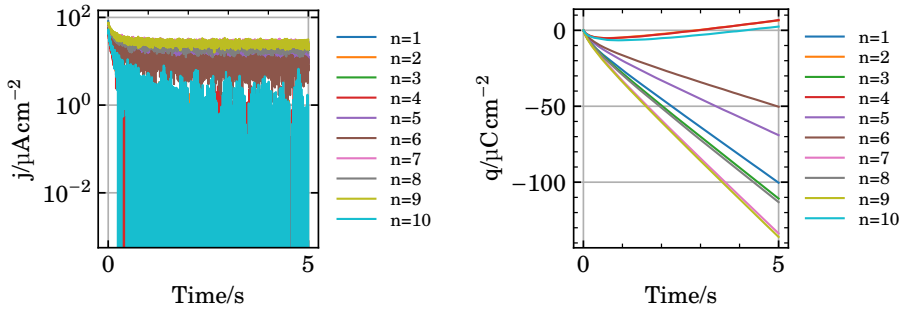

(a) (b)

Figure E.40: Current (a) and charge (b) versus time during each potential hold at 0.7 V in experiment 7.

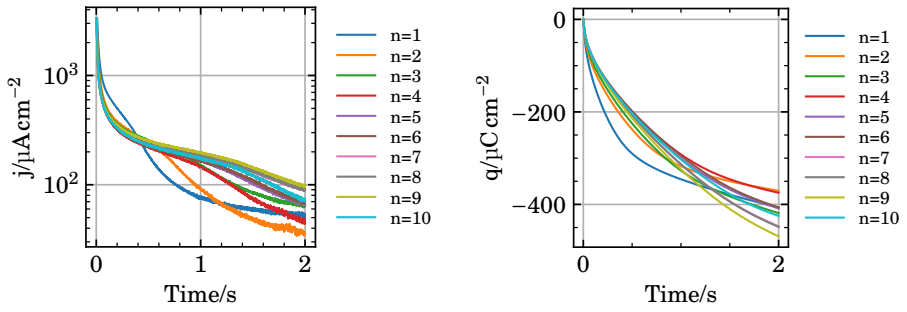

(a) (b)

Figure E.41: Current (a) and charge (b) versus time during each potential hold at 0.34 V in experiment 7.

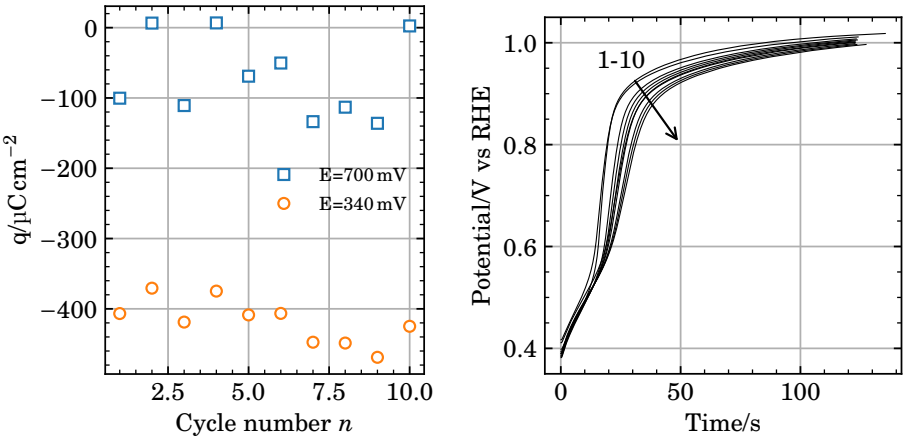

(a) (b)

Figure E.42: (a) is the total charge at the end of each potential hold at 0.7 V or 0.34 V in (blue squares) figure E.40 and (orange circles) figure E.41. (b) is the open circuit potential of the electrode after each potential hold at 0.34 V in figure E.41. The figure correspond to experiment 7.

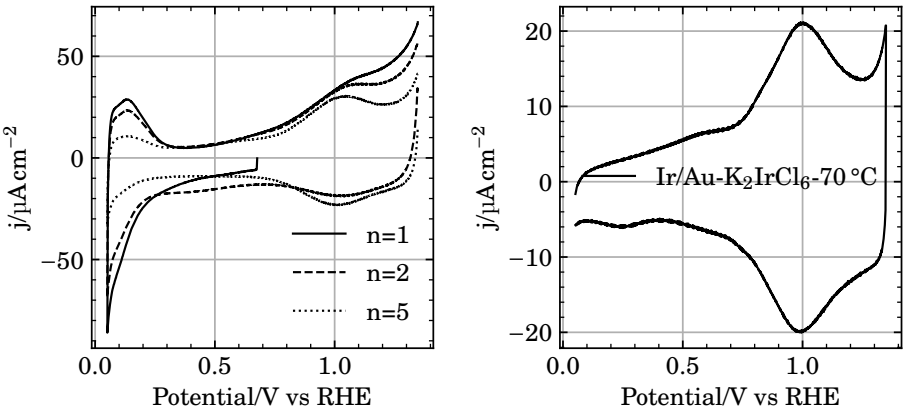

(a) (b)

Figure E.43: Voltammograms of the electrode prepared in experiment 7, obtained in 0.5 mol dm^{-3} H_2SO_4 ar 50 mV s^{-1}. (a) is the first, second and fifth potential cycle. (b) is the voltammogram obtained after extensive potential cycling. Ususally 50 cycles.

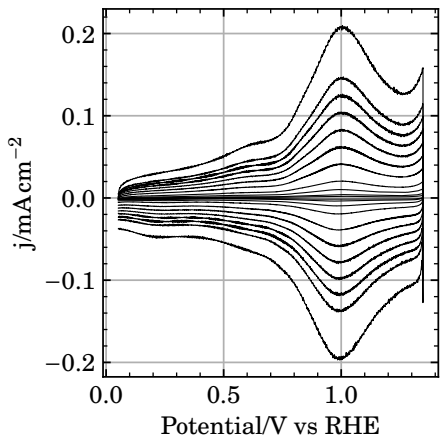

(a) CV charge from run 7

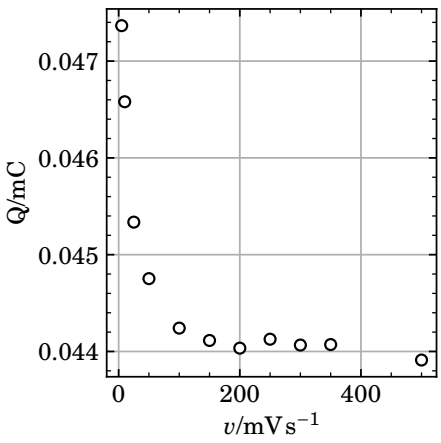

(b) Q vs v 7

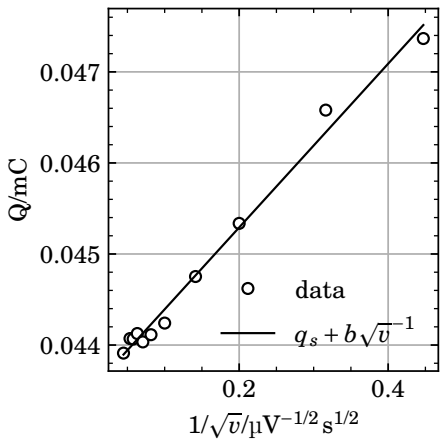

(c) CV charge from run 7

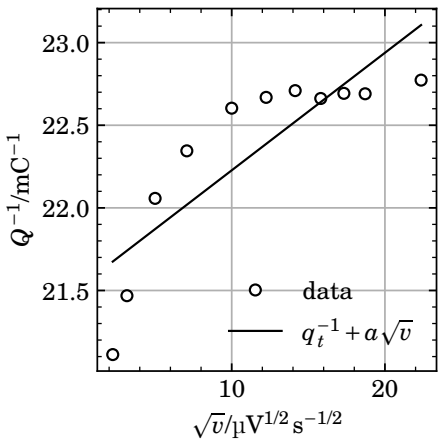

(d) CV charge from run 7

Figure E.44: (a) Voltammograms of an electrode prepared in experiment 7 performed at different potential sweep rates in 0.5 mol dm^{-3} H_2SO_4. (b) Anodic charge of the voltammograms between 0.4 V and 1.3 V versus potential sweep rate. (c) Anodic charge extrapolated to infinite potential sweep rate. (d) Anodic charge extrapolated to zero potential sweep rate.

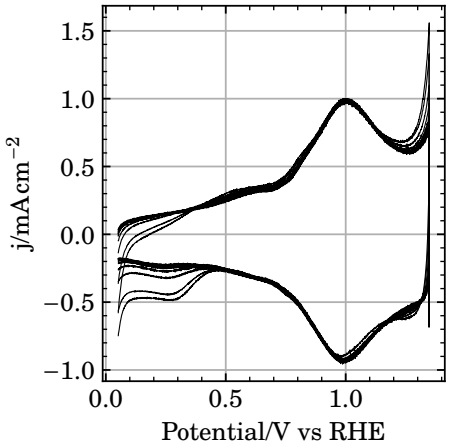

Figure E.45: The voltammograms from figure E.44 (a) normalized to the anodic peak current around 1 V.

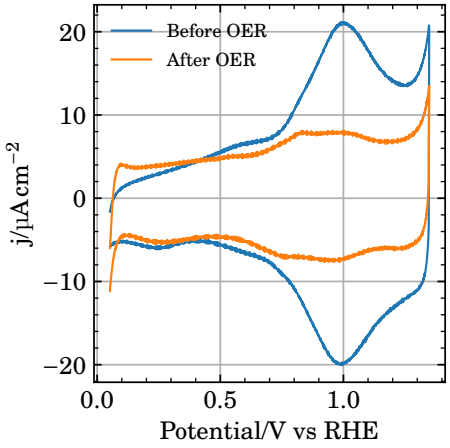

Figure E.46: Voltammograms of an electrode prepared in experiment 7 by the SLRR routine, before and after oxygen evolution. Voltammograms were obtained in 0.5 mol dm^{-3} H_2SO_4 at 50 mV s^{-1}.

E.9 Experiment 8

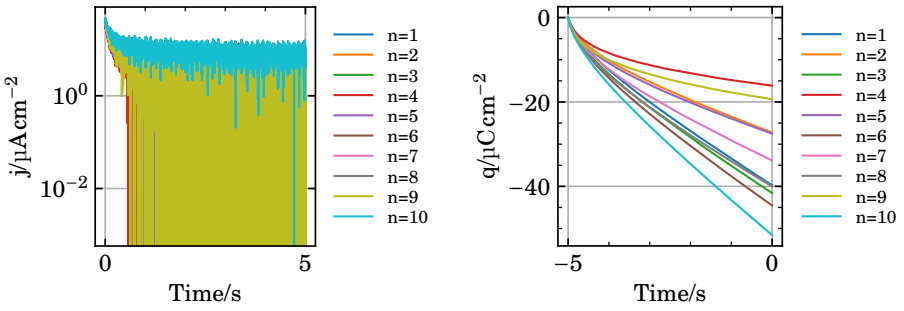

(a) (b)

Figure E.47: Current (a) and charge (b) versus time during each potential hold at 0.7 V in experiment 8.

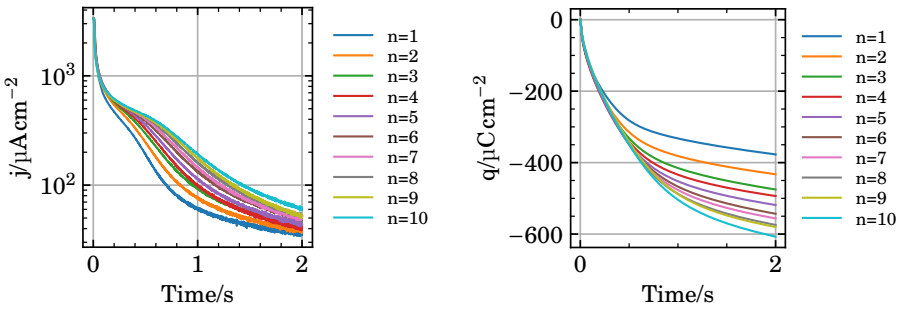

(a) (b)

Figure E.48: Current (a) and charge (b) versus time during each potential hold at 0.34 V in experiment 8.

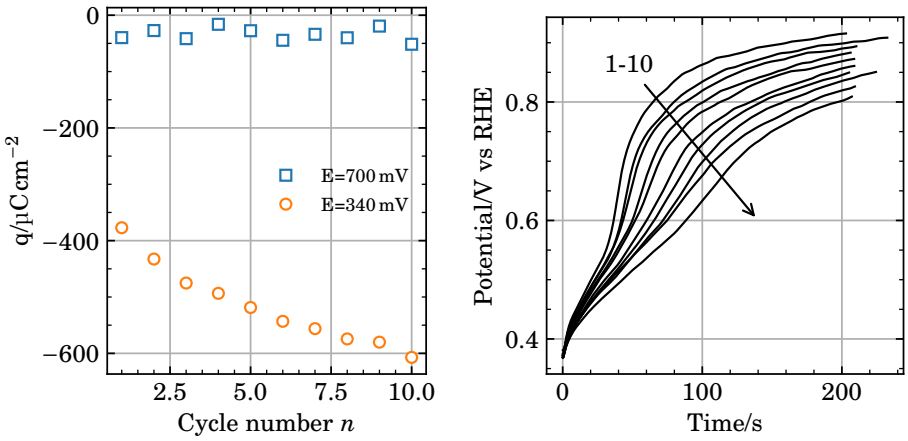

Figure E.49: (a) is the total charge at the end of each potential hold at 0.7 V or 0.34 V in (blue squares) figure E.47 and (orange circles) figure E.48. (b) is the open circuit potential of the electrode after each potential hold at 0.34 V in figure E.48. The figure correspond to experiment 8.

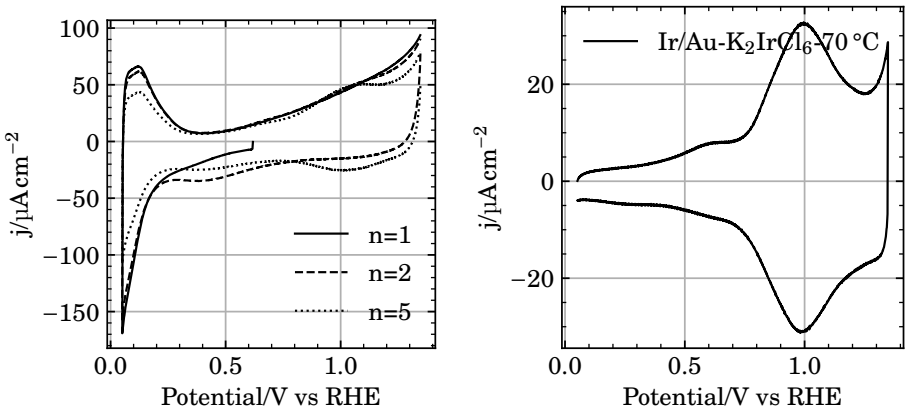

Figure E.50: Voltammograms of the electrode prepared in experiment 8, obtained in 0.5 mol dm^{-3} H_2SO_4 ar 50 mV s^{-1}. (a) is the first, second and fifth potential cycle. (b) is the voltammogram obtained after extensive potential cycling. Ususally 50 cycles.

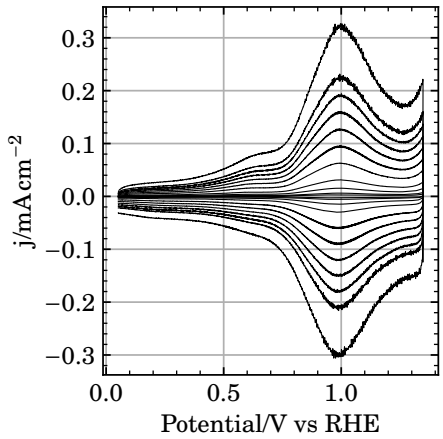

(a) CV charge from run 8

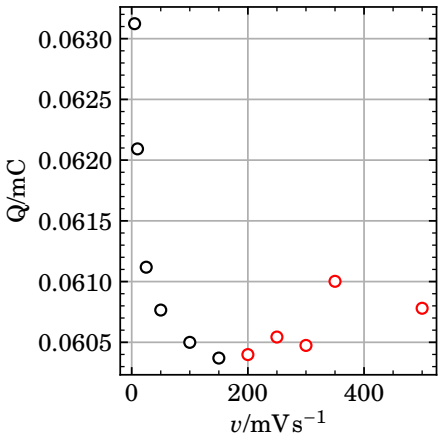

(b) Q vs v 8

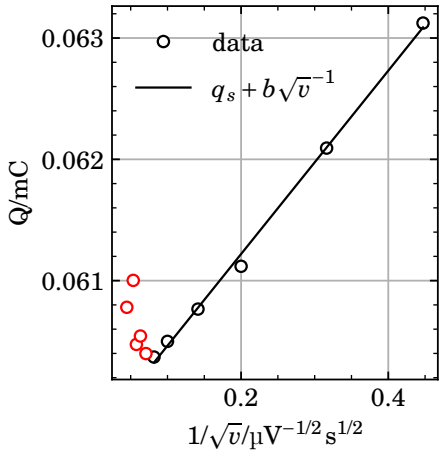

(c) CV charge from run 8

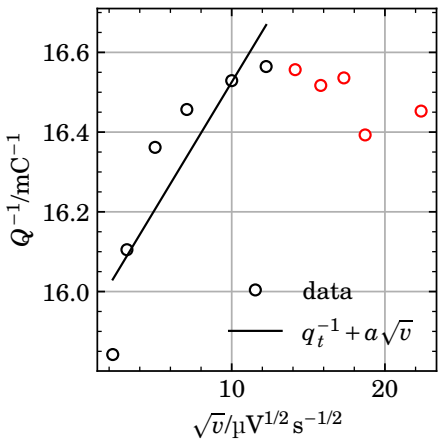

(d) CV charge from run 8

Figure E.51: (a) Voltammograms of an electrode prepared in experiment 8 performed at different potential sweep rates in 0.5 mol dm^{-3} H_2SO_4. (b) Anodic charge of the voltammograms between 0.4 V and 1.3 V versus potential sweep rate. (c) Anodic charge extrapolated to infinite potential sweep rate. (d) Anodic charge extrapolated to zero potential sweep rate.

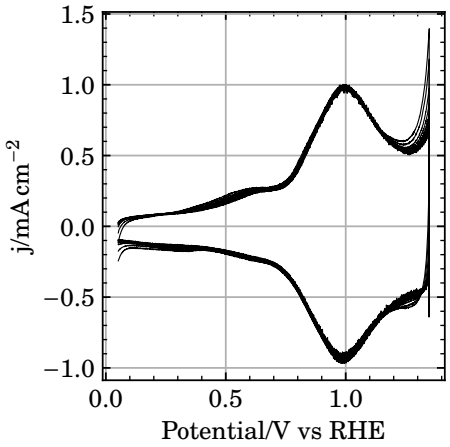

Figure E.52: The voltammograms from figure E.51 (a) normalized to the anodic peak current around 1 V.

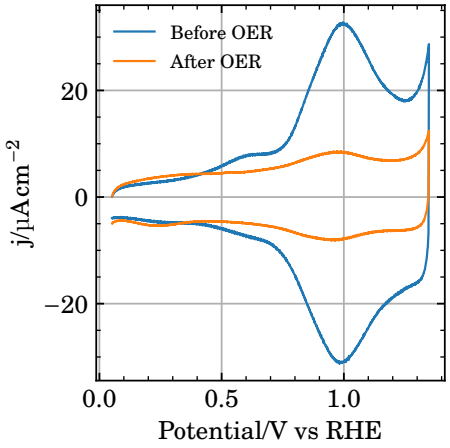

Figure E.53: Voltammograms of an electrode prepared in experiment 8 by the SLRR routine, before and after oxygen evolution. Voltammograms were obtained in 0.5 mol dm^{-3} H_2SO_4 at 50 mV s^{-1}.

E.10 Experiment 9

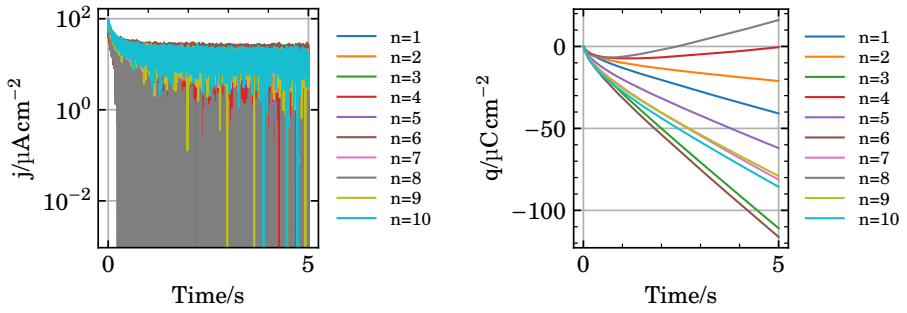

(a) (b)

Figure E.54: Current (a) and charge (b) versus time during each potential hold at 0.7 V in experiment 9.

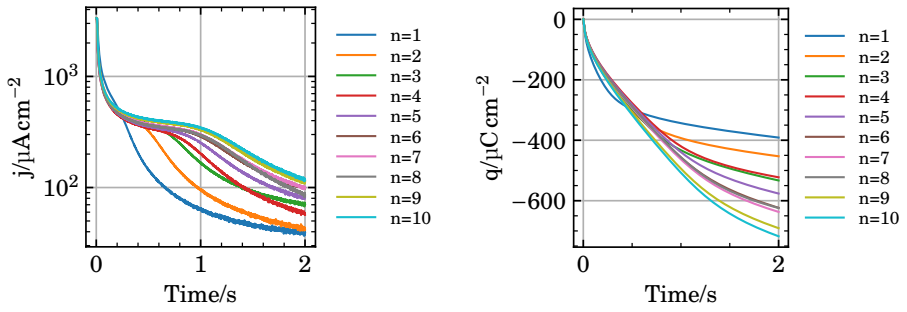

(a) (b)

Figure E.55: Current (a) and charge (b) versus time during each potential hold at 0.34 V in experiment 9.

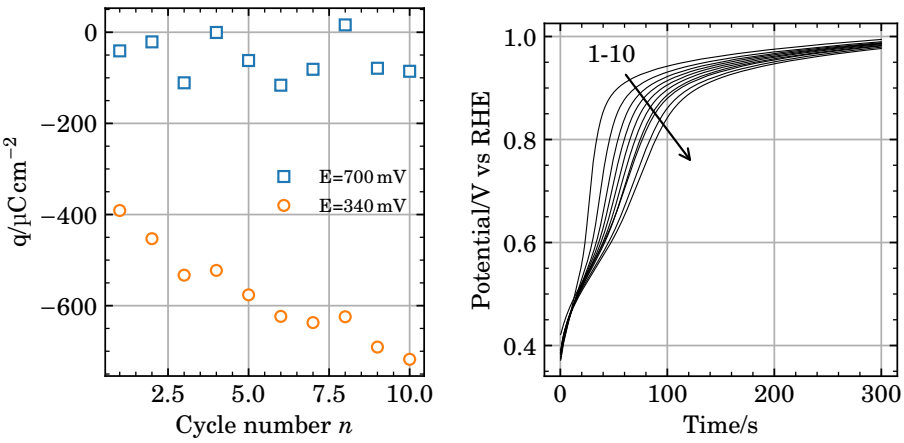

(a) (b)

Figure E.56: (a) is the total charge at the end of each potential hold at 0.7 V or 0.34 V in (blue squares) figure E.54 and (orange circles) figure E.55. (b) is the open circuit potential of the electrode after each potential hold at 0.34 V in figure E.55. The figure correspond to experiment 9.

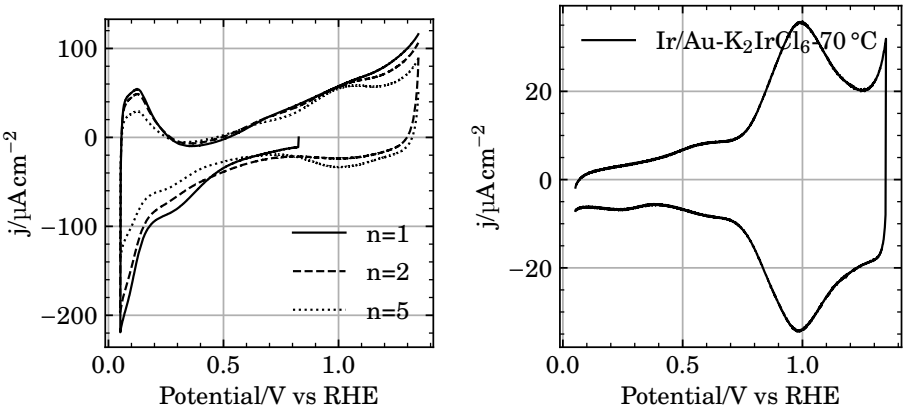

(a) (b)

Figure E.57: Voltammograms of the electrode prepared in experiment 9, obtained in 0.5 mol dm^{-3} H_2SO_4 ar 50 mV s^{-1}. (a) is the first, second and fifth potential cycle. (b) is the voltammogram obtained after extensive potential cycling. Ususally 50 cycles.

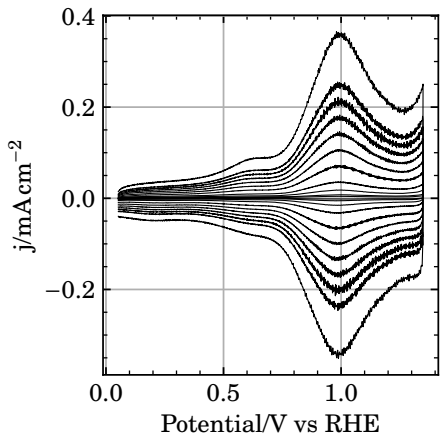

(a) CV charge from run 9

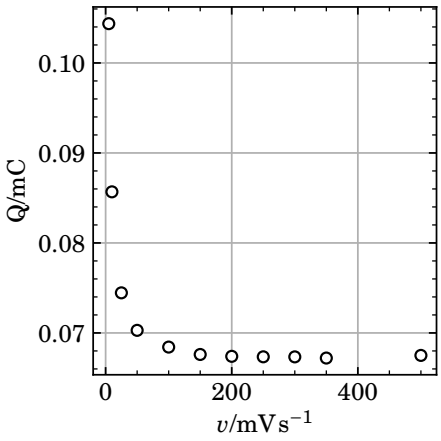

(b) Q vs v 9

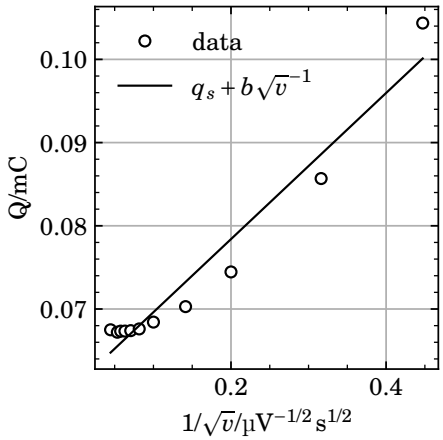

(c) CV charge from run 9

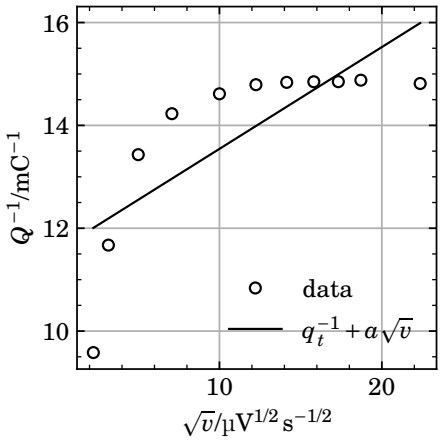

(d) CV charge from run 9

Figure E.58: (a) Voltammograms of an electrode prepared in experiment 9 performed at different potential sweep rates in 0.5 mol dm^{-3} H_2SO_4. (b) Anodic charge of the voltammograms between 0.4 V and 1.3 V versus potential sweep rate. (c) Anodic charge extrapolated to infinite potential sweep rate. (d) Anodic charge extrapolated to zero potential sweep rate.

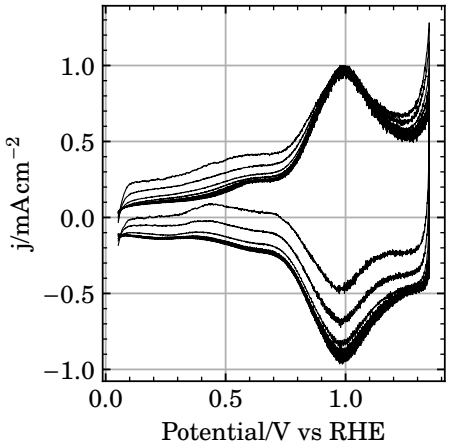

Figure E.59: The voltammograms from figure E.58 (a) normalized to the anodic peak current around 1 V.

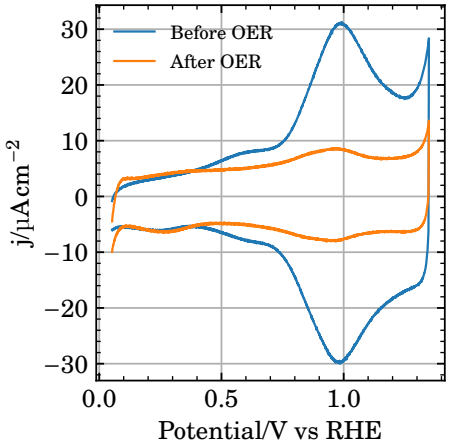

Figure E.60: Voltammograms of an electrode prepared in experiment 9 by the SLRR routine, before and after oxygen evolution. Voltammograms were obtained in 0.5 mol dm^{-3} H_2SO_4 at 50 mV s^{-1}.

E.11 Experiment 10

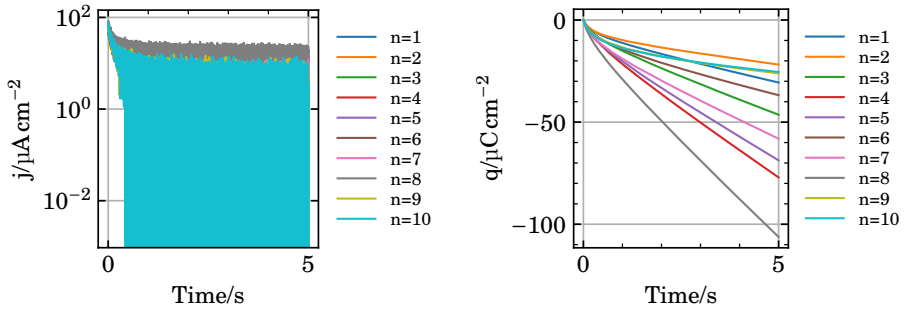

(a) (b)

Figure E.61: Current (a) and charge (b) versus time during each potential hold at 0.7 V in experiment 10.

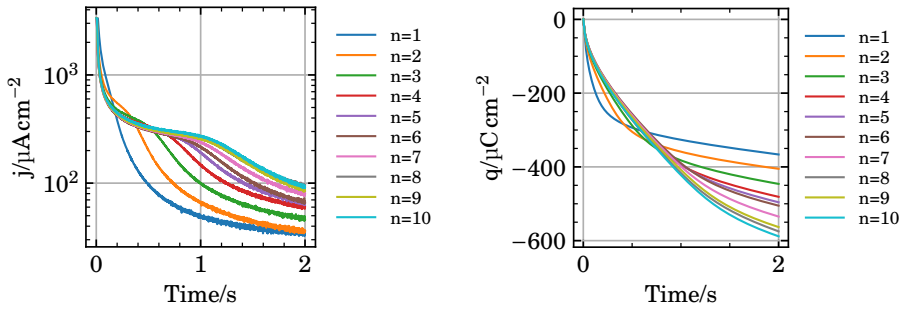

(a) (b)

Figure E.62: Current (a) and charge (b) versus time during each potential hold at 0.34 V in experiment 10.

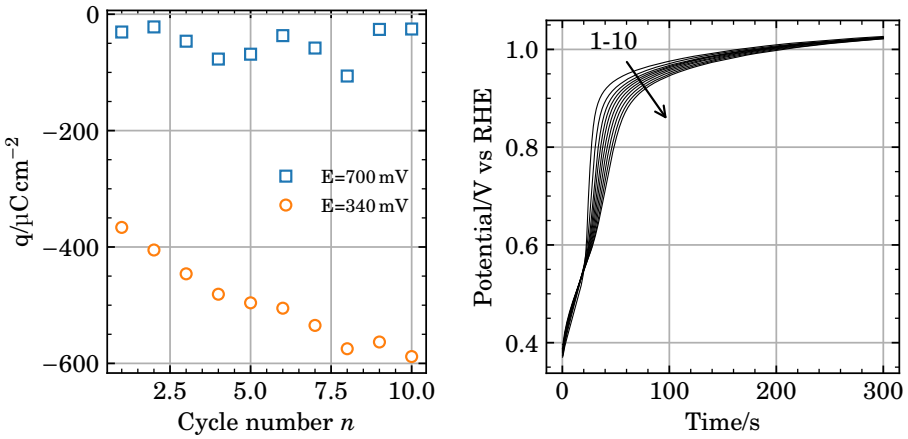

(a) (b)

Figure E.63: (a) is the total charge at the end of each potential hold at 0.7 V or 0.34 V in (blue squares) figure E.61 and (orange circles) figure E.62. (b) is the open circuit potential of the electrode after each potential hold at 0.34 V in figure E.62. The figure correspond to experiment 10.

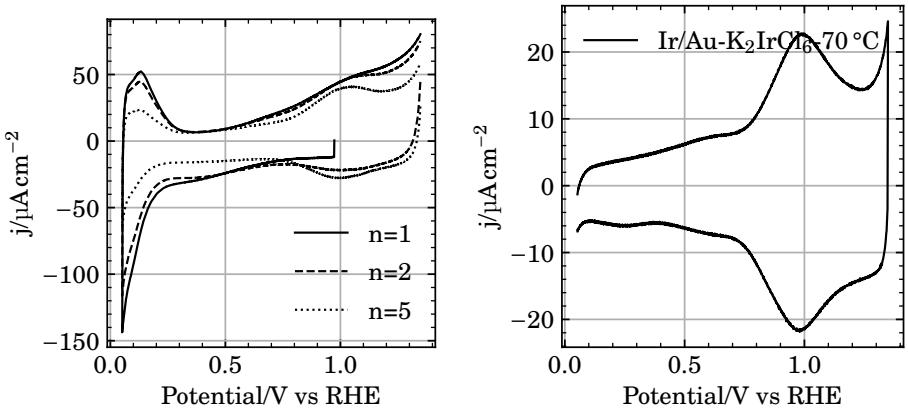

(a) (b)

Figure E.64: Voltammograms of the electrode prepared in experiment 10, obtained in 0.5 mol dm^{-3} H_2SO_4 ar 50 mV s^{-1}. (a) is the first, second and fifth potential cycle. (b) is the voltammogram obtained after extensive potential cycling. Ususally 50 cycles.

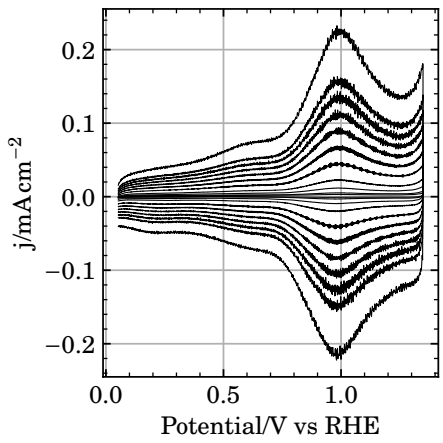

(a) CV charge from run 10

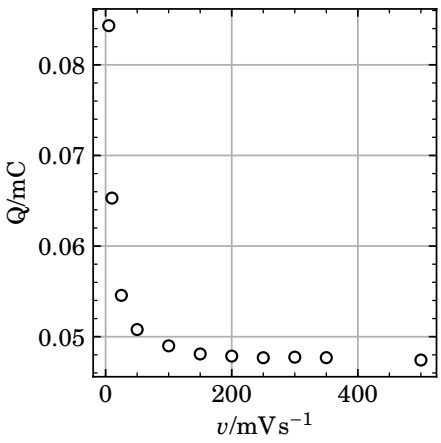

(b) Q vs v 10

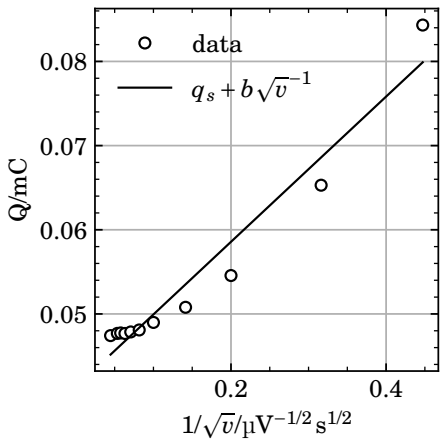

(c) CV charge from run 10

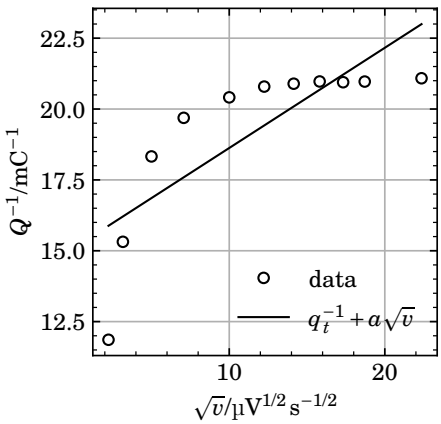

(d) CV charge from run 10

Figure E.65: (a) Voltammograms of an electrode prepared in experiment 10 performed at different potential sweep rates in 0.5 mol dm^{-3} H_2SO_4. (b) Anodic charge of the voltammograms between 0.4 V and 1.3 V versus potential sweep rate. (c) Anodic charge extrapolated to infinite potential sweep rate. (d) Anodic charge extrapolated to zero potential sweep rate.

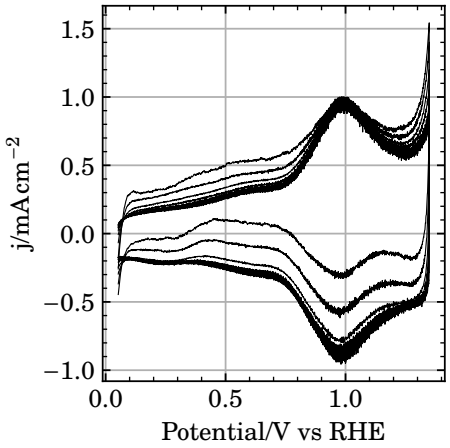

Figure E.66: The voltammograms from figure E.65 (a) normalized to the anodic peak current around 1 V.

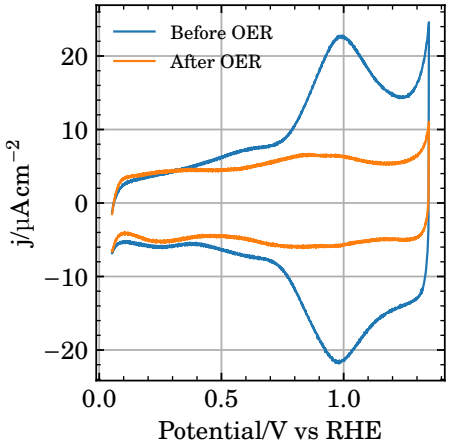

Figure E.67: Voltammograms of an electrode prepared in experiment 10 by the SLRR routine, before and after oxygen evolution. Voltammograms were obtained in 0.5 mol dm^{-3} H_2SO_4 at 50 mV s^{-1}.

E.12 Experiment 11

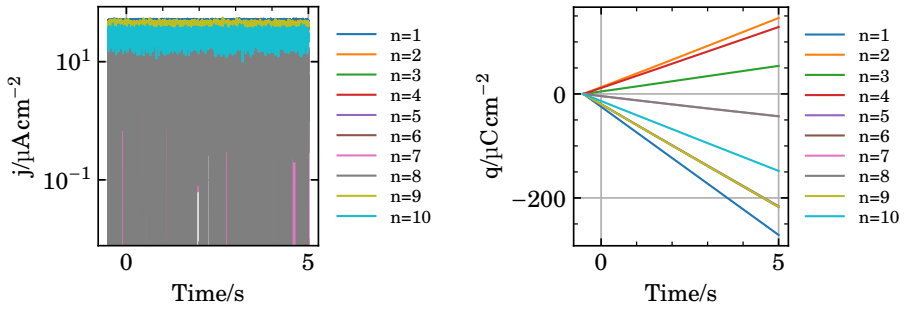

(a) (b)

Figure E.68: Current (a) and charge (b) versus time during each potential hold at 0.7 V in experiment 11.

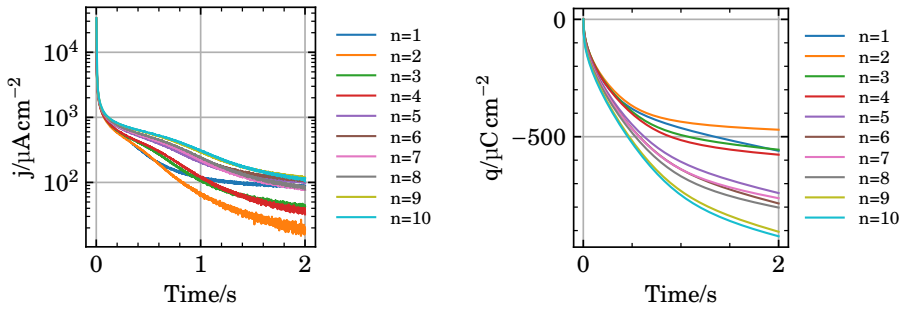

(a) (b)

Figure E.69: Current (a) and charge (b) versus time during each potential hold at 0.34 V in experiment 11.

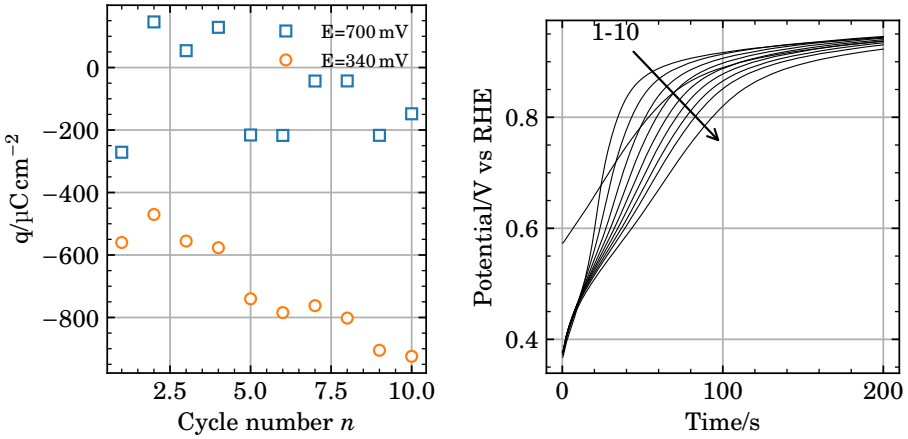

(a) (b)

Figure E.70: (a) is the total charge at the end of each potential hold at 0.7 V or 0.34 V in (blue squares) figure E.68 and (orange circles) figure E.69. (b) is the open circuit potential of the electrode after each potential hold at 0.34 V in figure E.69. The figure correspond to experiment 11.

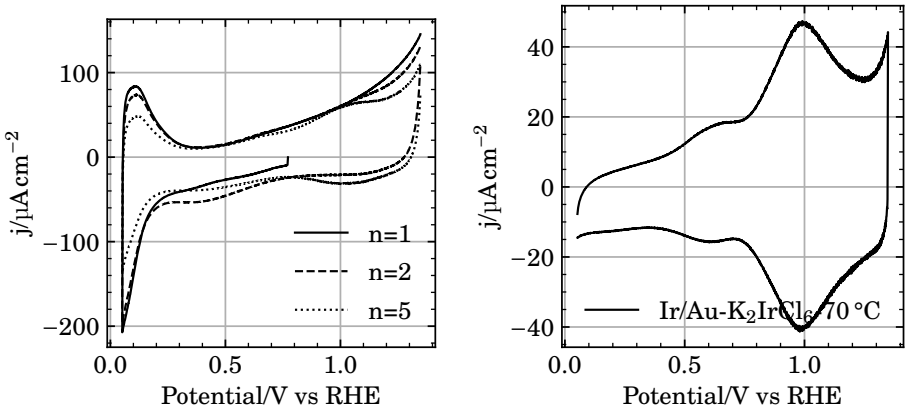

(a) (b)

Figure E.71: Voltammograms of the electrode prepared in experiment 11, obtained in 0.5 mol dm^{-3} H_2SO_4 ar 50 mV s^{-1}. (a) is the first, second and fifth potential cycle. (b) is the voltammogram obtained after extensive potential cycling. Ususally 50 cycles.

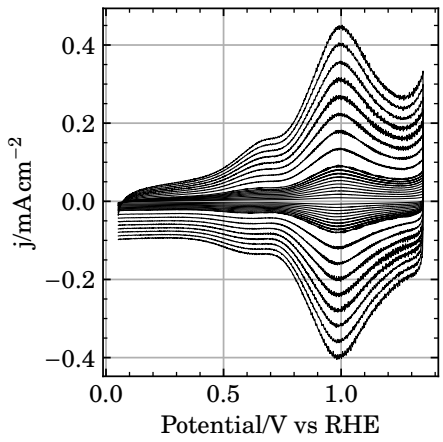

(a) CV charge from run 11

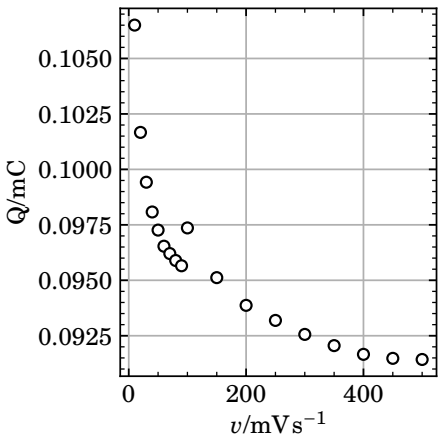

(b) Q vs v 11

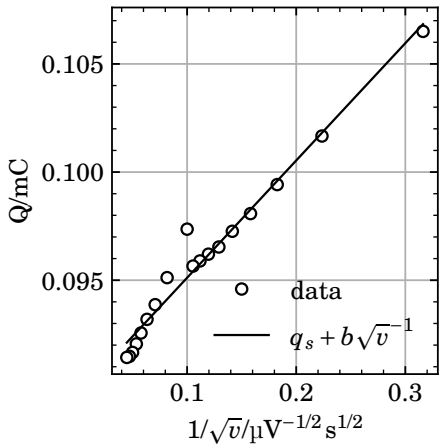

(c) CV charge from run 11

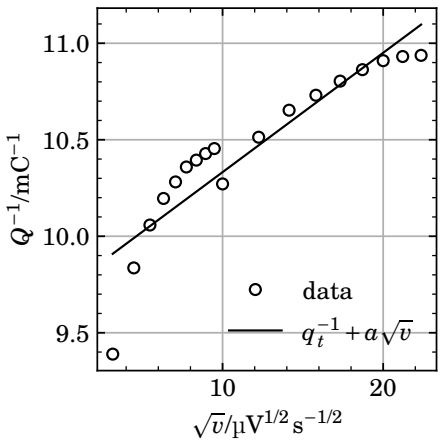

(d) CV charge from run 11

Figure E.72: (a) Voltammograms of an electrode prepared in experiment 11 performed at different potential sweep rates in 0.5 mol dm^{-3} H_2SO_4. (b) Anodic charge of the voltammograms between 0.4 V and 1.3 V versus potential sweep rate. (c) Anodic charge extrapolated to infinite potential sweep rate. (d) Anodic charge extrapolated to zero potential sweep rate.

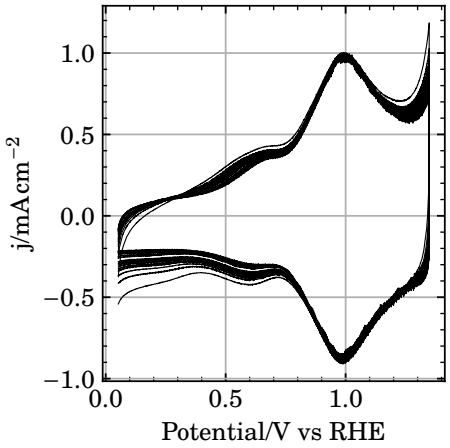

Figure E.73: The voltammograms from figure E.72 (a) normalized to the anodic peak current around 1 V.

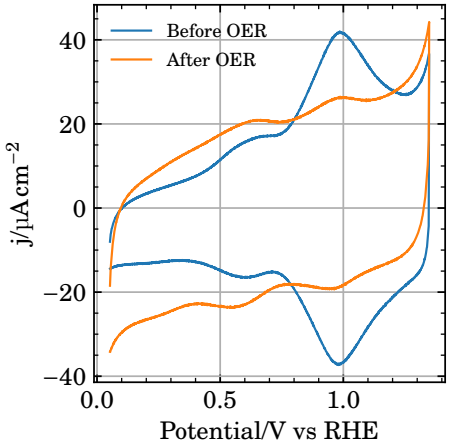

Figure E.74: Voltammograms of an electrode prepared in experiment 11 by the SLRR routine, before and after oxygen evolution. Voltammograms were obtained in 0.5 mol dm^{-3} H_2SO_4 at 50 mV s^{-1}.

E.13 Experiment 12

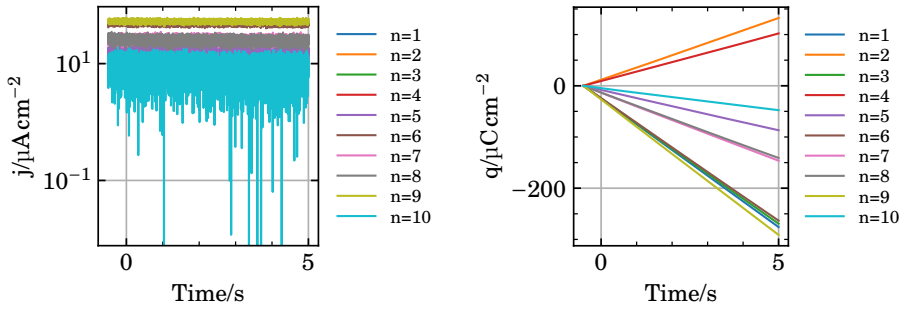

(a) (b)

Figure E.75: Current (a) and charge (b) versus time during each potential hold at 0.7 V in experiment 12.

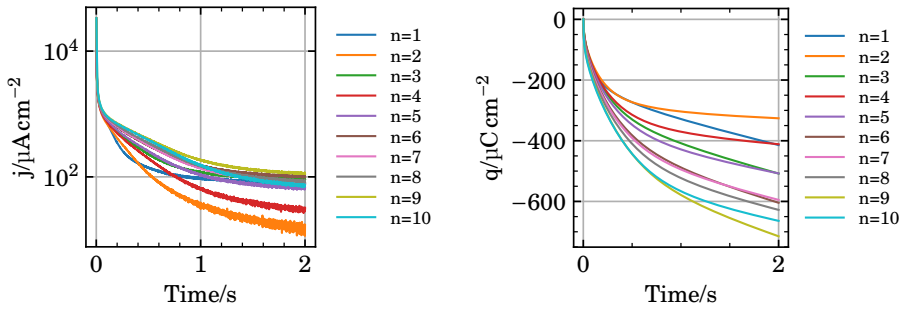

(a) (b)

Figure E.76: Current (a) and charge (b) versus time during each potential hold at 0.34 V in experiment 12.

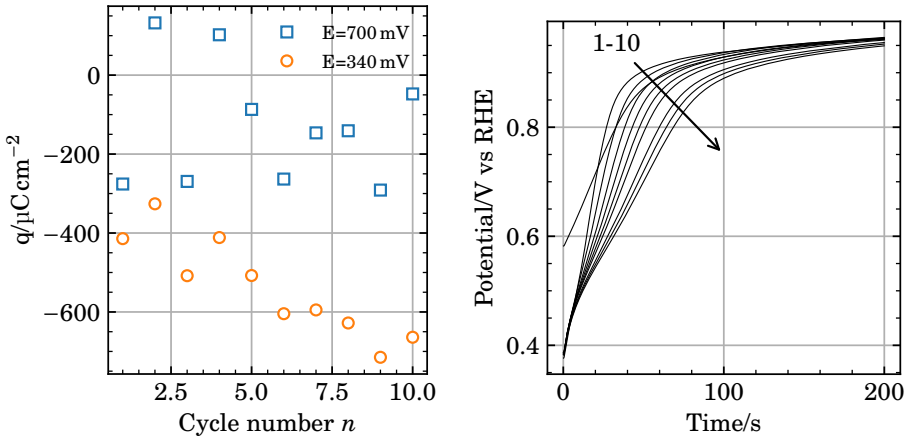

(a) (b)

Figure E.77: (a) is the total charge at the end of each potential hold at 0.7 V or 0.34 V in (blue squares) figure E.75 and (orange circles) figure E.76. (b) is the open circuit potential of the electrode after each potential hold at 0.34 V in figure E.76. The figure correspond to experiment 12.

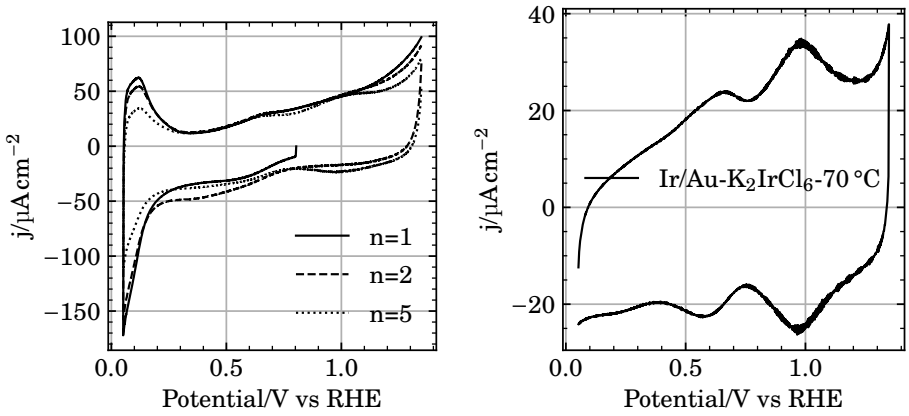

(a) (b)

Figure E.78: Voltammograms of the electrode prepared in experiment 12, obtained in 0.5 mol dm^{-3} H_2SO_4 ar 50 mV s^{-1}. (a) is the first, second and fifth potential cycle. (b) is the voltammogram obtained after extensive potential cycling. Ususally 50 cycles.

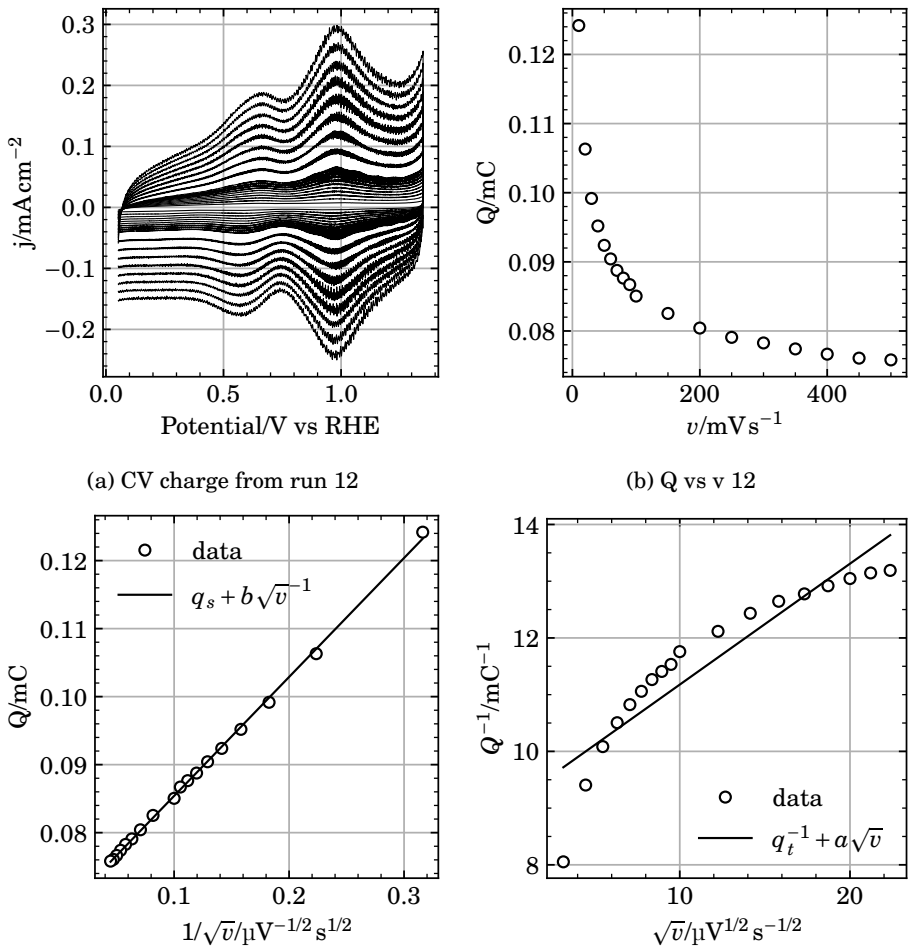

(a) CV charge from run 12

(b) Q vs v 12

(c) CV charge from run 12

(d) CV charge from run 12

Figure E.79: (a) Voltammograms of an electrode prepared in experiment 12 performed at different potential sweep rates in 0.5 mol dm^{-3} H_2SO_4. (b) Anodic charge of the voltammograms between 0.4 V and 1.3 V versus potential sweep rate. (c) Anodic charge extrapolated to infinite potential sweep rate. (d) Anodic charge extrapolated to zero potential sweep rate.

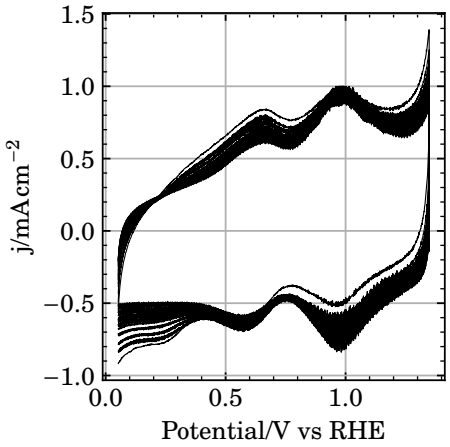

Figure E.80: The voltammograms from figure E.79 (a) normalized to the anodic peak current around 1 V.

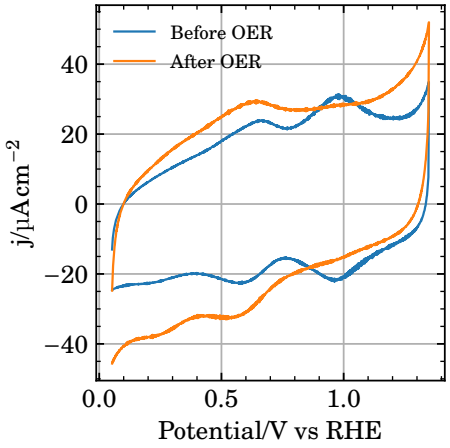

Figure E.81: Voltammograms of an electrode prepared in experiment 12 by the SLRR routine, before and after oxygen evolution. Voltammograms were obtained in 0.5 mol dm^{-3} H_2SO_4 at 50 mV s^{-1}.

E.14 Experiment 13

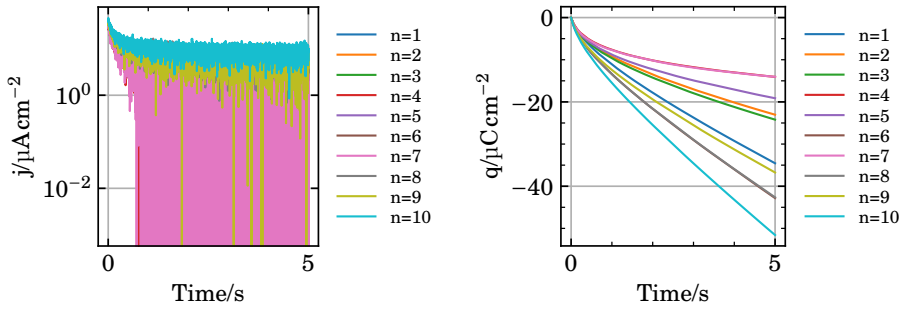

(a) (b)

Figure E.82: Current (a) and charge (b) versus time during each potential hold at 0.7 V in experiment 13.

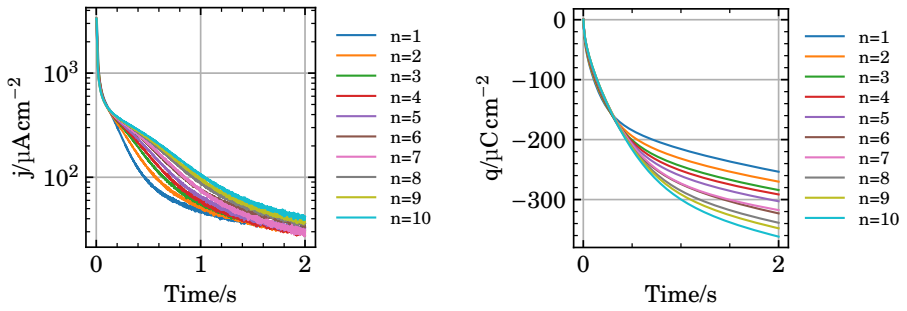

(a) (b)

Figure E.83: Current (a) and charge (b) versus time during each potential hold at 0.34 V in experiment 13.

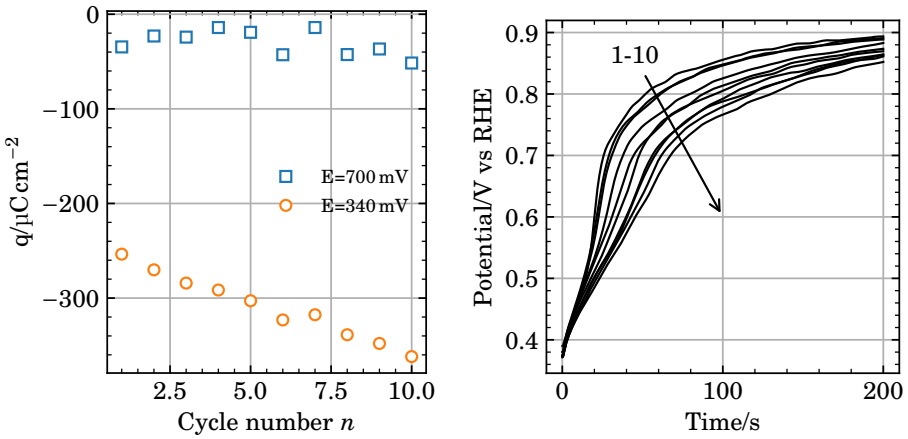

(a) (b)

Figure E.84: (a) is the total charge at the end of each potential hold at 0.7 V or 0.34 V in (blue squares) figure E.82 and (orange circles) figure E.83. (b) is the open circuit potential of the electrode after each potential hold at 0.34 V in figure E.83. The figure correspond to experiment 13.

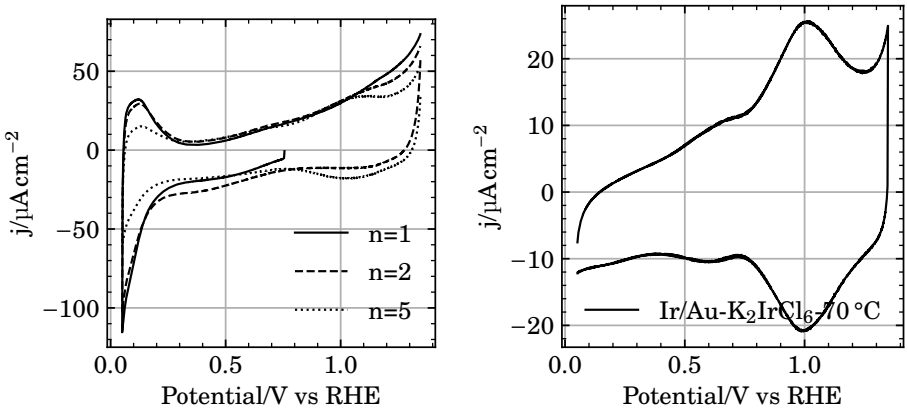

(a) (b)

Figure E.85: Voltammograms of the electrode prepared in experiment 13, obtained in 0.5 mol dm^{-3} H_2SO_4 ar 50 mV s^{-1}. (a) is the first, second and fifth potential cycle. (b) is the voltammogram obtained after extensive potential cycling. Ususally 50 cycles.

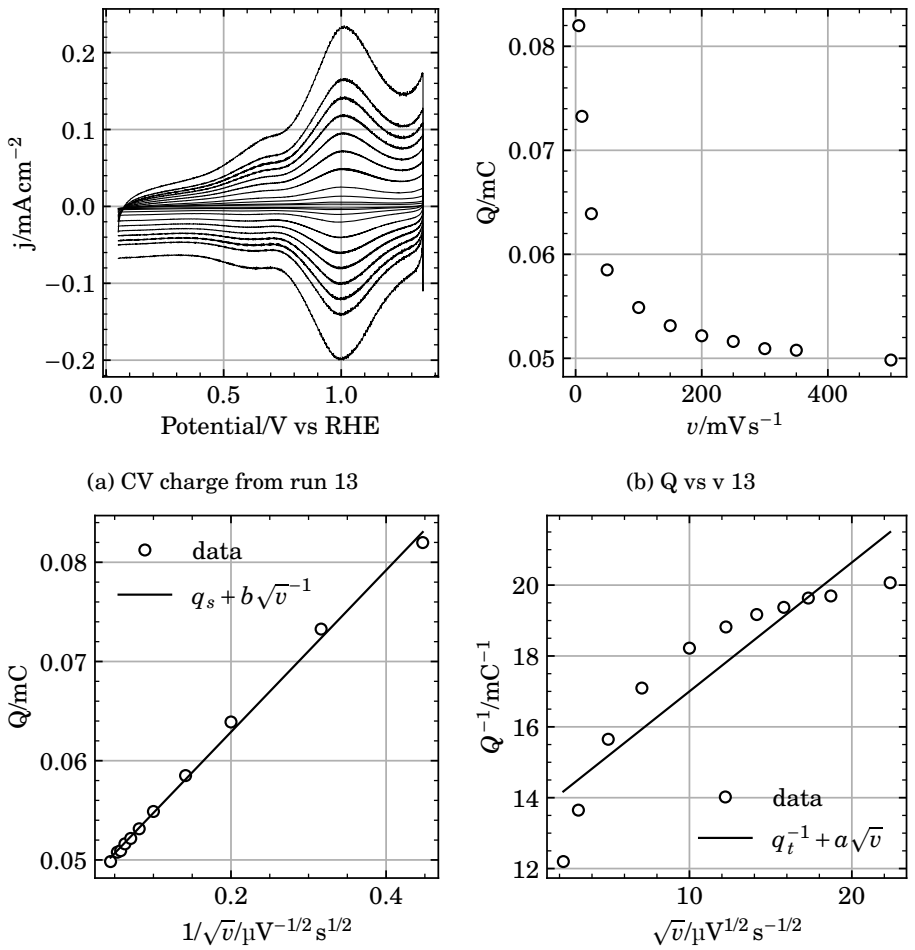

(a) CV charge from run 13

(b) Q vs v 13

(c) CV charge from run 13

(d) CV charge from run 13

Figure E.86: (a) Voltammograms of an electrode prepared in experiment 13 performed at different potential sweep rates in 0.5 mol dm^{-3} H_2SO_4. (b) Anodic charge of the voltammograms between 0.4 V and 1.3 V versus potential sweep rate. (c) Anodic charge extrapolated to infinite potential sweep rate. (d) Anodic charge extrapolated to zero potential sweep rate.

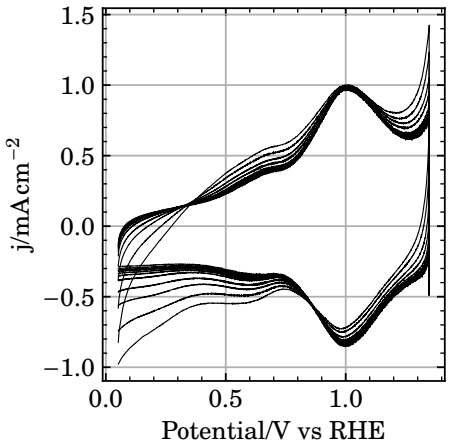

Figure E.87: The voltammograms from figure E.86 (a) normalized to the anodic peak current around 1 V.

E.15 Experiment 14

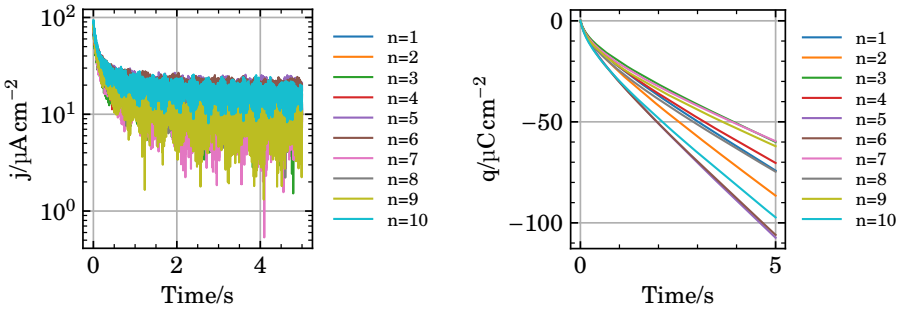

(a) (b)

Figure E.88: Current (a) and charge (b) versus time during each potential hold at 0.7 V in experiment 14.

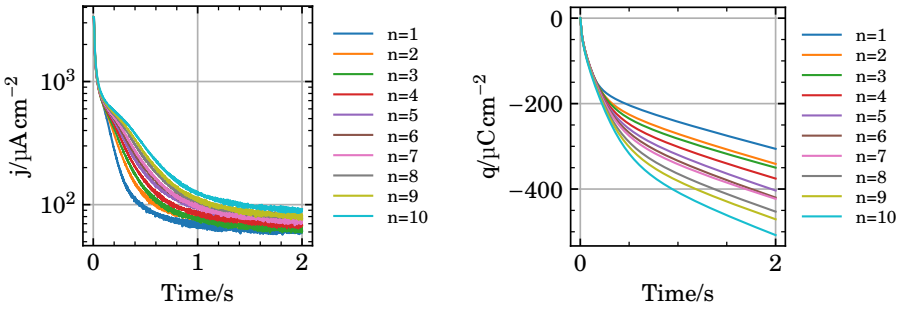

(a) (b)

Figure E.89: Current (a) and charge (b) versus time during each potential hold at 0.34 V in experiment 14.

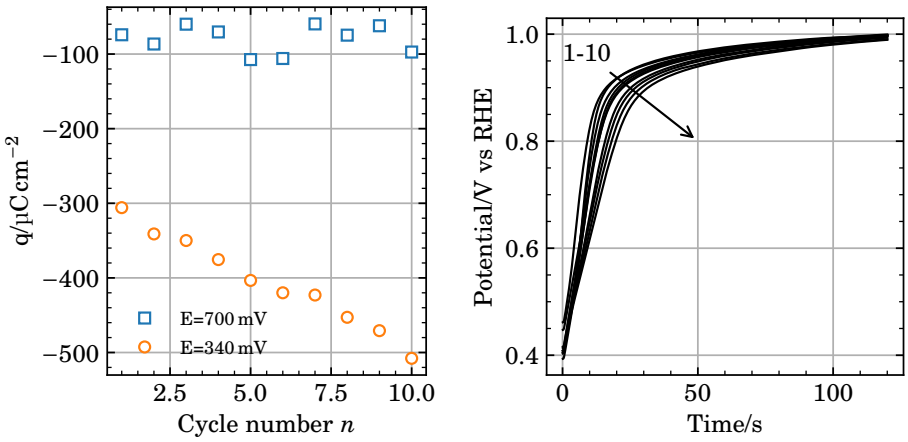

(a) (b)

Figure E.90: (a) is the total charge at the end of each potential hold at 0.7 V or 0.34 V in (blue squares) figure E.88 and (orange circles) figure E.89. (b) is the open circuit potential of the electrode after each potential hold at 0.34 V in figure E.89. The figure correspond to experiment 14.

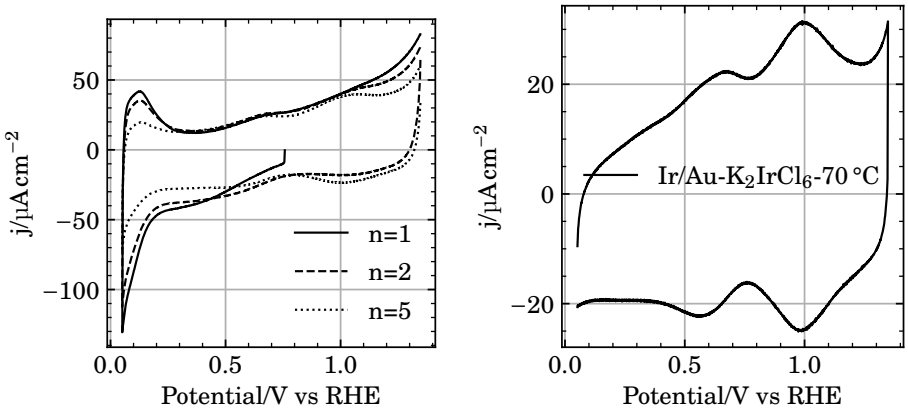

(a) (b)

Figure E.91: Voltammograms of the electrode prepared in experiment 14, obtained in 0.5 mol dm^{-3} H_2SO_4 ar 50 mV s^{-1}. (a) is the first, second and fifth potential cycle. (b) is the voltammogram obtained after extensive potential cycling. Ususally 50 cycles.

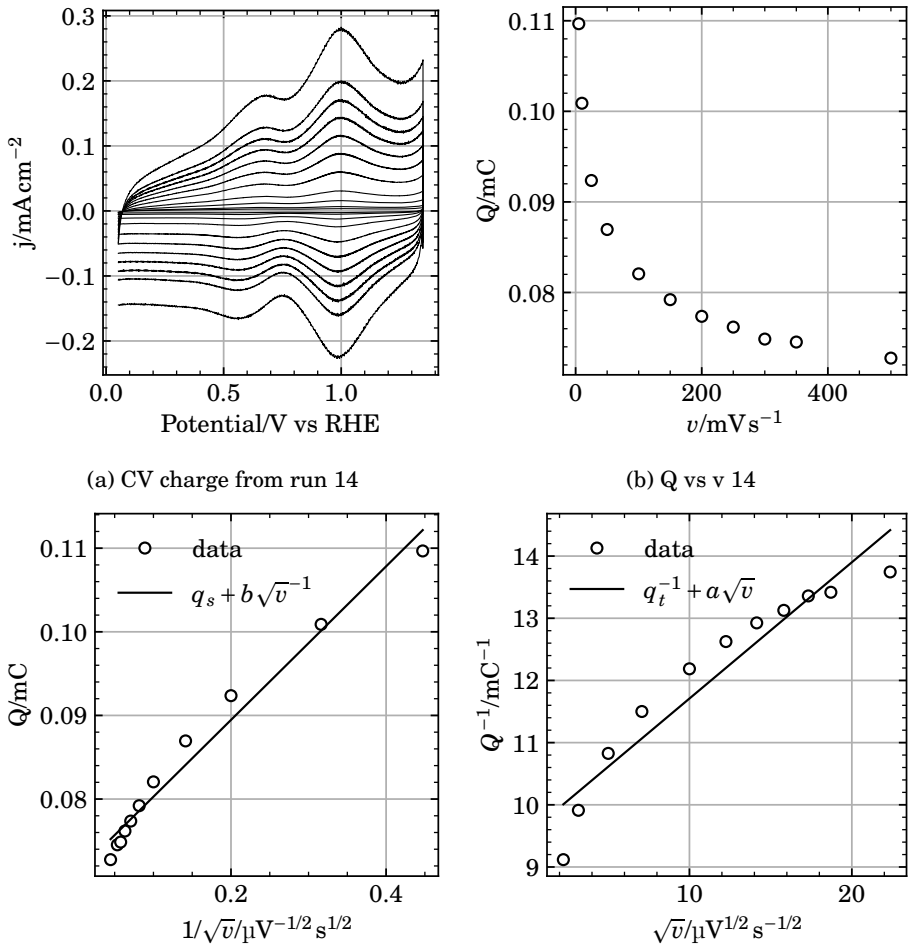

(a) CV charge from run 14

(b) Q vs v 14

(c) CV charge from run 14

(d) CV charge from run 14

Figure E.92: (a) Voltammograms of an electrode prepared in experiment 14 performed at different potential sweep rates in 0.5 mol dm^{-3} H_2SO_4. (b) Anodic charge of the voltammograms between 0.4 V and 1.3 V versus potential sweep rate. (c) Anodic charge extrapolated to infinite potential sweep rate. (d) Anodic charge extrapolated to zero potential sweep rate.

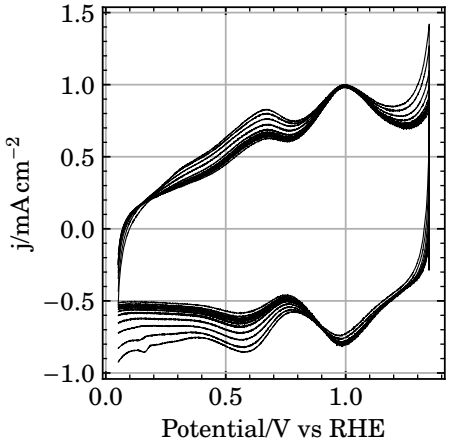

Figure E.93: The voltammograms from figure E.92 (a) normalized to the anodic peak current around 1 V.

E.16 Open circuit potential of the Au electrode under addition of Ir precursor solution

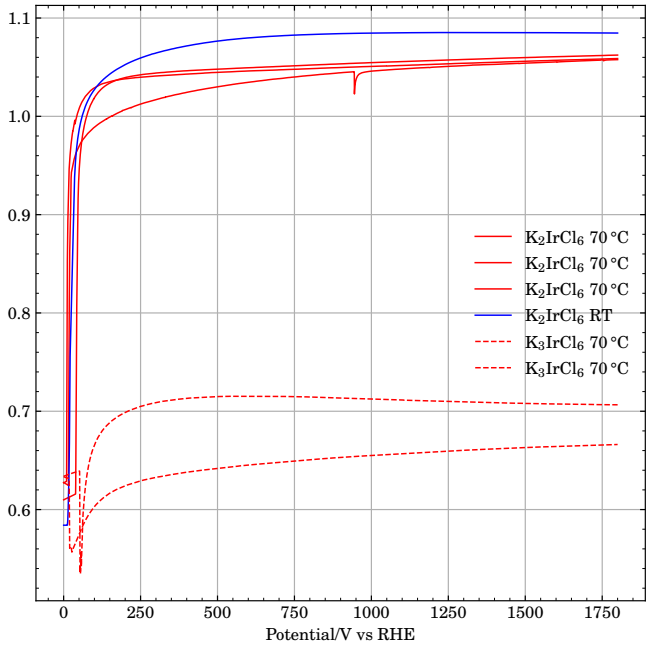

Figure E.94: Open circuit potential of a Au_{poly} working electrode during addition of K_3IrCl_6 or K_2IrCl_6 to a solution containing 0.5 mol dm^{-3} H_2SO_4 or 0.5 mol dm^{-3} H_2SO_4 and 1 mmol dm^{-3} $CuSO_4$ at room temperature or 70 °C. A solution containing 1 mmol dm^{-3} Ir-precursor and 0.5 mol dm^{-3} H_2SO_4 was added so that the final concentration of K_3IrCl_6 or K_3IrCl_6 was 10 µmol dm^{-3}.

E.17 Synthesis of Au_{np}

Au_{np} was prepared using a modified version of the Turkevich method [279, 280], where a solution containing $HAuCl_4$ was added to a refluxing citric acid buffer solution [261]. 15 mL 2.2 mL citric acid (≥ 99.0 %, Sigma) and 45 mL 2.2 mL trisodium citrate (≥ 99.5 %, Sigma) was added to a 100 mL three neck flask equiped with a water cooled condenser, heated by a metal heating mantle. The citrate buffer solution was refluxed for 15 min under vigorous stirring while kept under a N_2(g) blanket. 400 µL of a 25 mmol dm^{-3} $HAuCl_4$ (> 99.9 %, Sigma) solution was then added quickly

to the refluxing citrate buffer solution. After the solution turned wine red (almost immediately), the flask was removed from the heating mantle and left to cool down. The nominal loading of Au_{np} in the suspension was $32.6\,\mu g\,mL^{-1}$.

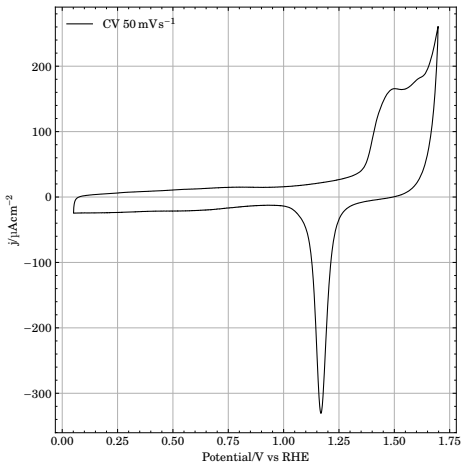

Figure E.95: Voltammograms of an electrode loaded with $40\,\mu L$ Au_{np} suspension. Voltammogram was obtained at $50\,mV\,s^{-1}$ in $0.5\,mol\,dm^{-3}$ H_2SO_4.

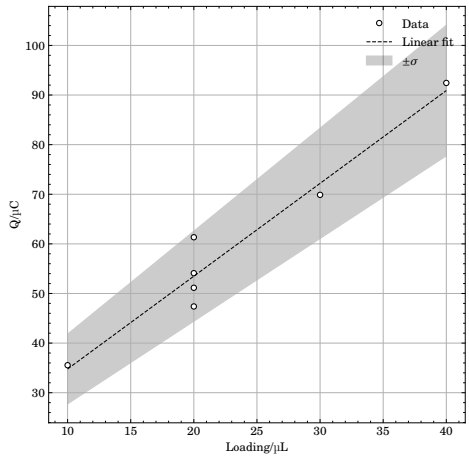

Figure E.96: Charge of the Au reduction peak around 1.15 V in voltammograms of electrodes loaded with 10 µL, 20 µL, 30 µL or 40 µL Au_{np} suspension, similar to figure E.95. Voltammograms were obtained at 50 mV s^{-1} in 0.5 mol dm^{-3} H_2SO_4.

Appendix F

Ir deposition onto Pd by galvanic displacement of PdH_x

Figure F.1 (a) shows voltammograms of IrO_xPd_{poly}:50 obtained in 0.5 mol dm^{-3} H_2SO_4 at sweep rates 5 mV s^{-1}, 10, 20, 30, 40, 50, 75, 100, 150, 200, 250, 300, 350, 400, 450 and 500 mV s^{-1} between 0.3 V and 1.45 V. Figure F.1 (b,c,d) show; (b) the charge between 0.3 V and 1.3 V in the positive going sweeps of the voltammograms in (a) as a function of potential sweeprate and (c) inverse of the charge as a function of the square root of the sweep rate, and (d) as a funtion of the inverse of the square root of the sweep rate.

Figure F.2 shows SEM micrographs of Pd_{poly}:50 (a,b) and IrO_xPd_{poly}:50 (c,d).

Palladium nanoparticles Pd/KB

Figure F.3 shows the current measured at Ir_nPd/KB:25 and Ir_nPd/KB:50 during a 5 mV s^{-1} potential sweep from 0.4 V to −0.1 V. Electrolyte was 0.5 mol dm^{-3} H_2SO_4 and the electrode was rotated at 1600 rpm. Large bubbles was observed at the working electrode at negative potentials. The HER+PdH_x current increased after each displacement event with iridium, indicative of modification of the surface. This is consistent with the higher activity towards HER of iridium to that of palladium [271]. Going from a pure palladium surface to one decorated with iridium, the HER-current increased with roughly 1.5 orders of magnitude.

The voltammograms in figure F.4 displays the H-UPD and PdH_x region of Ir_nPd/KB:25 (b) and Ir_nPd/KB:50 (a) after each successive displacement event. Voltammograms were obtained in 0.5 mol dm^{-3} H_2SO_4 at 50 mV s^{-1}. The Oxidation peak around 50 mV was shifted to more negative potentials and increased in magnitude after the first displacement event at 50 °C (a), and increased slightly in magnitude upon

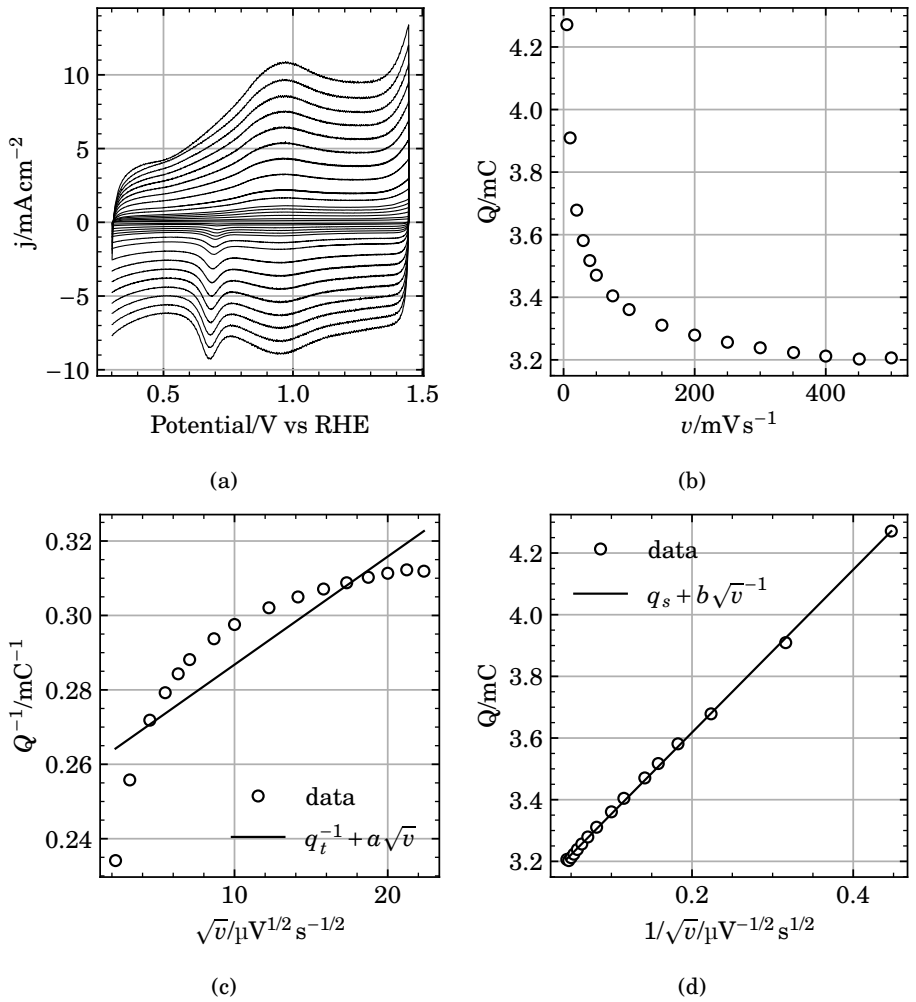

Figure F.1: (a) Voltammograms of IrO_xPd_{poly}:50 obtained in 0.5 mol dm^{-3} H_2SO_4 at sweep rates 5 mV s^{-1}, 10, 20, 30, 40, 50, 75, 100, 150, 200, 250, 300, 350, 400, 450 and 500 mV s^{-1} between 0.3 V and 1.45 V. (b) The anodic charge between 0.4 V and 1.4 V in the voltammograms in (a) asa function of potetial sweep rate. (c) The anodic charge from (b) extrapolated to zero potential sweep rate. (d) The anodic charge from (b) extrapolated to infinite potential sweep rate.

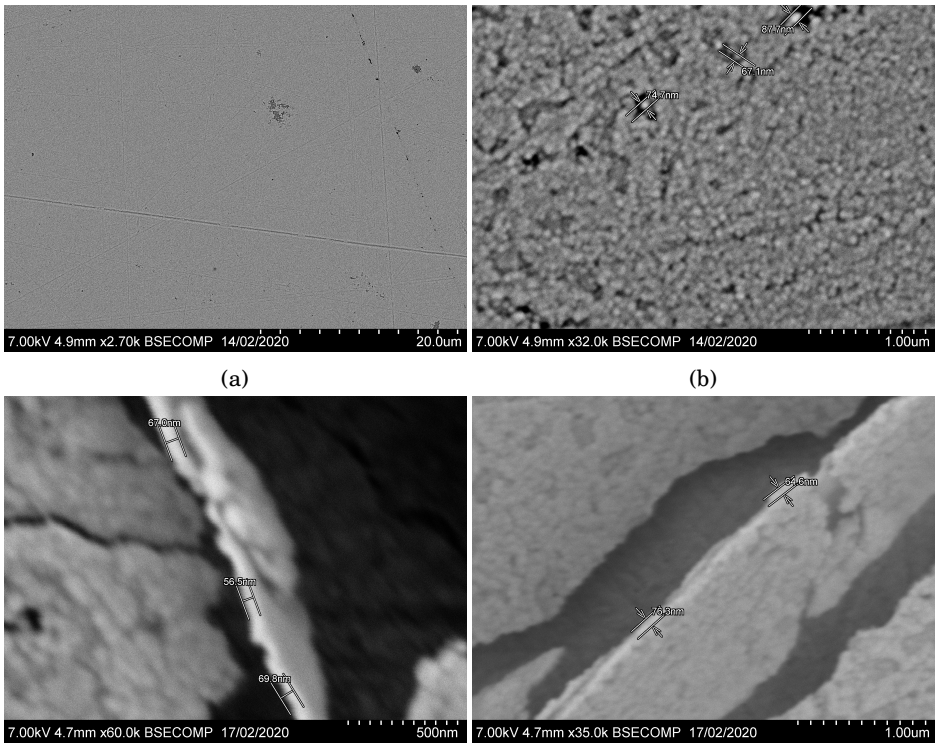

(a) (b)

(c) (d)

Figure F.2: SEM micrographs of Pd_{poly}:50 (a,b) and IrO_xPd_{poly}:50 (c,d).

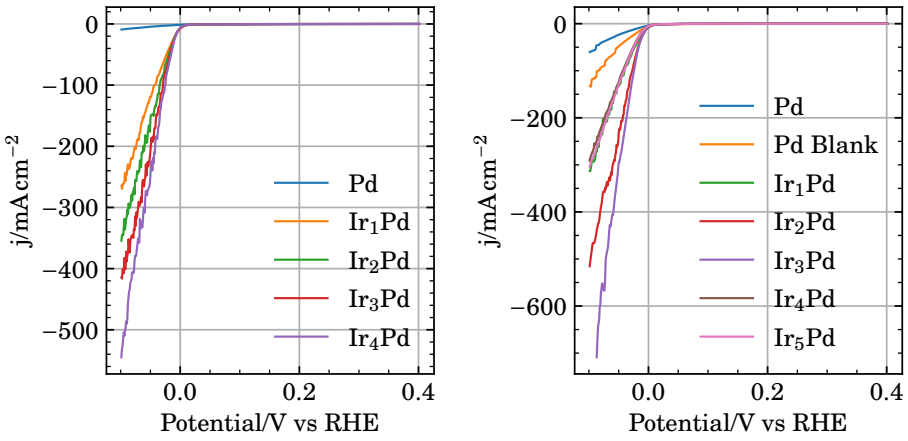

(a) Caption

(b) Caption

Figure F.3: Linear sweep voltammograms of Ir_nPd/KB:25 and Ir_nPd/KB:50. Anodic and cathodic limits was 0.4 V and −0.1 V. Potential sweep rate was 5 mV s^{-1}. Electrolyte was 0.5 mol dm^{-3} H_2SO_4 and the electrode was rotated at 1600 rpm.

further displacement events. This potential shift is consistent with submonolayers of Ir on Pd nanoparticles [113]. The onset potential of the corresponding reduction wave increased in magnitude in a same manner. This not observed to any *significant* extent after any number of displacement events at room temperature (b). The pair of PdH_α peaks around 0.25 V was reduced in magnitude after the first displacement event, and remained constant thereafter in both (a) and (b).

Figure F.5 display cycling voltammograms of Pd/KB, Ir_5Pd/KB:25 and IrO_xPd/KB:25 (b), and Ir_5Pd/KB:50 and IrO_xPd/KB:50 (a) obtained in 0.5 mol dm^{-3} H_2SO_4 at 50 mV s^{-1}.

At about 0.95 V IrO_xPd/KB:50 exhibits a pair of peaks typical for IrO_x in H_2SO_4, consistent with the results obtained on the polycrystalline Pd electrode in figure 9.5.

In the H-UPD region (≈60 mV), the anodic peak indicating weakly bound H_{ads} Ir_5Pd/KB:50 and IrO_xPd/KB:50 appears to be shifted to slightly lower potentials and has an increased magnitude after the displacement procedure.

The H_{ads}/PdH_x-region of Pd/KB and IrO_xPd/KB appears fairly identical between 0.1 V and 0.4 V in both figure F.5 (a) and (b). This is consistent with IrO_x not adsorbing molecular hydrogen like Pd if the coverage of IrO_x on Pd is small. The

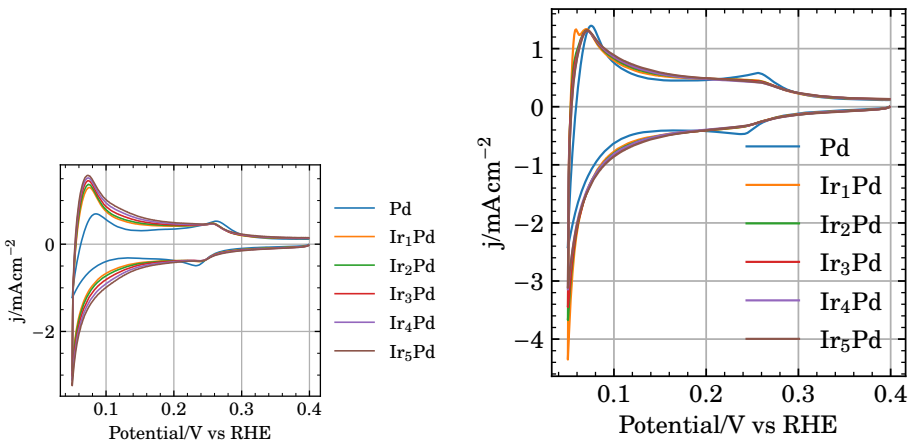

Figure F.4: Cyclic voltammograms of Ir_nPd/KB:25 (b) and Ir_nPd/KB:50 (a) during H-UPD and PdH_x formation and oxidation, and after 0, 1, 2, 3, 4 and 5 displacement events in 10 µmol dm^{-3} K_2IrCl_6 and 0.5 mol dm^{-3} H_2SO_4 at 50 °C (a) or room temperature (b) . Voltammogram obtained at 50 mV s^{-1} in 0.5 mol dm^{-3} H_2SO_4.

small H_{UPD} peaks between 0.1 V and 0.2 V in the voltammogram of Pd/KB disappeared in both Ir_5Pd/KB:25 and Ir_5Pd/KB:50. After transformation to IrO_x, the peaks reappeared.

Figure F.6 show cyclic voltammograms of Pd/C and Ir_5Pd/C. Potential sweep rate was 50 mV s^{-1} and electrolyte was 0.5 mol dm^{-3} H_2SO_4. The anodic potential limit was always 0.4 V, whereas the cathodic limited was reduced from 0.35 V to 0.01 V in steps of −10 mV for each voltammogram.

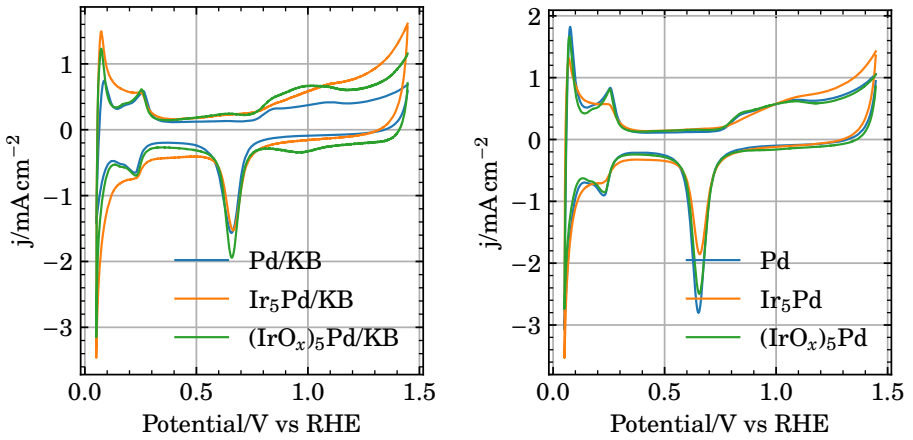

Figure F.5: Cyclic voltammograms of Pd/KB, Ir_5Pd/KB:25 and IrO_xPd/KB:25 (b), and Ir_5Pd/KB:50 and IrO_xPd/KB:50 (a). Potential sweep rate was $50\,mV\,s^{-1}$ and electrolyte was $0.5\,mol\,dm^{-3}$ H_2SO_4.

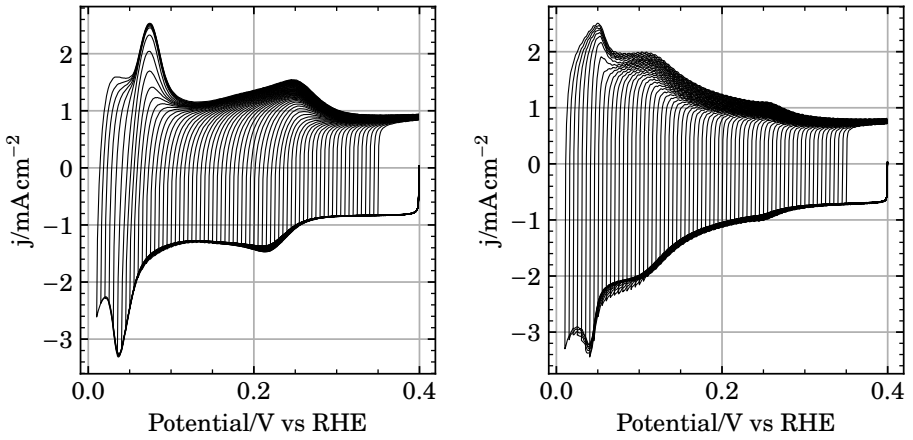

Figure F.6: Cyclic voltammograms of Pd/C and Ir_5Pd/C. Potential sweep rate was $50\,mV\,s^{-1}$ and electrolyte was $0.5\,mol\,dm^{-3}$ H_2SO_4. The anodic potential limit was always 0.4 V, whereas the cathodic limited was reduced from 0.35 V to 0.01 V in steps of −10 mV for each voltammogram.

Appendix G

Simulation of SLRR reactions

G.1 Discrete solution of the transport equation

G.1.1 Discretization

Equations (10.49) to (10.53) and (10.65) to (10.74) are coupled through the surface reactions, equations (10.49) to (10.53), of which are non-linear with respect to Ψ, θ_i and $C_i(X=0)$. An analytical solution to the differential equations presented in the previous paragraphs are unatainable. In order simulate the electrode processes described previously, we discretize the equations using accurate second order central differences in space, indexed j, and backward differences in time, indexed k. Assuming X is equally spaced as ΔX over nj points, we have

$$\mathbf{X} = \begin{bmatrix} X_1 \\ X_2 \\ X_3 \\ \vdots \\ X_j \\ \vdots \\ X_{nj} \end{bmatrix}^T = \begin{bmatrix} -\Delta X \\ 0 \\ \Delta X \\ \vdots \\ (j-2)\Delta X \\ \vdots \\ 1 \end{bmatrix}^T \tag{G.1}$$

where $\Delta X = \frac{1}{nj-2}$, and τ is discretized over nk points where $\Delta\tau_k = \tau_k - \tau_{k-1}$

$$\tau = \begin{bmatrix} \tau_1 \\ \tau_2 \\ \vdots \\ \tau_k \\ \vdots \\ \tau_{nk} \end{bmatrix}^T = \begin{bmatrix} 0 \\ \Delta\tau \\ \vdots \\ (k-1)\Delta\tau \\ \vdots \\ (nk-1)\Delta\tau \end{bmatrix}^T \tag{G.2}$$

Due to the central difference boundary conditions, equations (10.69) to (10.71), $X_1 = -\Delta X$ at $j = 1$ is a ghost point inside the electrode, and the electrode surface is located at $X_2 = 0$, $j = 2$ [15].

C_i, θ_i and Ψ are indexed as $C_{i,j,k}$, $\theta_{i,k}$ and Ψ_k . $\theta_{i,k}$ is bound to the surface, and so index j is implicit. Similarly, the reactions V_l, $l = 1-5$, equations (10.49) to (10.53) are index as $V_{l,k}$.

The indices are tabulated below in table G.1

Table G.1: Overview of the different indexes used in discretizing the model

Index	Dimension
i	Specie $C_{i,j,k}$ or $\theta_{i,k}$
j	Point in space
k	Point in time
l	Reaction number $l = 1,2,3,4$ or 5

Equations (10.65) to (10.68) are thus discretized in Equations (G.3) to (G.6)

$$\frac{\theta_{1,k} - \theta_{1,k-1}}{\Delta\tau} = V_{1,k} - V_{2,k} \tag{G.3}$$

$$\frac{\theta_{2,k} - \theta_{2,k-1}}{\Delta\tau} = V_{2,k} \tag{G.4}$$

$$\frac{\theta_{3,k} - \theta_{4,k-1}}{\Delta\tau} = V_{4,k} - V_{5,k} \tag{G.5}$$

$$\frac{\theta_{4,k} - \theta_{5,k-1}}{\Delta\tau} = V_{5,k} \tag{G.6}$$

and the boundary conditions at $X = 0$, equations (10.69) to (10.71) are discretized in equations (G.7) to (G.9)

$$\xi_1 \frac{C_{1,2,k} - C_{1,0,k}}{\Delta X_1} (1 - X_2)(2\ln 2)|_{X=0} = V_{1,k} \tag{G.7}$$

$$\xi_2 \frac{C_{2,2,k} - C_{2,0,k}}{\Delta X_1} (1 - X_2)(2\ln 2)|_{X=0} = V_{3,k} \tag{G.8}$$

$$\xi_3 \frac{C_{3,2,k} - C_{3,0,k}}{\Delta X_1} (1 - X_2)(2\ln 2)|_{X=0} = V_{4,k} - V_{3,k} \tag{G.9}$$

The main transport equation, equation (10.73), are discretized as equation (G.10)

$$\begin{aligned} \frac{C_{i,j,k} - C_{i,j,k-1}}{\Delta\tau} =& \xi_i \frac{C_{i,j+1,k} + C_{i,j-1,k} - 2C_{i,j,k}}{\Delta X^2} \left(1 - X_j\right)^2 (2\ln 2)^2 \\ &+ \beta \frac{\ln\left(1 - X_j\right)^2}{(2\ln 2)} \frac{C_{i,j+1,k} - C_{i,j-1,k}}{2\Delta X} \left(1 - X_j\right) \end{aligned} \tag{G.10}$$

and at all times, the outer boundary at $X = 1$ is discretized in equation (G.11)

$$\lim_{X \to 1} C_{i,nj,k} = C_{i,nj,0} \tag{G.11}$$

Finally, the expression for the total dimensionless current are discretized as

$$J_k = V_{1,k} + V_{2,k} + V_{3,k} + 3V_{5,k} + \mathscr{C}_{dl} \frac{\Psi_k - \Psi_{k-1}}{\Delta\tau} \tag{G.12}$$

G.1.2 The linear equation set

With the main transport equation equation (G.10) discretized, we move everything to the the left hand side, collect the terms and re-organize to obtain

$$\begin{aligned} & C_{i,j,k} - C_{i,j,k} \\ & \quad - \xi_i \frac{\Delta\tau}{\Delta X_l^2} \left(1 - X_j\right)^2 (2\ln 2)^2 \left(C_{i,j+1,k} + C_{i,j-1,k} - 2C_{i,j.k}\right) \\ & \quad - \beta \frac{\Delta\tau}{2\Delta X} \frac{\ln\left(1 - X_j\right)^2}{(2\ln 2)} \left(1 - X_j\right) \left(C_{i,j+1,k} - C_{i,j-1,k}\right) = 0 \end{aligned} \tag{G.13}$$

where we can collect the terms as

$$\left(-\lambda_{i,j}+\mu_j\right)C_{i,j-1,k}+\left(1+2\lambda_{i,j}\right)C_{i,j,k}+\left(-\lambda_{i,j}-\mu_j\right)C_{i,j+1,k}-C_{i,j,k-1}=0 \qquad \text{(G.14)}$$

where $\lambda_{i,j}=\xi_i\frac{\Delta\tau}{\Delta X_j^2}\left(1-X_j\right)^2\ln(4)^2$ and $\mu_j=\beta\frac{\Delta\tau}{2\Delta X}\frac{\ln(1-X_j)^2}{(2\ln 2)}\left(1-X_j\right)$

The same procedure can be applied to equations (G.3) to (G.9), (G.11) and (G.12)

Depending on whether a potentiostatic or galvanostatic experiment is simulated, the necessary equations at each grid point j in the system are as follows, where equation (G.15) is only included in the latter case. $X=0$ appears twice, as $X=-\Delta X$ is a ghost point inside the electrode [15].

at $X=0$**,** $j=1$

$$I+\left(V_{1,k}+V_{2,k}+V_{3,k}+3V_{5,k}+\mathscr{C}_{dl}\frac{\Psi_k-\Psi_{k-1}}{\Delta\tau}\right)=0 \quad \text{In galvanostatic mode} \qquad \text{(G.15)}$$

$$\theta_{1,k}-\theta_{1,k-1}-\Delta\tau\left(V_{1,k}-V_{2,k}\right)=0 \qquad \text{(G.16)}$$

$$\theta_{2,k}-\theta_{2,k-1}+\Delta\tau\left(V_{2,k}\right)=0 \qquad \text{(G.17)}$$

$$\theta_{3,k}-\theta_{3,k-1}-\Delta\tau\left(V_{4,k}-V_{5,k}\right)=0 \qquad \text{(G.18)}$$

$$\theta_{4,k}-\theta_{4,k-1}-\Delta\tau\left(V_{5,k}\right)=0 \qquad \text{(G.19)}$$

$$C_{1,2,k}-C_{1,0,k}-\frac{\Delta X}{\xi_1\ln(2)}V_{1,k}=0 \qquad \text{(G.20)}$$

$$C_{2,2,k}-C_{2,0,k}-\frac{\Delta X}{\xi_2\ln(2)}V_{3,k}=0 \qquad \text{(G.21)}$$

$$C_{3,2,k}-C_{3,0,k}-\frac{\Delta X}{\xi_3\ln(2)}\left(V_{4,k}-V_{3,k}\right)=0 \qquad \text{(G.22)}$$

Where I is the desired current density at the electrode in a galvanostatic simulaiton.

at $0\le X<1$**,** $1\le j<nj$

$$\left(-\lambda_{1,j}+\mu_j\right)C_{1,j-1,k}+\left(1+2\lambda_{1,j}\right)C_{1,j,k}+\left(-\lambda_{1,j}-\mu_j\right)C_{1,j+1,k}-C_{1,j,k-1}=0 \qquad \text{(G.23)}$$

$$\left(-\lambda_{2,j}+\mu_j\right)C_{i,j-1,k}+\left(1+2\lambda_{2,j}\right)C_{2,j,k}+\left(-\lambda_{2,j}-\mu_j\right)C_{2,j+1,k}-C_{2,j,k-1}=0 \qquad \text{(G.24)}$$

$$\left(-\lambda_{3,j}+\mu_j\right)C_{3,j-1,k}+\left(1+2\lambda_{3,j}\right)C_{3,j,k}+\left(-\lambda_{3,j}-\mu_j\right)C_{3,j+1,k}-C_{3,j,k-1}=0 \qquad \text{(G.25)}$$

at $X=1$**,** $j=nj$

$$C_{1,nj,k}=C_{1,nj,0} \qquad \text{(G.26)}$$

$$C_{2,nj,k}=C_{2,nj,0} \qquad \text{(G.27)}$$

$$C_{3,nj,k}=C_{3,nj,0} \qquad \text{(G.28)}$$

G.2 Pseudocode

```
function equations(c, mode, Z, dt, *constants):
    # c contain all the unknowns
    # dt is step size in time
    # constants contains rate constants, step size in space, etc.
    eqs = matrix_size_of(c)

    if mode is pstat:
        Z is potential
        save Z in eqs[0]
    if mode is gstat:
        Z is current
        calculate sum of currents J
        eqs[0] = Z - J
    eqs[1::] = other governing equations
    return eqs
#=========================================================
function integrate(func, t, Z, mode, c, *constants)
    c_old = c
    c_try = c
    c_out = []

    for each dt in gradient(t):
        while (iteration<max iterations) and (error>tolerance):
            A = jacobian(func, c_try, c_old, mode, Z, dt, *constants)
            b = -func(c, mode, Z, dt, *constants)
            dc = solve(A,b)
            c_try = c_try + dc
        append c_try to c_out
        c_old = c_try
    return c_out
 #=========================================================
function model(t, Z, mode, c0, cb, *constants):
    if c0 is 1 dimensional:
        n = number of unknonws at the electrode surface
        c = matrix_size_(n,nj)
    if c0 is 2 dimensionsional:
        c = c0
```

```
    simulation = integrate(equations, t, Z, mode, c, *constants)
    return simulation
#=========================================================
```

ISBN 978-82-326-6931-8 (printed ver.)
ISBN 978-82-326-5812-1 (electronic ver.)
ISSN 1503-8181 (printed ver.)
ISSN 2703-8084 (online ver.)

NTNU
Norwegian University of
Science and Technology